ESPOO 2004

VTT PUBLICATIONS 531

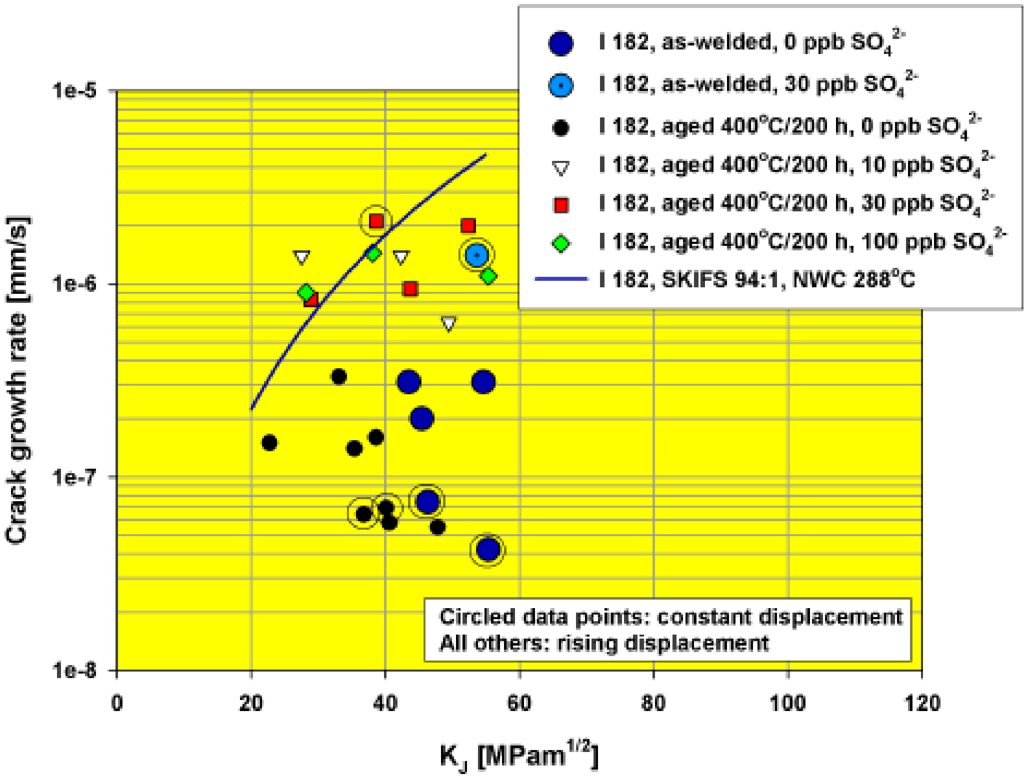

Aki Toivonen

Stress corrosion crack growth rate measurement in high temperature water using small precracked bend specimens

VTT PUBLICATIONS 531

Stress corrosion crack growth rate measurement in high temperature water using small precracked bend specimens

Aki Toivonen

VTT Industrial Systems

Dissertation for the degree of Doctor in Science in Technology
to be presented with due permission of the Department
of Mechanical Engineering, Helsinki University of Technology,
for public examination and debate in Auditorium E
at Helsinki University of Technology (Espoo, Finland)
on the 18th of June, 2004, at 12 noon.

ISBN 951–38–6382–4 (soft back ed.)
ISSN 1235–0621 (soft back ed.)

ISBN 951–38–6383–2 (URL: http://www.vtt.fi/inf/pdf/)
ISSN 1455–0849 (URL: http://www.vtt.fi/inf/pdf/)

JULKAISIJA – UTGIVARE – PUBLISHER

VTT, Vuorimiehentie 5, PL 2000, 02044 VTT
puh. vaihde (09) 4561, faksi (09) 456 4374

VTT, Bergsmansvägen 5, PB 2000, 02044 VTT
tel. växel (09) 4561, fax (09) 456 4374

VTT Technical Research Centre of Finland, Vuorimiehentie 5, P.O.Box 2000, FIN–02044 VTT, Finland
phone internat. + 358 9 4561, fax + 358 9 456 4374

VTT Tuotteet ja tuotanto, Rakenteiden elinikä ja kestävyys, Kemistintie 3, PL 1704, 02044 VTT
puh. vaihde (09) 4561, faksi (09) 456 7002, (09) 456 5875

VTT Industriella system, Material och strukturell integritet, Kemistvägen 3, PB 1704, 02044 VTT
tel. växel (09) 4561, fax (09) 456 7002, (09) 456 5875

VTT Industrial Systems, Materials and Structural Integrity,
Kemistintie 3, P.O.Box 1704, FIN–02044 VTT, Finland
phone internat. + 358 9 4561, fax + 358 9 456 7002, + 358 9 456 5875

Technical editing Leena Ukskoski

Otamedia Oy, Espoo 2004

Toivonen, Aki. Stress corrosion crack growth rate measurement in high temperature water using small precracked bend specimens. Espoo 2004. VTT Publications 531. 206 p. + app. 9 p.

Keywords stress corrosion cracking, stress corrosion testing, linear-elastic fracture mechanics, elastic-plastic fracture mechanics, boiling water reactor, stainless steel, nickel-base weld metal, crack growth rate, fracture surface morphology

Abstract

The applicability of elastic-plastic fracture mechanics to stress corrosion crack growth rate measurements was studied. Several test series were performed on small elastic-plastically loaded SEN(B) specimens in high temperature water. One test was performed on a 25 mm C(T) specimen under linear-elastic loading. The tests on the SEN(B) specimens were performed using either rising displacement or a combination of rising and constant displacement loading. The test on the 25 mm C(T) specimen was performed using a combination of constant load and constant displacement.

The studied materials were AISI 304 steel in sensitized, mill-annealed and irradiated conditions, AISI 316 in cold-worked condition, Inconel 82 and 182 weld metals in as-welded and thermally aged conditions and ferritic low activation steel F82H in tempered condition. The crack growth rate tests were performed in simulated pure BWR water and simulated BWR water with 10–100 ppb SO_4^{2-} at 230–290°C.

It was shown that intergranular stress corrosion cracking susceptibility can be determined using an elastic-plastic fracture mechanics approach. Fracture surface morphology in sensitized AISI 304 and welded AISI 321 steels depends on the applied loading rate in BWR water. The fracture surface morphology changes from transgranular to intergranular, when J-integral increase rate is decreased. However, extremely slow displacement rate is needed for the fracture surface morphology to be fully intergranular. Rising J results in transgranular stress corrosion cracking (or strain-induced corrosion cracking) also in the mill-annealed AISI 304 and 321 steels.

Tests on irradiated AISI 304 steel showed that welding together with exposure to low neutron fluence in the BWR operating conditions results in a higher susceptibility to stress corrosion cracking than welding or irradiation alone.

Ferritic low activation steel F82H (in tempered condition) is not susceptible to stress corrosion cracking under static loading conditions in high temperature water. However, its fracture resistance is clearly lower in water than in inert environment.

Even as low an amount as 10 ppb SO_4^{2-} in the otherwise pure BWR water results in one order of magnitude higher stress corrosion crack growth rate than the crack growth rate is in the pure water. Higher sulphate concentrations do not increase the crack growth rate further. Inconel 82 weld metal is much more resistant to stress corrosion cracking than Inconel 182 weld metal. No relevant crack growth rates could be measured for Inconel 82 weld metal in this work.

Cold-worked (20%) AISI 316 steel is susceptible to intergranular stress corrosion cracking in BWR water. Sulphate in BWR water increases the crack growth rate also for AISI 316 steel. However, the observed effect was not as pronounced as for Inconel 182 weld metal.

The results indicate that the same crack growth rates can be obtained using small SEN(B) specimens under elastic-plastic loading conditions and large specimens predominantly under linear-elastic loading conditions. The crack growth rates of the studied IGSCC susceptible materials were independent of the stress intensity factor level, K_J or K_I, in the studied stress intensity ranges. At very low J-integral increase rates, the crack growth rate is linearly dependent on the loading rate.

Loading rate may be a better parameter to correlate with the crack growth rate than the load, e.g., stress intensity factor. The observed dependence between crack growth rate and dJ/dt implicates that the specimen size has an effect on the crack growth rate in constant load tests. In constant load tests the specimen size, dJ/dt and crack growth rate are interconnected.

Preface

This work was carried out at VTT Industrial Systems, Technical Research Centre of Finland.

This work consists of 6 separately performed experimental test series. The different test series were performed under several national research programmes, i.e., the Nuclear Power Plant Structural Safety Research Programme, the Programme on the Structural Integrity of Nuclear Power Plants, the Research Programme on Plant Life Management and the Finnish Fusion Programme. The research programmes were funded mainly by the Finnish Ministry of Trade and Industry, the Radiation and Nuclear Safety Authority STUK, Teollisuuden Voima Oy, Fortum Oy, the National Technology Agency Tekes, VTT and to a smaller extent by other energy and process industries in Finland. All of them are gratefully aknowledged.

I wish to express my gratitude to professors Hannu Hänninen and Kim Wallin for their advice, guidance, and criticism during the preparation of this thesis.

This work would never have been concluded without a number of colleagues. Some, but not all, people who have contributed, in one way or other, are Pertti Aaltonen, Esko Arilahti, Ulla Ehrnstén, Päivi Karjalainen-Roikonen, Petri Kinnunen, Arvo Käki, Timo Laitinen, Eero Lindegren, Marketta Mattila, Pekka Moilanen, Kari Mäkelä, Timo Saario, Laura Taivalaho, and Seppo Tähtinen. All of them (and those who are not mentioned, but have had some contribution to this work) are gratefully acknowledged.

I am also thankfull to my parents Pentti and Pirkko Toivonen for encouraging me to push a little further.

Contents

Original features

This work aims at the understanding of the conditions under which elastic-plastic fracture mechanics based approach can be used to generate relevant stress corrosion crack growth rate data for safety analysis of crack containing structures in environments causing stress corrosion cracking. The following features of this work are believed to be original:

1. A large amount of crack growth rate data was generated using small SEN(B) specimens under elastic-plastic loading conditions. Based on the results, elastic-plastic fracture mechanics is applicable when stress corrosion based structural safety analysis is performed.

2. A new method to determine energy release rate solution for J-integral was developed (Appendix 1). It was shown that ASTM E 1820-99 procedure to calculate J-integral can be utilized even though the displacement rate was varying during the test.

3. A plateau crack growth rate independent of stress intensity factor was observed in sensitized AISI 304 steel and in Inconel 182 weld metal in BWR water.

4. It is claimed that J-integral increase rate is a better loading parameter than K_I, at least when the plateau crack growth rate is of interest. This approach can be used also in safety analyses for structures under changing loading conditions.

5. In the plateau crack growth rate range, the dependence between the crack growth rate and J-integral increase rate can be described using a linear relation:

   CGR = y(0) + y(1) * dJ/dt

6. It was observed that as low as 10 ppb SO_4^{2-} in BWR water results in a considerable increase in stress corrosion crack growth rate in Inconel 182 weld metal. Available literature data covers higher sulphate concentrations.

List of abbreviations and used terminology

1T CT	One inch compact tension (specimen type)
A	Area under load-load line displacement curve, crack tip plastic zone size or material and environment dependent constant in slip oxidation model
A_{pl}	Plastic part of the area under load-load line displacement curve
a	Crack length, atomic diameter or interatomic spacing
a_0	Initial crack length
Δa	Crack extension
Δa_{max}	Maximum allowed crack extension
b	Remaining ligament
b_0	Initial ligament
B	Specimen thickness
B_n	Net thickness of a side-grooved specimen
B_e	Effective thickness, $B_e = B-(B-B_n)^2/B$
CEFM	Coupled environment fracture model
CGR	Crack growth rate
C-ring	Specimen type
C_{LL}	Elastic slope
d	Half crack length of a finger nail shape crack
D_s	Surface diffusion coefficient
Daisy-chain	Two or more specimens in serial connection in a single loading frame
DCB	Double cantilever beam (specimen type)
dpa	Displacements per atom (measure for irradiation damage)
E	Young’s modulus
EAC	Environmentally assisted cracking
F	Faraday’s constant
HAZ	Heat affected zone of a weld
HRR singularity model	Model developed by Hutchinson, Rice, and Rosengren
HWC	Hydrogen water chemistry
IASCC	Irradiation assisted stress corrosion cracking

i_0	Dissolution current density when the crack tip is free of oxide
i_t	Time dependent current density
IGSCC	Intergranular stress corrosion cracking
I_n	Integration constant, which depends on n (HRR singularity model)
ITER	International thermonuclear experimental reactor
J	J-integral
J_{IC}	J-level for crack initiation
J_{pl}	Plastic component of J
J-R curve	Fracture resistance curve (J as a function of crack extension)
k	Boltzman's constant
K_I, K_{II}, K_{III}	Stress intensity factors for mode I, II and III loading, respectively
K_{IC}	Critical stress intensity
K_J	J presented in K_I units
K_{ISCC}	Threshold stress intensity factor for SCC
L	Diffusion path length
LAS	Low activation steels (more common: low alloy steel)
LAF	Low activation ferritic steel
LAM	Low activation martensitic steel
LEFM	Linear-elastic fracture mechanics
LTS	Low temperature sensitization
m	Dimensionless constant, ~1 in plane stress and ~2 in plane strain condition
M	Atomic weight
n	Strain hardening exponent or material and environment dependent constant in slip oxidation model
PD	Potential drop (method for crack length measurement)
PWR	Pressurized water reactor
Q	Oxidation charge density
r	Distance from the crack tip (behind or ahead)
r_p	Size of the plastic zone ahead of the crack tip
r_y	Plastic zone radius
R	A zone size proportional to the plastic zone (RDS model) or load ratio in fatigue

RDS model	Model developed by Rice, Drugan and Sham
S	Roller pin span
SCC	Stress corrosion cracking
SDVC	Selective dissolution –vacancy creep model
SEN(B)	Single edge notched bend (specimen type)
SIMS	Secondary ion mass spectrometer
SSRT	Slow strain rate test
T	Temperature
t	Time after the crack tip is free of oxide
t_0	Time when the crack tip is free of oxide
TGSCC	Transgranular stress corrosion cracking
U	Potential between potential drop measurement leads or area below load-displacement curve
U_p	Area under the plastic part of load-displacement curve
U_0	Initial potential between potential drop measurement leads
U-bend	Specimen type
V_{pl}	Plastic component of load line displacement
W	Specimen width
Y	Geometrical factor
y	Distance of potential drop measurement leads from the crack plane
z	Number of electrons involved in the oxidation of a metal atom
α	Dimensionless constant (HRR singularity model or RDS model)
β	Dimensionless constant (RDS model)
Δ	Load line displacement
ε	Strain
ε_{ct}	Crack tip strain
ε_f	Strain needed for oxide to rupture
ε_p	Plastic strain at a distance r ahead of the crack tip
δ	Crack tip opening displacement
δ_5	Modified crack tip opening displacement according to Brocks et al.
ρ	Density

λ	Dimensionless constant (according to the model of Shoji et al.)
κ	Geometry and stress state dependent factor (δ_5 and J relation) or conductivity
ζ	Geometry and stress state dependent factor (δ_5 and J relation)
λ	Geometry and stress state dependent factor (δ_5 and J relation)
η	Dimensionless specimen geometry dependent constant
ν	Poisson's ratio
σ	Stress
σ_0	Yield stress
σ_{YS}	Uniaxial yield stress of the material
σ_f	Flow stress, average of both yield stress and ultimate tensile strength
σ_{UTS}	Ultimate tensile strength
θ	Angle relative to the crack plane
$\widetilde{\sigma}_{ij}$	Dimensionless function of n and θ (HRR singularity model)
$\widetilde{\varepsilon}_{ij}$	Dimensionless function of n and θ (HRR singularity model)

1. Introduction

Stress Corrosion Cracking (SCC) is caused by tensile stress and corrosive environment together. The stress may be residual, applied, or a combination of both of them. It is typical for SCC that cracking takes place at lower stress levels than in dry air or in an inert environment. Cracks can propagate through grains (transgranular stress corrosion cracking, TGSCC) or along grain boundaries (intergranular stress corrosion cracking, IGSCC) depending on material, environment and loading conditions.

Actual stress corrosion mechanisms are not clearly known, although many explanations have been presented [1]. Probably different mechanisms are in action depending on the environment, material and loading condition. Generally, the mechanisms can be divided to anodic dissolution mechanisms and cathodic hydrogen induced cracking mechanisms [2].

SCC may lead to a component failure or even to a catastrophic failure of a structure when the crack reaches a critical size. Not all of the problematic material-environment-loading combinations are known. New materials are developed, old materials are used in new applications, material properties may change with time (e.g., thermal aging) or due to material processing (e.g., welding, cold work). Therefore, it is important to test the SCC susceptibility of the materials that are candidates for a structural component or a construction before they are taken into use. This may prevent long term economic losses and even accidents.

The available selection of SCC testing methods is very wide. The test methods range from qualitative tests, which are suitable for material screening, to quantitative tests, in which crack propagation rate is measured as a function of a loading parameter, e.g., stress intensity factor K_I. However, the distinction between the qualitative and quantitative test methods is not very clear. Another way to classify the test methods is to divide them into smooth specimen testing and pre-cracked specimen testing.

SCC in smooth specimens includes both crack initiation and crack propagation. The crack initiation is a statistical process and it may take a very long time. Tests can be accelerated using increased concentration of corrosive species, electrochemical stimulation, or more severe loading conditions than the material will experience in service conditions. Loading type can be divided into three categories: 1) constant strain, 2) constant load and 3) slow strain rate.

Typical constant strain (or extension) test specimens are bent-beam, U-bend and C-ring specimens. The loading is passive loading, which can be provided by simple fixtures. In constant strain tests, the driving force for cracking decreases with increasing crack length [3].

Constant load tests, in the case of smooth specimens, are usually performed on tensile type specimens. Similar specimens are used in slow strain rate tests. Active loading is provided by servo-hydraulic or step motor controlled loading machines. In both cases, the driving force for cracking increases with increasing crack length [3].

Besides the geometries mentioned, also several other specimen geometries are used in SCC testing and several other ways are used to provide the loading. A large number of them is presented for example in reference [4].

Pre-cracking enables fracture mechanical stress analysis of the crack tip. Crack growth rate can be determined as a function of stress intensity factor K_I, if the specimen fulfils the requirements of linear-elastic fracture mechanics, LEFM. Application of fracture mechanics enables prediction of the behavior of real components or structures. It is possible to predict when an existing crack reaches a critical size if the relation between the crack growth rate and K_I is known. LEFM applies if the size of the plastic zone is small compared to the ligament length [5].

The tests are usually constant load tests (increasing K_I) or constant displacement tests (decreasing K_I). Because linear-elastic fracture mechanics approach is usually applied in these tests, the specimens are quite large. Specimens are typically 25 mm (thickness) or larger C(T)-specimens (Compact Tension). Other geometries are also used, e.g., round C(T), DCB (Double Cantilever Beam) and SEN(B) (Single Edge Notched Bend) [3, 4].

Active load control is used in constant load tests, but passive loading is normally used in constant displacement tests. Constant displacement can be achieved for example by using wedge loading. Wedge loading enables testing of several specimens at the same time.

Crack growth rate vs. K_I has been proposed to have three stages [6]. At low K_I-levels just above the threshold stress intensity factor for stress corrosion cracking, K_{ISCC}, the crack growth rate is assumed to be strongly dependent on K_I. Above that, the crack growth rate is assumed to be relatively independent of K_I until the critical stress intensity factor, K_{IC}, is reached. At K_{IC}, the specimen fails mechanically. The crack growth rate vs. K_I behavior is presented schematically in Figure 1. It must be noted, however, that the behavior of different alloys in different environments varies. It also is not quite clear whether there really is a material-environment specific threshold stress intensity factor or not.

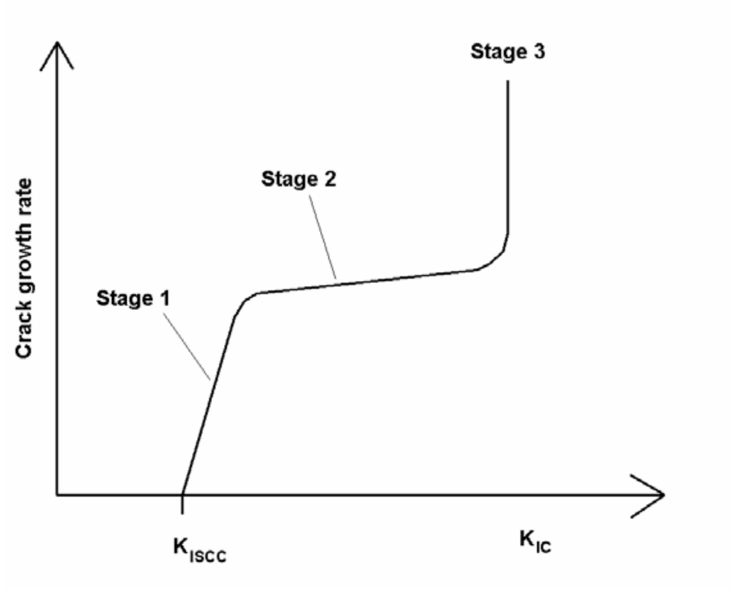

Figure 1. Schematic dependency between stress corrosion crack growth rate and stress intensity factor K_I.

If significant plasticity (plastic zone size significant relative to the ligament length) occurs, the loading condition can be determined using elastic-plastic loading parameters, e.g., J-integral. This kind of tests are usually slow rising displacement tests on C(T) or SEN(B) specimens.

Typically only one or, if a "daisy-chain" connection is used, two specimens can be tested simultaneously in one autoclave using constant load tests under linear-elastic condition. Elastic-plastic approach enables testing of several specimens simultaneously in one autoclave because the specimens and loading tools require less space. Sometimes the availability of the test material is also very limited. In this case, elastic-plastic fracture mechanics may be the only solution.

1.1 Basics of linear-elastic and elastic-plastic fracture mechanics

1.1.1 Linear-elastic K as a stress intensity parameter

In linear-elastic fracture mechanics, the stress and strain fields around the crack tip can be characterized by the stress intensity factor K. K has three modes, K_I, K_{II}, and K_{III} depending on the loading geometry. In fracture mechanics and stress corrosion testing, most of the interest concentrates on mode I loading, in which the loading vector is parallel to the crack plane normal. K_I is a function of body geometry, load and crack length [5, 7]:

$$K_I = Y \sigma \sqrt{a}, \qquad (1)$$

where Y is a dimensionless function of crack size and specimen geometry, σ is nominal stress, and a is the crack length. Solutions for K_I are available for various geometries in several sources, e.g., reference [5].

In linear-elastically behaving cracked specimen under mode I loading, the crack tip stress field is defined by stress intensity factor K_I as follows [5, 7]:

$$\sigma_{xx} = K_I (2\pi r)^{-1/2} \cos(\theta/2) [1 - \sin(\theta/2) \sin(3\theta/2)]$$

$$\sigma_{yy} = K_I (2\pi r)^{-1/2} \cos(\theta/2) [1 + \sin(\theta/2) \sin(3\theta/2)]$$

$$\tau_{xy} = K_I (2\pi r)^{-1/2} \cos(\theta/2) \sin(\theta/2) \cos(3\theta/2), \qquad (2)$$

where r is the distance from the crack tip and θ is the angle relative to the crack plane, Figure 2. Equation (2) can be written as [5, 7]:

$$\sigma_{ij} = K_I \, r^{-1/2} f_{ij}(\theta). \tag{3}$$

The elastic strain field follows a similar behaviour:

$$\varepsilon_{ij} = (K_I/E)\, r^{-1/2} g_{ij}(\theta, \nu), \tag{4}$$

where the functions f_{ij} and g_{ij} depend on Poisson's ratio and plane strain/plane stress conditions.

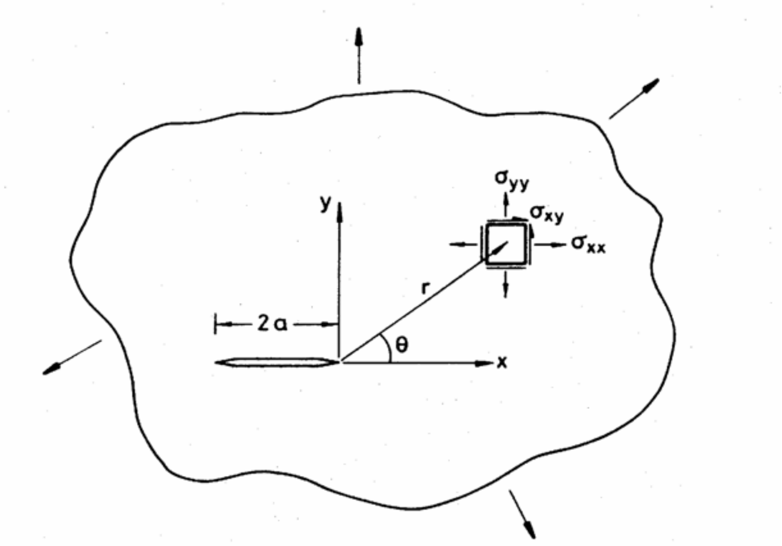

Figure 2. Crack tip coordinate system in a cracked body under tension [7].

As can be seen from equations (3) and (4), the stresses and strains approach infinity when the distance from the crack tip, r, decreases towards zero. In real elastic-plastically behaving metals this is not possible and the stress results in plastic yielding at the crack tip. The effect of yielding shifts the singularity ahead and the crack behaves as it were longer. According to Irwin's approach [5] the plastic zone correction in plane stress condition is equal to the plastic zone radius:

$$r_y = 1/(2\pi)\,(K_I/\sigma_{YS})^2, \tag{5}$$

where σ_{YS} is the uniaxial yield stress. In the plane strain condition multiaxial constraint increases the stress when the material yields and decreases r_y to [5]:

$$r_y = 1/(6\pi)\,(K_I/\sigma_{YS})^2. \tag{6}$$

The effective crack tip is in the middle of a roughly circular plastic zone. The size of the plastic zone is twice as large as the Irwin's plastic zone correction. These solutions for the plastic zone size are approximate, because they are based on the stress-field distribution in a linear-elastic material. In an elastic-plastic material the plastic zone redistributes the stress field and, thus, the strain field also redistributes.

In order to measure size-independent fracture toughness values, the size of the plastic zone has to be small compared to the ligament length. Adequate small-scale yielding condition for linear-elastic plane-strain fracture toughness testing predominates when:

$$W\text{-}a \geq \alpha\,(K_I/\sigma_{YS})^2, \tag{7}$$

where W-a is the remaining ligament and α is a dimensionless constant between 1.1 and 1.5 [8]. In the previous years it was assumed that the minimum value for α was 2.5 and also that the specimen thickness B had to fulfill the same criterion as W-a in order to ensure the plane-strain condition. However, according to Wallin [8] the specimen thickness is not as important factor as was previously thought. The new criterion presented in equation (7) is proposed to be taken into account in the next revision of the standard ASTM E 399 "Standard Test Method for Plane-Strain Fracture Toughness of Metallic Materials" [8]. In some cases, e.g., fatigue crack growth rate measurement, even less strict size limits are allowed. According to the standard ASTM E 647 “Standard Test Method for Measurement of Fatigue Crack Growth Rates”, flow stress can be used instead of the uniaxial yield stress in the case of highly strain hardening materials (in this standard, $\alpha = 4/\pi$). The effects of the strain hardening are shortly discussed in the end of this study.

The plastic deformation at the crack tip results in blunting, i.e., opening, of the originally sharp crack tip. This crack tip opening displacement, Figure 3, is:

$$\delta = K_I^2(1-\nu^2) / (m\,\sigma_{YS}\,E), \tag{8}$$

where m is a dimensionless constant, which is theoretically ~1 in plane stress and ~2 in plane strain condition [5].

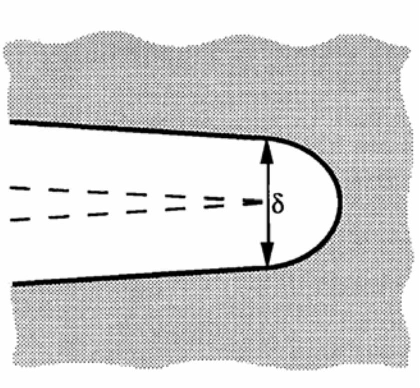

Figure 3. Definition of the crack tip opening displacement, δ. Original sharp crack tip is marked with the dashed line [5].

1.1.2 Elastic-plastic J-integral as a stress intensity parameter

When the size of the plastic zone increases, linear-elastic approach does not apply, i.e., K_I estimated from the nominal stress does not characterize the crack tip stress-strain field. A one parameter solution applicable to describe the stresses and strains close to the crack tip in large scale yielding is the J-integral. J is a path-independent line integral around the crack tip. A simple expression for J for a variety of specimen geometries is [5]:

$$J = \eta U/(B\ b), \qquad (9)$$

where η is a dimensionless constant, which depends on the specimen geometry ($\eta \approx 2$ for 3-point bend geometry), U is the area under the elastic-plastic load-displacement curve, and b is the remaining ligament of the specimen [5]. Equation (9) describes J as energy, both elastic and plastic, absorbed by the remaining ligament and multiplied by the geometry factor η. J can be divided into elastic and plastic components. The elastic component is proportional to K_I calculated from the nominal stress. The total J can be expressed as:

$$J = K_I^2\ (1-\nu^2)/E + \eta U_p/(B\ b), \qquad (10)$$

where U_p is the area under the plastic part of the load-displacement curve [5].

According to HRR singularity model developed by Hutchinson, Rice and Rosengren [5], the stress and strain fields ahead of a crack tip are defined by J as:

$$\sigma_{ij} = \sigma_{YS} \, [E\, J/(\alpha\, \sigma_{YS}^2\, I_n\, r)]^{1/(n+1)}\, \tilde{\sigma}_{ij}(n, \theta) \qquad (11)$$

and

$$\varepsilon_{ij} = (\alpha\, \sigma_{YS}/E)\, [E\, J/(\alpha\, \sigma_{YS}^2\, I_n\, r)]^{n/(n+1)}\, \tilde{\varepsilon}_{ij}(n, \theta), \qquad (12)$$

where α is a dimensionless constant, n is the strain hardening exponent, I_n is an integration constant, which depends on n, and $\tilde{\sigma}_{ij}$ and $\tilde{\varepsilon}_{ij}$ are dimensionless functions of n and θ [5]. Equation (11) predicts similar growth in stress towards infinity as r decreases towards zero as seen in equation (3). The increasing stress results in a plastic zone and crack tip blunting. Crack tip blunting reduces stress triaxiality locally. The σ_{yy} component of the stress reaches a maximum ahead of the crack tip where the stress triaxiality is high and then decreases as r decreases towards zero. Also, σ_{xx} has to vanish at $r = 0$ because the crack tip is a free surface. Figure 4 shows the stress distribution ahead of the crack tip according to HRR singularity and according to finite element analysis conducted by McMeeking and Parks [5]. The stress maximum is located roughly at the distance of 2x crack tip opening displacement from the crack tip. Between the crack tip and this distance the stresses predicted by HRR singularity are reduced by very high plastic strains.

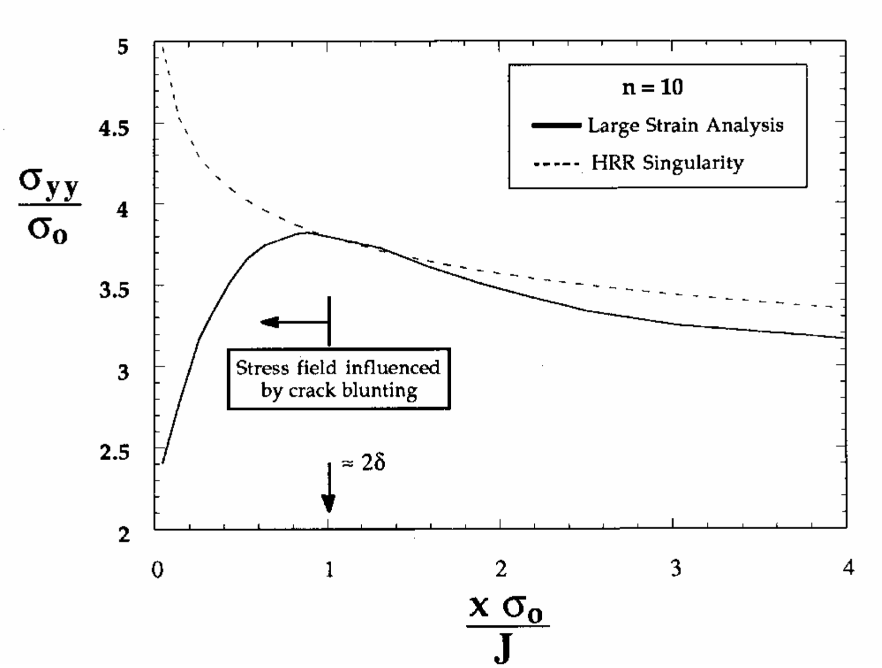

Figure 4. Stress distribution ahead of the crack tip according to HRR singularity and according to finite element analysis conducted by McMeeking and Parks [5]. σ_o *= yield stress in this figure.*

In small scale yielding, the relation between J and δ can be derived from the relations between J and K_I, and K_I and δ:

$$J = m\,\sigma_{YS}\,\delta. \qquad (13)$$

It has been shown that equation (13) applies well beyond the validity limits of linear-elastic fracture mechanics [5].

There are material, specimen dimension, and J-level dependent limits outside of which the fracture is not controlled by J. However, the limits are not as restrictive as in linear-elastic fracture mechanics. The size requirements to maintain sufficient plane strain conditions to result in J controlled fracture are according to ASTM E 1820-99 "Standard Test Method for Measurement of Fracture Toughness":

$$W\text{-}a \text{ and } B \geq 20\,J/\sigma_f, \qquad (14)$$

where W-a is the initial uncracked ligament, and σ_f (flow stress) is the average of yield and ultimate tensile stresses. The maximum crack extension capacity of a specimen is limited:

$$\Delta a_{max} = 0.25\ W\text{-}a_0 \tag{15}$$

and

$$a_0 \geq 0.45 \text{ and } \leq 0.70\ W, \tag{16}$$

where a_0 is the initial crack length and W is the specimen width. The limits are specifically for the determination of ductile cracking resistance (e.g., J_{IC} determination).

The validity limits for K_I and J to describe the stress and strain fields ahead of a crack depend on specimen dimensions and yield strength of the material. The K_I and J limits for three different specimen geometries and two different yield strengths have been collected in Table 1. 1T CT specimen is a commonly used specimen type in plane-strain fracture toughness testing (i.e., K_{IC} determination) and constant load stress corrosion tests. 10 mm x 10 mm x 55 mm (Charpy size) bend specimen is a commonly used specimen in impact and J-resistance tests in nuclear power plant surveillance programs, and 3 mm x 4 mm x 27 mm miniature bend specimen is also used in impact tests. The yield stress of AISI 304 steel in mill-annealed condition is typically around 200 MPa and the ultimate tensile strength around 500 MPa. After a long time exposure to neutron irradiation (fluence >10 dpa) in reactor core, the yield stress is around 800–900 MPa and the ultimate tensile strength about the same.

Table 1. Limits for valid linear-elastic K_I and elastic-plastic J for three specimen geometries (a/W = 0.5).

Specimen size	σ_{YS}/σ_{UTS}, MPa	K_I validity limit, MPa√m	J validity limit, kJm^{-2}	Limiting dimension
1T CT	200/500	20	440	B, W-a = 25.4 mm
	800/850	80	1000	
10x10x55 mm^3	200/500	9	87	W-a = 5 mm
	800/850	35	200	
3x4x27 mm^3	200/500	5	35	W-a = 2 mm
	800/850	22	82	

1.1.3 Influence of crack growth on the crack tip parameters

According to Brocks and Yuan [9], it has been suggested that as soon as the crack initiates, J loses its theoretical background, i.e. path independence. It has also been proposed that if the J-resistance curve increases rapidly during crack extension and the crack extension is small, then the J-integral still controls crack growth [9]. However, as stated earlier, J is a parameter that describes the energy absorbed by the remaining ligament of the specimen. If crack growth has occurred, the total work absorbed by the specimen, i.e. area under the load displacement curve (U), does not describe the energy absorbed by the momentary un-cracked ligament [10]. Crack growth correction, which takes the decreasing ligament size into account, has been presented for example in standard ASTM E 1820-99 and even a newer solution has been presented by Wallin and Laukkanen [10].

Crack growth results in redistribution of the crack tip stress-strain field. The redistribution, on the other hand, results in a change in the crack tip opening. The following expression for the crack opening displacement rate has been formulated using finite element method in the case of a growing crack in ideally plastic solid under small-scale yielding and plane-strain conditions by Rice et al. [11]:

$$d\delta/dt = \alpha * \frac{dJ/dt}{\sigma_0} + \beta * \frac{\sigma_0}{E} * da/dt * \ln\left(\frac{R}{r}\right), \text{ as r} \rightarrow 0, \quad (17)$$

where α and β are dimensionless constants (α depends on σ_0/E and strain hardening exponent n, and β = 5.08), R is a size, which scales approximately with the size of the plastic zone, and r is a distance behind the propagating crack tip. By asymptotic integration they got the following expression for the crack opening displacement [11]:

$$\delta = \frac{\alpha \cdot r}{\sigma_0}\frac{dJ}{da} + \beta \cdot r \frac{\sigma_0}{E}\ln\left(\frac{e \cdot R}{r}\right), \text{ as r} \rightarrow 0, \quad (18)$$

where *e* is the natural logarithm base.

Rice et al. [11] speculate that R increases linearly with increasing J in the small scale yielding conditions. In the large scale yielding conditions, R saturates to some fraction of the ligament size b. The approach is based on rigid ideally plastic material behaviour, where strain hardening is not taken into account.

Gao and Hwang [12] have presented the following solutions for the stress and strain ahead of a steadily growing crack in strain hardening material under quasi-static elastic-plastic loading:

$$\sigma \sim \left(\ln\frac{A}{r}\right)^{1/(n-1)} \quad (19)$$

and

$$\varepsilon \sim \left(\ln\frac{A}{r}\right)^{n/(n-1)}, \quad (20)$$

where A is the size of the plastic zone, r is the distance from the crack tip and n is the Ramberg-Osgood strain hardening exponent.

1.2 Major SCC models

The purpose of this chapter is to give a short summary of the variety of possible EAC mechanisms and models proposed in the literature. More detailed treatments of the alternative SCC models have been published by Galvele [13], Hänninen et al. [14], Turnbull and Psaila-Dombrowski [15], Turnbul [16] and Rebak and Szklarska-Smialowska [17].

It is worth realizing that a single mechanism can most probably not explain in detail the complex phenomena related to the EAC of different materials. This view has been expressed for instance by Rebak and Szklarska-Smialowska [17] when discussing about the stress corrosion cracking of Inconel 600. They also pointed out that almost no explanations have been given in the literature for the events leading to crack initiation in this alloy. This seems to be true also for other materials: the mechanisms presented in the literature deal mainly with crack growth but not with crack initiation. The order of the models and mechanisms reviewed below is arbitrary.

1.2.1 Slip-oxidation model

The slip-oxidation model gives a mechanistic interpretation for SCC. It has been used to predict crack growth rates in austenitic stainless steels and nickel-based alloys such as Inconel 182 weld metal in different environments [18-40]. According to Turnbull [16], the slip-oxidation model is increasingly perceived to be relevant only to intergranular cracking.

The slip-oxidation model is to a great extent based on early ideas and concepts of cracking presented, for instance, by Vermilyea [41] and others, as reviewed by Ford [30, 32]. These early ideas relate crack growth to oxidation reactions at the crack tip. The concepts behind the model have been supported for instance by Congleton and Yang [42] and Shoji et al. [43].

A simplistic view of the slip-oxidation process is shown in Figure 5 [19]. Oxide film is formed on the bare metal surface. The oxide film ruptures at the location of the bulk metal grain boundary. Subsequently, the dissolution of the grain boundary occurs and the crack advances. The oxidation of the metal leads to passivation, until the oxide ruptures again and the process is repeated again and again. Fundamentally, this process requires both corrosion and mechanical phenomena working together to advance the crack.

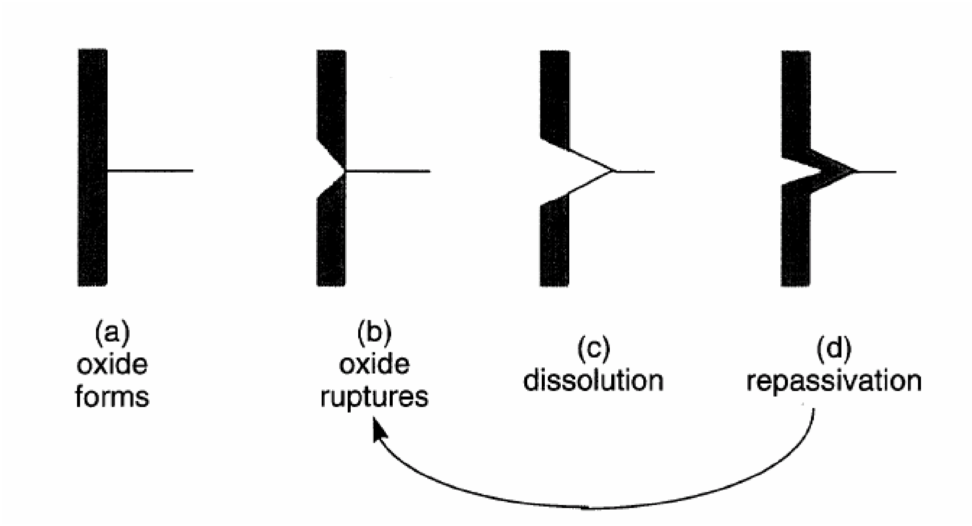

Figure 5. A schematic presentation of the slip-oxidation process for crack advance. An oxide film forms on a bare surface, a), the oxide film ruptures on a grain boundary, b), dissolution of the grain boundary occurs and the crack advances, c), the metal oxidizes and passivates again, d). This process is repeated continuously. [19]

The crack advance is proposed to be correlated with the oxidation charge density associated with the dissolution and passivation of the bare metal surface exposed to the solution as a result of the rupture, Figure 6. This correlation is based on the idea that a slip emergence at the crack tip induces a structural damage on the passive film. In order to restore the earlier state, a certain degree of oxidation has to take place. Variables affecting the localized crack tip system can be separated into mechanical and chemical/electro-chemical factors. The mechanical factors (e.g., stress and strain states, creep rate, yield stress, oxide ductility, crack growth rate, grain boundary structure at the crack tip) control the crack tip strain rate and thereby the periodicity of the oxide rupture events. The chemical factors (e.g., material composition at the crack tip and crack tip water chemistry, which is influenced by corrosion potential, impurities, flow rate etc.) determine the repassivation response of the crack tip [27, 29].

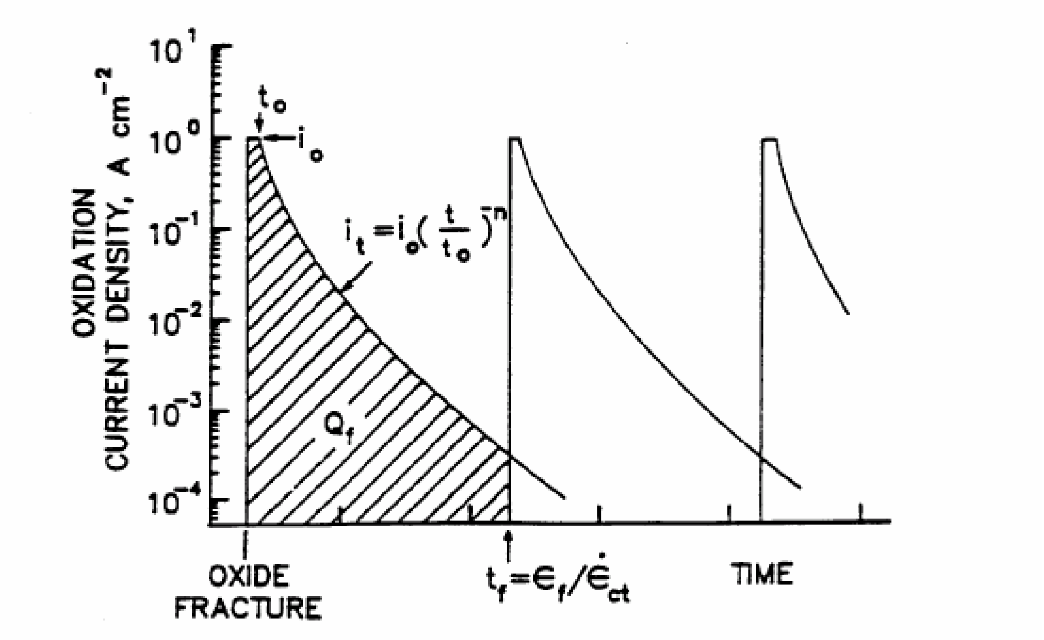

Figure 6. Schematic presentation of oxidation current density vs. time following repeated oxide rupture events [19].

As shown in Figure 7, the slip-oxidation model assumes that anodic reactions take place within the crack, while cathodic reactions may take place both within the crack and on the surface external to the crack. The anodic and cathodic reactions within the crack are assumed to be spatially separated. This spatial separation has been supported by the SIMS measurements performed by McIntyre et al. [44]. The cathodic reactions on the external surfaces do not control or limit the anodic processes within the crack. In other words, the slip-oxidation model assumes that the crack tip is essentially decoupled from the external driving force of oxygen reduction on the surfaces external to the crack (see also [45]).

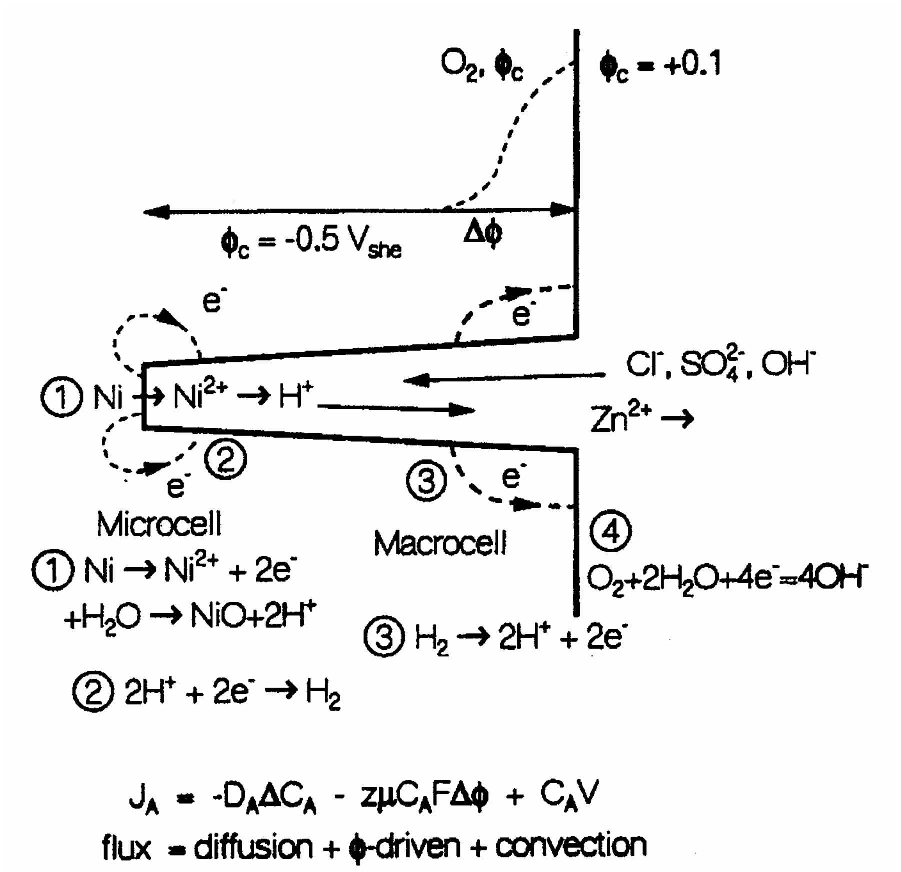

Figure 7. Schematic presentation of the processes during growth of a stress corrosion crack; concepts based on the slip-oxidation model [21, 33].

The main purpose in the development of the slip-oxidation model has been to find a predictive equation for crack growth rate. The predictions of material behaviour have been based on the expression reported by Ford and Andresen for the crack velocity as a function of crack tip strain rate and a parameter n (see for instance [32]). According to the slip-oxidation theory, the crack growth rate is:

$$\overline{V_t} = \frac{M}{z\rho F}\frac{Q_f}{\varepsilon_f}d\varepsilon_{ct}/dt\,, \tag{21}$$

where M is the atomic weight of the dissolving metal, ρ is the density of the metal, F is Faraday’s constant, z is number of electrons involved in the oxidation of a metal atom, Q_f is the oxidation charge density, ε_f is the strain needed for the oxide to rupture and $d\varepsilon_{ct}/dt$ is the crack tip strain rate [32].

According to Andresen et al. [38], repassivation current generally shows high dissolution current density, when the surface is bare for a short time (i_0 and t_0, respectively). After that, oxide formation or precipitation results in a decay in the oxidation current density. The decay follows a power law relationship:

$$i_t = i_0\left(\frac{t}{t_0}\right)^{-n} . \tag{22}$$

Equation (21) can be reformulated as:

$$\overline{V_t} = A(d\varepsilon_{ct}/dt)^n , \tag{23}$$

where A and n are material and environment dependent constants. If oxide free surface is maintained in the crack tip (i.e., $\varepsilon_f/(d\varepsilon_{ct}/dt) < t_0$), crack growth rate results directly from dissolution. This maximum environmental crack growth rate is:

$$\overline{V}_{\max} = \frac{M}{z\rho F} i_0 . \tag{24}$$

Nearly all of the re-passivation aspects in the slip-oxidation model are incorporated into the parameter n, which is the empirically determined slope of the current decay curve of repassivation. It thus depends on the corrosion potential, solution conductivity and material characteristics. The predictive power of the proposed equation has proven to be good in many cases [17].

The views on the rate-controlling step of cracking according to the slip-oxidation model have changed during the years. When deriving the predictive equation discussed above, a clear stand on the rate-determining step of the crack growth has not been necessary to take. In a paper published in 1985, Andresen [22] has stated that various parameters may control the growth of stress corrosion cracks:

- The rate of film rupture, which is proportional to the strain rate at the crack tip.

- The extent of dissolution following rupture occurences.
- The rate of transport of various reactants to or from the reaction surfaces.

Earlier Andresen [20, 22] himself has been in favour of the rate-controlling role of mass transport in the solution within the crack in the case of both iron and nickel-based alloys. He has presented the following evidence to support his views:

- Increase of temperature decreases the solubility of iron and nickel oxides, contributing to a less effective role of mass transport.
- Determination of activation energies for crack growth indicates a change in mechanism at around 150…200°C, the corresponding values suggesting a change from an oxidation-dissolution control to mass transport control. (The former most probably refers to a kinetically controlled process.)
- Variations in the value of the critical threshold potential for cracking indicate that the corrosion potential is not the single factor contributing to the crack growth rate.
- A correlation established for crack length and time can be explained by assuming mass transport control.
- The shape of current-time transients simulating current flow after film rupture can be explained assuming a diffusion-controlled process.
- The effect of impurity addition on crack growth rate is larger at high temperatures, at which mass transport and, thus, also the transport of impurities is assumed to be the rate-determining factor than at low temperatures.
- In cyclic loading with a high stress ratio (e.g., $R = 0.9$) or constant loading, when the pumping effect is low, the crack advances much faster at crack edges than in the center. This can be understood via increased rate of mass transport close to the bulk solution.

In spite of the above list, the proof for mass transport control in the solution within the crack is not very convincing. For instance, any conclusions based on the magnitude of activation energies can be considered only very tentative. In addition, most of the facts listed above can be associated with mass transport in a solid phase, as well.

In the discussions of the slip-oxidation model Andresen and co-authors [19, 32, 33] recognize that the kinetics of repassivation, i.e., the formation and growth of the passive film on the freshly exposed surface at the crack tip, is the main rate determining factor of the crack growth rate. Thus, in material-environment conditions, where the crack tip chemistry is aggressive, the crack growth rate is predicted to be high because of high re-oxidation rate between the oxide rupture events.

The rate-controlling step of cracking in slip-oxidation model has been subject to debate in the literature. Taylor [46] has proposed that aqueous diffusion in the crack controls the rate of crevice corrosion of Inconel 600 in high-purity water at 288°C. Congleton and Parkins [47] have suggested that the cracking mechanism is electrochemically controlled and that the detailed nature of the oxide film is important. Ruther et al. [48, 49] have proposed that a more likely rate-controlling step in the stress corrosion cracking of AISI 304 stainless steel involves the cathodic reaction, e.g., reduction of oxygen or oxyanions that contain a central atom, which has multiple oxidation states (e.g., MoO_4^{2-} and CrO_4^{2-} anions).

The slip-oxidation model has also been subject to some criticism. The strongest arguments against it have been presented by Macdonald [50]. According to Macdonald, the model of Andresen and Ford violates Faraday’s law and conservation of charge. Rebak and Szklarska-Smialowska [17] have on the other hand commented that the slip-oxidation model does not explicitly address variables such as temperature, pH, presence of carbides at the grain boundaries etc.

The slip-oxidation model has also been criticized by Turnbull and Psaila-Dombrowski [15], because at least part of the test results used in the development of the model have been obtained using a simulated crack in a Teflon compact tension specimen. This kind of arrangement leads to the ignorance of reactions on the crack walls, their influence on conductivity and potential profiles within the crack, current magnitudes etc.

The slip-oxidation model is based on several well-established concepts. This model is a good example of a cross-correlation between well established theoretical issues of crevice and crack chemistry and completely empirical characteristics of a process of which little is fundamentally known in BWR environments, i.e., oxide breakdown and repassivation.

1.2.2 Coupled environment fracture model (CEFM)

The coupled environment fracture model (CEFM) presented by Macdonald and Urquidi-Macdonald [51] is based largely on the same ideas as the slip-oxidation model. Macdonald and Urquidi-Macdonald [51], however, emphasize the strong coupling of the external and internal environments and that charge conservation has to be carefully taken into account in the formulation of the model concepts. The latter means that the sum of currents within the crack and of the currents due to the oxidation of hydrogen, the reduction of oxygen, the reduction of hydrogen peroxide and the dissolution of metal at the external surfaces has to be zero. A schematic presentation of the environmental processes of CEFM is shown in Figure 8.

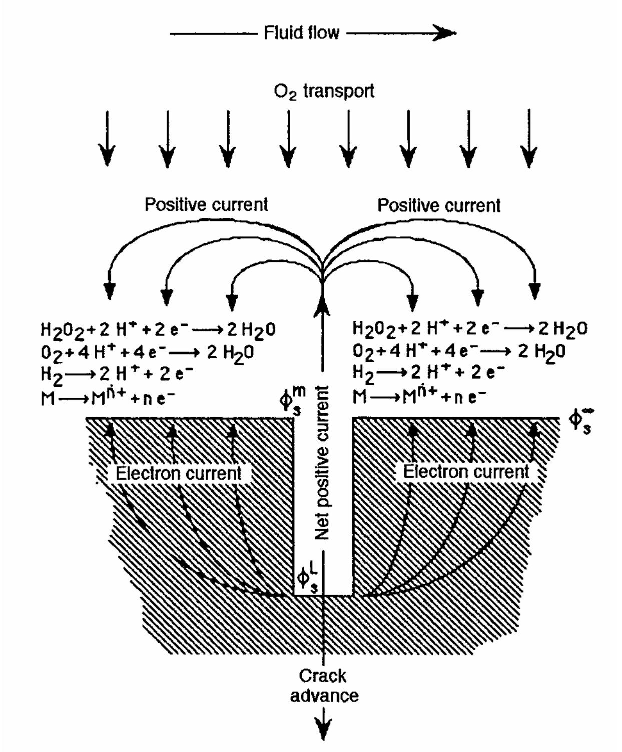

Figure 8. A schematic presentation of the coupling of the external and internal environments in the coupled environment fracture model, CEFM. [52]

The coupled environment fracture model has been proposed originally for sensitized AISI 304 SS in LWR environments, and at the moment it is used to model and to serve as a base for mitigation of cracking of stainless steels [52, 53, 54].

In analogy to the slip-oxidation model, the CEFM assumes that the crack growth proceeds via anodic dissolution. Partly in contrast to the ideas behind the slip-oxidation model, the CEFM takes a clearer stand to the rate-limiting step of the crack growth: it was considered to be the cathodic reaction on the external surface of the cracked body. Because of the relatively small currents emanating from the crack, mainly the cathodic reactions on regions close to the crack mouth are assumed to play an important role [52]. Macdonald and co-workers [55] have done extensive work to show that a dominating part of the cathodic reactions takes place at the external surface of the crack.

CEFM is continuously under active development [50, 53, 54, 56]. Macdonald [50] has, for instance, relatively recently partly relaxed his statement of the dominating role of the cathodic reaction on the external surface. He has accepted that the anodic currents are partly compensated by small cathodic currents on the crack walls. Based on his experimental results, he still strongly argues the role of the cathodic reaction on the external surface is considerable. At the present stage, the CEFM divides the crack into three parts (starting from the crack tip) [57]:

- First region: the current that is produced at the crack tip is compensated by cathodic processes.
- Second region: the potential passes through a plateau, where the cathodic current density approximately compensates the anodic current density (current that flows through the solution in the crack is very small).
- Third region near the crack mouth: the cathodic current on the crack sides cannot compensate the anodic passive current.

A fast algorithm for estimating crack growth rates introduced recently by Engelhardt et al. [57] is based on the concepts of the CEFM, and it emphasizes again the strong coupling of the external and internal environments. The importance of this coupling has been emphasized also, for instance, by Turnbull [45], who recognized the importance of the hydrogen and water reduction reactions in the crack, as well.

The CEFM leads to essentially the same accuracy of prediction of actual crack growth depending on potential and solution conductivity (i.e., anionic impurities) as the slip-oxidation model [52]. CEFM, however, requires less calibration data for the prediction of crack growth in given conditions than the slip-oxidation model. A theory of crack initiation is being incorporated in the predictive algorithms [53]. This is likely to increase the determinism of the model by taking into account the role of the passive film in the coupling of the electrochemical reactions during crack growth. The fact that the current densities of repassivation at the crack tip are fundamentally different from the passive current density at the crack walls has been also taken into account [54].

Several assumptions and concepts of the CEFM have been stated to be controversial, and a discussion on the validity of the model is going on [25, 31, 50]. The criticism towards the idea of cathodic reactions taking place only on the external surfaces [15] has led to further development of the CEFM, as discussed above. Another factor criticized by Andresen and Ford has been that the CEFM does not account for the dramatically different SCC responses of the different impurity anions even at identical conductivity, but it instead considers only the value of the total conductivity [25]. Macdonald [50] has, however, commented that the CEFM takes into account the specific ion issues, because they are reflected in the equivalent conductances and in the kinetics of the charge transfer reactions. Andresen and Ford [25] have also criticized that the CEFM relies only upon a potential gradient for transport of species along the crack, but this criticism has been rejected by Macdonald [50].

Other points subject to criticism have been the simplifying assumptions concerning:

- the geometry of the crack [45] and
- the lack of equilibrium reactions (referring most probably to solution equilibria), solubility limits and interactive effect of environment on crack tip kinetics [45, 15].

In addition, the CEFM has been critisized because of its inability to explain the cracking of Inconel 600 at open circuit potential and at applied negative potentials [17] and because of the use of Laplace's equation ($\nabla^2\Phi = 0$), although this equation is invalid in the presence of steady-state concentration gradients. However, the Laplace equation has been used also by Turnbull in another elaborated treatment of the occluded cell chemistry within the crack [45].

One of the values of the CEFM has been considered to be in the recognition of the possible effect of the net current flowing from the crack on the potential distribution just outside the mouth of the crack [15]. Another additional value is certainly in the active discussion that has resulted from the conceptual differences between the CEFM and the slip-oxidation model. Albeit the CEFM and the slip-oxidation model have approximately the same predictive force, the deterministic and scientifically sound base of the CEFM deserves to be recognized.

CEFM is based on the cyclic film rupture just like the slip-oxidation model [51]. The crack growth rate is calculated from Faraday's law as:

$$\frac{dL}{dt} = \frac{MI_0}{2\rho_m zFW\delta} \ , \tag{25}$$

where ρ_m is the density of the metal, F is Faraday's constant, M is the composition weighted atomic weight, I_0 is the mean current at the crack tip and z is the composition weighted oxidation state of the dissolving metal. Factor I_0 contains the effect of the cyclic film rupture on the current.

CEFM predicts, for instance, that even a very small addition of NaCl into BWR coolant water increases the crack growth rate of AISI 304 steel dramatically, whereas the effects of higher concentrations are less pronounced [51]. Similarly, the crack growth rate increases sharply with K_I at low K_I-levels. At higher K_I-levels the crack growth rate becomes relatively independent on the stress intensity level [51].

1.2.3 Enhanced surface mobility model

The enhanced surface mobility model of Galvele gives an alternative mechanistic interpretation for the crack growth in several materials. The model can also be used to predict the crack growth rate. The model has been originally presented in fully formulated form in 1987 [58]. It is still under active development, as shown by the recent results reported in 1997 and 2000 [59, 60]. According to Turnbull [16], Galvele has developed this model, because according to his view the measured high crack growth rates cannot be explained by oxidation currents at the crack tip. For instance, at crack velocities > 10^{-7} m/s the current densities should be so high (0.3 Acm^{-2}) that the cracks would become plugged with corrosion products.

The enhanced surface mobility model of Galvele [13] is based on the transport of atoms from the crack tip by surface diffusion from the highly stressed crack tip to the less stressed sides, advancing thereby the crack by one atom spacing for each movement, Figure 9. The crack growth is explained to result from the capture of vacancies by the stressed lattice at the crack tip. A clear stand is taken to the rate-limiting step: the movement of ad-atoms along the surface of the crack is stated to control the crack growth rate. These atoms are then lost by dissolution or by the introduction of surface vacancies. The environment can be explained to affect the rate of surface diffusion through enhancement of the rate of consumption of ad-atoms or through the effect of surface compounds on the surface diffusivity of the metal or alloy.

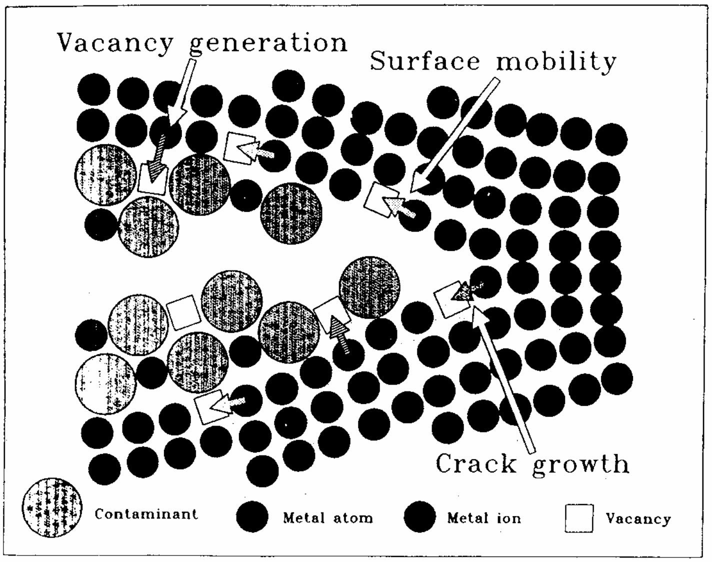

Figure 9. A sketch of the concepts underlying the enhanced surface mobility model [61].

Galvele has also presented a predictive equation for the crack growth rate as a function of the surface diffusion coefficient D_s, the diffusion path length L, atomic diameter a, maximum stress at the crack tip σ, temperature T and Boltzman's constant k [59]:

$$\frac{da}{dt} = \frac{D_s}{L}\left[\exp\left(\frac{\sigma a^3}{kT}\right) - 1\right]. \qquad (26)$$

According to Galvele [58], the crack tip stress σ in his model for a precracked specimen with a sharp elliptical crack is (combining Equations (13) and (14) of his work):

$$\sigma = \frac{K_I}{\sqrt{\pi d}}\left(0.34\frac{d}{a}+1\right), \tag{27}$$

where d is the half crack length and a is the interatomic spacing.

According to Galvele [58] there is a plateau, i.e., the crack crowth rate does not increase above some K_I-level because dislocation emission from the crack tip leads to crack tip blunting. This means that the stress does not increase but, instead, the material yields.

The prediction capability of the model has been found to be good in some cases [62]. One point subject to criticism has been that his model overestimates stress corrosion crack velocities in ductile fcc metals by several magnitudes [63]. Galvele [62] has pointed out that this criticism was based on calculations in which the role of the environment was ignored. He commented that the environment greatly increases the injection of vacancies into the metal surface, leading to predicted stress corrosion crack growth rates that correspond well with practical observations. Turnbull [16] has criticized the validity of the assumptions about the surface mass transport behind the surface mobility model. He has also commented that although the local chemistry has been described to determine the nature of surface films, the model lacks any relationship between the environment and the film.

1.2.4 Internal oxidation model

The internal oxidation model was originally based on the concepts presented for the grain boundary oxygen embrittlement of nickel and its alloys at temperatures above 500°C. Scott and Le Calvar [64, 65, 66] have suggested that the same phenomenon may be involved in the intergranular stress corrosion cracking of nickel-based alloys, particularly Inconel 600 in PWR environments.

As indicated above, the internal oxidation model is based on the diffusion of oxygen into the metal lattice. The reason for embrittlement has been explained to be either the presence of a layer of oxygen atoms on the grain boundary or the formation of gas bubbles such as CO and CO_2. Scott and Le Calvar [64, 65] have argued that the narrow range of potentials in which IGSCC in PWR environments occurs can only be associated with an oxidation process controlling the cracking mechanism. The high value of activation energy on the other hand has been stated to rule out liquid or gas phase diffusion as a rate-controlling step. The importance of the anionic conductivity of the protective oxide film has been pointed out by Combrade and Scott [67].

The internal oxidation model has been explained to be favoured when the corrosion potentials are close to the oxidation potential of the solvent metal [64]. As described by Combrade and Scott [67], under such conditions less noble minor alloying elements of an alloy may oxidize within the material while leaving the main metallic element of the alloy largely untouched. This can be considered as a particularly severe problem for nickel-based alloys in atmospheres with very low partial pressures of oxygen which satisfy the thermodynamic requirement that the less noble alloying elements (Fe, Cr) can oxidize while the more noble solvent metal Ni does not. The concentration of the oxidizing species such as chromium must be below a critical minimum value in order to avoid formation of a protective external film by that species alone. Internal oxidation has been stated to be transgranular at temperatures higher than 700…800°C and intergranular at lower temperatures.

An equation to predict the crack growth rate has been presented by Scott and Le Calvar [65]. The equation takes into account the temperature, the grain boundary diffusion coefficient of oxygen in the alloy, the void surface energy, the interatomic spacing, the grain boundary thickness, the surface solubility of oxygen, the number of sites explored per gas atom jump, yield stress and the stress intensity. The model predicts that the crack growth rate is directly proportional to the stress intensity factor K_I. However, the model has been criticized by Staehle and Fang [68] especially because the experimentally observed diffusion rates of oxygen in nickel are several orders of magnitude lower than needed to explain the observed low potential stress corrosion crack growth rates of Inconel 600.

The internal oxidation model is not very relevant to BWR conditions, in which the corrosion potentials are much higher than in PWR conditions. It may, however, have some relevance in conditions prevailing inside the crack, where the local corrosion potentials may be relatively low because of the depletion of oxygen in the water phase.

1.2.5 Selective dissolution – vacancy creep (SDVC) model

Aaltonen et al. [69] have presented the selective dissolution – vacancy creep (SDVC) model for crack growth in Inconel 600 in PWR conditions. The model is based on the idea that the formation of vacancies in the metal contributes to crack growth via their accumulation in the near-surface layers and subsequent diffusion in the bulk causing significant changes in the defect distribution and dislocation structure of the bulk metal. Vacancies can interact with crack tip dislocations enhancing crack tip deformation together with the applied external loads. This leads to passive film breakdown at the crack tip and repeated selective dissolution, vacancy generation, deformation cycle.

One of the original assumptions of this model is that the crack growth rate is determined by the transport of cation vacancies (V_M^{z-}) through the oxide film on the crack walls. These cation vacancies can be formed at the film/solution interface by the following reaction [70]:

$$M_M = M^{z+}(aq) + V_M^{z-}. \tag{28}$$

When the cation vacancies reach the metal/film interface, they react with the substrate metal, leading to the formation of vacancies in the metal as follows:

$$m_m + V_M^{z-} = V_m + M_M + ze^-. \tag{29}$$

When the concentration of vacancies migrated in the bulk metal becomes high enough, they can cause changes in the dislocation structure of the metal affecting the initiation and growth of stress corrosion cracks.

According to the mixed-conduction model (MCM) developed recently to explain the conduction mechanism in the passive films of ferrous alloys [71, 72, 73], another important route for the generation of vacancies in the metal substrate, V_m, can be the injection of interstitial cations ${M^{x+}}_i$ at the metal / film interface:

$$m_m \rightarrow {M^{x+}}_i + xe^- + V_m \ . \tag{30}$$

The interstitial cations are transported through the passive film and are dissolved at the film/solution interface [71, 72]:

$${M^{x+}}_i \rightarrow {M^{z+}}_{aq} + (z - x)e^- \ . \tag{31}$$

It has been suggested that the conduction in passive films formed on ferrous alloys at potentials lower than ca. –0.3 V vs. SHE in a tetraborate solution at 200...300°C is dominated by interstitial cations [73]. Thus, it can be expected that the interstitial route of metal dissolution through the film may dominate at the low potentials close to the crack tip. The extent of the influence of anionic impurities on that dissolution route remains to be quantified.

The most significant value of the SDVC model is in its comprehensive treatment of the generation and transport of vacancies in the metal (see also [74, 75, 76]). The processes within the oxide, however, have not yet been quantitatively clarified. This certainly deserves more attention in the future, especially because the rate-limiting step of the cracking has been proposed to be in the oxide film.

The (SDVC) model differs fundamentally from the slip-oxidation model and the CEFM model in that it does not involve the rupture of the oxide film as a cause for the propagation of the crack. Instead, the rupture of the film in the SDVC model can be considered to be a consequence of the accumulation of vacancies in the near-surface layers of the metal and subsequent processes in the metal.

1.2.6 Film-induced cleavage model

Paskin et al. [77] and Sieradzki and Newman [78] have presented a film-induced cleavage model. According to their model, the cracking of the brittle film in the crack tip results in a secondary crack in the bulk metal.

Ford [30] has described SCC via film-induced cleavage as a combination of oxidation related mechanisms, i.e., slip-oxidation and brittle-fracture mechanism. He has summarized the film-induced cleavage model as follows: initially, the crack front moves forward by an oxidation process governed by the same rate-determining steps as those in the slip-oxidation model, but when the oxide rupture event due to an increment in strain in the underlying material occurs the crack in the oxide may readily penetrate a small amount into the underlying ductile metal matrix. The extent of this additional “environmentally-assisted cleavage” component of the crack advance may be governed by the degree of the coherency between the oxide and the matrix, and the fracture toughness of the substrate. Factors of importance which control the effectiveness of the oxide in initiating the cleavage event include the oxide-matrix misfit, the strength of bonding across the oxide-matrix interface, the oxide thickness and ductility and the ductility of the underlying metal matrix.

According to Turnbull [16], the range of applicability of this kind of film-induced cleavage mechanisms remains contentious and requires further work. Andresen and Ford [38] have, on the other hand, proposed that the film-induced cleavage model may explain transgranular crack growth better than the slip-oxidation model.

1.2.7 Models based on the effects of hydrogen

Another approach to modelling EAC is based on the role of hydrogen formed during the cracking. These models have generally not been developed to a quantitative stage.

Hydrogen-induced cracking is one of the most popular models for Inconel 600 [79, 17], although the present evidence has been stated to provide only weak support that hydrogen plays a predominant role in environmental cracking in hot water [29]. Hydrogen is likely to be formed in the cathodic reaction within the crack as a result of the low corrosion potential at the crack tip. The formation of gaseous hydrogen during corrosion fatigue crack growth at the open circuit potential has been proven for instance with AISI 316L stainless steel in $MgCl_2$ solution at 117 °C using video optical microscopy [80]. The formation of hydrogen may subsequently result in diffusion of atomic hydrogen into the alloy.

Ruther et al. [48] have proposed that the rate-controlling step of cracking via hydrogen embrittlement may in analogy to the slip-oxidation model be liquid diffusion, passivation and oxide rupture, because these factors may influence the ad-atom coverage and subsequent hydrogen permeation.

The entry of hydrogen through the crack tip process zone plays an important role in the model developed by Hall [81] for the intergranular stress corrosion cracking (IGSCC) of Inconel 600. This model is based on thermally-activated dislocation creep mechanism. The crack growth rate is assumed to be controlled by a diffusion controlled creep process. It has been shown to depend, among other factors, on the local hydrogen overpotential, pH and the hydrogen permeability of the crack tip corrosion film. According to Rebak and Szklarska-Smialowska [17], the use of this model for predictive purposes requires extensive assumptions.

1.2.8 Crack tip strain rate model

The slip-oxidation, coupled environment fracture, and film-induced cleavage models involve crack tip strain rate as a key factor for quantitative prediction of crack growth rate. The enhanced surface mobility model involves crack tip stress. All other earlier presented models are either not mature enough to be used for quantitative prediction of crack growth rate (e.g., selective dissolution-vacancy creep model) or are not relevant to common austenitic construction materials used in oxidizing high temperature water conditions.

The definition of the crack tip strain rate is ambiguous as there is, from fracture mechanics point of view, a singularity in the crack tip strain, i.e., $\varepsilon = \infty$, when the distance from the crack tip is 0 at any K_I or J-value above 0. Similarly, the definition of the crack tip stress is ambiguous because there is always plastic strain present in the crack tip and the stress is at the yield stress level.

Shoji et al. [43] have incorporated the work of Gao and Hwang [12] into their model, which is based on the same fundamental approach as the slip-oxidation model. According to the model, the crack tip strain rate needed for the calculation of crack growth rate is:

$$\frac{d\varepsilon_p}{dt} = \beta \frac{\sigma_y}{E} \frac{n}{n-1} \left[\ln\left(\frac{\lambda}{r} \left(\frac{K}{\sigma_y} \right)^2 \right) \right]^{\frac{1}{n-1}} \left[2 \frac{dK/dt}{K} + \frac{da/dt}{r} \right], \tag{32}$$

where $d\varepsilon_p/dt$ is the plastic strain rate at a characteristic distance r ahead of the crack tip, β and λ are dimensionless constants (5.08 and 0.3 used by Shoji et al. [43], respectively), n is the Ramberg-Osgood strain hardening exponent and K is the stress intensity factor. The fracture mechanics singularity is avoided in this approach by using the characteristic distance r, at which the strain is calculated. The characteristic distance is a function of several yet uncharacterized factors. Peng et al. [82] have determined a value of around 3 μm for r in sensitized AISI 304 steel in simulated BWR water. They used the data generated by rising displacement tests at three different displacement rates on 1T CT specimens. They also used the data generated in simulated BWR water on 10 x 10 x 55 mm^3 sensitized AISI 304 SEN(B) specimens by VTT. The VTT data resulted in a value around 3 μm for r. The original VTT data is presented in this work.

In their earlier work, Suzuki et al. [83] had obtained a value of 0.17-0.2 mm for the characteristic distance r in sensitized AISI 304 steel in oxygenated high temperature water using 1T CT specimens under various loading modes. Suzuki et al. [83] suggested that when the logarithmic term in Equation (32) is 0, specimen/environment specific threshold stress intensity, from an engineering point of view, becomes:

$$K_{ISCC} = \sigma_Y \sqrt{r/\lambda}\ . \tag{33}$$

They also suggest that, under suitable environmental conditions, there is a range of loading rates (in terms of dK/dt) in which the crack growth rate does not depend on the loading rate, i.e., the crack growth rate is solely controlled by environmentally generated crack tip strain rate. At higher loading rates the loading rate begins to control the crack tip strain rate and, thus, also the crack growth rate. The model also predicts that there is a diffusion controlled plateau crack growth rate in the high K-range [84].

1.3 Crack growth rate data and design lines

In-service inspections are needed to ensure the operational safety of the nuclear power plants. In-service inspection includes the methods and actions performed at specified time intervals for assuring the structural and pressure retaining integrity of the power plant components [85]. Each nuclear power plant operator must have an inspection program approved by a governmental regulatory organization. Typical inspection subjects with regards to stress corrosion cracking are piping, reactor vessel internals, steam-generator tubes and pressure vessel nozzles and penetrations [85].

Stress corrosion crack growth rate design lines (disposition lines) are used to perform safety assesments. The design lines are based on known stress corrosion crack growth rates vs. stress intensity factor K_I. It is important that the design lines do not overestimate the crack growth rate. Overestimated crack growth rate results in unnecessarily tight inspection schedules and economic losses. On the other hand, underestimated crack growth rate increases the risk for a leak or component failure.

In 1995, Swedish utilities began using design lines established by the Swedish Nuclear Power Inspectorate (SKI). The design lines were based on the laboratory and field data measured on stainless steels and nickel-base alloys Inconel 600 and Inconel 182. The design curves were divided into three categories: normal water chemistry (NWC) with low conductivity (≤ 0.3 μS/cm), hydrogen water chemistry (HWC) with low conductivity and for conditions out of nominal, i.e., conductivity ≥ 0.3 μS/cm [86]. The typical average conductivity in the presently operating boiling water reactors is ~0.1 μS/cm and the dissolved oxygen content, in NWC conditions, is 200–300 ppb.

The regulation collection containing the design lines is SKIFS 1994:1 [87]. An updated version of the regulation, SKIFS 2000:2, was approved in December 2000 [88].

More commonly used design lines are based on models approved by US Nuclear Regulatory Commission (USNRC): BWRVIP model and GE-PLEDGE model. The VIP model is based on a multivariable least square fit to the documented crack growth rate data and the PLEDGE model is based on the slip-oxidation theory and the experimental data [89].

Usually the design line is determined so that it coincides with the upper bound of the available experimental crack growth rate vs. K_I data. Specific design lines are needed for different materials and environments because of different crack growth rate vs. K_I behaviours. However, determination of the design lines is difficult because a large number of datapoints is needed for the sake of reliability. Also, the quality of the data is very important. Poor control of water chemistry, loading or material condition result in large scatter in the crack growth rates. Jansson and Morin [89] have presented an example how challenging it is to determine a design line from an existing data base. Figure 10 shows all the crack growth rate results of their data base for sensitized AISI 304 steel in high temperature BWR water. It is obvious that the data had to be screened. Jansson and Morin [89] screened their data base to include only the crack growth rates measured under conditions that are relevant to the present conditions of the Swedish boiling water reactors. The screened data, screening criteria and the design line (MD01 Rev 2.1) they determined for BWR NWC are presented in Figure 11.

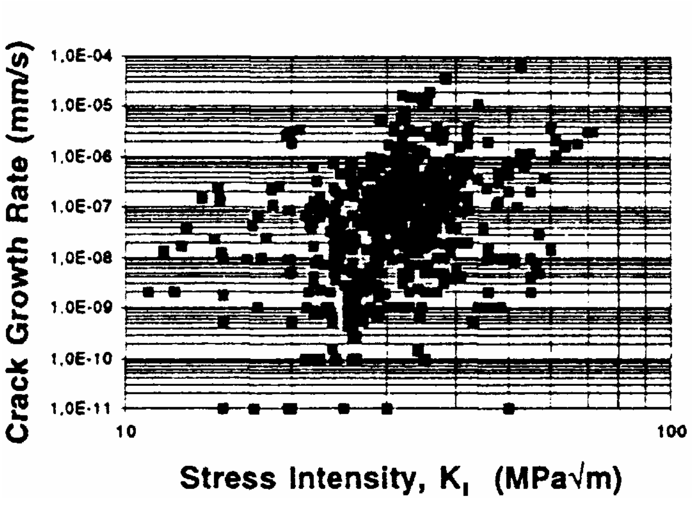

Figure 10. Initial crack growth rate data for the determination of the Swedish design line MD01 Rev 2.1 (BWR NWC) for sensitized AISI 304 steel [89].

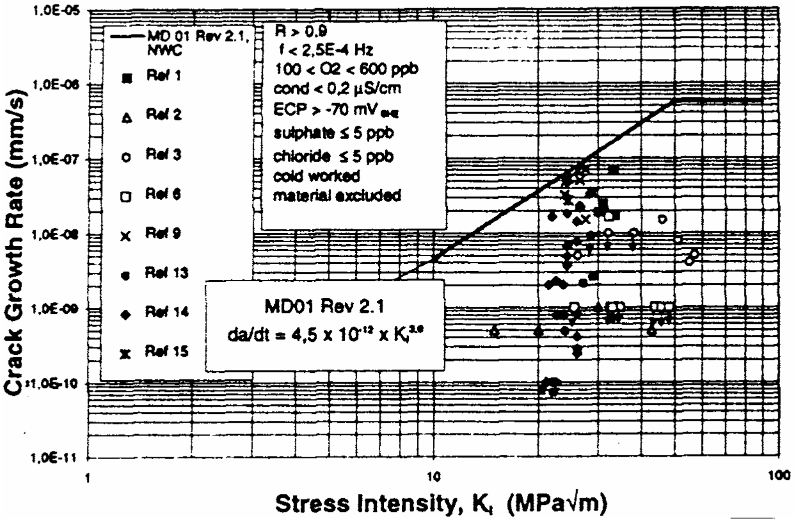

Figure 11. Screened data, screening criteria and the determined design line MD01 Rev 2.1 (BWR NWC) for sensitized AISI 304 steel [89].

Not only poor test control results in large scatter in the crack growth rate. Also small differences in the chemical composition may cause large differences in the crack growth rate in the same environment as shown, for example, by Ljungberg et al. [90] for Inconel 182 weld metal with various amounts of sulphur and phosphorus. They also showed that the effect of BWR water impurities on the crack growth rate depends on the small differences in the chemical composition of the alloy.

Figure 12 shows screened data collected by Morin et al. [91] for the crack growth rate of Inconel 182 weld metal in BWR NWC. They also proposed a design line, which covers the upper bound of the screened crack growth rate data. Before the design line was determined, Swedish utilities had to use the NUREG 0313 line, which was much more conservative at low stress intensities than the new line. Both lines are shown in Figure 12.

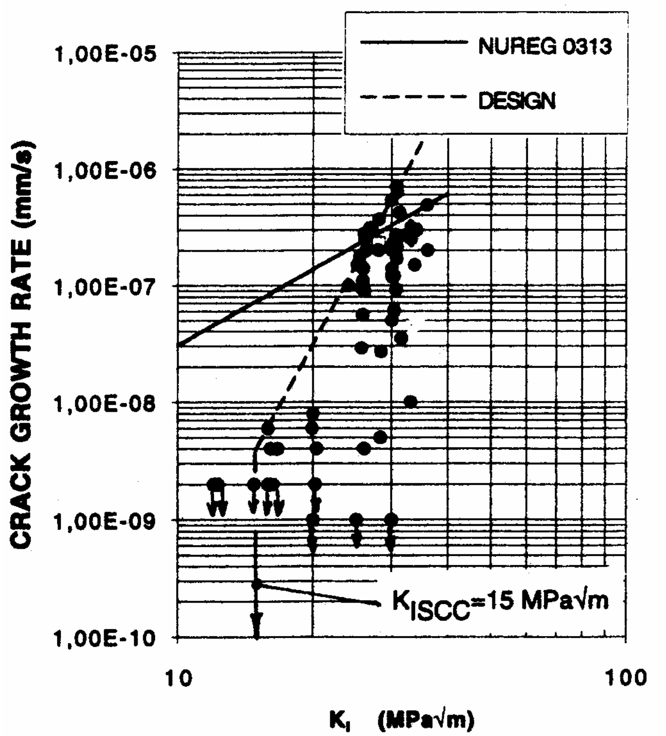

Figure 12. Screened data collected by Morin et al. [91] for the crack growth rate of Inconel 182 weld metal in BWR NWC, proposed design line and the NUREG 0313 line (USNRC line) Swedish utilitities had to use before.

It is difficult to measure reliable crack growth rates using present monitoring methods, especially in nonhomogeneous materials such as Inconel 182 weld metal. The crack growth tends to be uneven in the welds where the crack follows the dendrite boundaries which, on the other hand, tend to follow randomly some other path than loading line or plane. In the literature, a solution to overcome this kind of problems is proposed, for example, by Andresen et al. [92] who periodically perform unloadings/reloadings during a constant load test. The unloadings keep the crack front even because the severity of the loading condition results in crack propagation even in the less SCC susceptible locations of the crack front. In the extreme cases, the unloading/reloading can result in the crack propagation even across the dendrites or through the grains.

It is important to recognize the factors influencing the laboratory crack growth rate measurement results, when the design lines are formulated. As a consequence, the literature data is screened so that only the data for which the test conditions are reported accurately enough are accepted. It is typical that only results obtained using compact tension, C(T), or wedge opening loaded, WOL, specimens fulfilling or only slightly exceeding the K_I limits of the linear-elastic fracture mechanics standards are accepted [89]. It is also typical that only crack growth rates measured under constant load, constant displacement or, for appropriate purposes, fatigue are accepted. However, acceptance of the crack growth rate data generated using elastic-plastic fracture mechanics approach would be beneficial because of reduced testing costs.

2. Objectives

One of the objectives of this study was to determine under which conditions small specimens can be utilized for stress corrosion crack growth rate measurement for safety analysis purposes and screening of possible construction materials. Another objective was to characterize the stress corrosion cracking susceptibilities of several construction materials in simulated reactor water environment (mainly boiling water reactor, BWR).

Two austenitic stainless steels were studied in the first test series. The tests were performed on AISI 304 and 321 steels in order to study the effects of J-level and applied displacement rate on the SCC crack growth rate and fracture morphology in simulated BWR water. The tests were groundwork for the subsequent characterization of the stress corrosion susceptibility of the core shroud surveillance material of Olkiluoto 1.

The core shroud (moderator tank) surveillance material of Olkiluoto 1 was characterized after 10 years exposure to neutron irradiation. The characterization began by tensile tests. The purpose of the tensile tests was to determine the effects of the fast neutron fluence on the mechanical properties of the core shroud.

After the tensile tests, the irradiation assisted stress corrosion cracking (IASCC) susceptibility of the material was studied by performing a series of slow strain rate tests in simulated BWR water at various corrosion potentials relevant to the reactor core.

The final phase of the characterization was to study the SCC susceptibility more closely by performing a series of slow rising displacement tests, heat treatments, and chemical and electrochemicals tests. The main objective of this part of the characterization was to differentiate the effects of:

- low temperature sensitization (LTS),
- thermal sensitization due to welding and
- irradiation

on the stress corrosion cracking susceptibility of the core shroud material in BWR water. LTS occurs in AISI 304 weldments exposed for long periods of time to power plant operating temperatures. The $M_{23}C_6$ carbides which have nucleated as a result of welding can grow at low temperatures, in which the nucleation of new carbides is not possible [93].

The tests on the irradiated core shroud specimens resulted in a need to study the effects of the loading rate on the stress corrosion crack growth rate and fracture morphology. A test series was conducted on AISI 304 steel in mill-annealed and in sensitized conditions in simulated BWR water using varying displacement rates. The applicability of standard procedures for J-calculation in the case of intentionally varying displacement rates is considered in Appendix 1.

The next test series was performed on low activation steel F82H, which is a candidate material for the future fusion reactors. Materials of fusion reactors will be exposed to high-energy neutron radiation, up to over 100 dpa fluences [94]. Austenitic stainless steels, which are used in experimental fusion reactors, suffer from severe swelling at so high neutron fluences. The relative swelling resistance of ferritic/martensitic steels is one order of magnitude better: swelling increases about 1%/10 dpa in austenitic stainless steels and about 1%/100 dpa in ferritic/martensitic steels [95].

Several ferritic/martensitic steels have been selected by EC Fusion Materials Long Term Programme as prime candidate materials for the first wall of the blanket structure of ITER fusion reactor (International Thermonuclear Experimental Reactor) [94, 95]. These ferritic/martensitic steels have been designed low long-term activity in mind by modifying the chemical composition by using alloying elements with lower activation tendency under neutron irradiation (thus, Low Activation Steel, LAS).

The materials are subjected to high temperature water in the first wall cooling channels. The exposure of the cooling water to high neutron flux results in radiolysis and formation of, for example, hydrogen peroxide, which increases corrosion potential and risk of stress corrosion cracking (SCC).

This test series aimed to evaluate the SCC susceptibility of non-irradiated low activation ferritic/martensitic (LAF or LAM) stainless steel F82H in high temperature water at increased corrosion potential using combined rising/constant displacement tests. Also, the influence of specimen size on fracture resistance measurement capacity was of interest.

In the fifth test series, the effect of BWR water sulphate ion concentration on the stress corrosion crack growth in Inconel 82 and 182 weld metals was studied. The effects of the stress intensity level and loading rate on the crack growth rate were also of interest.

The effect of sulphate ions on stress corrosion crack initiation and propagation in Inconel 182 weld metal in BWR water has also been investigated in many other studies [96-101]. Sulphate ions have been observed to have an accelerating effect on the crack growth rate. Initiation is also enhanced, if the sulphate ion concentration is high enough to change the pH value from near neutral to acidic. However, the amounts of sulphate ion additions have commonly been high, of the order of 1 ppm, and only few results are available on the effects of small amounts, i.e., 30 ppb of sulphate, comparable to a possible ion exchange resin intrusion induced concentrations in a real BWR plant. In the surveyed literature, no data was found on the effects of sulphate ion concentrations at the level of 10 ppb or less.

The presence of anionic impurities has been shown to enhance the crack growth rate in Inconel 182 weld metal even at low temperatures. The decrease of the corrosion potential, e.g., by hydrogen water chemistry (HWC), reduces the crack growth rate and therefore also reduces the detrimental effect of impurities. However, with increasing temperature, the crack growth rate can be significant even in de-aerated water, i.e., at low corrosion potentials at high temperatures, if the anion concentration is high [99, 100].

Stress corrosion cracking in Inconel 182 weld metal is interdendritic, and uneven crack propagation is common. The accuracy of the commonly used crack length measurement method, Potential Drop (PD) method, is sensitive to the unevenness of the crack extension. The uneven crack propagation and remaining uncracked ligaments behind the crack tip may result in a considerable difference between the crack extension measured using PD and actual physical crack extension observed on the fracture surface.

The critical sulphate ion level required to accelerate crack growth depends on the flow conditions and the duration of the impurity transients. In tests conducted in Studsvik, two sulphate extrusions of short duration (<14 h) were needed before measurable acceleration in the crack growth rate was observed [101]. On the other hand, the decrease in the crack growth rate after returning to low impurity level in the bulk environment can be prolonged up to >100 h.

Because of the dependencies between crack growth rate and elastic-plastic stress intensity factor (K_J) observed during the previous five test series, one more test series was performed. The objective of the test series was to compare the stress corrosion crack growth rates obtained using small SEN(B) specimens under elastic-plastic loading conditions and 25 mm C(T) specimens under linear-elastic loading conditions. The tests were performed on AISI 304 steel in sensitized condition in simulated BWR water using combinations of rising displacement, constant load, and constant displacement type loading.

3. Experimental procedures

3.1 Test methods, materials, specimens, and environments

The tests, if not otherwise mentioned, were performed in autoclaves connected to water recirculation loops. A typical water recirculation loop with a materials testing autoclave is schematically presented in Appendix 2. The outlet and inlet waters were continuously circulated through mixed bed ion exchangers in order to keep the inlet water as clean as possible.

The autoclave temperatures were measured and controlled using K-type thermocouples and West or Eurotherm PID controllers. The autoclave pressures were controlled using Tescom pressure regulators. The inlet and outlet water dissolved oxygen contents were measured using Orbisphere O_2 meters. The inlet water oxygen contents were controlled by computers, which also measured and saved the water chemistry parameters. The inlet and outlet conductivities were measured using Contronic or Kemotron conductivity meters. pH was measured using Contronic pH meters. Oxygen contents, conductivities and pH were measured at ambient temperature.

Crack growths were monitored using reversing direct current potential drop method (DCPD). Reversing DCPD method was used in order to prevent electrochemical polarization of the specimens, and to eliminate possible thermoelectric effects from the potential drop signal. The crack length was monitored in ½ h intervals. Between the measurements, the DCPD current was off. The specimens were electrically insulated from the autoclave body by aluminium or zirkonium oxide roller pins.

Corrosion potentials of the specimens were measured at the test temperature using 0.01 or 0.005 M KCl AgCl/Ag reference electrodes.

In most cases, load line displacement was measured using linear variable displacement transducers (LVDT) and load was measured using external commercial Interface load cells.

Post-test fatigue was conducted for the specimens before they were broken open in order to prevent possible damage to the fracture surfaces. After the specimens were opened, the fracture surfaces were examined using a scanning electron microscope (SEM) and the initial and final crack lengths were measured on an x-y table equipped with displacement sensors and an optical microscope.

3.1.1 J-R tests on AISI 304 and 321 steels in BWR water

The applicability of J-R tests to SCC testing was studied using specimens made of sensitized AISI 304 and welded AISI 321 steels.

The AISI 304 specimens were 10 mm x 10 mm x 55 mm SEN(B) specimens, Figure 13, which were cut from the original blocks by electric discharge machining (EDM). After machining, the specimens were furnace sensitized for 2 h at 600 ^{o}C after which they were prefatigued to the a_o/W ratio of 0.5. Finally, 10 % side grooves were machined on the both sides of the specimens.

The AISI 321 specimens were 10 mm x 5.5 mm x 55 mm SEN(B) specimens, Figure 14. The specimens were cut from a welded pipe sample and etched to reveal the precise location of the coarse grained zone in the HAZ. Small notches were machined to the coarse grained zone and the specimens were prefatigued to the initial crack length of about 2.5 mm after the etching. The chemical analyses of the materials are presented in Table 2.

Table 2. The chemical compositions of AISI 304 and AISI 321 steels (wt %).

Material	C	Si	Mn	S	P	Cr	Ni	Mo	Cu	Ti
AISI 304	0.043	0.38	1.82	0.015	0.023	19.1	10.2	0.10	0.11	0.01
AISI 321	0.046	0.34	1.62	0.005	0.032	17.8	10.7	0.34	0.16	0.50

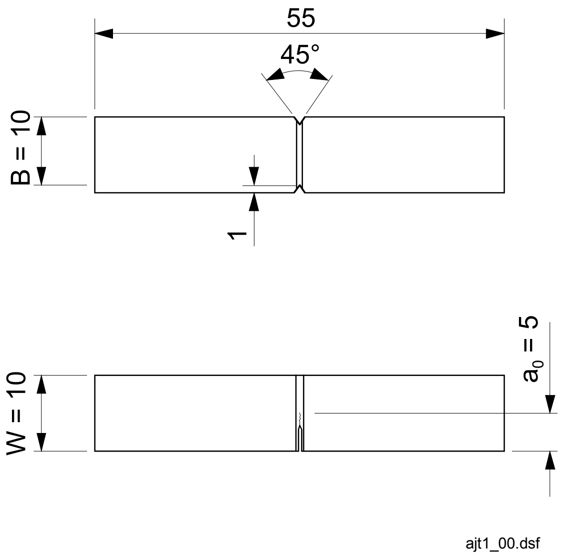

Figure 13. Main dimensions of the AISI 304 steel specimens tested in simulated BWR water.

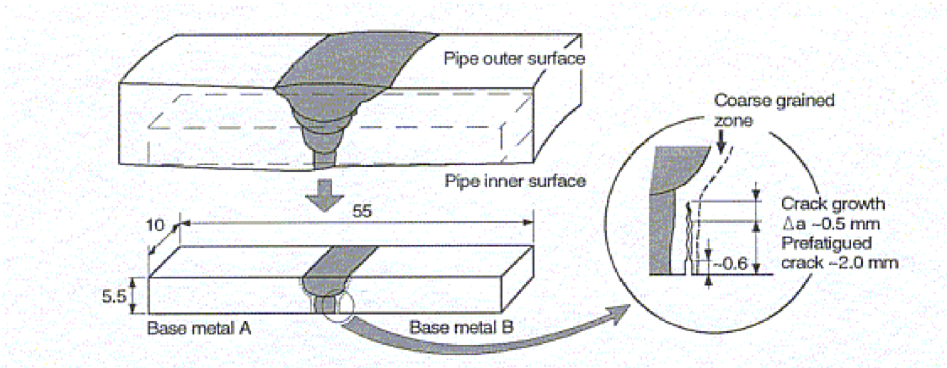

Figure 14. Schematic presentation of the preparation and the main dimensions of the AISI 321 steel specimens tested in simulated BWR water.

The sensitized AISI 304 and welded AISI 321 steels were tested in simulated BWR water with controlled oxygen content and feed water conductivity at 288 ^oC. The water chemistry parameters are presented in Table 3. The specimens were polarized to the potentials of either +400 mV_{SHE} (AISI 304 specimens) or +200 mV_{SHE} (AISI 321 specimens). The conductivity was increased by Na_2SO_4 addition (30 ppb as SO_4^{2-}).

Table 3. Water chemistry parameters for the tests in simulated BWR water.

Temperature [^{o}C]	288
Pressure [bar]	100
Conductivity [µS/cm]	0.3
O_2 content [ppb]	200

The J-R tests on AISI 304 and 321 steels were performed in an autoclave equipped with a servo-hydraulic testing machine. The test parameters are presented in Table 4.

Table 4. Test matrix for the SCC tests on AISI 304 and 321 steels.

Test material	Displacement rate [mm/s]	ECP [mV_{SHE}]
AISI 304	8.0×10^{-4}	+ 400
AISI 304	1.2×10^{-5}	+ 400
AISI 304	2.4×10^{-6}	+ 400
AISI 321	3.0×10^{-6}	+ 200
AISI 321	3.0×10^{-7}	+ 200

3.1.2 SCC susceptibility of Olkiluoto 1 core shroud material

The material was austenitic stainless steel with chemical composition according to Swedish standard SIS 2333, corresponding to AISI 304 type steel. The test material originated from the core shroud surveillance program of Olkiluoto 1. The surveillance specimens were cut from a block consisting of two base metal plates and a weld seam between them before they were installed into the reactor. The specimens were smooth tensile test specimens with 36 mm gauge section length and 5 mm gauge section diameter. The average chemical analysis of the base metal plates is presented in Table 5.

Table 5. The average chemical analysis of the base metal plates (wt %).

C	Si	Mn	S	P	Cr	Ni	Mo	Co	Fe
0.05	0.42	1.65	0.010	0.027	18.5	9.2	0.28	0.11	Bal.

The surveillance program was initiated at the same time with the plant start-up to follow the degradation of mechanical properties of stainless steels due to irradiation. The specimens were irradiated in the reactor tank for a period of 80 000 h. The fast neutron flux in the irradiation position corresponds with the flux in the most severe locations of the core shroud. The fluence of the irradiated specimens was about 1.5×10^{20} n/cm^2, $E > 1$ MeV. The cutting plan is shown in Figure 15 and the surveillance specimen geometry in Figure 16.

Tensile test specimens, which were not needed for the evaluation of the tensile properties, were used for slow strain rate tests (SSRT) in simulated BWR conditions.

Only a small amount of non-deformed irradiated material remained after completion of the tensile and slow strain rate tests. Applicable non-deformed parts were cut from the tensile specimen heads and small prefatigued SEN(B) specimens were made to study the IASCC susceptibility of the base metals. Two remaining tensile specimens with a weld seam in the gauge section were utilized to prepare four SEN(B) specimens to study the combined effects of thermal sensitization and irradiation on the IASCC susceptibility of HAZ. Due to the small size of the available pieces the SEN(B) specimens were prepared using reconstitution welding.

The reconstitution welding was performed using a stud arc welding machine. The heat input was low and the welding time was short, so the formed heat affected zone was narrow. Figure 17 shows the specimen temperature as a function of time at various distances from the reconstitution weld seam in 4 mm x 4.8 mm x 10 mm AISI 304 steel middle sections. The temperatures were measured using thermocouples in metallic contact with the welded material. The minimum distance between the reconstitution weld seam and the fatigue crack plane in the test material was 4 mm.

After the reconstitution welding the specimens were electric discharge machined to final geometry, notches for prefatiguing were electric discharge machined and, finally, the specimens were prefatigued.

Prefatigue was performed using a computer controlled fatigue device. Crack length was monitored using potential drop method and the specimens were fatigued to the a_0/W ratio of about 0.5. The load amplitude was measured with a strain gauge and the amplitude was adjusted continuously during the crack growth process. The K_{max} value used for these specimens in prefatigue was 8 MPa√m and applied load ratio, R, was 0.1. No side grooves were made. The dimensions of the specimens were typically 3 mm × 4 mm × 27 mm. The SEN(B) specimen preparation procedure is presented in Figure 18.

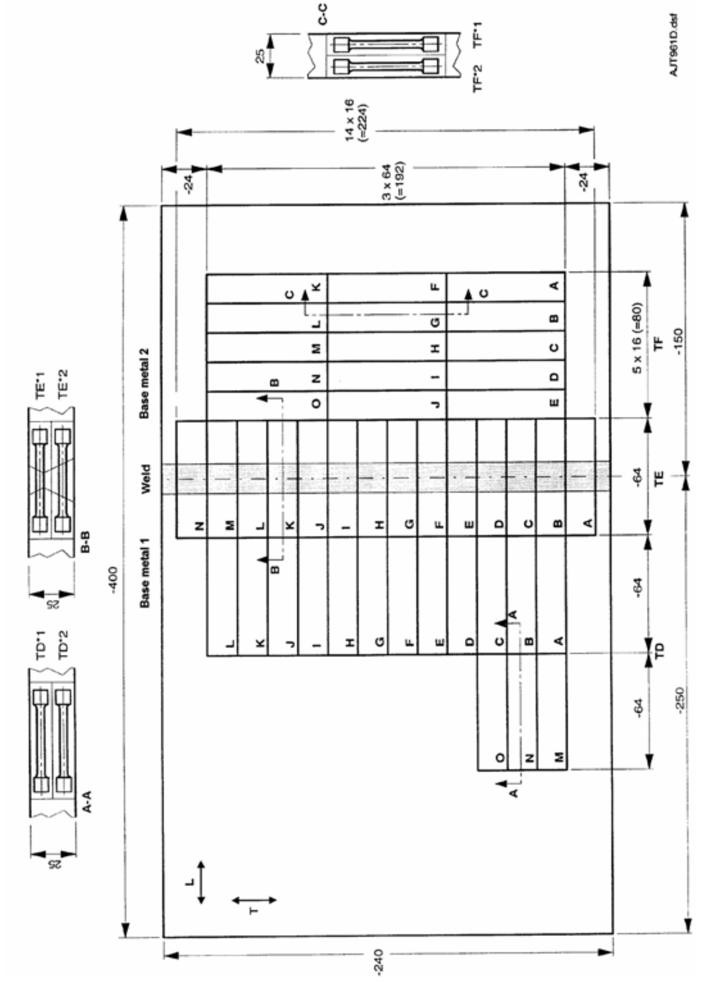

Figure 15. Cutting plan for the tensile and SSRT specimens.

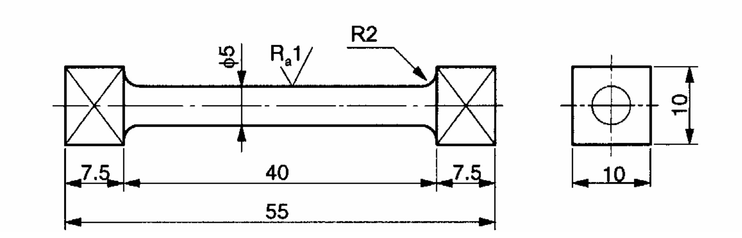

Figure 16. Surveillance tensile specimen geometry.

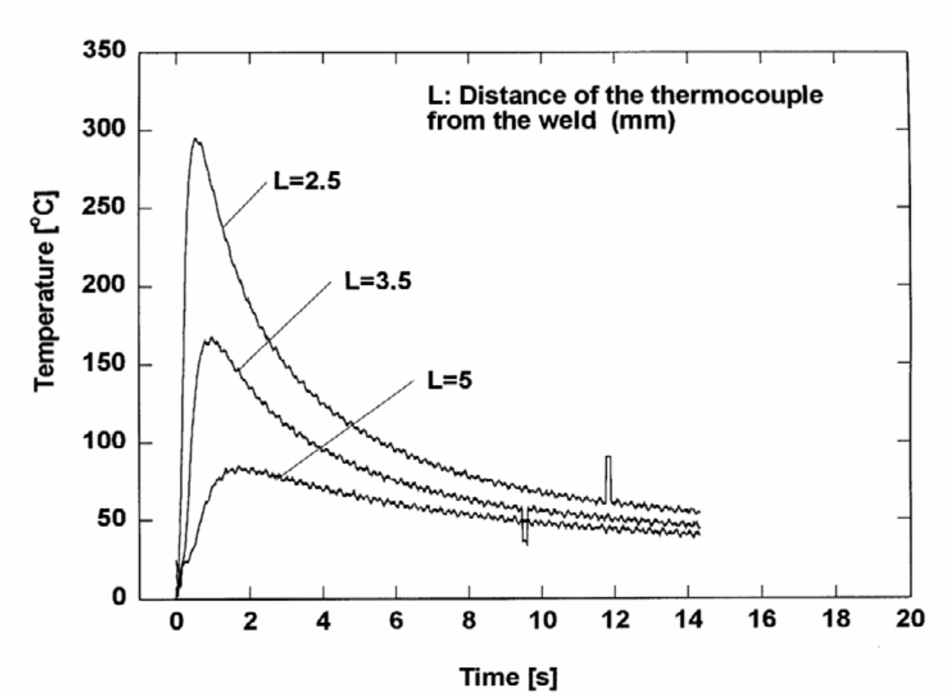

Figure 17. Time-temperature curves at various distances from the fusion line during reconstitution welding of 4 x 4.8 x 10 mm^3 AISI 304 steel middle sections.

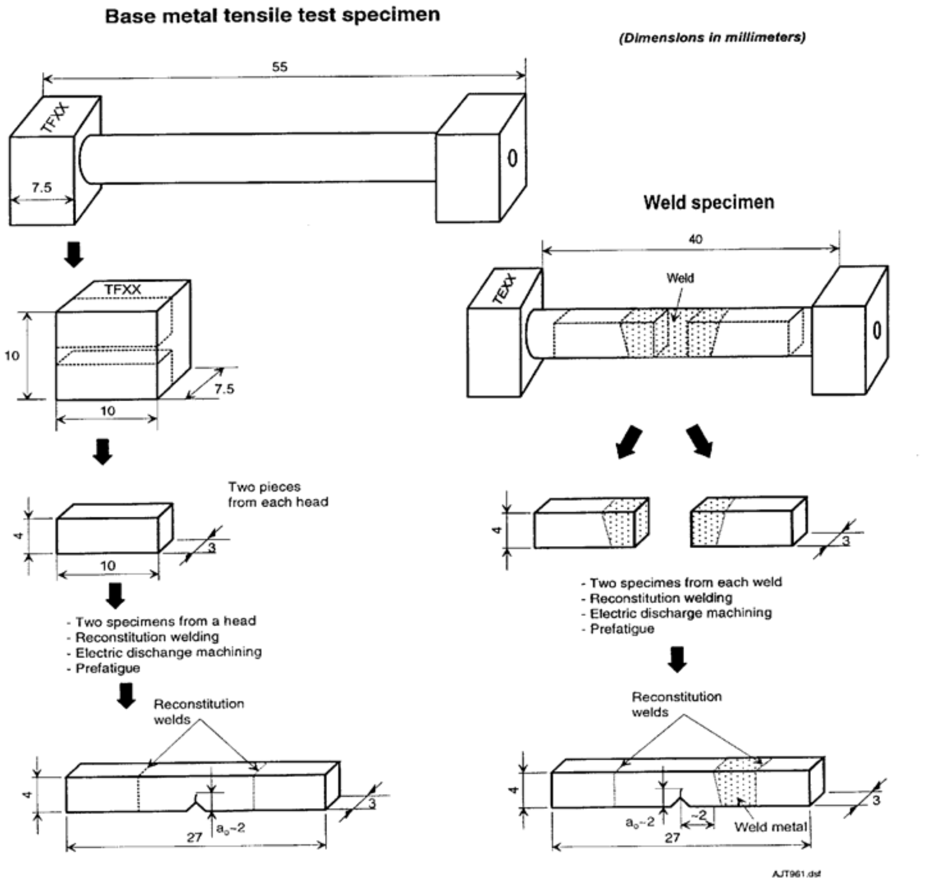

Figure 18. SEN(B) specimen preparation from the original surveillance tensile specimens.

Microstructural studies

The chemical compositions of the base metals were measured by optical emission spectrometry and the microstructures were documented by optical microscopy. δ-ferrite content measurements were also applied to characterize the microstructures.

Tensile tests

Tensile tests were conducted to evaluate the effects of irradiation on the mechanical properties of the materials. Tensile tests were performed according to SFS-EN 10 002-1 standard. The specimens were tested with a strain rate of 0.1 mm/min until yielding occurred. After yielding, the strain rate was increased to 0.3 mm/min.

Slow strain rate tests

SSRTs were used as preliminary tests to compare the susceptibility of irradiated and non-irradiated austenitic stainless steels to stress corrosion cracking in simulated BWR water. SSRTs were performed according to the standard ISO 7539-7 in simulated BWR water at different electrochemical corrosion potentials (-200, 0 and +100 mV_{SHE}) with a strain rate of 2.8×10^{-7} s^{-1}. Stress-strain curve was determined for all specimens. The specimens were loaded in a step motor driven loading frame in an autoclave. All fracture surfaces were investigated with a scanning electron microscope (SEM) and the amount of SCC, i.e., IGSCC and TGSCC on the fracture surfaces, was determined.

Slow J-R tests

J-R curves with slow displacement rates were determined for the austenitic stainless steel in order to evaluate the stress corrosion crack growth rate in the base metal and in the heat affected zone close to the weld. The tests were performed using constant displacement rates of either 1.8×10^{-6} mm/s or 2.6×10^{-7} mm/s. Additionally, one test on a non-irradiated HAZ specimen was conducted by varying the displacement rate between $1.8 \times 10^{-6} – 4.0 \times 10^{-7}$ mm/s.

The actual SCC tests were performed at the potential of +200 mV_{SHE} (potentiostatic control). “Inert” tests with expected minor environmental impact on crack growth rate were performed at the potential of -500 mV_{SHE} (polarized). Additionally, one test was conducted at the potential of -90 mV_{SHE} (polarized). The environmentally assisted crack growth rate, $(da/dt)_{EAC}$, for the material tested at the potentials of +200 and -90 mV_{SHE} were evaluated using a superposition-based analysis method. This is explained more closely in the description of the analysis methods (chapter 3.2).

The application of slow J-R tests to measure the crack growth rate was supported by the following points of view:

- There was not enough test material to perform tests on linear-elastic loading conditions at reasonably high K_I-levels.

- Earlier experience on the other austenitic stainless steels has indicated that slow J-R tests on pre-cracked SEN(B) specimens reveal the IGSCC susceptibility of the material more easily than SSRTs on tensile type specimens.

- The application of the superposition analysis was assumed to reduce the effect of the applied loading rate on the crack growth rate.

Heat treatments

Jacobs et al. [102] have observed that annealing at 450–500°C decreases the IGSCC susceptibility of irradiated AISI 304 steel. In an other test series, Jacobs and Dumbill [103] studied the effects of post-irradiation low temperature annealing at 475–500°C on the grain boundary chemistry and IASCC susceptibility of AISI 304 steel irradiated to the fluence of 1.74–2.95 x 10^{21} n/cm^2 (E > 1 MeV). They observed that the level of radiation induced grain boundary segregation of Cr, Mn and Si decreased even during relatively short annealing periods (0.75–24 h). At the same time, the annealing reduced the susceptibility to intergranular cracking in bent-beam and constant extension rate tests performed in high-purity water containing 32 ppm dissolved oxygen at the temperature of 288°C.

Low temperature annealing was made for some of the irradiated core shroud SEN(B) specimens at the temperature of 450°C for 24 h. The goal of this heat treatment was to reduce the effects of radiation induced segregation (RIS), and at the same time to emphasize the effects of thermal sensitization. One non-irradiated HAZ specimen was annealed at 500°C for 4 h to study the effect of LTS without the interference due to RIS.

The effects of annealing on the material properties were studied using hardness measurements and electric resistivity measurements. The annealing was performed at 380°C and 440°C.

Intergranular corrosion tests

The degree of sensitization (DOS) was measured according to the standard ASTM G-108-92 "Electrochemical Reactivation (EPR) for Detecting Sensitization of AISI 304 and 304L Stainless Steels". The polarization during the EPR tests was performed using double loop method (DL-EPR) instead of the single loop method described in the standard. The tests were conducted in an electrochemical cell designed for the field use. DL-EPR tests were conducted for every material condition except for the material, which was heat treated at 500 °C.

Modified Huey tests with increased Cr^{6+} content were made otherwise following the instructions given in ASTM A262 Practice C. The modified Huey test has been used especially to reveal the segregation in irradiated stainless steels. The tests were performed in a boiling 5 N HNO_3 + 5 g/l Cr^{6+} solution for 24 h. After the tests the weight losses of the samples were measured and the samples were studied using a scanning electron microscope. The modified Huey tests were conducted to all surveillance material conditions used in the stress corrosion crack growth tests.

Test environment for the slow strain rate and J-R tests

The tensile tests were conducted in air. The slow strain rate tests and the J-R-tests were performed in a simulated BWR core water: inlet water O_2 content 200 ppb, conductivity 0.3 µS/cm (increased with Na_2SO_4 addition), temperature 288°C and pressure 100 bar (10 MPa). The SSRT and SEN(B) specimens were isolated from the autoclave body and polarized to the desired potentials using a potentiostat. Dissolved oxygen content and conductivity were measured in the inlet water, and conductivity as well as pH value in the outlet water.

3.1.3 Tests on AISI 304 steel using varying displacement rate

The test material was AISI 304 austenitic stainless steel both in as-received (mill-annealed) and in furnace-sensitized condition. The sensitization was conducted at 620°C for 24 h. The degree of sensitization of the furnace-sensitized material was determined using DL-EPR method. The measured reactivation ratio, I_r/I_a, was 67% which indicates severe chromium carbide precipitation at the grain boundaries.

The specimens were 10 mm x 10 mm x 55 mm SEN(B) specimens prefatigued to the a_o/W ratio of 0.5. The specimens were prefatigued in air using frequency of about 80 Hz and K_{max} of 8 MPa√m and load ratio, R, was 0.1. In the case of the sensitized material, prefatigue was conducted after the furnace sensitization.

Three specimens were prepared from the sensitized material and one from the material in as-received condition. One of the sensitized specimens was 10% side grooved. No side grooves were made to the other three specimens.

The tests were conducted as a combination of rising and constant displacement tests in two autoclaves connected to a water recirculation loop. Load line displacement rate was intentionally varied during each test in order to reduce the number of tests needed to determine the influence of the loading type/loading rate on da/dt and fracture morphology.

The autoclaves were equipped with step motor controlled testing machines. Load line displacement was determined from the step motor control commands. The determined load line displacement was verified with a dial indicator.

The tests were conducted in simulated BWR water, Table 6, in two AISI 316L autoclaves. The autoclave volumes were 1.2 l of which the loading tools occupied about 0.2 l. The total water flow rate during the tests was 18 l/h, i.e., the average water refreshing time inside each autoclave was 7 min.

Table 6. Water chemistry conditions for the tests.

Temperature	288°C
Pressure	10 MPa
Dissolved oxygen (inlet)	300 ppb
Dissolved oxygen (outlet)	200–300 ppb
Conductivity (inlet)	0.08 μScm^{-1}
Conductivity (outlet)	0.18–0.22 μScm^{-1}

3.1.4 Tests on low activation steel (LAS) F82H

The test material was ferritic/martensitic stainless steel F82H-mod. The steel was manufactured by Japanese NKK-corporation in an induction vacuum furnace (charge No. 9753). The material was hot rolled at 1250°C, normalized at 1040°C for 40 min, and finally tempered at 750°C for 60 min. The test material plate code, cut from the original ingot, is 31W-18. Chemical composition of the material is presented in Table 7 and mechanical properties in Table 8.

Table 7. Chemical composition of ITER candidate material F82H (wt %) [104].

C	Cr	W	Mn	V	Ta	Si	P	S	Fe
0.09	7.7	1.95	0.16	0.16	0.02	0.11	0.002	0.002	Bal.

Table 8. Mechanical properties of ITER candidate material F82H (estimations from graphs presented in [104]).

Temperature [°C]	YS [MPa]	UTS [MPa]	Elongation [%]	Reduction of area [%]	Charpy impact energy [J]
RT	550	650	22	79	250 (-20°C)
200	500	580	20	82	

The specimens of this study were 3 mm x 4 mm x 27 mm and 5 mm x 10 mm x 55 mm SEN(B) specimens prefatigued to $a_0/W = 0.5$. All 4 of the smaller specimens and two larger specimens were side grooved, 10% side grooves on each side. Two of the 5 mm x 10 mm x 55 mm specimens were not side grooved. The specimen geometries (side-grooved specimens) are presented in Figure 19.

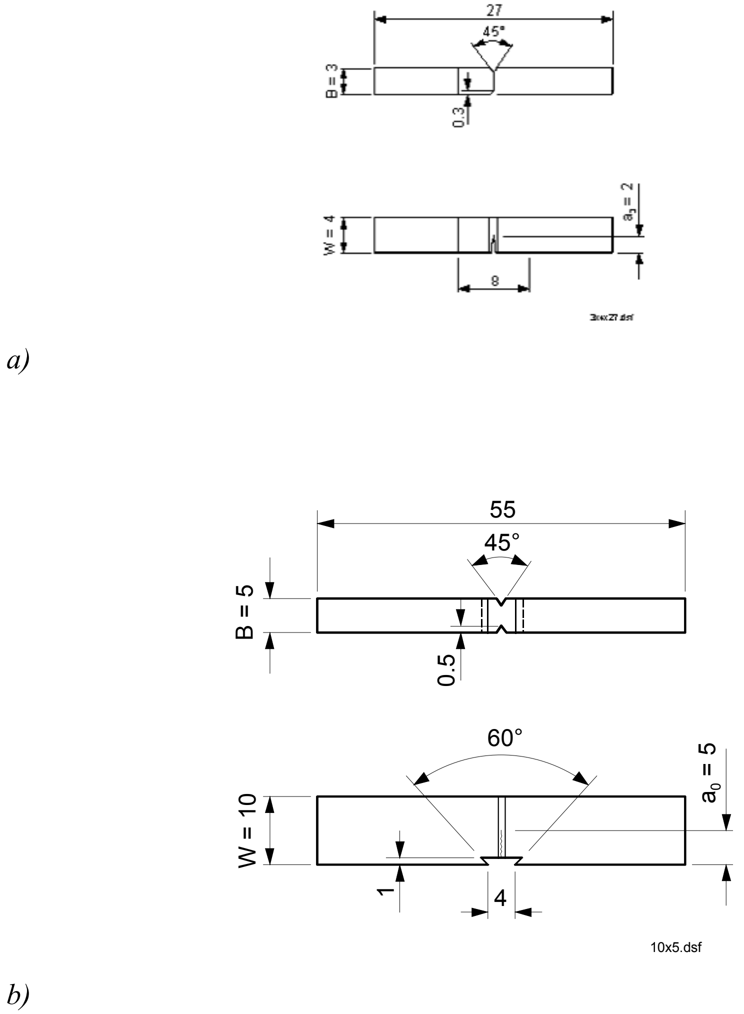

Figure 19. SEN(B) specimen geometries used in tests on F82H steel.

Tests on 3 mm x 4 mm x 27 mm specimens were conducted in silicon oil bath (i.e., in inert environment) at 20^{o}C, 100^{o}C and 200^{o}C. Two tests on 5 mm x 10 mm x 27 mm specimens were conducted using constant load line displacement rates (5 x 10^{-7} and 1 x 10^{-6} mm/s) in nitrogen atmosphere at 230^{o}C.

Two stress corrosion cracking tests on 5 mm x 10 mm x 55 mm specimens were made. These tests were bending tests with a combination of rising/constant displacement. The tests were conducted simultaneously in two autoclaves, equipped with step motor controlled testing machines, in demineralized high temperature water (230°C) with sulphate addition. The specimens were polarized using a potentiostat. The tests were started at the potential of +400 mV_{SHE} using load line displacement rate of ~2 x 10^{-7} mm/s. Later the displacement rate was increased to 2 x 10^{-6} mm/s. At last, the displacement rate was decreased to 0 mm/s. The same displacement rate sequence was then repeated at 0 mV_{SHE} with the same specimens. Both specimens were tested with the same test parameters. The test environment of the stress corrosion tests is presented in Table 9.

Table 9. Water chemistry parameters of the tests conducted in high temperature water at the potentials of +400 and 0 mV_{SHE}.

Conductivity	0.3 µS/cm
SO_4^{2-} concentration	30 ppb
Dissolved oxygen, O_2	300 ppb
Pressure	100 bar
Temperature	230°C

3.1.5 Effect of BWR water sulphate concentration on SCC crack growth rate

Test materials were Inconel 182 and 82 weld metals in thermally aged condition. The thermal aging was conducted by annealing at 400°C for 200 h. The chemical compositions of the studied test materials are presented in Table 10. In addition to Inconel 182 and 82 weld metals, one cold-worked AISI 316 stainless steel specimen was tested. Cold-worked AISI 316 steel is known to be susceptible to intergranular stress corrosion cracking in BWR conditions [105]. The specimens were 10 mm x 10 mm x 55 mm SEN(B) specimens with 10% side grooves fatigued to the a_0/W ratio of 0.5.

Table 10. Chemical compositions, wt %, of the test materials, Inconel 182 and 82 weld metals and cold-worked AISI 316 steel. The compositions are based on the analyses of the material suppliers.

	Fe	C	N	Cr	Mn	Si	S	Ti/Mo	Ni
I 182	8.07	0.03	-	15.24	7.57	0.52	0.001	0.52/-	Bal.
I 82	0.71	0.036	-	20.23	2.92	0.05	0.001	0.38/-	Bal.
AISI 316	Bal.	0.013	0.056	16.96	1.86	0.28	0.004	-/2.55	10.5

The tests were very slow rising displacement or constant displacement tests (displacement rates $2x10^{-7}$, $2x10^{-8}$, and 0 mm/s) using prefatigued 10 mm x 10 mm x 55 mm SEN(B) specimens. From 4 to 6 specimens were loaded simultaneously in the same autoclave using separate loading frames and instrumentation for each specimen. The test matrix is presented in Table 11.

Table 11. Test matrix for stress corrosion crack growth tests on Inconel 82 and 182 weld metals and cold-worked AISI 316 steel in simulated BWR water ($T = 273^oC$, $O_{2\,outlet} = 300$ ppb).

	Material	Specimen size (BxW) and orientation	Loading method	SO_4^{2-} content, ppb
1^{ST} series	I 82 (aged)	10x10, T*	Rising displacement	0, 10, 30 and 100 ppb
	I 82 (aged)	10x10, P*		
	I 182 (aged)	10x10, T		
	I 182 (aged)	10x10, T		
	I 182 (aged)	10x10, P		
	AISI 316, 20% cold-worked	10x10, L-S		
2^{ND} series	I 82 (as-welded)	10x10, P	Rising displacement, subsequent change to constant displacement	0 ppb
	I 82 (aged)	10x10, P		
	I 182 (as-welded)	10x10, T		
	I 182 (aged)	10x10, T		
3^{RD} series	I 82 (as-welded)	10x10, P	Rising displacement, subsequent change to constant displacement	30 ppb
	I 82 (aged)	10x10, P		
	I 182 (as-welded)	10x10, T		
	I 182 (aged)	10x10, T		

* T, crack plane transverse to the weld pass; P, crack plane parallel to the weld pass.

The test environment was simulated BWR water: temperature 273°C and outlet oxygen content 300 ppb. Diluted H_2SO_4 pre-mixture solution was added into the high temperature and pressure autoclave inlet water by a liquid chromatograph pump. The flow rate of the injected solution was adjusted to obtain the wanted concentration of SO_4^{2-} in the water. The outlet flow was purified with ion exchangers before returning the water into the re-circulation tank. The circulation flow rate through the autoclave was 0.3 l/min, which means that the autoclave water was refreshed in every 20 min.

3.1.6 Comparison of SCC crack growth rates of sensitized AISI 304 steel using 10 mm SEN(B) and 25 mm C(T) specimens

The test material was austenitic stainless steel AISI 304 in furnace-sensitized condition. The sensitization was conducted at 680°C/1 h and after that 500°C/24 h. The steel was provided by Studsvik Nuclear AB. The sensitization was performed at VTT.

Yield stress and tensile strength of the steel at 290°C are 163 and 477 MPa, respectively. Grain size of the steel is ASTM 5-6, i.e., 65 to 45 µm. The P_a-value (degree of sensitization) was 10–20 C/cm^2 after the sensitization heat treatment. The tensile properties, grain size and degree of sensitization were measured by Studsvik Nuclear AB for similarly heat treated steel of the same heat. The chemical composition of the steel was provided by the material supplier (Avesta AB) and is shown in Table 12.

Table 12. Chemical composition of AISI 304 steel, wt %.

C	Si	Mn	P	S	Cr	Ni	Fe
0.042	0.47	0.88	0.026	0.018	18.2	10.2	Bal.

The specimens were 10 mm x 10 mm x 55 mm SEN(B) and 25 mm C(T) specimens. The geometry of the C(T) specimen is presented in Figure 20. The SEN(B) specimens were pre-fatigued to the a_o/W ratio of 0.5 in air using frequency in the range of 80–100 Hz and K_{Imax} of 8 MPa√m. The applied stress ratio R was 0.1. Pre-fatigue was performed after the sensitization heat treatment.

10% side grooves on both sides of the specimens were machined after the pre-fatigue. The C(T) specimen was prepared following the same procedure except that K_{Imax} was 15 MPa√m (the specimen was also side grooved although the grooves are not shown in Figure 20).

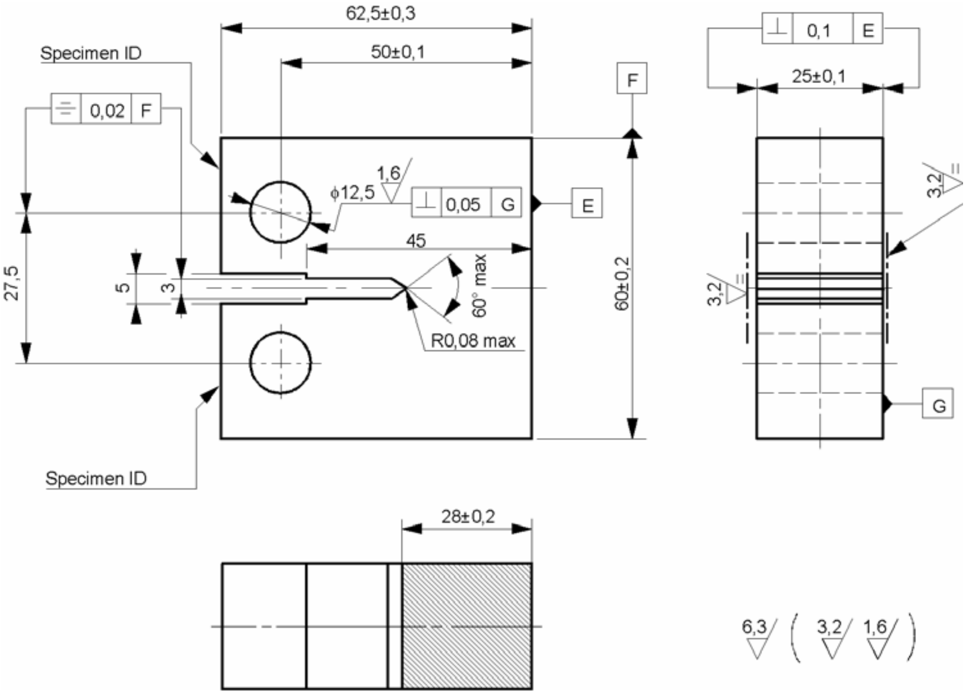

Figure 20. Main dimensions (in millimeters) and geometry of the C(T) specimen.

The tests on the SEN(B) specimens were slow rising displacement tests with different load line displacement rates. The displacement rates were between 5 x 10^{-9} mm/s and 1 x 10^{-7} mm/s. The target K_J for the crack growth rate measurement was the same as the K_I-level of the C(T) specimen, around 30 MPa√m. In the case of four specimens, the crack growth rates were planned to be measured using monotonously rising displacements, i.e., constant displacement rates, in the beginning, and constant displacements in the end of the tests. In the case of one specimen, the crack growth rates were planned to be measured using several different displacement rates for comparison purposes. The test plan for the SEN(B) specimens is presented in Table 13.

Table 13. Test plan for the SEN(B) specimens.

Specimen No.	Displacement rate [mm/s]
1	5.0×10^{-9}
	0
2	5.0×10^{-9}
	0
3	2.5×10^{-8}
	0
4	5.0×10^{-8}
	0
5	1.0×10^{-7}
	5.0×10^{-8}
	2.5×10^{-8}
	5.0×10^{-9}
	0

The SEN(B) specimens were tested using pneumatic servo-controlled loading frames. Load was determined from the internal pressure of the bellows that provide the load to the specimens.

The C(T) specimen was tested in an autoclave equipped with a servo-hydraulic materials testing machine. The target stress intensity level K_I was 30 MPa√m for the crack growth rate measurement. Before the crack growth rate was measured, the stress corrosion crack was initiated using fatigue under increasing stress ratio R and decreasing frequency f. In the beginning, the applied R was 0.5 and f was 0.1 Hz. In the end, immediately before the constant load phase, the loading was constant except for three times a day performed unloadings with R = 0.7 and f = 0.001 Hz. After the stress corrosion crack was properly initiated, the crack growth rate was measured both under constant load and under constant displacement. Load was measured using a commercial load cell.

The tests on the SEN(B) and C(T) specimens were performed in simulated BWR water at the temperature of 290°C. The inlet water conductivity was 0.06 µS/cm, and the content of dissolved oxygen was 500 ppb.

3.2 Analysis methods

SEN(B) specimens

The crack lengths were calculated from the potential drop signals by applying the following equation presented in ASTM E 1820-99 "Standard Test Method for Measurement of Fracture Toughness":

$$\frac{a}{W} = \frac{2}{\pi}\cos^{-1}\left[\frac{\cosh\left(\frac{\pi y}{2W}\right)}{\cosh\left[\left(\frac{U}{U_0}\right)\cosh^{-1}\left[\frac{\cosh\left(\frac{\pi y}{2W}\right)}{\cos\left(\frac{\pi a_0}{2W}\right)}\right]\right]}\right], \tag{34}$$

where y is the distance of the potential drop leads from the crack plane, U is momentary voltage difference between the leads and U_0 is the initial voltage difference between the leads. The crack extension measured by the potential drop method was then corrected to the physical crack extension measured on the x-y table.

J-R curves were calculated from the measured load-load line displacement and crack length data by following the procedures presented in standard ASTM E 1820-99. The J-value corresponding the momentary load-load line displacement is:

$$J_{(i)} = \frac{K_{(i)}^2\left(1-\nu^2\right)}{E} + J_{pl(i)}, \tag{35}$$

where

$$K_{(i)} = \left[\frac{P_i S}{(BB_n)^{1/2} W^{3/2}} \right] f\left(\frac{a_i}{W} \right), \tag{36}$$

where function $f(a_i/W)$ is:

$$f\left(\frac{a_i}{W}\right) = \frac{3\left(\frac{a_i}{W}\right)^{1/2}\left[1.99 - \left(\frac{a_i}{W}\right)\left(1-\left(\frac{a_i}{W}\right)\right)\left(2.15 - 3.93\left(\frac{a_i}{W}\right) + 2.7\left(\frac{a_i}{W}\right)^2\right)\right]}{2\left(1+2\left(\frac{a_i}{W}\right)\right)\left(1-\left(\frac{a_i}{W}\right)\right)^{3/2}}. \tag{37}$$

The plastic component of $J_{(i)}$, $J_{pl(i)}$, in eq. (35) is:

$$J_{pl(i)} = \left[J_{pl(i-1)} + \left(\frac{2}{b_{(i-1)}} \right) \left(\frac{A_{pl(i)} - A_{pl(i-1)}}{B_n} \right) \right] \left[1 - \frac{a_{(i)} - a_{(i-1)}}{b_{(i-1)}} \right]. \tag{38}$$

Plastic area $A_{pl(i)}$ under the load-load line displacement curve is:

$$A_{pl(i)} = A_{pl(i-1)} + [P_{(i)} + P_{(i-1)}]\ [V_{pl(i)} - V_{pl(i-1)}]/2, \tag{39}$$

where the plastic component of the load line displacement, $V_{pl(i)}$, is:

$$V_{pl(i)} = V_{(i)} - P_{(i)} C_{LL(i)}. \tag{40}$$

$C_{LL(i)}$ in eq. (40) is elastic slope $(\Delta V/\Delta P)_i$. The elastic slope, $C_{LL(i)}$, is:

$$C_{LL(i)} = \frac{1}{E' B_e} \left(\frac{S}{W - a_i} \right)^2 \left[1.193 - 1.98\left(\frac{a_i}{W}\right) + 4.478\left(\frac{a_i}{W}\right)^2 - 4.443\left(\frac{a_i}{W}\right)^3 + 1.739\left(\frac{a_i}{W}\right)^4 \right], \tag{41}$$

where

$$E' = \frac{E}{1 - \nu^2}, \tag{42}$$

and effective thickness B_e is:

$$B_e = B - \frac{(B - B_n)^2}{B}. \tag{43}$$

Before the J-R curves were calculated, the load line displacement data was corrected, when necessary, so that the linear part of the load-load line displacement curve followed the theoretical elastic slope calculated using eq. (41):

$$V_{(i)} = V_{m(i)} - \alpha P_{(i)}, \tag{44}$$

where $V_{(i)}$ is the corrected displacement, $V_{m(i)}$ is the measured displacement, α is a constant and $P_{(i)}$ is the load. This correction compensates the compliance of the loading tools. Young's modulus was assumed to be 180 GPa and Poisson's ratio 0.3 when the theoretical elastic slope was calculated.

After the J-R curves were calculated, average J-integral increase rate, dJ/dt, was determined graphically from J-integral vs. testing time curve. Crack growth rates were determined using a similar procedure. Also, the average J-integral level was determined for each crack growth rate measurement phase. As the crack growth rates are usually presented as a function of K_I, the J-values were converted to K-scale by applying eq. (45):

$$K_J = \sqrt{\frac{JE}{1-\nu^2}}. \tag{45}$$

Young's modulus E was assumed to be 180 GPa and Poisson's ratio ν 0.3 in the conversion.

In one test series, tests on the Olkiluoto 1 core shroud surveillance specimens, superposition based analysis was applied. Superposition analysis evaluates the environmental impact on the crack growth rate by subtracting the mechanical crack growth rate measured in ”inert” environment from the total measured crack growth rate in the simulated core environment [106]:

$$(da/dt)_{EAC} = (da/dt)_{TOT} – (da/dt)_{MECH}, \tag{46}$$

where $(da/dt)_{TOT}$ = crack growth rate at a certain J-integral value obtained from the slow J-R curve measured in the actual test environment, i.e., at +200 or -90 mV_{SHE}, and $(da/dt)_{MECH}$ = crack growth rate at a certain J-integral value due to mechanical loading only. $(da/dt)_{MECH}$ is obtained from the “inert” J-R curve measured at low potential, i.e., at -500 mV$_{SHE}$, where SCC should be minimal. It must be noted that the feasibility of this method has not been clearly verified.

The load-displacement-crack length data quality was studied by determining normalized load vs. displacement curves. The normalized data provides a simple tool to check the data quality and, sometimes, to recognize the error sources [107]. The normalized load can be defined as the momentary load divided by the limit load as, e.g., in references [108, 109], or as bending momentum divided by the stiffness of the specimen multiplied with the strength of the material [107]:

$$P_n = \frac{P * W}{B * b^2 * \sigma}, \tag{47}$$

where P is the momentary load, W is the width of the specimen, B is the thickness of the specimen (or the effective thickness B$_e$), σ is the yield stress and b is the momentary remaining ligament. When specimens with the same yield stress and loading geometry are compared, eq. (47) can be simplified:

$$P_n = \frac{P}{B * b^2}. \tag{48}$$

When the normalized curves of specimens with different loading spans are compared (in three-point bend geometry), the displacement has to be also normalized. A natural normalization method is the ratio of width/span. This, of course, is not needed when comparing the results obtained using the same specimen sizes and loading geometries as is the case in most of the results of this work.

<u>25 mm C(T) specimen</u>

The crack length was calculated from the potential drop signal by applying eq. (34). K$_I$ was calculated from the measured load and crack length data using the relation presented in the standard ASTM E 1820-99:

$$K_{(i)} = \left[\frac{P_i}{(BB_nW)^{1/2}}\right] f\left(\frac{a_i}{W}\right), \tag{49}$$

where

$$f\left(\frac{a_i}{W}\right)=\frac{\left[\left(2+\left(\frac{a_i}{W}\right)\right)\left(0.886+4.64\left(\frac{a_i}{W}\right)-13.32\left(\frac{a_i}{W}\right)^2+14.72\left(\frac{a_i}{W}\right)^3-5.6\left(\frac{a_i}{W}\right)^4\right)\right]}{\left(1-\left(\frac{a_i}{W}\right)\right)^{3/2}}. \qquad (50)$$

After the crack lengths and the corresponding K_I-levels were calculated, the average J-integral increase/decrease rates both for the constant load and constant displacement phase were determined by solving J from eq. (45). Crack growth rates were determined using a similar procedure as in the case of the SEN(B) specimens, i.e., they were determined graphically from the crack length vs. testing time plot.

4. Results

4.1 J-R tests on AISI 304 and 321 steels in BWR water

The load vs. load line displacement and normalized load vs. load line displacement of the tests are presented in Figures 21–22. The load vs. load line displacement curves normalized by the size of the remaining ligament should all follow the same curve if the material properties are the same. Figure 22 shows that the load vs. load line displacement curves of the sensitized AISI 304 steel specimens follow the same path. The curves of the AISI 321 steel specimens also follow the same path, but different than the curves of the AISI 304 steel specimens. The different behaviour of these two stainless steel grades can be attributed to the differences in yield stress, tensile strength and strain hardening behaviour.

The J-R curves of the tests are presented in Figure 23. The fracture resistance of the test materials decreased with the decreasing displacement rate. The maximum allowable J-integral, J_{max}, and crack extension, Δa_{max}, for the two specimen sizes (10 mm x 10 mm x 55 mm and 10 mm x 5.5 mm x 55 mm) according to ASTM E 1820-99 are marked in Figure 23. The maximum J-values are calculated for the flow stress of 300 MPa, which should be a conservative value for both steel grades (the actual flow stresses were not measured for the test materials).

The crack growth rates are presented as a function of K_J in Figure 24. As can be seen, the crack growth rates are independent of the K_J-level at high K_J-levels. At lower levels the crack growth rates seem to slightly increase with increasing K_J, but this can be attributed to the initiation process. The crack initiation does not take place at the same time in every place of the pre-fatigue crack tip. The crack growth rate depends also on the applied displacement rate, being lower at lower displacement rates. The crack growth rates are presented as a function of specimen size/geometry independent loading rate, dJ/dt, in Figure 25. At lower dJ/dt levels the crack growth rates are lower for both steel grades.

The fracture surface morphologies are presented in Figures 26–30. At the highest applied displacement rate, the crack tip has only blunted in AISI 304 steel (specimen No. 1), Figure 26. At the intermediate displacement rate (specimen No. 2), the fracture surface morphology is mixed intergranular and transgranular stress corrosion cracking, Figure 27. At the lowest displacement rate, the fracture surface morphology in AISI 304 steel (specimen No. 3) is almost pure intergranular stress corrosion cracking, Figure 28.

In AISI 321 steel, the fracture morphology also changes when the displacement rate is changed. At higher displacement rate the fracture surface morphology is pure transgranular stress corrosion cracking (specimen No. 4), Figure 29, and at lower displacement rate it is mixed intergranular and transgranular stress corrosion cracking (specimen No. 5), Figure 30. The results are summarized in Table 14.

Table 14. The environmentally assisted crack growth rates and the observed environmentally assisted cracking on the fracture surfaces.

Material	Specimen size [BxWxL, mm]	Displacement rate [mm/s]	Crack growth rate [mm/s]	SCC morphology
AISI 304	10x10x55	8.0×10^{-4}	No SCC	No SCC
AISI 304	10x10x55	1.2×10^{-5}	$3…5 \times 10^{-6}$	IGSCC (~30%) TGSCC (remainder)
AISI 304	10x10x55	2.4×10^{-6}	$2…3 \times 10^{-6}$	IGSCC (~90%) TGSCC (remainder)
AISI 321	10x5.5x55	3.0×10^{-6}	$7…10 \times 10^{-7}$	TGSCC (100%)
AISI 321	10x5.5x55	3.0×10^{-7}	$2…3 \times 10^{-7}$	IGSCC (>30%) TGSCC (remainder)

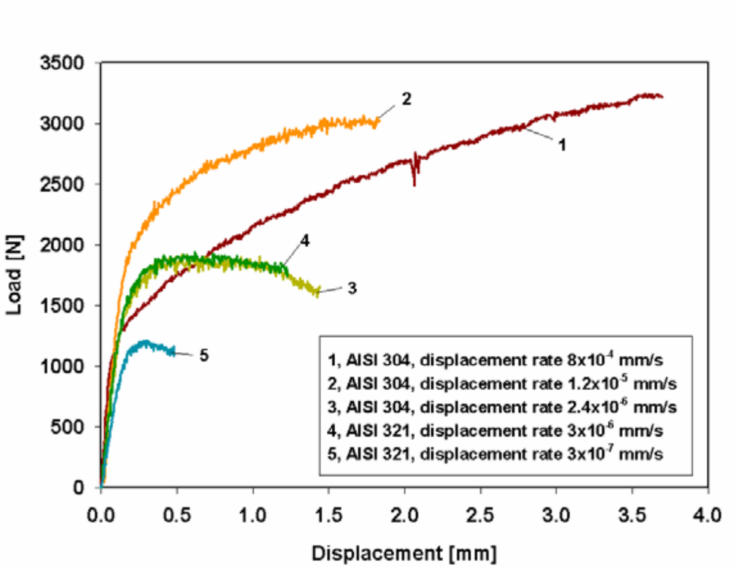

Figure 21. Load vs. load line displacement curves measured using various constant displacement rates in simulated BWR water at 288°C.

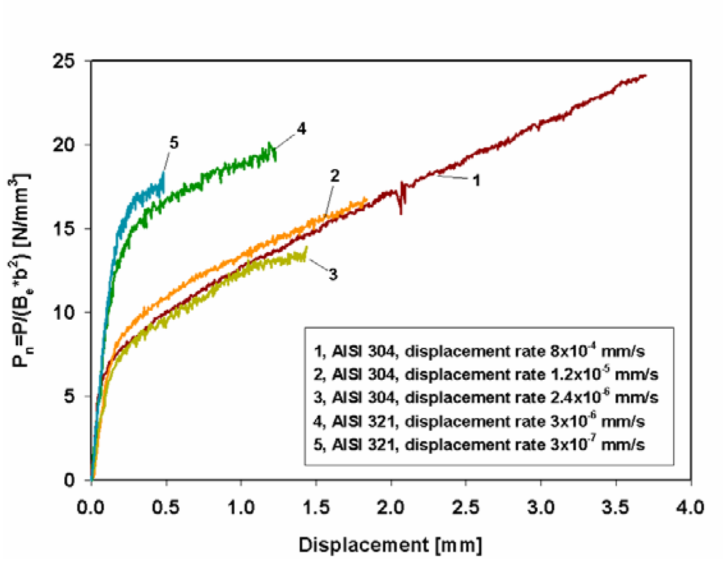

Figure 22. Load vs. load line displacement curves normalized by the size of the remaining ligament measured using various displacement rates in simulated BWR water at 288°C.

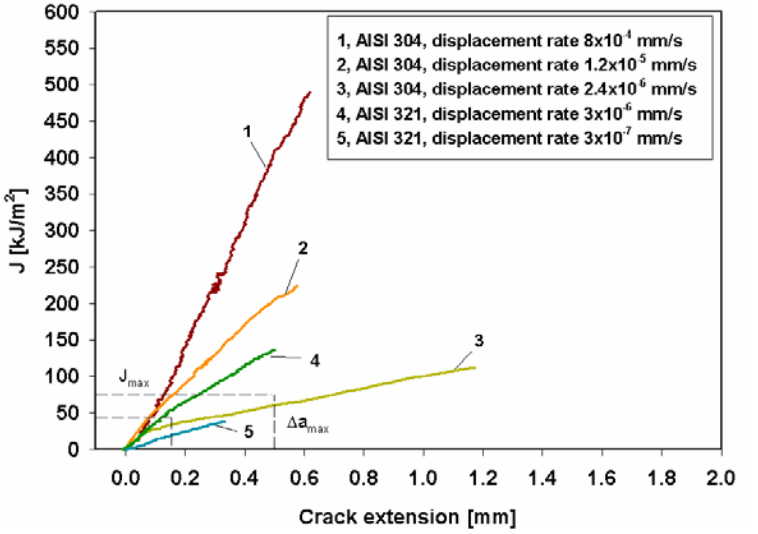

Figure 23. J-R curves measured using various displacement rates in simulated BWR water at 288^{o}C. J and crack growth limits are calculated according to ASTM E 1820 - 99 (σ_f = 300 MPa and b_0 = 5 mm or 3 mm). The limits are marked by horizontal and vertical dashed lines.

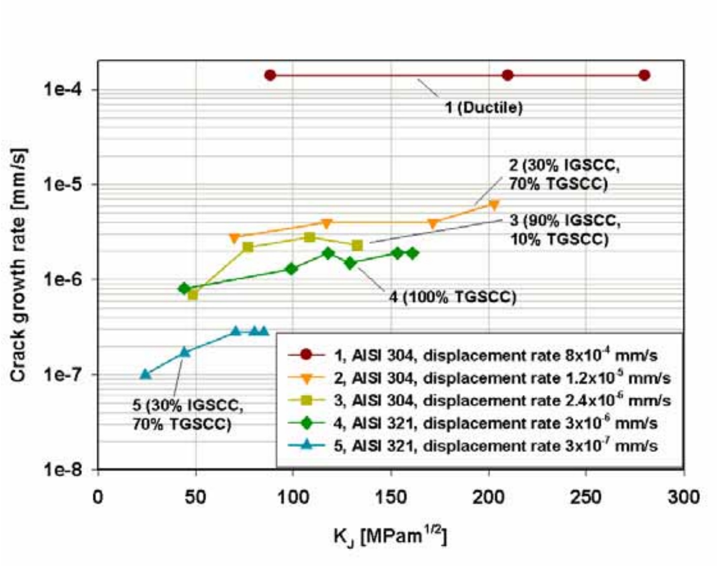

Figure 24. Crack growth rates determined from the J-R data presented in Figure 23. Temperature 288^{o}C, conductivity 0.3 μS/cm (increased using Na_2SO_4), dissolved O_2 200 ppb and corrosion potentials +400 (AISI 304) and +200 (AISI 321) mV_{SHE}. The potentials were controlled using a potentiostat.

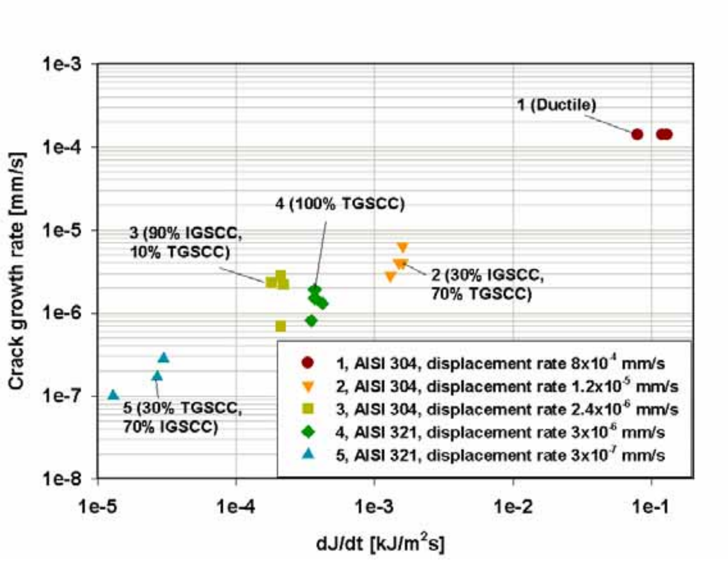

Figure 25. Crack growth rates presented as a function of specimen size or geometry independent loading rate dJ/dt. Temperature 288°C, conductivity 0.3 µS/cm (increased using Na_2SO_4), dissolved O_2 200 ppb and corrosion potentials +400 (AISI 304) and +200 (AISI 321) mV_{SHE}. The potentials were controlled using a potentiostat.

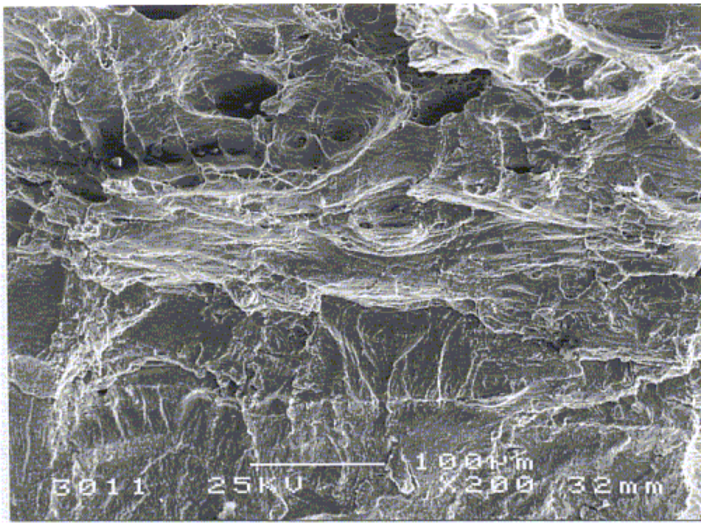

Figure 26. Fracture surface morphology of AISI 304 steel specimen tested at the highest displacement rate showing ductile crack tip blunting (specimen No. 1, tested using the displacement rate of 8.0 x 10^{-4} mm/s).

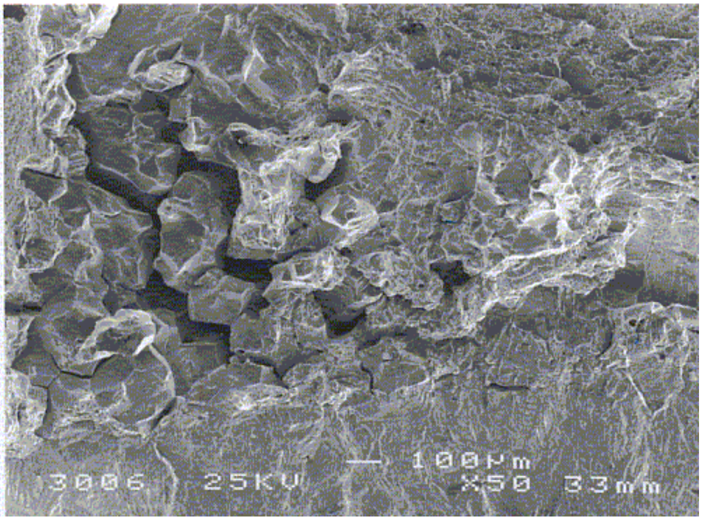

Figure 27. Fracture surface morphology of AISI 304 steel specimen tested at the intermediate displacement rate showing mixed intergranular and transgranular cracking (specimen No. 2, tested using the displacement rate of 1.2 x 10^{-5} mm/s).

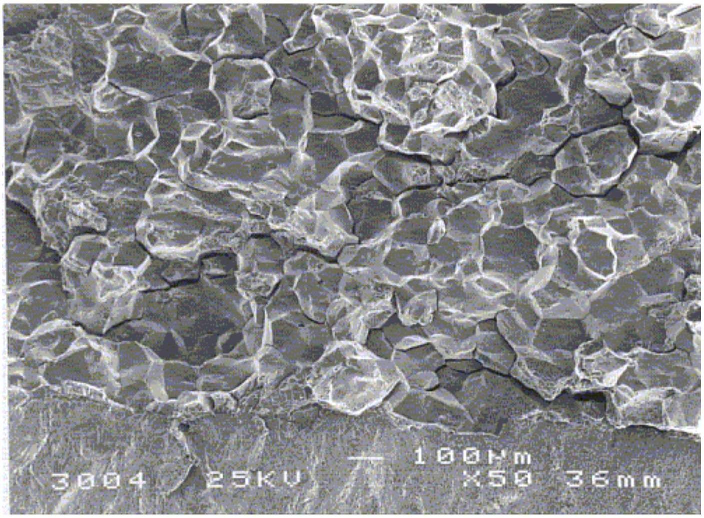

Figure 28. Fracture surface morphology of AISI 304 steel specimen tested at the intermediate displacement rate showing almost pure intergranular cracking (specimen No. 3, tested using the displacement rate of 2.4 x 10^{-6} mm/s).

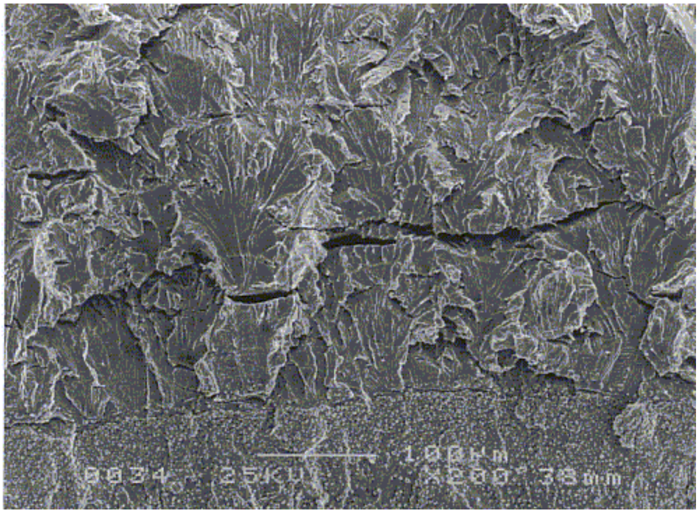

Figure 29. Fracture surface morphology of AISI 321 steel specimen tested using a high displacement rate showing almost pure transgranular cracking (specimen No. 4, tested using the displacement rate of 3.0×10^{-6} mm/s).

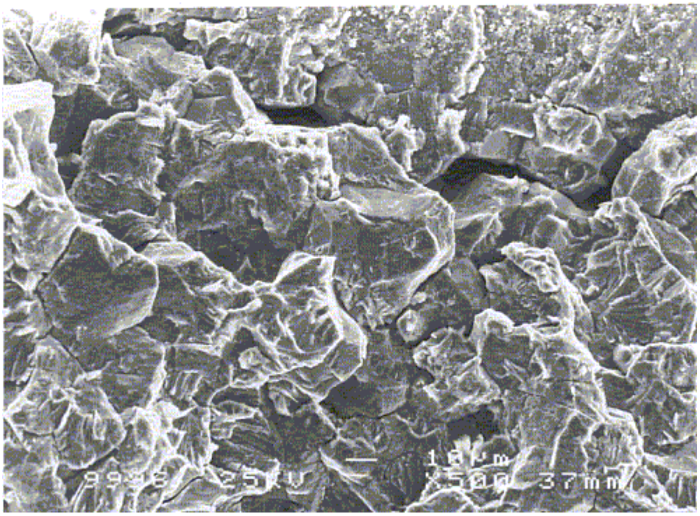

Figure 30. Fracture surface morphology of AISI 321 steel specimen tested using a low displacement rate showing mixed intergranular and transgranular cracking (specimen No. 5, tested using the displacement rate of 3.0×10^{-7} mm/s).

4.2 SCC susceptibility of Olkiluoto 1 core shroud material

4.2.1 Microstructural studies

The chemical compositions of the two base metal plates are presented in Table 15. The compositions were measured from non-irradiated tensile specimens. The compositions are so close to each other that the plates probably originate from the same heat.

Table 15. The chemical compositions of the base metals, wt %, measured using an optical emission spectrometer.

	C	Si	Mn	P	S	Cr	Ni	Mo	Co	Fe
Base metal 1	0.05	0.42	1.65	0.027	0.009	18.6	9.1	0.28	0.33	Bal.
Base metal 2	0.05	0.43	1.66	0.028	0.010	18.4	9.3	0.29	0.36	Bal.

Microstructures of the base metals 1 and 2 are presented in Figures 31 and 32, respectively. The base metals contained δ-ferrite lamellas in the austenitic matrix. A macrograph of the gauge section of a weld specimen showing the amount and the distribution of weld metal can be seen in Figure 33. The results of δ-ferrite content measurements are presented in Figure 34.

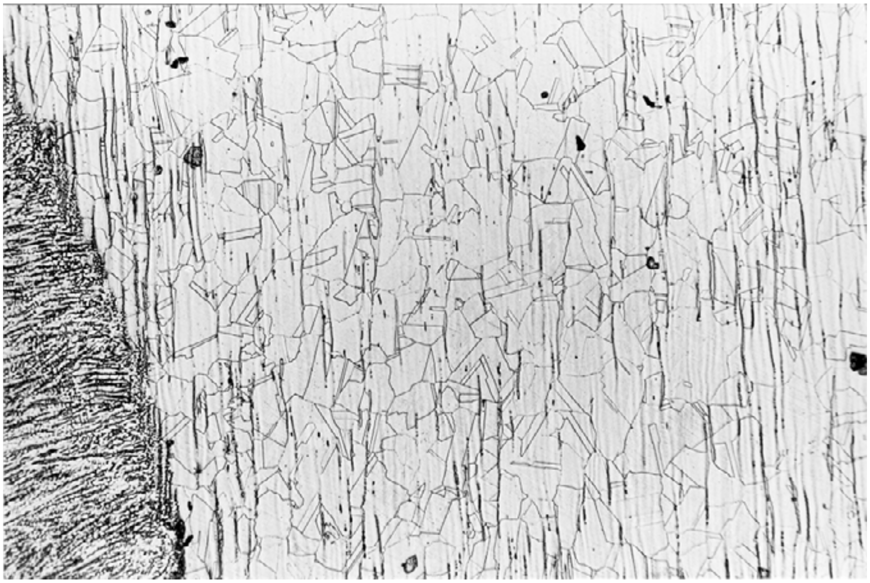

Figure 31. The microstructure of non-irradiated base metal 1 close to the weld fusion line. The matrix contains large δ-ferrite lamellas (100x).

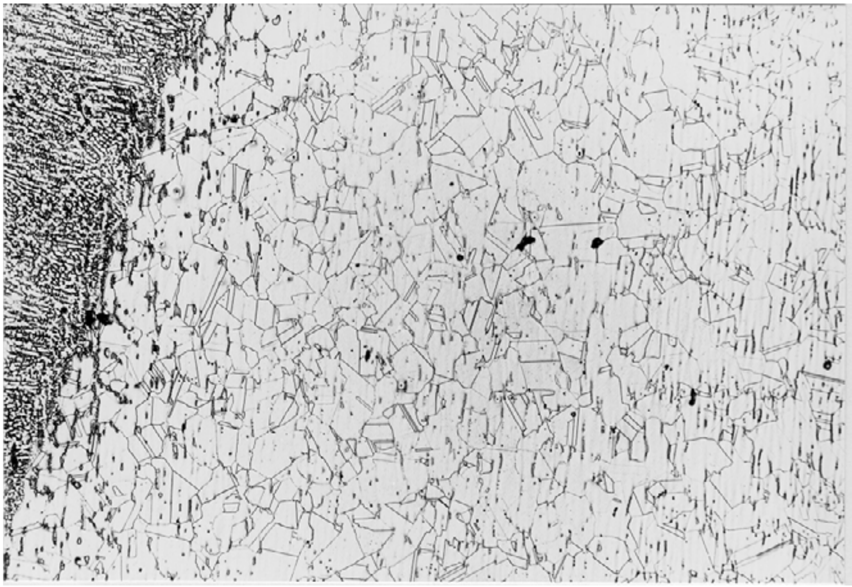

Figure 32. The microstructure of non-irradiated base metal 2 close to the weld fusion line. The δ-ferrite lamellas are smaller than those in base metal 1 (100x).

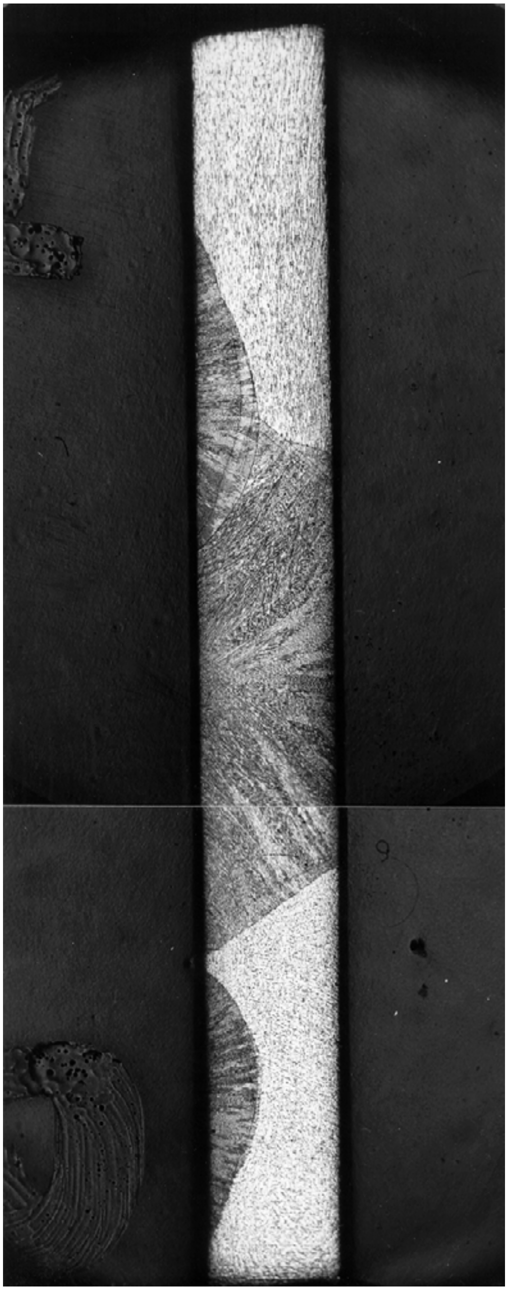

Figure 33. A macrograph of the gauge section of a weld specimen (8x).

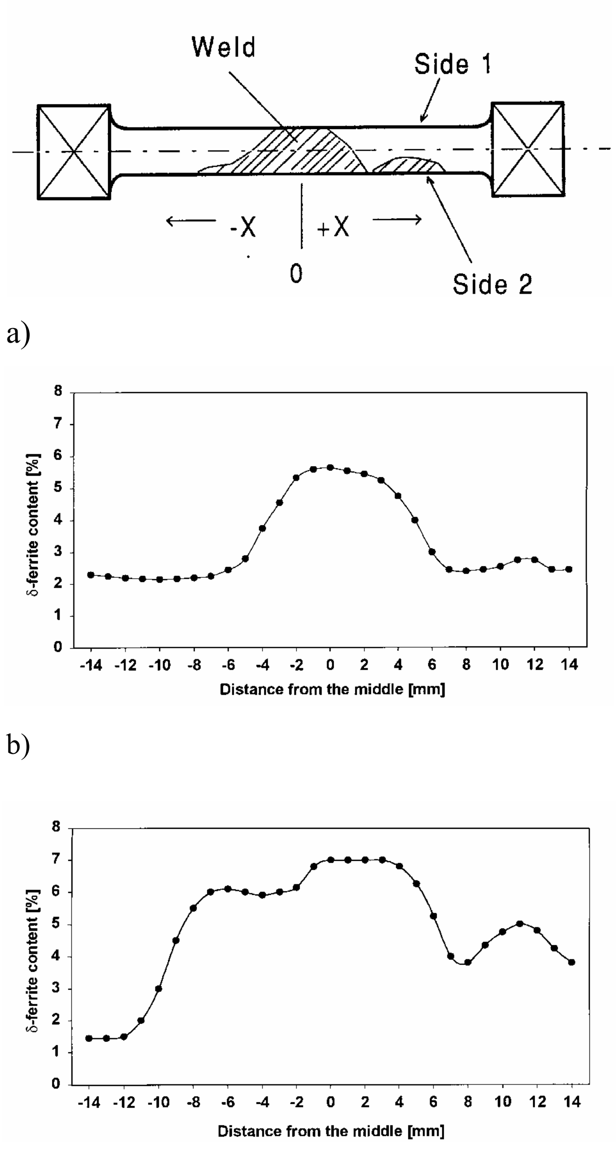

Figure 34. The measured δ-ferrite content profiles in a surveillance tensile test specimen with a weld in the gauge section. a) Weld location in the gauge section. b) δ-ferrite content profile on side 1. c) δ-ferrite content profile on side 2.

4.2.2 Tensile tests

Tensile tests were conducted at temperatures of 20 and 280°C for 6 irradiated and non-irradiated specimens including two weld specimens, in which a part of the gauge length consisted of weld metal. The tensile test results are presented in Table 16 and the effects of neutron fluence on tensile strength, yield stress and elongation to fracture are presented in Figures 35–37.

Table 16. Summary of the tensile test results.

Specimen type	Weld metal/ gauge length, [%]	Test temperature, [°C]	Tensile strength, [MPa]	Yield stress, [MPa]	Elongation to fracture, [%]	Reduction in area, [%]
Base metal 1 Non-irradiated	-----	20	634	243	73.1	58
Base metal 1 Irradiated	-----	20	653	289	63.9	80
Base metal 2 Non-irradiated	-----	20	636	242	56.0	68
Base metal 2 Irradiated	-----	20	651	274	59.1	70
Weld specimen Non-irradiated	26	20	616	342	40.2	59
Weld specimen Irradiated	50	20	648	424	26.2	61
Base metal 1 Non-irradiated	-----	280	450	182	33.0	57
Base metal 1 Irradiated	-----	280	487	192	31.0	58
Base metal 2 Non-irradiated	-----	280	448	167	32.9	59
Base metal 2 Irradiated	-----	280	484	214	34.2	59
Weld specimen Non-irradiated	26	280	433	261	17.1	47
Weld specimen Irradiated	50	280	502	314	20.2	49

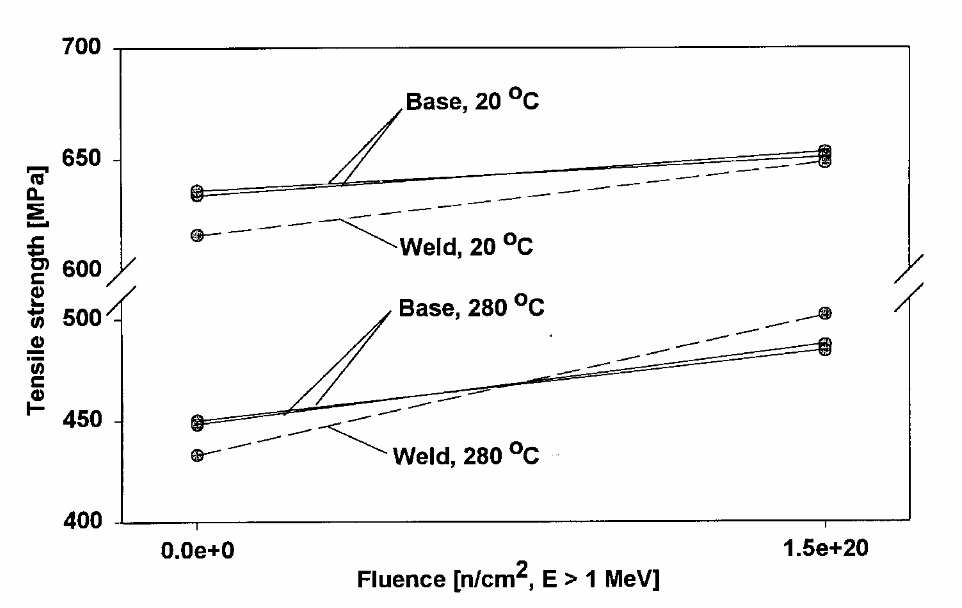

Figure 35. The effect of irradiation on tensile strength.

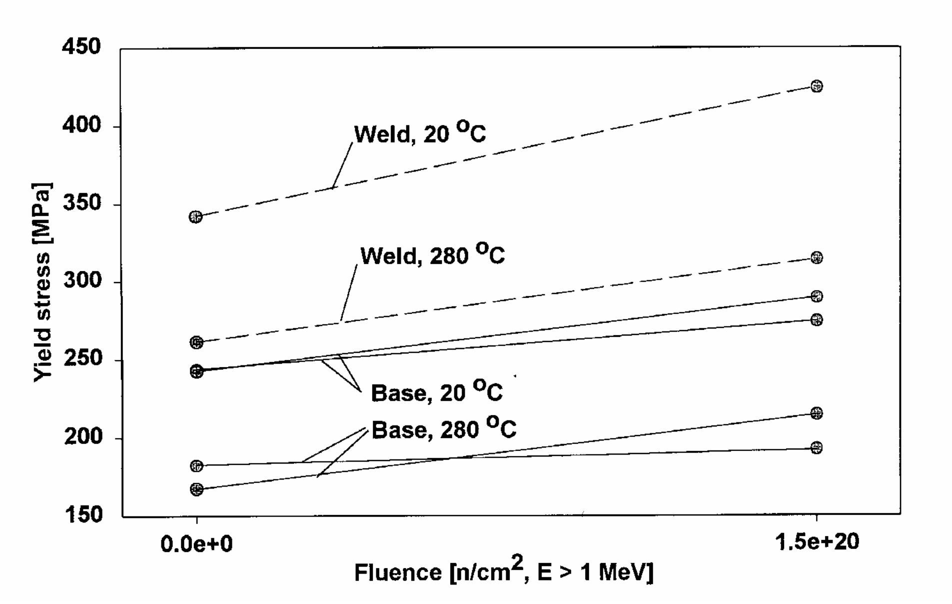

Figure 36. The effect of irradiation on yield stress.

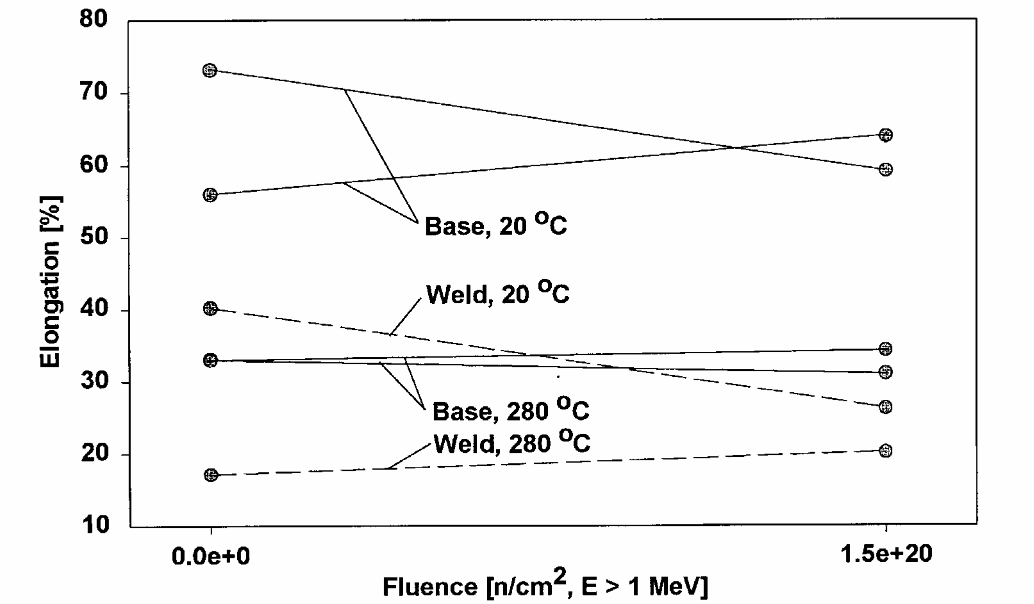

Figure 37. The effect of irradiation on elongation to fracture.

4.2.3 Slow strain rate tests

The effects of irradiation on stress corrosion susceptibility of core shroud surveillance material was investigated by SSRT tests. The tests were performed in simulated BWR water at 288°C in an autoclave connected to a re-circulation loop. The SSRT tests were performed for irradiated and non-irradiated base metal and weld specimens at the potentials of -200, 0 and +100 mV_{SHE}.

The results of SSRT tests are summarized in Table 17. The elongations to fracture are compared with those of tensile tests in Table 18. Regardless of the potential in which the SSRT tests were performed, the elongation to fracture was smaller in the case of irradiated specimens than in the case of non-irradiated specimens. The results also indicate, when tensile and SSRT test results are compared, that the test environment has an effect on the elongation to fracture in the case of the irradiated specimens but not in the case of the non-irradiated specimens.

The stress strain curves of the SSRT tests are presented in Figures 38-41. SEM investigation revealed that the mode of environmentally assisted cracking (EAC) during SSRT in all base metal specimens was mainly TGSCC. On the fracture surfaces of irradiated base metal specimens only a small amount of intergranular cracking (~1% IGSCC) was observed. On the fracture surfaces of irradiated weld specimens with HAZ, a slightly increased amount of intergranular cracking (~5% IGSCC) was visible. No SCC was observed on the fracture surfaces of non-irradiated weld specimens. The fracture surface of every irradiated specimen had a step-like appearance. This kind of fracture surface is caused by partial crack growth along δ-ferrite-austenite phase boundaries, Figure 42. No comparison between fracture morphologies in SSRT and tensile tests could be made, because the tensile tests were performed several years before the SSRT tests and no scanning electron microscopy was then carried out.

Table 17. The results of Slow Strain Rate Tests (SSRT).

Specimen type	Weld metal in the gauge section [%]	ECP [mV_{SHE}]	Elongation to fracture [%]	Amount and mode of SCC fracture surface	Number of initiation sites
Base metal 2 Non-irradiated	0	+ 100	37	15% TGSCC	1
Base metal 2 Irradiated	0	+ 100	23	30% TGSCC ~1% IGSCC	2
Weld specimen Non-irradiated	26	+ 100	28	---	---
Weld specimen Irradiated	50	+ 100	14	40% TGSCC ~5% IGSCC	1
Base metal 2 Non-irradiated	0	0	30	25% TGSCC	1
Base metal 2 Irradiated	0	0	19	30% TGSCC ~1% IGSCC	4
Weld specimen Non-irradiated	26	- 200	21	---	---
Weld specimen Irradiated	26	- 200	14	40% TGSCC ~3% IGSCC	4

Table 18. Comparison of the elongations to fracture between tensile and SSRT tests (average values).

	Polarization potential, mV_{SHE}	Elongation to fracture, % (amount of IGSCC on fracture surface, %)			
		Base metal		Weld	
		Non-irradiated	Irradiated	Non-irradiated	Irradiated
Tensile test at 280°C	-----	33 (0)	33 (0)	17 (0)	20 (0)
SSRT at 288°C	-200			21 (0)	14 (~3)
	0	30 (0)	19 (~1)		
	+100	37 (0)	23 (~1)	28 (0)	14 (~5)

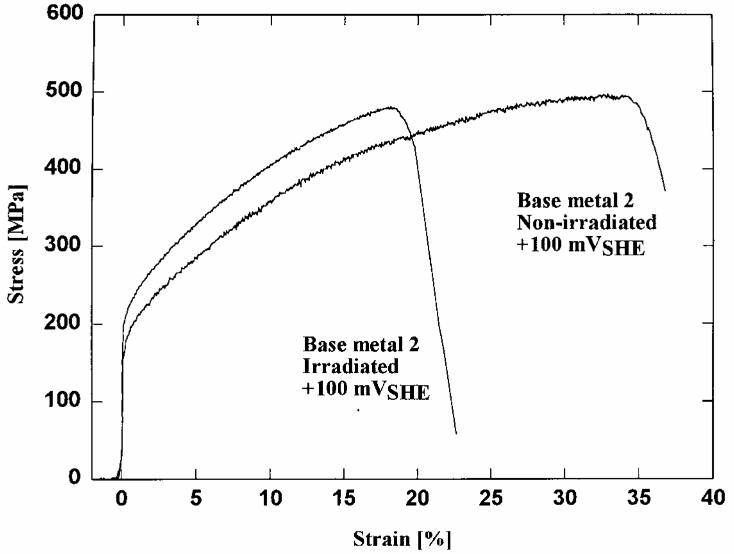

Figure 38. SSRT stress-strain curves for non-irradiated and irradiated base metal specimens obtained with a strain rate of 2.8 x 10^{-7} s^{-1} in simulated BWR water; temperature 288°C, ECP +100 mV_{SHE}, O_2 content 200 ppb, conductivity 0.2–0.3 μS/cm and $pH_{25°C}$ 7.

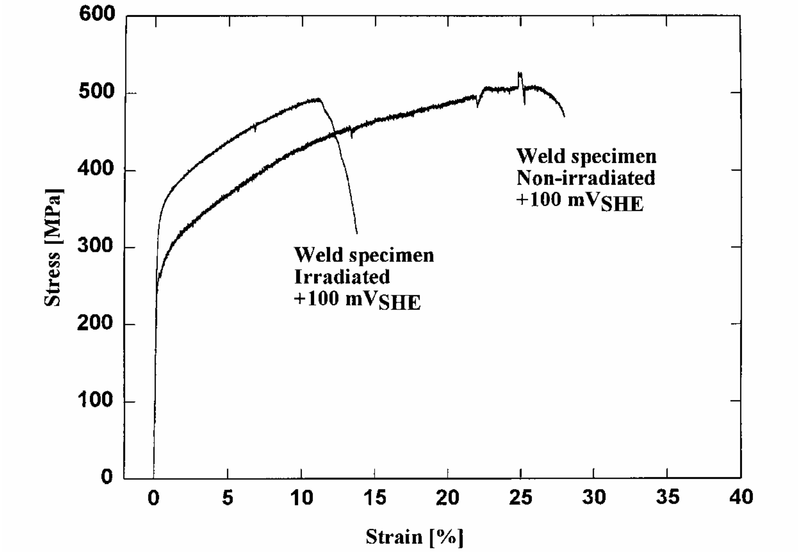

Figure 39. SSRT stress-strain curves for non-irradiated and irradiated weld specimens obtained with a strain rate of 2.8 × 10^{-7} s^{-1} in simulated BWR water; temperature 288°C, ECP +100 mV$_{SHE}$, O_2 content 200 ppb, conductivity 0.2–0.3 μS/cm and pH$_{25°C}$ 7.

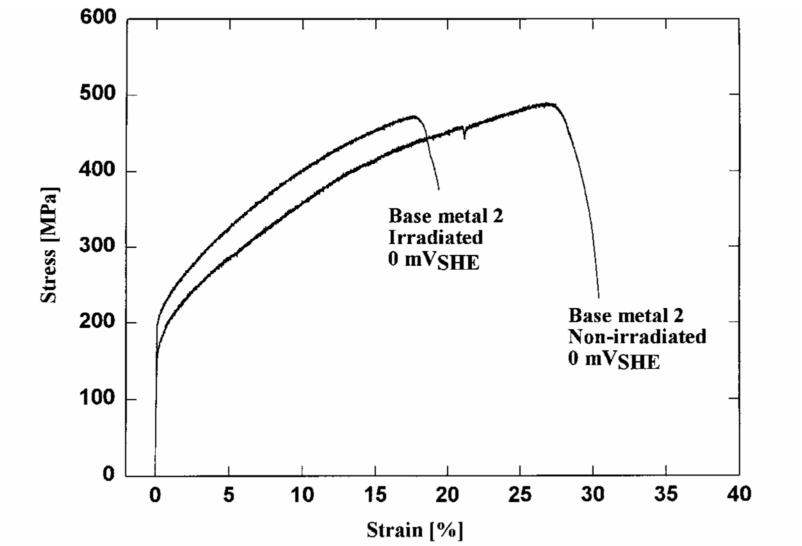

Figure 40. SSRT stress-strain curves for non-irradiated and irradiated base metal specimens obtained with a strain rate of 2.8 x 10^{-7} s^{-1} in simulated BWR water; temperature 288°C, ECP 0 mV$_{SHE}$, O_2 content 200 ppb, conductivity 0.2–0.3 μS/cm and pH$_{25°C}$ 7.

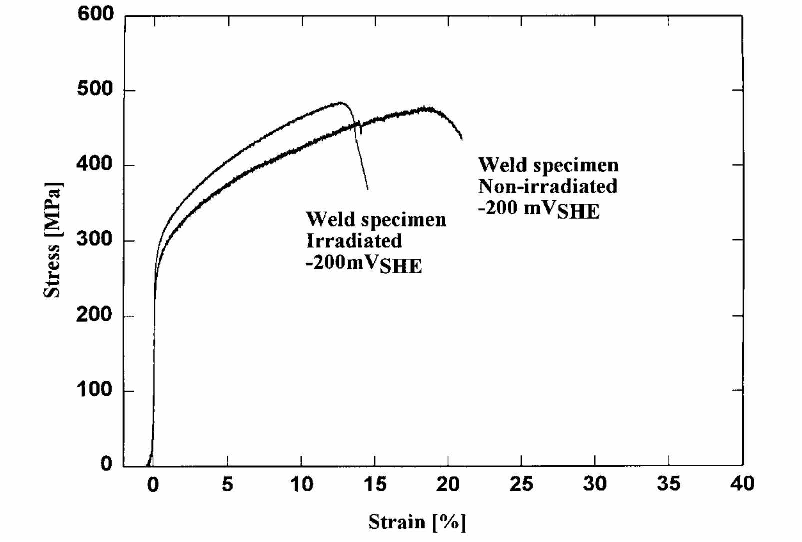

Figure 41. SSRT stress-strain curves for non-irradiated and irradiated weld specimens obtained with a strain rate of 2.8 × 10^{-7} s^{-1} in simulated BWR water; temperature 288°C, ECP -200 mV_{SHE}, O_2 content 200 ppb, conductivity 0.2–0.3 μS/cm and $pH_{25°C}$ 7.

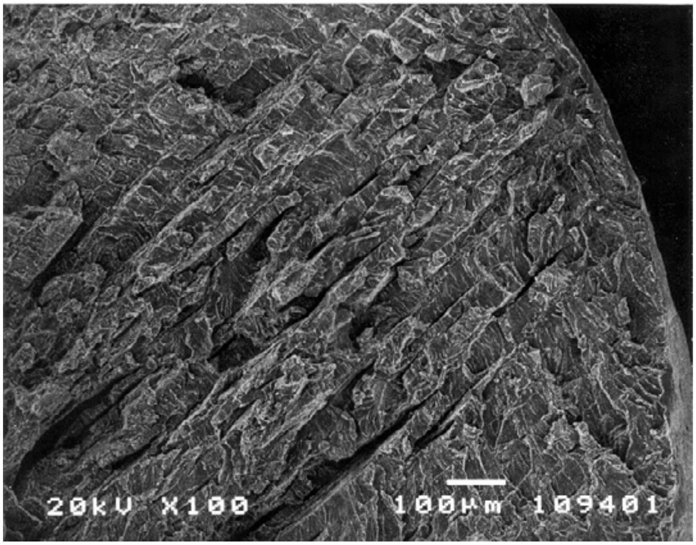

Figure 42. Step-like fracture in irradiated base metal 2 specimen. SSRT test was performed with a strain rate of 2.8 × 10^{-7} s^{-1} in simulated BWR water; temperature 288°C, ECP +100 mV_{SHE}, O_2 content 200 ppb, conductivity 0.2–0.3 μS/cm and $pH_{25°C}$ 7.

4.2.4 Slow J-R tests

The J-R test matrix and the supposed significance of each test is presented in Table 19. The tests were conducted for each specimen type both at simulated in-core potentials as well as at the potential of -500 mV_{SHE}. The function of the reduced potential test is to give the “inert” crack growth rate due to mechanical loading only, without any environmental effects.

The measured slow J-R curves are presented in Figures 43 a) and b). The environmentally assisted crack growth rates, $(da/dt)_{EAC}$, determined using superposition based analysis method as described in eq. (46), and the fracture modes for all specimens are summarized in Table 20 and presented in Figure 44. Threshold stress intensity factors J_{TH} and K_{TH}, J-integral value and stress intensity factor K_I at the initiation point of stress corrosion cracking for irradiated HAZ specimens tested at +200 mV_{SHE} are also presented in Table 20. The values were estimated from the J-R curves. These values, in this case, are loading rate, material, environment and probably also specimen-size specific values. No initiation values could be estimated except for two tests on irradiated HAZ. The crack growth rates are also presented as a function of J-integral increase rate, dJ/dt, in Figure 45.

Typical fracture surfaces after J-R tests in simulated BWR water are shown in Figures 46 to 51.

Table 19. J-R test parameters. Test specimen type, load line displacement rate, corrosion potential (external polarization) and the objective of each test. The fluence of the irradiated material is ~1.5 x 10^{20} n/cm^2, E > 1 MeV.

Specimen type	Load line displacement rate [mm/s]	ECP [mV$_{SHE}$]	Objective of the test
Base metal 2 Non-irradiated	1.8 x 10^{-6}	+200	SCC susceptibility of base metal
Base metal 2 Irradiated	1.8 x 10^{-6}	+200	Effects of LTS and IASCC on SCC in base metal
Base metal 2 Irradiated, annealed at 450 °C/24 h	1.8x10^{-6}	+200	Effect of LTS on SCC in base metal. Effects of IASCC reduced by annealing
HAZ in base metal 2 Non-irradiated	1.8 x 10^{-6}	+200	SCC in base metal HAZ
HAZ in base metal 2 Irradiated	1.8 x 10^{-6}	+200	Effects of LTS and IASCC on SCC in HAZ
HAZ in base metal 2 Irradiated, annealed at 450 °C/24 h	1.8x10^{-6}	+200	Effects of LTS on SCC in HAZ. Effect of IASCC reduced by annealing
HAZ in base metal 1 Irradiated	1.8 x 10^{-6}	-90	Effect of ECP on SCC
HAZ in base metal 1 Irradiated	2.6 x 10^{-7}	+200	Effect of strain rate on IASCC
HAZ in base metal 2 Non-irradiated, annealed at 500 °C/4 h	1.8x10^{-6} 8.5x10^{-7} 4.0x10^{-7}	+200	Effects of LTS and strain rate on SCC
Base metals and HAZ specimens	1.8 x 10^{-6}	-500	Mechanical crack growth rates for irradiated and non-irradiated specimens

Table 20. Summary of J-R test results. The tests were performed in simulated BWR water: temperature 288^{o}C, conductivity 0.2–0.3 μS/cm, pH$_{25°C}$ ~7, O$_2$ content 200 ppb and pressure 100 bar.

Specimen type	Load line displacement rate [mm/s]	ECP [mV_{SHE}]	Steady state $(da/dt)_{EAC}$ [mm/s]	J_{TH} [kJ/m^2], K_{TH} [MPa√m]	Fracture surface observations
Base metal 2 Non-irradiated	1.8×10^{-6}	+200	2×10^{-7}		TGSCC
Base metal 2 Irradiated	1.8×10^{-6}	+200	$3\text{-}4 \times 10^{-7}$		TGSCC, ~1% IGSCC
Base metal 2 Irradiated, annealed at 450 °C/24 h	1.8×10^{-6}	+200	2×10^{-7}		TGSCC
HAZ in base metal 2 Non-irradiated	1.8×10^{-6}	+200	2×10^{-7}		TGSCC
HAZ in base metal 2 Irradiated	1.8×10^{-6}	+200	1×10^{-6}	J_{TH}=25 K_{TH}=70	TGSCC, interface cracking*, ~2% IGSCC**
HAZ in base metal 2 Irradiated, annealed at 450 °C/24 h	1.8×10^{-6}	+200	7×10^{-7}		TGSCC, interface cracking*, ~1% IGSCC**
HAZ in base metal 1 Irradiated	1.8×10^{-6}	-90	3×10^{-7}		TGSCC, interface cracking*, ~1% IGSCC**
HAZ in base metal 1 Irradiated	2.6×10^{-7}	+200	1×10^{-6}	J_{TH}=4 K_{TH}=28	TGSCC, interface cracking*, ~40% IGSCC**
HAZ in base metal 2 Non-irradiated, annealed at 500 °C/4 h	1.8×10^{-6} 8.5×10^{-7} 4.0×10^{-7}	+200	2×10^{-7} 0.8×10^{-7} 0.3×10^{-7}		TGSCC TGSCC TGSCC
Base metals and HAZ	1.8×10^{-6}	-500	-----------		Crack tip blunting

**Interfacial cracking along austenite-δ-ferrite phase boundary. **Estimation of the amount of IGSCC on the fracture surfaces of the irradiated HAZ specimens is difficult due to interfacial cracking.*

.

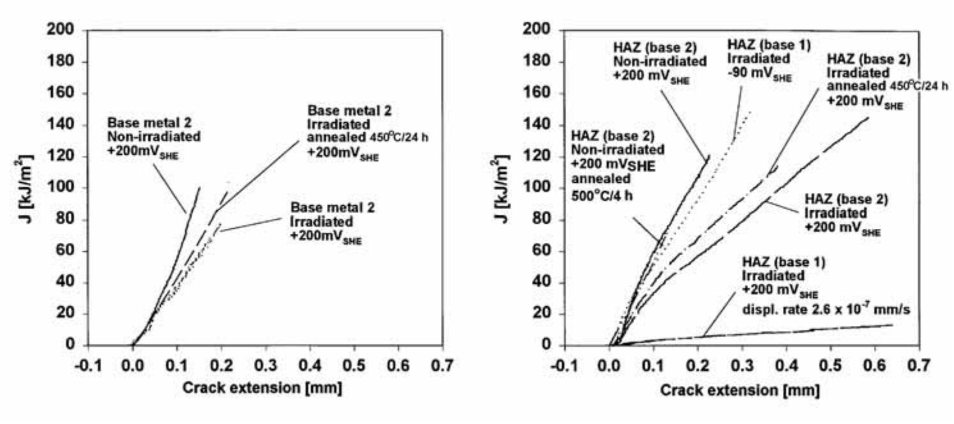

a)

b)

Figure 43. a) The measured J-R curves for base metal specimens. b) The measured J-R curves for HAZ specimens. The tests were carried out in simulated BWR water; temperature 288^{o}C, conductivity 0.2–0.3 μS/cm, pH$_{25°C}$ ~7, O$_2$ content 200 ppb and pressure 100 bar. The displacement rate was 1.8 x 10^{-6} mm/s unless otherwise indicated.

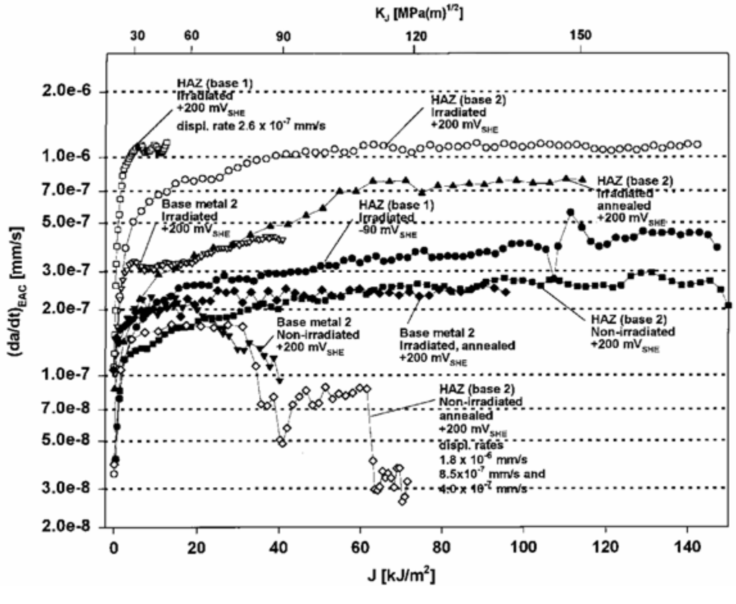

Figure 44. The determined environmentally assisted crack growth rates, (da/dt)$_{EAC}$, for all material states. The curves are determined by superposition based analysis method from the J-R curves presented in Figure 43. The displacement rate was 1.8x10^{-6} mm/s unless otherwise indicated.

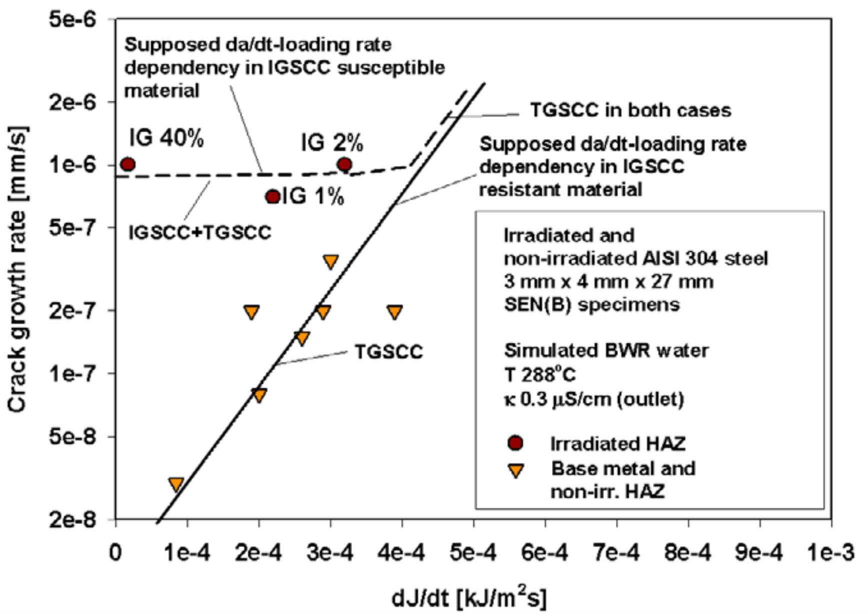

Figure 45. Crack growth rates as a function of J-integral increase rate, dJ/dt, in irradiated HAZ, irradiated base metal and non-irradiated HAZ.

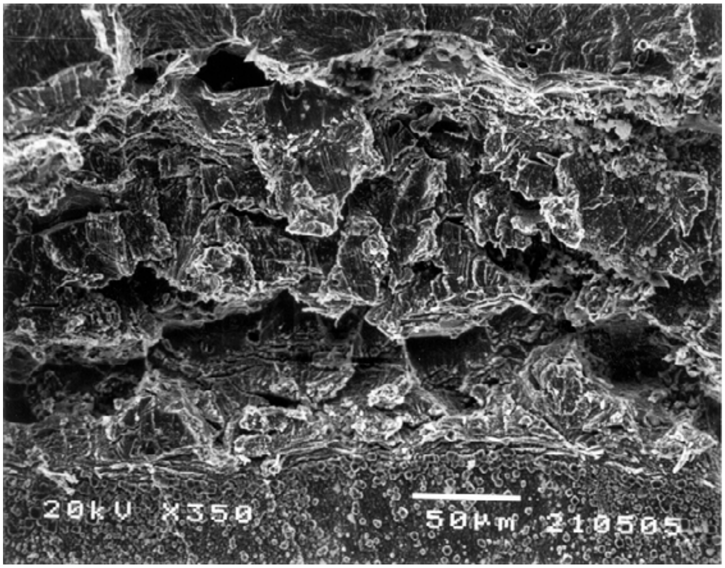

Figure 46. Fracture surface of the non-irradiated base metal 2 specimen after J-R test at the potential of +200 mV_{SHE}. Crack has propagated by mixed ductile fracture and TGSCC. The measured $(da/dt)_{EAC}$ was about 2×10^{-7} mm/s.

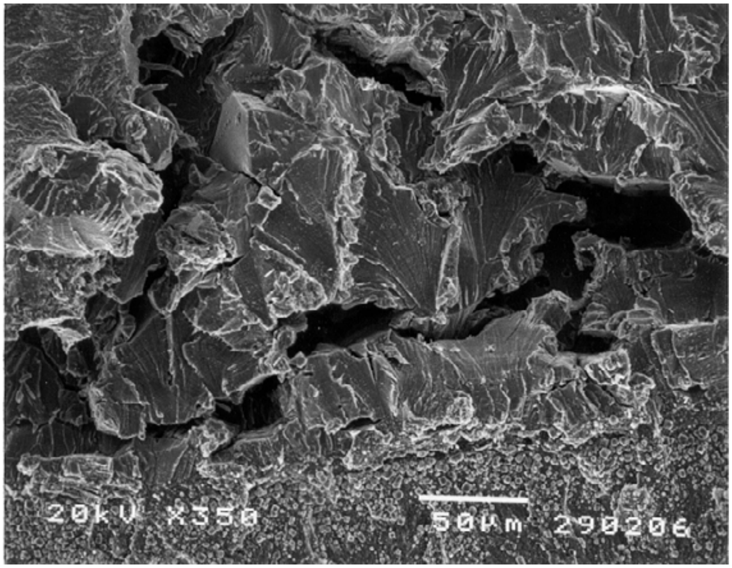

Figure 47. Fracture surface of the irradiated base metal 2 specimen after J-R test at the potential of +200 mV_{SHE}. Crack has propagated mostly by TGSCC mechanism, but some traces of IGSCC can be observed. The measured $(da/dt)_{EAC}$ was about 3×10^{-7} mm/s.

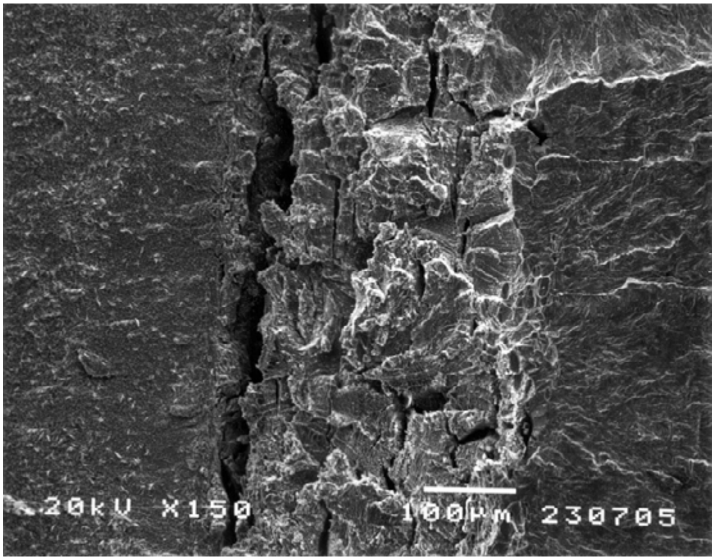

Figure 48. Fracture surface of the non-irradiated HAZ in base metal 2 after J-R test at the potential of +200 mV_{SHE}. Crack has propagated by mixed ductile fracture and TGSCC. The measured $(da/dt)_{EAC}$ was about 2×10^{-7} mm/s.

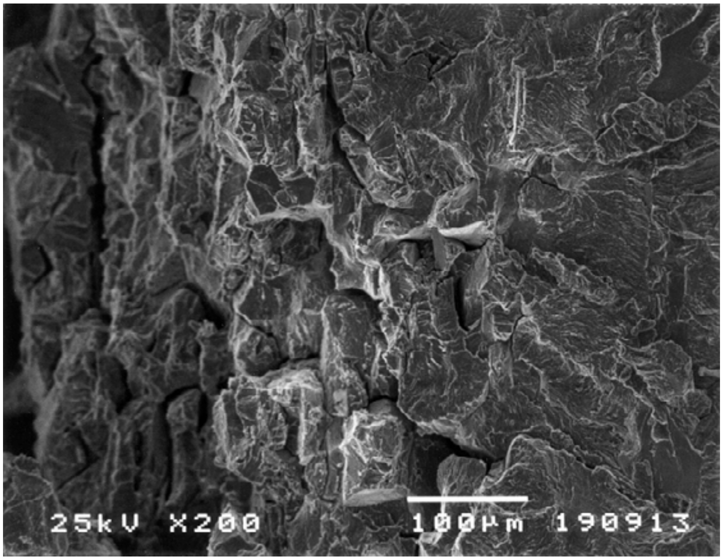

Figure 49. Fracture surface of the irradiated HAZ in base metal 2 after J-R test at the potential of +200 mV_{SHE}. Crack has propagated partly by TGSCC mechanism and partly along austenite-δ-ferrite phase boundaries. IGSCC is not easily detected due to the phase boundary cracking. The measured $(da/dt)_{EAC}$ was about 1×10^{-6} mm/s.

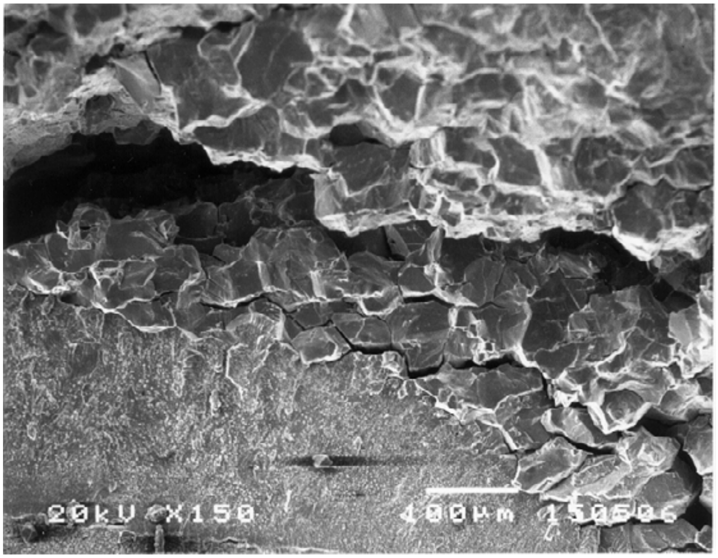

Figure 50. Fracture surface of the irradiated HAZ in base metal 1 after J-R test at the potential of +200 mV_{SHE} with reduced displacement rate. A significant part of the crack growth has taken place by the IGSCC mechanism. The measured $(da/dt)_{EAC}$ was about 1 x 10^{-6} mm/s (the same as with the higher displacement rate).

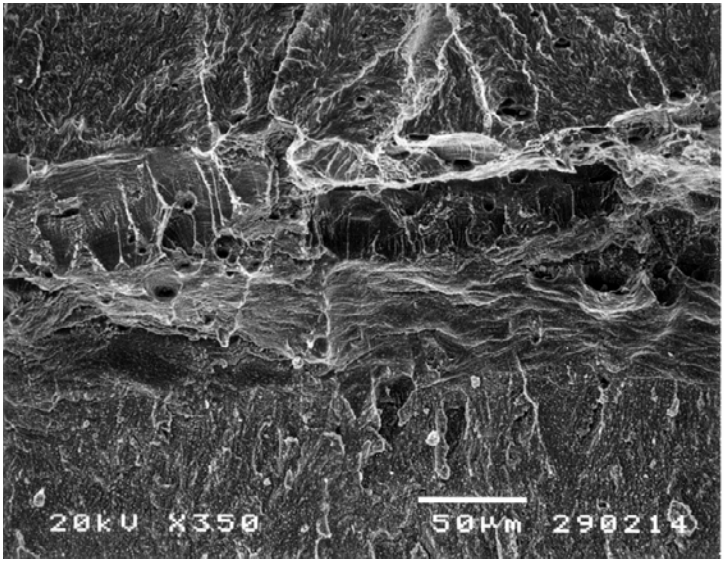

Figure 51. Fracture surface of the irradiated base metal 2 specimen tested at the potential of -500 mV_{SHE}, showing crack tip blunting. The fracture morphology is typical for all specimens tested at this corrosion potential.

4.2.5 Effect of annealing on hardness and specific resistivity

The effects of annealing time and temperature on the irradiation damage recovery were studied by hardness and resistance measurements. Annealing temperatures were 380°C (non-irradiated and irradiated) and 440°C (non-irradiated). The specimens were annealed in argon atmosphere in a furnace after which the specimens were cooled in air. The hardness and resistivity measurement samples were cut from the heads of the surveillance tensile test specimens. The cutting locations are presented in Figures 52 and 53.

The hardness measurement surfaces were ground by emery paper #1000 after every annealing period before the measurements. The hardness was measured by Vickers hardness tests with 10 N weight (HV10). The hardness values vs. annealing time are presented in Figure 54.

The specific resistances vs. annealing time for irradiated and non-irradiated material conditions are presented in Figure 55. The specific resistances were measured both in air at room temperature and at -196 °C in liquid nitrogen.

Effects of annealing at 380°C and 440°C on the Vickers hardness number and specific resistance of both irradiated and non-irradiated steels were small. It is not possible to relate the results to the stress corrosion test results.

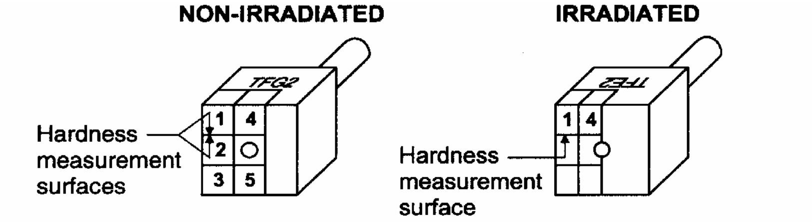

Figure 52. The cutting locations of the hardness measurement specimens.

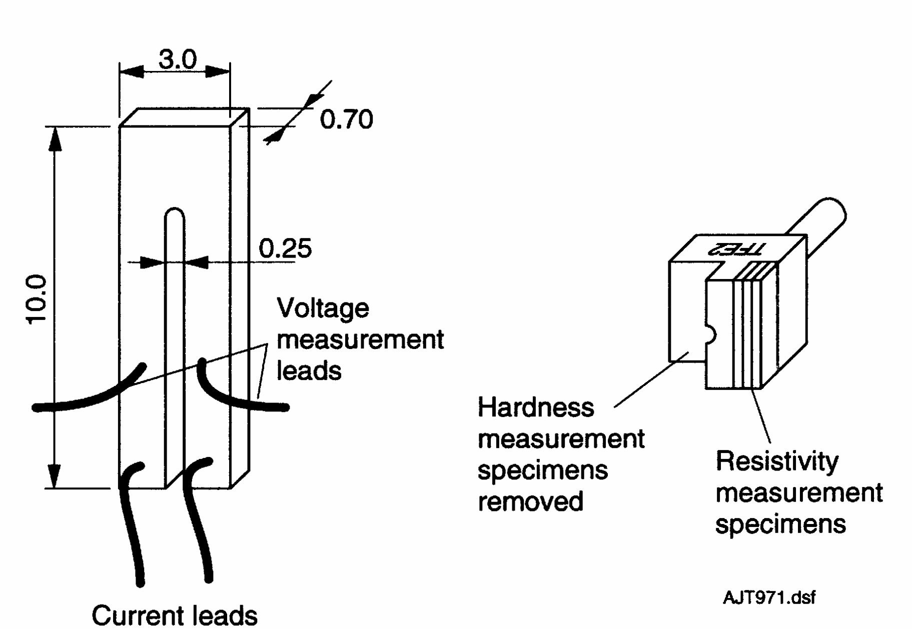

Figure 53. Resistivity measurement sample geometry and cutting locations.

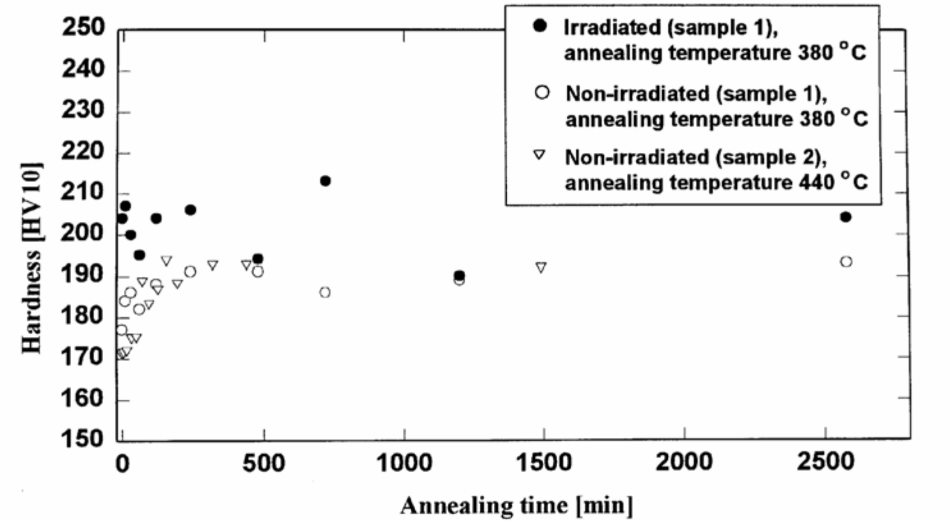

Figure 54. Hardness vs. annealing time.

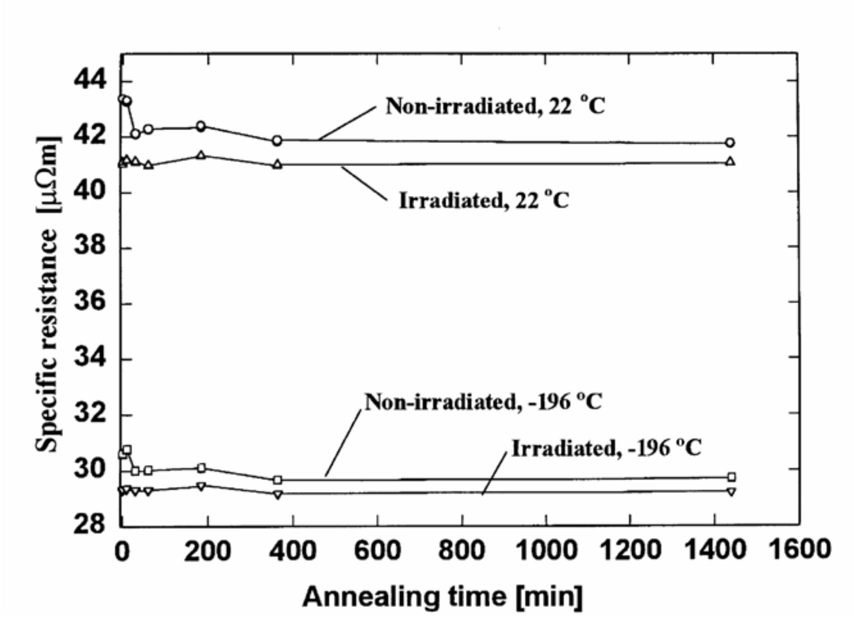

Figure 55. The effect of annealing time on specific resistance of irradiated and non-irradiated core shroud surveillance material at room temperature and at -196 °C in liquid nitrogen. The annealing temperature was 380 °C.

4.2.6 Intergranular corrosion tests

The degree of sensitization (DOS) was determined by reactivation ratio, I_r/I_a, which was measured using DL-EPR tests for every test material. The measured reactivation ratios for the core shroud surveillance material in various conditions are presented in Table 21. The polarization curves were measured in an electrochemical cell, which was designed for field use. The measured I_r/I_a ratios are a little higher than a laboratory cell would yield but they are comparable to each other. In a laboratory cell the measured I_r/I_a ratio for the non-irradiated base metal specimen (1.9 %) would correspond to thermal sensitization at 620°C for two to three hours [110]. No significant grain boundary dissolution in the core shroud material could be observed in post-test SEM studies.

The measured reactivation ratios indicate slight healing in the degree of sensitization (DOS) during plant exposure. In the case of base metal, the measured reactivation ratio in irradiated material was even smaller than in non-irradiated base metal. However, annealing at 450 ^{o}C for 24 h increased the reactivation ratios both in irradiated and non-irradiated base metals. In the case of HAZ, the difference between the reactivation ratios for irradiated and non-irradiated materials is smaller. With the annealing at 450 ^{o}C for 24 h, the reactivation ratios decreased slightly.

Table 21. Reactivation ratios measured by DL-EPR method (I_r/I_a) for non-irradiated and irradiated core shroud base metals and weld specimens with HAZ, before and after annealing at 450^{o}C for 24 h.

Specimen type	Heat treatment	Reactivation ratio Ir/Ia [%]
Base metal 2, non-irradiated	------------	1.9
Base metal 2, non-irradiated	Annealed at 450°C/24h	2.7
Base metal 2, irradiated	------------	0.9
Base metal 2, irradiated	Annealed at 450°C/24h	1.4
HAZ in base metal 1 with weld metal, non-irradiated	------------	1.0
HAZ in base metal 1 with weld metal, non-irradiated	Annealed at 450°C/24h	0.4
HAZ in base metal 1 with weld metal, irradiated	------------	1.2
HAZ in base metal 1 with weld metal, irradiated	Annealed at 450°C/24h	0.5

Modified Huey test is supposed to correlate better with the susceptibility to IASCC in irradiated materials than the EPR measurements. Due to the nature of Huey test it is not obvious that it attacks the chromium depleted zone near the grain boundaries, but the carbides or the segregated grain boundaries, e.g., due to phosphorus segregation are attacked.

There is a clear difference in weight losses between irradiated and non-irradiated specimens both in the case of base metal and HAZ, as can be seen in Table 22. However, the weight loss in the HAZ specimens including weld metal was smaller than in the base metal specimens. Annealing had no effect on the weight loss in irradiated nor in non-irradiated base metal specimens, but seemed to increase the weight losses in HAZ specimens slightly.

The relation between the condition of the material, modified Huey test results, DL-EPR test results and J-R test results can be seen in Table 23. There seems to be no clear relation between the DL-EPR results and fracture morphology or crack growth rate. On the other hand, a clear relation can be seen between the weight loss in modified Huey test and fracture morphology and crack growth rate with the exception of the annealed materials.

No changes due to annealing could be observed in post-test SEM studies, neither in non-irradiated nor irradiated specimens. In the non-irradiated base metal specimens the dissolution took place at the grain boundaries, Figure 56. The irradiated base metal specimens showed both general dissolution and grain boundary dissolution. In addition, slip lines were revealed in the irradiated base metal specimens, Figure 57.

The dissolution in the non-irradiated HAZ at the distance of over 1 mm from the weld fusion line was similar to the dissolution in the base metal specimens. The grain boundary attack was more severe close to the fusion line than further away. Dissolution of δ-ferrite phase was observed in addition to the grain boundary attack.

In the irradiated HAZ specimens further away from the fusion line, the dissolution was otherwise similar to that in the base metal specimens, but no slip lines could be observed in post-test studies. Closer to the interface, the behaviour was contradictory to what occurred in the non-irradiated HAZ specimens: grain boundary dissolution was minimal, Figures 58 and 59.

In order to understand better the results of the modified Huey tests, reference specimens from corresponding SIS 2333 material were tested. The weight losses in the reference material in various conditions were higher than in the non-irradiated core shroud base metal and HAZ specimens, but clearly lower than in irradiated materials. Cold working had no clear effect on the weight loss of the reference material, but sensitization increased it significantly. The dissolution in the as-received and in the cold-worked reference materials was similar to what occurred in the non-irradiated core shroud specimens. No clear general corrosion could be observed, only grain boundary dissolution. On the other hand, the sensitized reference material showed general dissolution and the slip lines were revealed in some grains, Figure 60.

Table 22. The weight losses per surface area unit in an hour in modified Huey tests.

Specimen type	Treatment	Weight loss rate/area [g/m^2h]
Base metal 2, non-irradiated	As-received	17
Base metal 2, non-irradiated	Annealed at 450°C/24 h	17
Base metal 2, irradiated	As-received	52
Base metal 2, irradiated	Annealed at 450°C/24 h	51
HAZ in base metal 1 with weld metal, non-irradiated	As-received	13
HAZ in base metal 1 with weld metal, non-irradiated	Annealed at 450°C/24 h	16
HAZ in base metal 1 with weld metal, non-irradiated	Annealed at 500°C/4 h	13
HAZ in base metal 1 with weld metal, irradiated	As-received	37
HAZ in base metal 1 with weld metal, irradiated	Annealed at 450°C/24 h	41
Reference SIS 2333	As-received	24
Reference SIS 2333	Cold-worked 25%	25
Reference SIS 2333	Sensitized 650 °C/1 h	30

Table 23. The effects of core shroud surveillance material's condition on fracture mode and environmentally assisted crack growth rate measured at 288 °C, $(da/dt)_{EAC}$, with load line displacement rate of $1.8x10^{-6}$ mms^{-1} in slow J-R tests at +200 mV_{SHE}.

	Base metal			HAZ			
	Non-irradiated	Irradiated	Irradiated, annealed at 450°C/24 h	Non-irradiated	Non-irradiated, annealed at 500 °C/4 h	Irradiated	Irradiated, annealed at 450°C/24 h
DL-EPR (I_r/I_a) [%]	1.9	0.9	1.4	1.0	----	1.2	0.5
Mod. Huey [g/m^2h]	17	52	51	13	13	37	41
Fracture morphology	TGSCC	TGSCC, 1%IGSCC	TGSCC	TGSCC	TGSCC	TGSCC, interface cracking, 2% IGSCC	TGSCC, interface cracking, 1% IGSCC
$(da/dt)_{EAC}$ [mm/s]	2 x 10^{-7}	3–4 x10^{-7}	2 x 10^{-7}	2 x 10^{-7}	2 x 10^{-7}	1 x 10^{-6}	7 x 10^{-7}

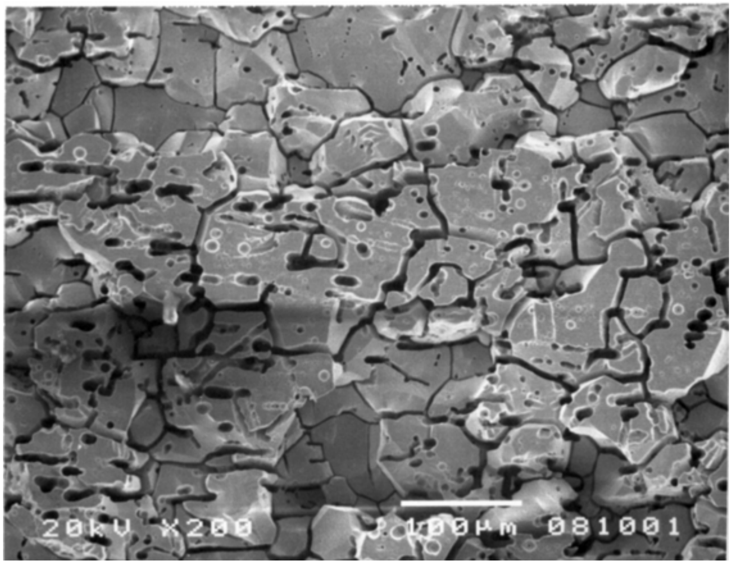

Figure 56. Strong grain boundary dissolution in non-irradiated annealed (450°C/24 h) base metal 2 specimen in modified Huey test.

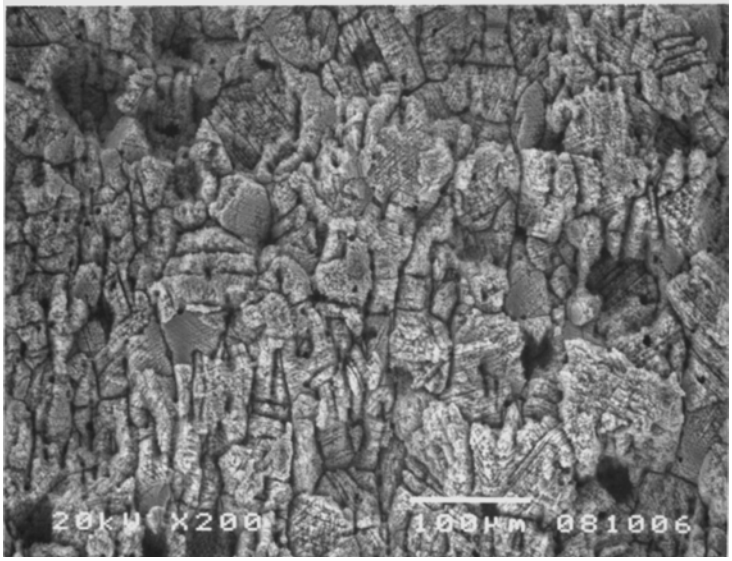

Figure 57. Irradiated base metal 2 specimen showing general dissolution in addition to the grain boundary dissolution. Slip lines are revealed. Annealed at 450°C for 24 h.

Figure 58. General and grain boundary dissolution about 1.5 mm from the weld / base metal 1 fusion line in irradiated HAZ specimen. δ-ferrite dissolution was minimal. No heat treatments.

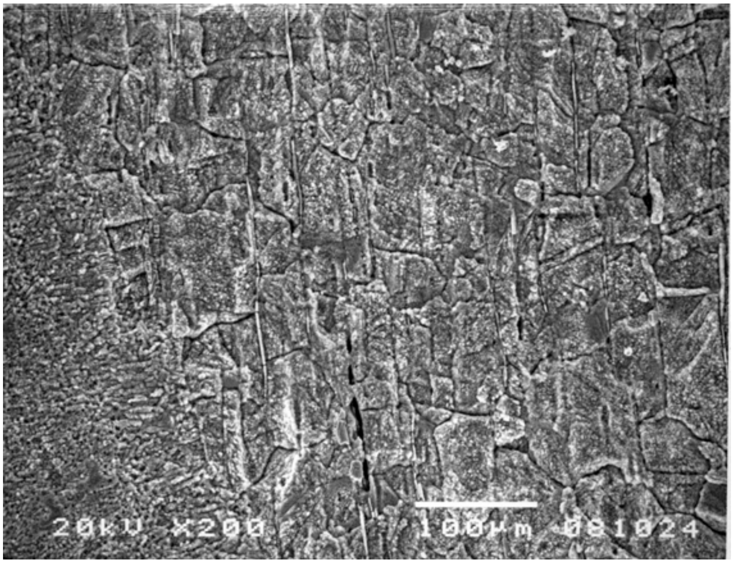

Figure 59. General and grain boundary dissolution close the weld / base metal 1 fusion line in irradiated HAZ specimen. No heat treatments.

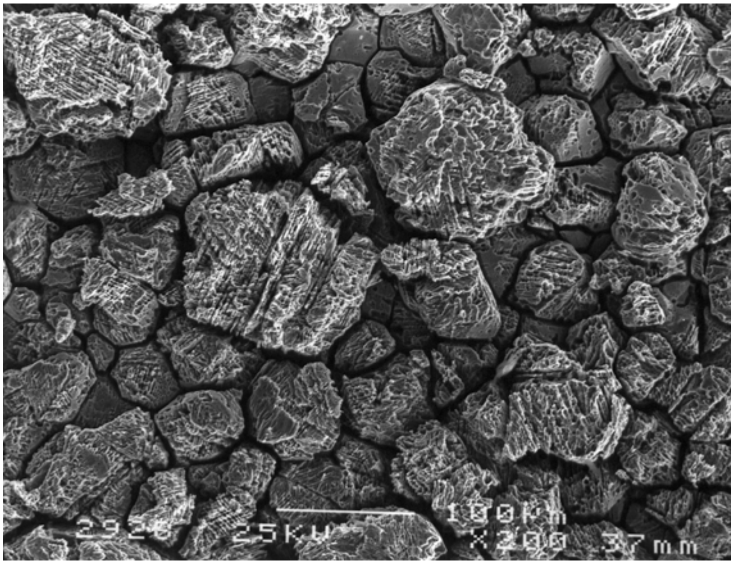

Figure 60. Grain boundary and general dissolution in sensitized (650^oC/1 h) reference material. Slip lines are revealed in some of the grains.

4.3 Tests on AISI 304 steel using varying displacement rate

The displacement vs. testing time curves and applied displacement rates of all 4 specimens are presented in Figure 61. The load-load line displacement curves are presented in Figure 62. Figure 63 shows the load-load line diplacement curves in normalized form. J-R curves of the tests are presented in Figure 64. Figures 65 and 66 show the crack lengths vs. testing time. Specimens No. 1 and 2 were tested simultaneously in separate autoclaves using one water re-circulation loop. After that, specimens No. 3 and 4 were tested in the same autoclaves.

The differences between the load-load line displacement curves of specimens 1 and 2 result from easier crack propagation in sensitized steel than in non-sensitized steel. The differences between the curves of specimens 3 and 4 result from different ligament size: specimen No. 3 was side grooved and the initial pre-fatigue crack was longer than in specimen No. 4. In normalized form the load-displacement curves of the sensitized specimens follow the same path. The normalized load-displacement curve of specimen No. 1 is slightly above the others probably because the sensitization heat treatment of specimens No. 2-4 has changed the tensile properties of the steel.

The J-R curves show that the fracture resistance of the sensitized steel is lower than that of the non-sensitized steel. The curves are also sensitive to the changes in displacement rate, showing steeper slope at higher displacement rates for sensitized steel. There is also a small difference between the J-R curves of specimens No. 3 and No. 4, which experienced the similar load line displacement rate sequences, probably because specimen No. 3 was side grooved and specimen No. 4 was not. Side grooves are known to make crack growth easier since side grooves increase stress triaxiality at the sides of the crack front [5, 7].

As can be seen from Figure 65, crack growth is faster in the sensitized than in the mill-annealed steel at each applied load line displacement rate. Also the applied load line displacement rate has a clear effect on the crack growth rate both in the mill-annealed and in the sensitized steel.

The influence of the load line displacement rate on the crack growth rate can also be seen in Figure 66, which shows the crack length as a function of time for the two simultaneously tested specimens, No. 3 and No. 4. Also, as can be seen, the crack growth rate is, on the average, slightly faster in the side grooved specimen than in the specimen without side grooves.

Figures 67–70 show the fracture surfaces of each specimen. The initial and final crack front locations are marked with a_0 and a_f, respectively. Figure 71 shows a section through the fracture zone of specimen No. 4. There is an area of almost pure IGSCC in the middle. The location of this area fits well, if the uneven crack growth is taken into account, to the range where the load line displacement rate was zero for the first time. The test resulted also in TGSCC at the end of the test, when the applied load line displacement rate was 1-2 x 10^{-6} mm/s, and in mixed TGSCC and IGSCC at the intermediate load line displacement rates, i.e., 2.1-7.5 x 10^{-7} mm/s. Similar dependencies between the fracture morphology and load line displacement rate were also observed on the fracture surface of the other two sensitized specimens. Figure 72 shows the typical fracture morphology, TGSCC, obtained at the highest load line displacement rate in the sensitized steel and at all load line displacement rates in non-sensitized steel, and Figure 73 shows IGSCC obtained under constant displacement condition in the sensitized steel.

Figures 74 and 75 show the observed crack growth rates as a function of K_J and dJ/dt. The crack growth rate data was plotted as a function of dJ/dt instead of the load line displacement rate because dJ/dt is a specimen and loading geometry independent measure, whereas load line displacement rate is not. K_J was used instead of J because K is the more commonly used parameter.

High strain level, i.e., high K_J, does not have any noticeable influence on the crack growth rate or the fracture morphology under constant displacement type loading in the elastic-plastic loading conditions. In the case of specimen No. 4, fracture morphology was IGSCC at $K_J = 63$ MPa√m. IGSCC was observed also on the fracture surfaces of the other sensitized specimens at high K_J-levels. Crack branching was observed locally, e.g., in the IGSCC region in Figure 71, but it is not clear whether the branching resulted from the high strain level or not.

The crack growth rates seem to be more dependent on dJ/dt than on K_J. Also there appears to be a plateau in the crack growth rate of the sensitized steel when it is presented as a function of dJ/dt. The plateau crack growth rate is a little higher than the crack growth rate prediction of the slip-oxidation model (GE-PLEDGE code) [38] for constant load tests at $K_I = 30$ MPa√m in the same environment. On the other hand, the crack growth rates measured under constant displacement are a little lower than predicted by the slip-oxidation model.

Figure 76 shows the dependence between dJ/dt and crack growth rate below the plateau range. The relation between dJ/dt and crack growth rate is linear in this range. A linear regression curve fitted to the data points is also shown in Figure 76. One data point measured under constant displacement was excluded because the crack growth rate deviated considerably from the other data. The exceptionally low crack growth rate (1.4×10^{-8} mm/s) may have resulted from the loading history. If the fracture morphology was mostly TGSCC before the loading was changed from rising to constant displacement, intergranular crack growth may have taken place only locally.

The measured water chemistry parameters are shown in Figures 77 and 78. The corrosion potentials (ECP) increased from 120 mV to 160 mV (SHE) during each test. The inlet oxygen content was 250 ppb during the tests on specimens No. 1 and 2. The level of the measured outlet oxygen content was ~100 ppb in the beginning, but calibration of the equipment resulted in an increase in the measured value, thus the actual oxygen level in the beginning was probably ~200 ppb. The inlet oxygen level during the tests of specimens No. 3 and 4 was 250 ppb and the outlet oxygen level was 200 ppb. Outlet conductivities were 0.2 μS/cm during the tests. Inlet conductivities were not measured continuously, but the periodically measured values were 0.07–0.1 μS/cm.

The applied load line displacement rates, average J-integral increase rates (dJ/dt) during each applied load line displacement rate, average K_J-levels (converted from J-integral), crack growth rates (da/dt) and observed SCC morphologies are collected in Table 24.

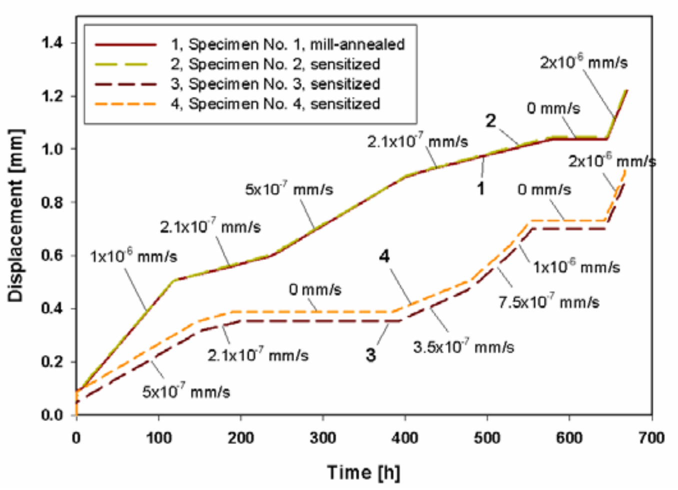

Figure 61. Load line displacement vs. testing time curves and applied displacement rates (mm/s) during the tests on a mill-annealed and 3 sensitized ($620^oC/24$ h) 10 mm x 10 mm x 55 mm SEN(B) specimens tested in simulated BWR water. T = 288^oC, conductivity (outlet) = 0.2 $\mu S/cm$, dissolved O_2 (outlet) = 200 ppb, ECP (average) = 140 mV_{SHE}.

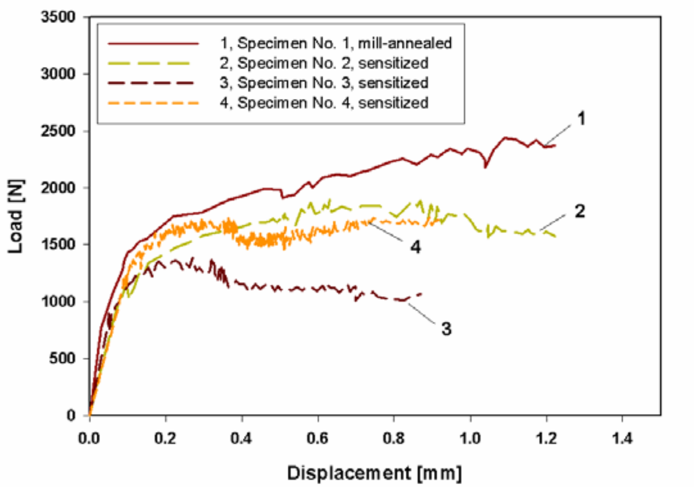

Figure 62. Load vs. load line displacement curves measured on a mill-annealed and 3 sensitized ($620^oC/24$ h) 10 mm x 10 mm x 55 mm SEN(B) specimens tested using varying displacement rates in simulated BWR water. T = 288^oC, conductivity (outlet) = 0.2 $\mu S/cm$, dissolved O_2 (outlet) = 200 ppb, ECP (average) = 140 mV_{SHE}.

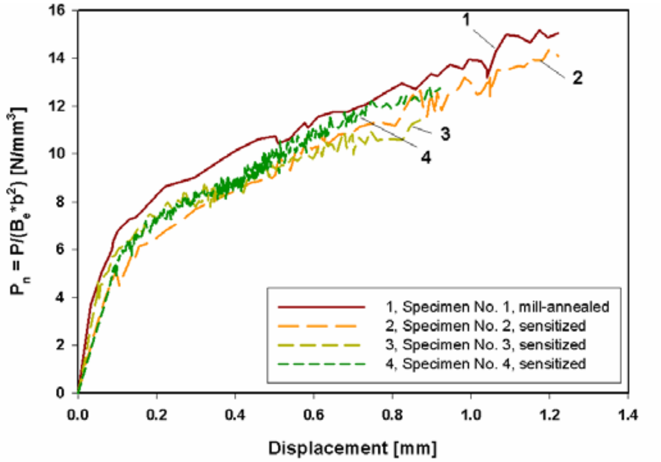

Figure 63. Normalized load vs. load line displacement curves measured on a mill-annealed and 3 sensitized (620^{o}C/24 h) 10 mm x 10 mm x 55 mm SEN(B) specimens tested using varying displacement rates in simulated BWR water at 288 ^{o}C. B_e = effective thickness and b = momentary remaining ligament.

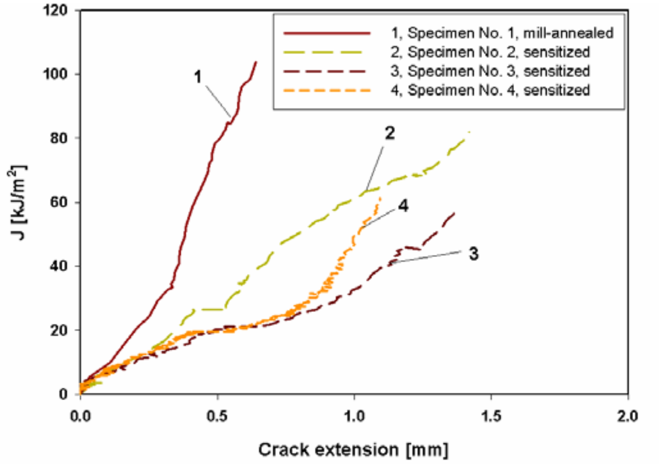

Figure 64. J vs. crack extension curves measured on a mill-annealed and 3 sensitized (620^{o}C/24 h) 10 mm x 10 mm x 55 mm SEN(B) specimens tested using varying displacement rates in simulated BWR water. T = 288^{o}C, conductivity (outlet) = 0.2 µS/cm, dissolved O_2 (outlet) = 200 ppb, ECP (average) = 140 mV$_{SHE}$.

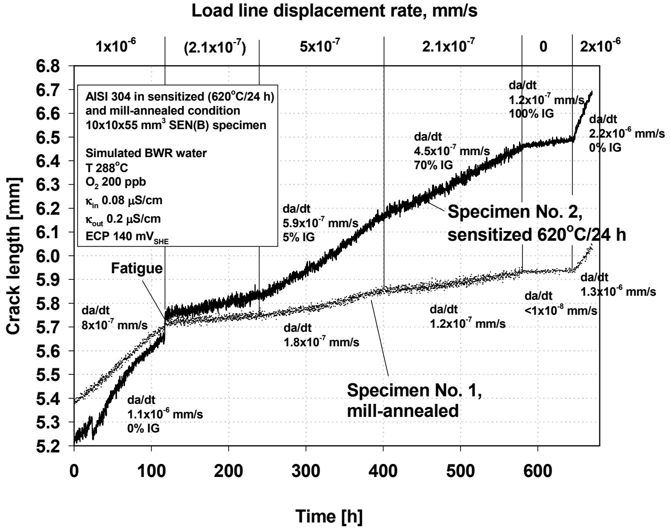

Figure 65. Crack length vs. time of the first two tests performed on AISI 304 steel in sensitized (620°C/24 h) and in mill-annealed condition in simulated BWR water. The applied displacement rates are shown on the top.

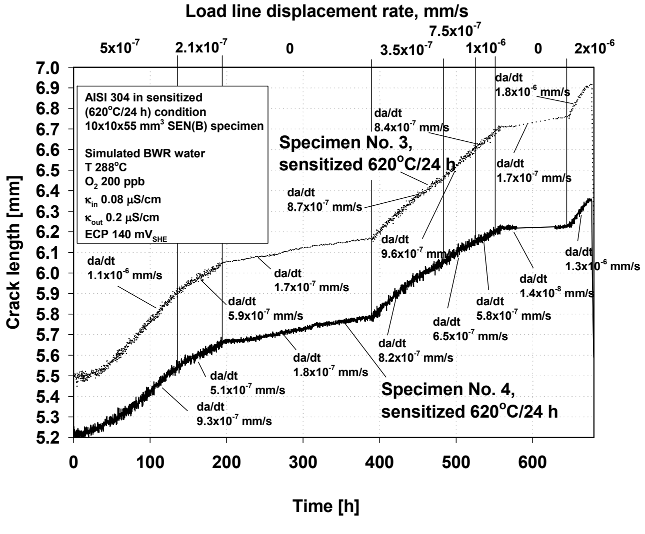

Figure 66. Crack length vs. time during the second two tests performed on AISI 304 steel in sensitized condition (620°C/24 h) in simulated BWR water. The applied displacement rates are shown on the top.

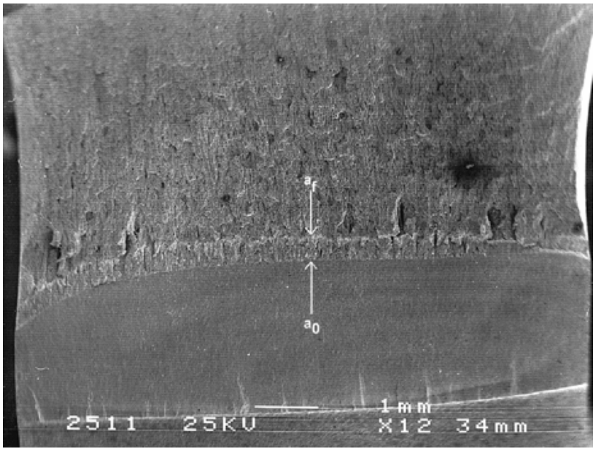

Figure 67. Fracture surface of specimen No. 1 (mill-annealed) tested using varying displacement rate in simulated BWR water. Pre-fatigue crack tip = a_0*, crack tip after the test =* a_f*.* $T = 288^oC$*, conductivity (outlet) = 0.2* $\mu S/cm$*, dissolved* O_2 *(outlet) = 200 ppb, ECP (average) = 140* mV_{SHE}*.*

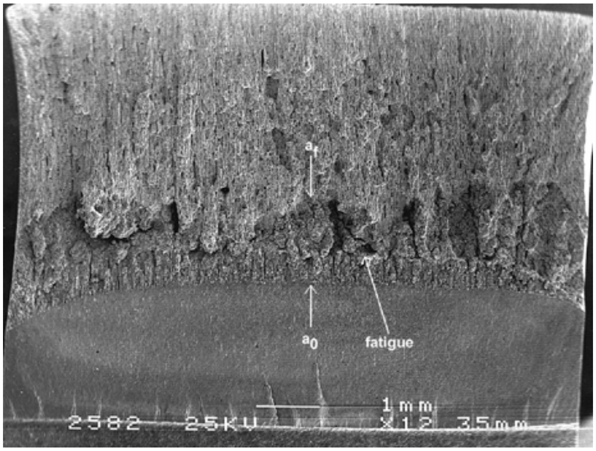

Figure 68. Fracture surface of specimen No. 2 (sensitized at 620^oC *for 24 h) tested using varying displacement rate in simulated BWR water. Pre-fatigue crack tip =* a_0*, crack tip after the test =* a_f*. The location of the end of the first applied displacement rate was marked by fatigue.* $T = 288^oC$*, conductivity (outlet) = 0.2* $\mu S/cm$*, dissolved* O_2 *(outlet) = 200 ppb, ECP (average) = 140* mV_{SHE}*.*

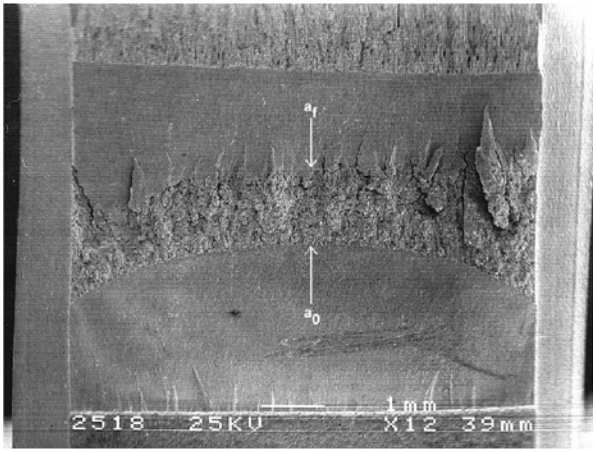

Figure 69. Fracture surface of specimen No. 3 (sensitized at 620°C for 24 h). Pre-fatigue crack tip = a_0*, crack tip after the test =* a_f*. The specimen was side-grooved which probably is the reason why the crack extension is more even than in the other sensitized specimens. T = 288°C, conductivity (outlet) = 0.2* μ*S/cm, dissolved* O_2 *(outlet) = 200 ppb, ECP (average) = 140* mV_{SHE}*.*

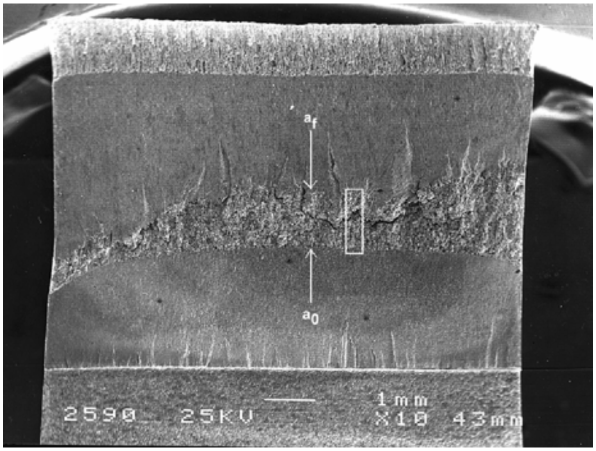

Figure 70. Fracture surface of specimen No. 4 (sensitized at 620°C for 24 h). The area marked with the rectangle is presented in Figure 71. Pre-fatigue crack tip = a_0*, crack tip after the test =* a_f*. T = 288°C, conductivity (outlet) = 0.2* μ*S/cm, dissolved* O_2 *(outlet) = 200 ppb, ECP (average) = 140* mV_{SHE}*.*

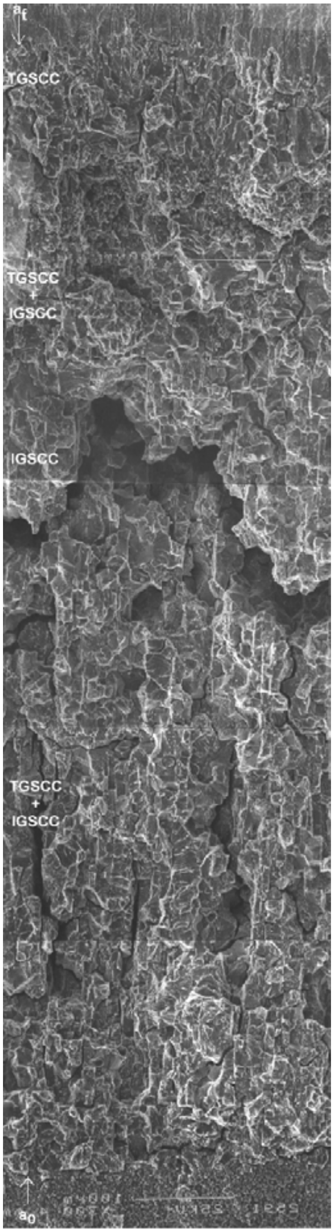

Figure 71. A section through the fracture surface of specimen No. 4. The initial crack tip is marked by a_0 and the final crack tip by a_f. The area of mainly IGSCC is (presumably) formed under constant displacement loading and the TGSCC zone in the end of the test, when the highest load line displacement rate, $2x10^{-6}$ mm/s, was applied. Mixed TGSCC+IGSCC zones have formed when the intermediate load line displacement rates, $2.1 \times 10^{-7} – 1 \times 10^{-6}$ mm/s, were applied.

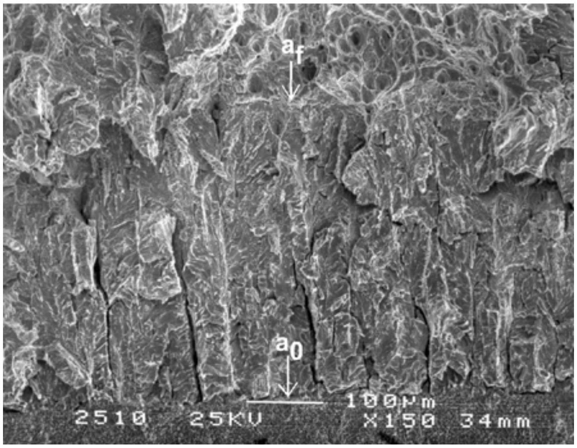

Figure 72. A detail of the fracture surface of specimen No. 1 showing typical TGSCC obtained at all load line displacement rates in mill-annealed AISI 304 steel. Pre-fatigue crack tip = a_0*, crack tip after the test =* a_f*. T =* 288^{o}*C, conductivity (outlet) = 0.2* μ*S/cm, dissolved* O_2 *(outlet) = 200 ppb, ECP (average) = 140* mV_{SHE}*.*

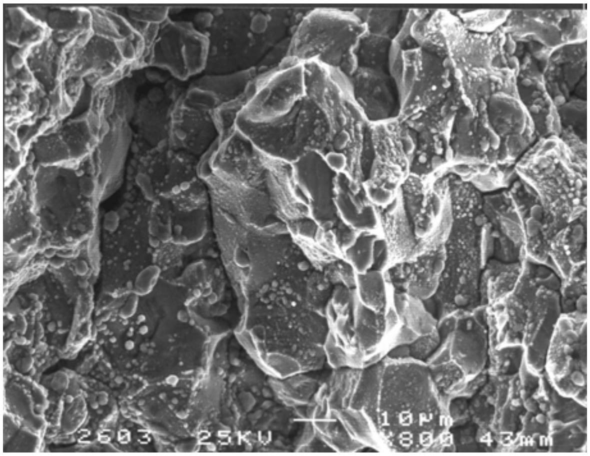

Figure 73. Typical IGSCC in sensitized AISI 304 steel obtained in constant displacement loading (a detail of the fracture surface of specimen No. 4, sensitized at 620^{o}*C for 24 h). T =* 288^{o}*C, conductivity (outlet) = 0.2* μ*S/cm, dissolved* O_2 *(outlet) = 200 ppb, ECP (average) = 140* mV_{SHE}*.*

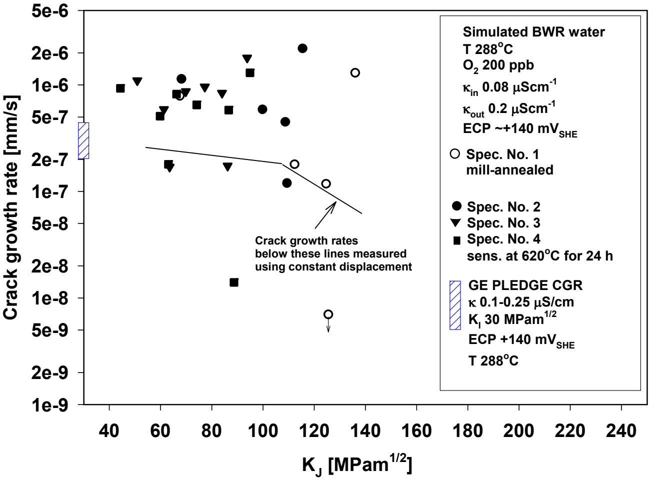

Figure 74. Crack growth rates as a function of elastic-plastic K_J. The crack growth rates were measured on AISI 304 steel in sensitized (620°C/24 h) and in mill-annealed condition in simulated BWR water using varying displacement rates. T = 288°C, conductivity (outlet) = 0.2 µS/cm, dissolved O_2 (outlet) = 200 ppb, ECP (average) = 140 mV$_{SHE}$. The crack growth rate range for the same environment predicted by slip-oxidation model (GE-PLEDGE crack growth rate prediction [38]) is also marked in the figure.

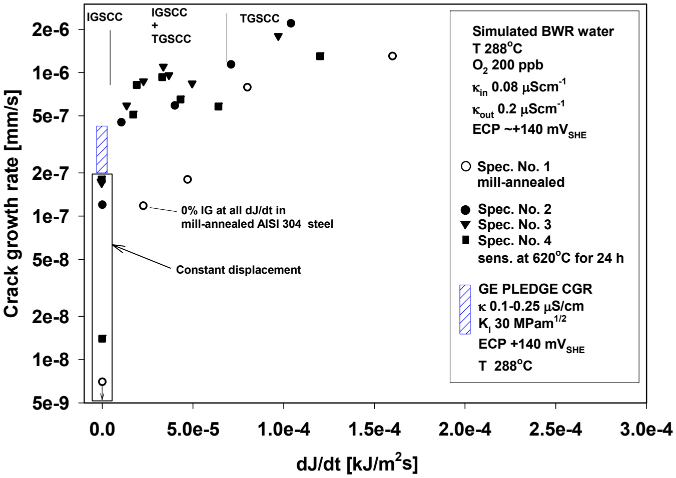

Figure 75. Crack growth rate vs. J-integral increase rate, dJ/dt, in AISI 304 steel in sensitized (620°C/24 h) and non-sensitized conditions in simulated BWR water. There is less scatter as compared to the crack growth rates vs. K_J in the previous figure.

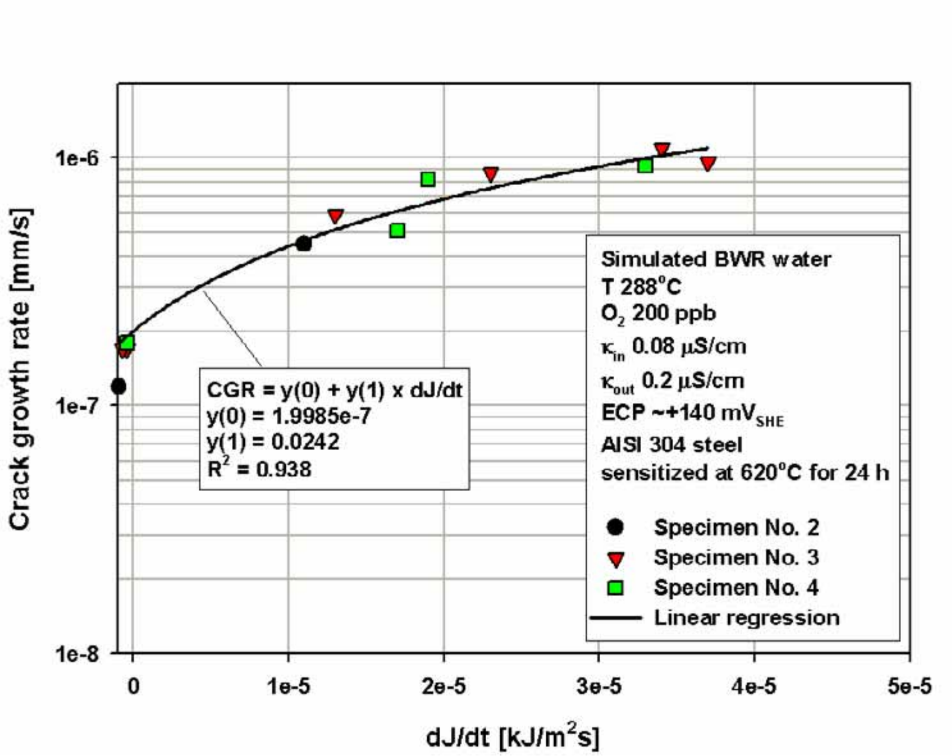

Figure 76. Crack growth rates as a function of J-integral increase rate, dJ/dt, at low dJ/dt levels, and linear regression of the data (CGR = crack growth rate). The correlation between the crack growth rate and dJ/dt is very good as indicated by the correlation coefficient, R^2. The linear regression is seen as curved because the crack growth rate is shown in the logarithmic scale. The slowest crack growth rate measured under constant displacement was excluded. The crack growth rates were measured on AISI 304 steel in sensitized (620^oC/24 h) condition in simulated BWR water using varying displacement rates. T = 288^oC, conductivity (outlet) = 0.2 μS/cm, dissolved O_2 (outlet) = 200 ppb, ECP (average) = 140 mV_{SHE}.

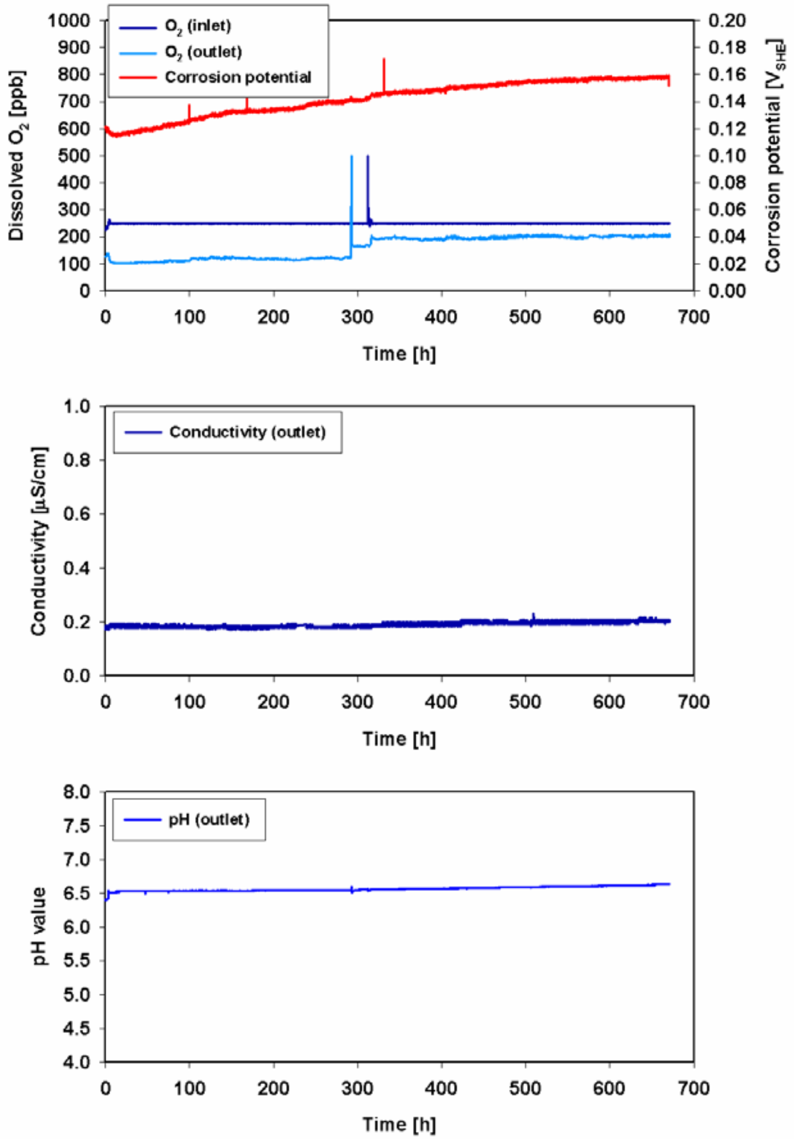

Figure 77. Water chemistry during the first tests (specimens No. 1 and 2 were tested simultaneously). The tests were performed on AISI 304 steel in mill-annealed and in sensitized ($620^oC/24$ h) condition in simulated BWR water at 288^oC. The apparent increase in the outlet oxygen content resulted from the re-calibration of the oxygen sensor.

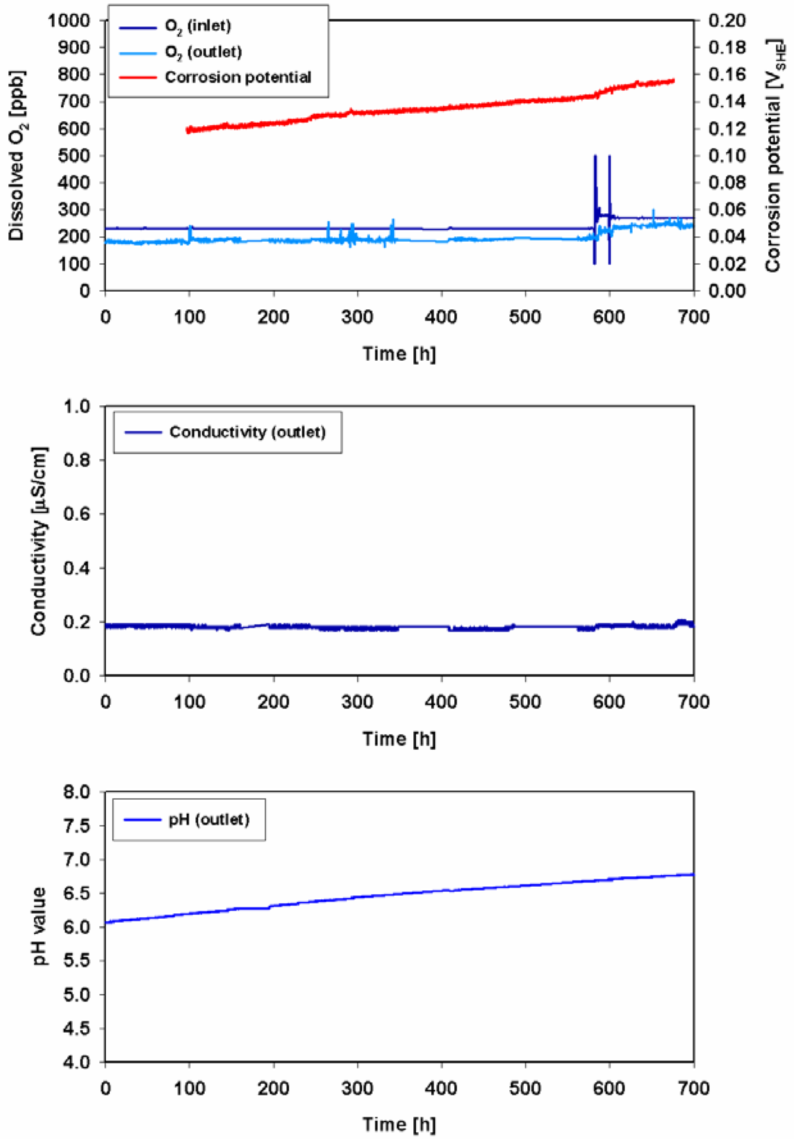

Figure 78. Water chemistry during the second tests (specimens No. 3 and 4 were tested simultaneously). The tests were performed on AISI 304 steel in sensitized (620°C/24 h) condition in simulated BWR water at 288°C.

Table 24. Measured crack growth rates and observed fracture morphologies.

Specimen No. and material condition	Load line displacement rate [mm/s]	dJ/dt [kJ/m^{2}s]	K_J* [MPa$\sqrt{m}$]	da/dt [mm/s]	Observed SCC morphology
No. 1 Mill-annealed	1.0e-6	8.0e-5	67	7.9e-7	TGSCC
	5.0e-7	4.7e-5	112	1.8e-7	TGSCC
	2.1e-7	2.3e-5	124	1.2e-7	TGSCC
	0	-1e-7	125	<1e-8	-
	2.1e-6	1.6e-4	136	1.3e-6	TGSCC
No. 2 Sensitized	1.0e-6	7.1e-5	68	1.1e-6	Specimens 2–4: IGSCC under constant displacement TGSCC+IGSCC at 2.1–7.5 x 10^{-7} mm/s displacement rates TGSCC at equal or higher than 1 x 10^{-6} mm/s displacement rates
	5.0e-7	4.0e-5	100	5.9e-7	
	2.3e-7	1.1e-5	109	4.5e-7	
	0	-9.3e-7	109	1.2e-7	
	2.2e-6	1.0e-4	115	2.2e-6	
No. 3 Sensitized	5.0e-7	3.4e-5	51	1.1e-6	
	2.1e-7	1.3e-5	61	5.9e-7	
	0	-4.2e-7	64	1.7e-7	
	3.5e-7	2.3e-5	70	8.7e-7	
	7.5e-7	3.7e-5	77	9.6e-7	
	1.0e-6	4.9e-5	84	8.4e-7	
	0	-7.2e-7	86	1.7e-7	
	2.0e-6	9.7e-5	94	1.8e-6	
No. 4 Sensitized	5.0e-7	3.3e-5	44	9.3e-7	
	2.1e-7	1.7e-5	60	5.1e-7	
	0	-4.2e-7	63	1.8e-7	
	3.5e-7	1.9e-5	66	8.2e-7	
	7.5e-7	4.3e-5	74	6.5e-7	
	1.0e-6	6.4e-5	87	5.8e-7	
	0	-6.9e-7	89	1.4e-8	
	2.0e-6	1.2e-4	95	1.3e-6	

**Average of the initial and final K_J of each applied load line displacement rate sequence.*

4.4 Tests on low activation steel (LAS) F82H

The load vs. load line displacement curves of all the tests are shown in Figure 79, and in the normalized form in Figure 80. J-R curves are shown in Figure 81. J-R test results are summarized in Table 25. J_Q-value is the J-value at which the J-R curve intersects the 0.2 mm offset line. As can be seen, the J_Q value decreases with the increasing temperature and even more when the specimen is exposed to high temperature water. The tests in silicon oil bath and in nitrogen gas atmosphere resulted in dimpled fracture surface, which is typical for ductile fracture. The tests in high temperature water resulted in brittle-like transgranular cracking observed also in austenitic stainless steels in high temperature water, when high displacement rates are used.

Figure 82 shows the measured crack lengths vs. testing time for specimens F82H/3.1 and F82H/3.2, which were tested in the high temperature water. As can be seen, the crack growth rate is strongly dependent on the applied displacement rate.

The strong dependency between the loading rate and the crack growth rate can be also seen in Figure 83, which shows the crack growth rate as a function of J-integral increase rate, dJ/dt. The dependence between dJ/dt and the crack growth rate seems to be linear both in the high temperature water and in the nitrogen gas, although the crack growth rate increases much faster with the increasing dJ/dt in the high temperature water than in the nitrogen atmosphere. The dependence can actually be expected to be linear in nitrogen gas because in inert environments the crack growth takes place purely due to mechanical loading.

No continuous crack growth was observed under constant displacement loading in either environment. Under constant displacement, the crack growth rate decreased to 0 mm/s soon after the loading was changed from rising displacement to constant displacement.

The crack growth rate seems to be independent on the applied potential. Although the crack growth rate, as a function of dJ/dt, is a little higher at 0 mV_{SHE} than at +400 mV_{SHE}, the difference probably results from the J-level rather than the potential (polarization to +400 mV_{SHE} was carried out at a lower J-level than to 0 mV_{SHE}). At higher J-levels, the contribution of ductile cracking to the measured crack growth rate is larger. The results of the tests performed in high temperature water are summarized in Table 26 and the water chemistry parameters are shown in Figure 84.

Table 25. Summarized results of the J-R tests conducted in silicon oil, in nitrogen gas atmosphere and in high temperature water.

Specimen code	Specimen size (B*W*L) [mm]	Test environment	Temperature [^{o}C]	J_Q [kJ/m^2]	Fracture surface morphology
F82H/6.4	3x4x27	Silicon oil	20	283	Ductile
F82H/6.6	3x4x27	Silicon oil	100	>220	Ductile
F82H/6.5	3x4x27	Silicon oil	200	>230	Ductile
F82H/6.3	3x4x27	Silicon oil	200	234	Ductile
F82H/3.3	5x10x55	Nitrogen	230	220	Ductile
F82H/3.4	5x10x55	Nitrogen	230	186	Ductile
F82H/3.1	5x10x55	Water	230	32	TGSCC
F82H/3.2	5x10x55	Water	230	16	TGSCC

Table 26. Summarized results of the tests conducted with varying load line displacement rate at 230^{o}C in high temperature water containing 300 ppb O_2 and 30 ppb SO_4^{2-}.

Specimen code	Potential [mV$_{SHE}$]	Displacement rate [mm/s]	J [kJ/m^2]	dJ/dt [kJ/m^{2}s]	K_J [MPa√m]*	Crack growth rate [mm/s]
F82H/3.1	+400	2x10^{-7}	6...43	3.1x10^{-5}	75	2.6x10^{-7}
		2x10^{-6}	43...78	2.2x10^{-4}	118	1.4x10^{-6}
		0	78	~0	134	→ 0**
	0	2x10^{-7}	78...103	4.6x10^{-5}	145	3.9x10^{-7}
		0	103	~0	154	→ 0**
		2x10^{-6}	103...132	1.9x10^{-4}	165	1.4x10^{-6}
F82H/3.2	+400	2x10^{-7}	8...44	2.9x10^{-5}	77	4.1x10^{-7}
		2x10^{-6}	44...70	1.6x10^{-4}	115	1.6x10^{-6}
		0	70	~0	127	→ 0**
	0	2x10^{-7}	70...94	3.1x10^{-5}	138	5.3x10^{-7}
		0	94	~0	147	→ 0**
		2x10^{-6}	94...107	1.3x10^{-4}	152	1.6x10^{-6}

**Average values calculated from initial and final J-levels (E assumed to be 210 GPa)*

***Decreased slowly towards 0 mm/s*

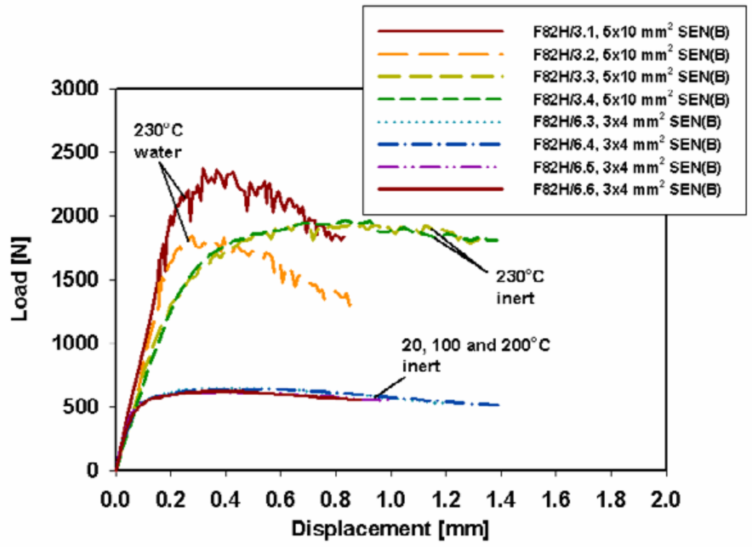

Figure 79. Load vs. load line displacement curves of the specimens. The tests at 20, 100, and 200°C were performed on 3 mm x 4 mm x 27 mm SEN(B) specimens in silicon oil. The tests at 230°C on 5 mm x 10 mm x 55 mm SEN(B) specimens were performed in high temperature water (specimens F82H/3.1 and F82H/3.2) or nitrogen gas (specimens F82H/3.3 and F82H/3.4).

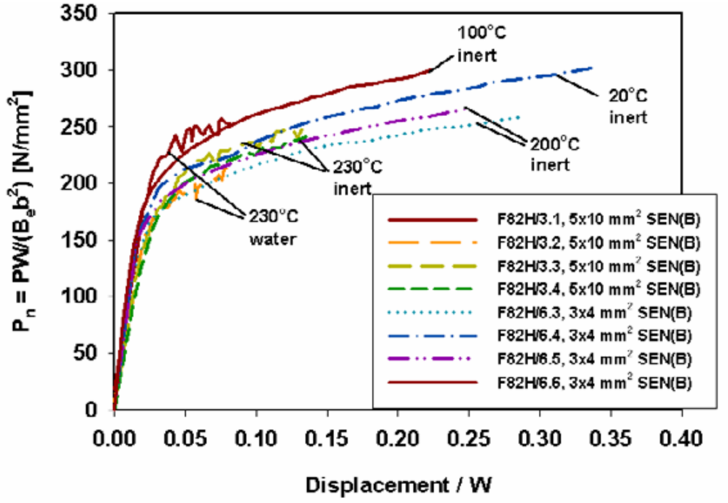

Figure 80. Normalized load-displacement curves. The curves are normalized in order to make the curves independent of the specimen size and crack length. P = load, W = specimen width, B_e = effective thickness and b = remaining ligament.

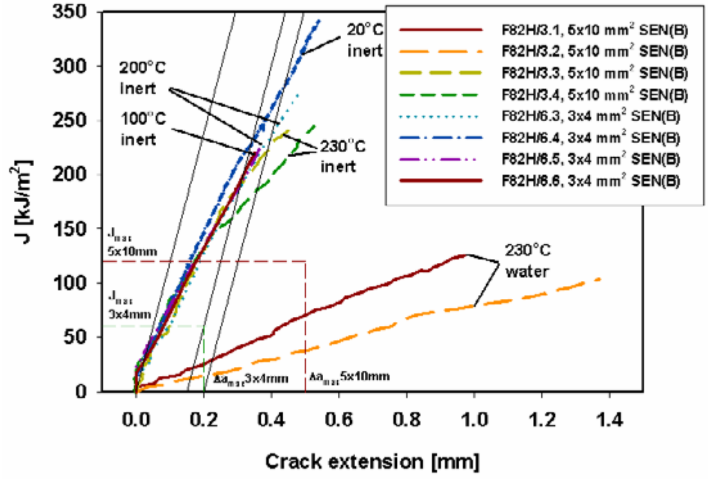

Figure 81. J-R-curves showing the influence of high temperature water on the fracture resistance of F82H steel. No clear specimen size effect can be seen in ductile tearing, even though the maximum crack extension and J limits of ASTM E 1820–99 are exceeded. The specimens were 3 mm x 4 mm x 27 mm and 5 mm x 10 mm x 55 mm SEN(B) specimens.

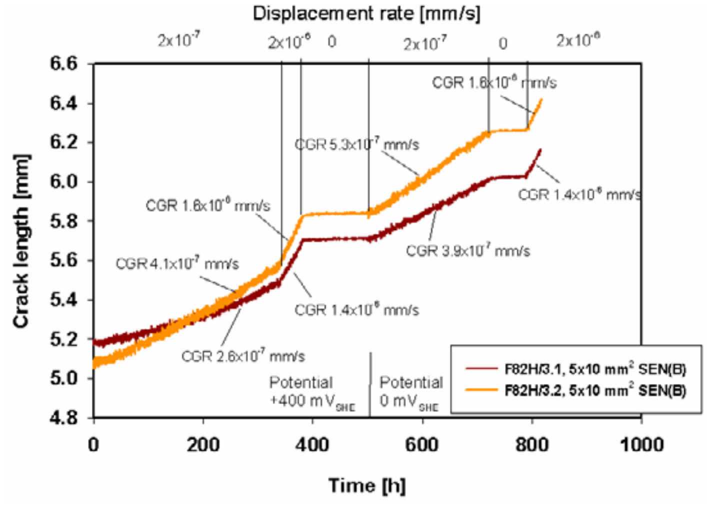

Figure 82. Crack length vs. testing time for specimens F82H/3.1 and F82H/3.2, which were tested using varying displacement rates at 230^{o}C in high temperature water containing 300 ppb O_2 and 30 ppb SO_4^{2-}. The specimens were polarized to +400 mV_{SHE} during the first half of the test and to 0 mV_{SHE} during the second half of the test.

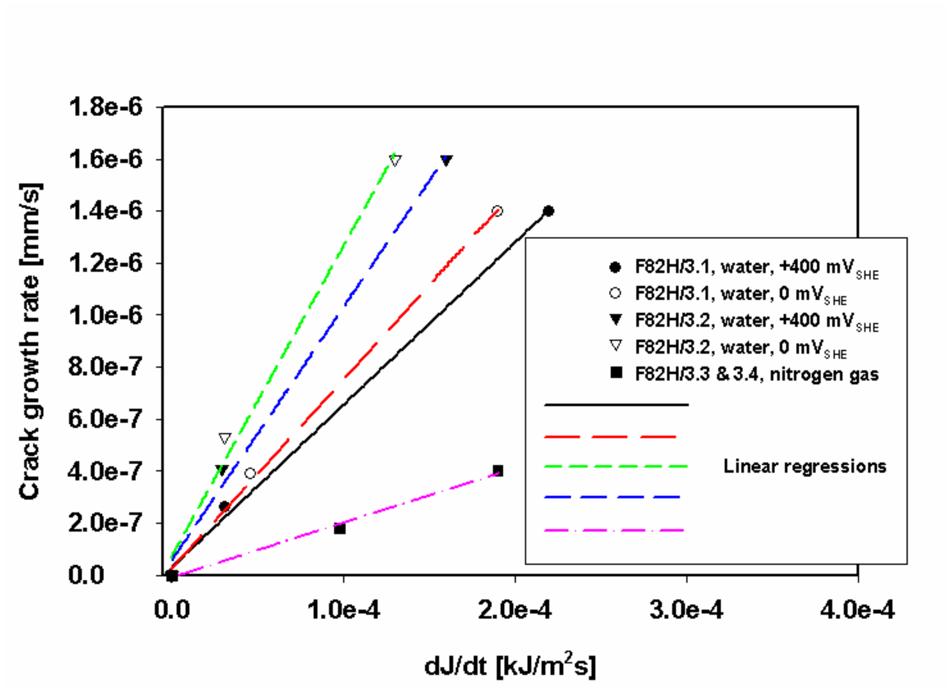

Figure 83. Effect of J-integral increase rate, dJ/dt, on the crack growth rate of ferritic F82H steel at 230°C in water at the corrosion potentials of 0 and +400 mV$_{SHE}$ and in nitrogen gas atmosphere. The specimens were 5 mm x 10 mm x 55 mm SEN(B) specimens. The corrosion potential in the high temperature water was controlled using a potentiostat.

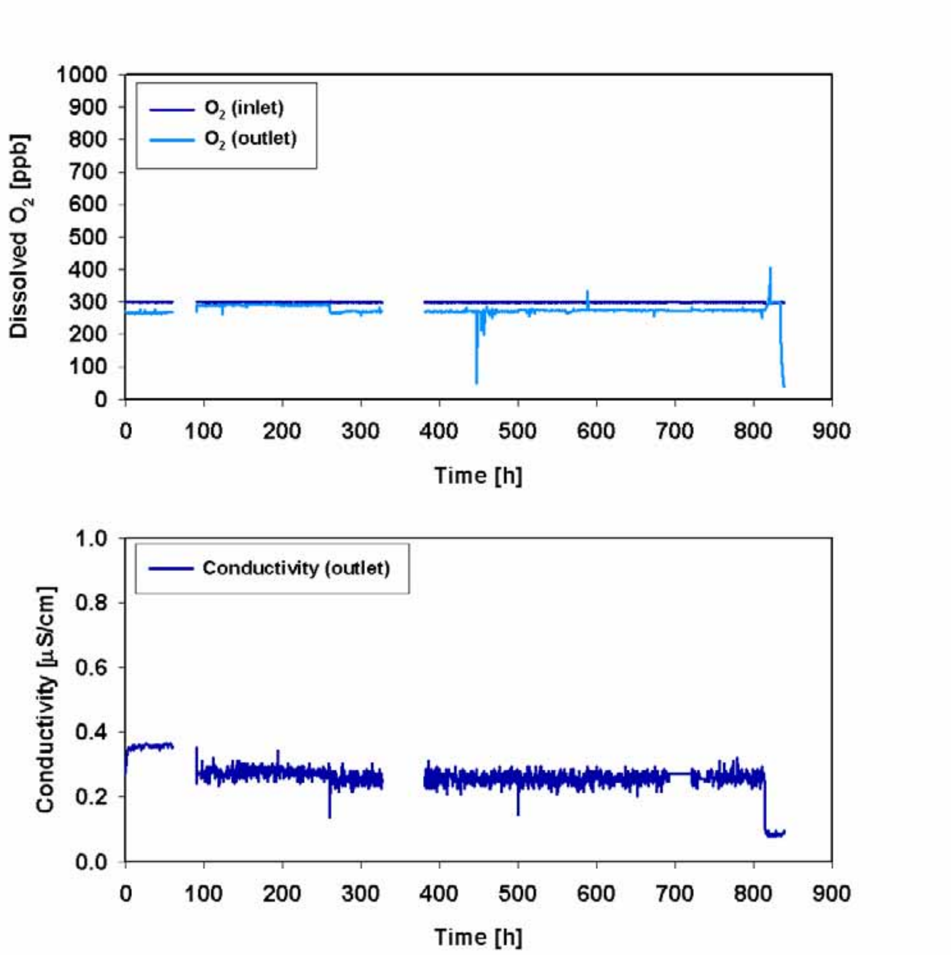

Figure 84. Water chemistry parameters during the tests performed on ferritic F82H steel. The specimens were 5 mm x 10 mm x 55 mm SEN(B) specimens (specimens F82H/3.2 and F82H/3.2). The specimens were tested simultaneously in high temperature water at 230°C in separate autoclaves. The corrosion potentials of the specimens were +400 mV_{SHE} during the first half and 0 mV_{SHE} during the second half of the test (under potentiostatic control). The conductivity was increased by injecting 30 ppb SO_4^{2-} to the autoclave feed water (injected as H_2SO_4).

4.5 Effect of BWR water sulphate concentration on SCC crack growth rate

4.5.1 Test series 1

The load vs. load line displacement curves of the first test series are presented in Figure 85. The tests were started by pre-loading the specimens using the displacement rate of 2 x 10^{-7} mm/s. After pre-loading, the tests were continued using the displacement rate of 2 x 10^{-8} mm/s. Crack growth rate measurement was started in pure water, after which three different sulphate levels were added into the inlet water. The load starts to decrease quickly after the sulphate intrusion. When the sulphate intrusion is finished, the load decrease rate begins to slow down immediately.

The crack extension measured by PD and calculated using the closed form expression remained below the real crack extension due to the uneven crack growth leaving uncracked ligaments behind the crack tip in Inconel 182 weld metal. The PD data was linearly corrected to average real crack extension measured on the fracture surface of each specimen. The linearly corrected PD data could not be used for the calculation of J-integral because of the uncracked ligaments behind the crack tip. An effective crack length was determined by forcing the normalized load vs. load line displacement curves to follow power law. However, the effective crack length was not as sensitive to the effects of sulphate in the end of the tests as PD data. For this reason, the crack lengths presented in the following are the crack lengths measured using PD (and linearly corrected), although the J calculations and load normalizations were performed using the effective crack lengths. This problem was observed only with Inconel 182 weld metal specimens.

The normalized load vs. load line displacement curves are presented in Figure 86. All the curves do not follow the same material dependent paths. The reason for this is not necessarily an error in the determined effective crack length. The different paths may be related to an nonhomogeneous microstructure in the weld metal. This can be seen in the normalized curves of the Inconel 82 weld metal specimens in Figure 86. The curves do not follow the same path even though no crack growth was observed, not using PD nor in the post-test fracture surface investigations. In addition to the nonhomogeneous microstructure, the reason for the different behaviour may be related to specimen orientation, different thermal history due to welding in different locations of the weld or an error in the displacement or load measurement.

The J-R curves of the first test series are presented in Figure 87. The effects of sulphate can be seen also in the slopes of the J-R curves of Inconel 182 weld metal specimens.

The crack growth rates obtained during the tests are presented in Figure 88. The outlet water conductivity is also shown. The lowest crack growth rates were measured in pure water prior to the first sulphate transient. Injection of a small amount of sulphate, producing a minor increase in the conductivity of the outlet water, affected the measured crack growth rate considerably. The increase in the crack growth rate was most pronounced due to the first impurity transients, when the sulphate content of the water was increased to 10 ppb in the beginning of the test. However, the crack growth rate enhancement caused by small additions of sulphate later during the test are also clearly detectable.

The effect of increased sulphate concentration on the crack growth rate became visible after a 25–45 h incubation period. Purification of the water started to decrease the crack growth rate immediately, but the decrease took place slowly and at least several hundred hours were needed to reduce the crack growth rate to the level where it was before the first sulphate transient in the case of Inconel 182 weld metal. The effect of the sulphate transient on the crack growth rate of cold-worked AISI 316 steel was not as pronounced as of Inconel 182 weld metal, but the incubation periods were similar. No crack growth was observed in Inconel 82 weld metal specimens at any of the applied sulphate levels.

Water chemistry parameters for the first test series are shown in Figure 89. Typical initial corrosion and redox potential values prior to the first sulphate transient were +100 mV_{SHE} and +275 mV_{SHE}, respectively (redox potential not shown in Figure 89), and the measured conductivity was ~ 0.1 μS/cm. When the first sulphate transient, 10 ppb, was introduced, an immediate increase in the conductivity, up to 0.18 μS/cm, was observed, and the corrosion potential of the specimens decreased about 50 mV. During the following water purification period, after the sulphate injection was interrupted, the conductivity decreased back to ~0.1 μS/cm level, and the corrosion potential increased to a level corresponding to the initial pure water condition. No changes in redox potential, measured using a Pt electrode, resulting from the sulphate transients were observed. The changes in corrosion potential and in conductivity were reproducible, when subsequent increased sulphate concentrations were applied.

The fracture surfaces of Inconel 182 weld metal specimens showed typically irregular crack fronts already after pre-fatigue in air, Figure 90. In the autoclave during the rising displacement tests the cracks continued to propagate unevenly, leaving uncracked ligaments behind the crack tip. The fracture morphology of Inconel 182 weld metal was interdendritic, Figure 91. In the cold-worked AISI 316 steel, the fracture morphology was intergranular, Figure 92.

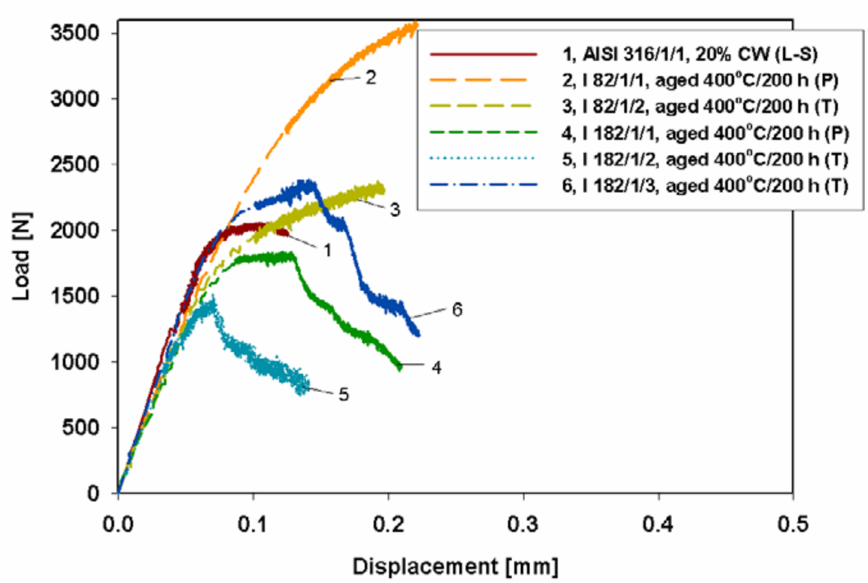

Figure 85. Load vs. load line displacement curves of test series 1. The specimens were tested simultaneously in the same autoclave in simulated BWR water with 0–100 ppb SO_4^{2-}. T = 273°C, conductivity (outlet) = 0.1–0.9 µS/cm, dissolved O_2 (outlet) = 300 ppb, ECP = 50–150 mV_{SHE} (lowest in water with 100 ppb SO_4^{2-} and highest in pure water). P and T in the legends of Inconel 82 and 182 weld metals indicate orientation: P = crack plane parallel and T = transverse to the weld pass direction.

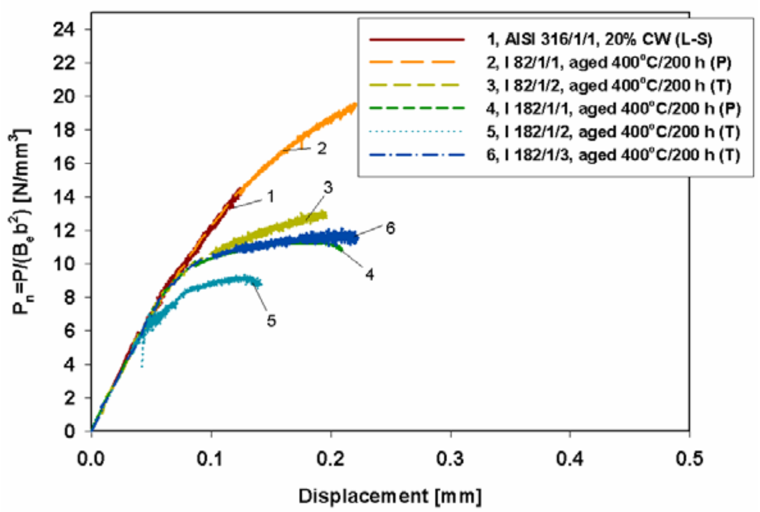

Figure 86. Normalized load-displacement curves of test series 1 (P = load, B_e = effective thickness, b = remaining ligament). The tests were performed in simulated BWR water with 0–100 ppb SO_4^{2-}. T = 273°C, conductivity (outlet) = 0.–0.9 μS/cm, dissolved O_2 (outlet) = 300 ppb, ECP = 50–150 mV_{SHE}. P = crack plane parallel and T = transverse to the weld pass direction.

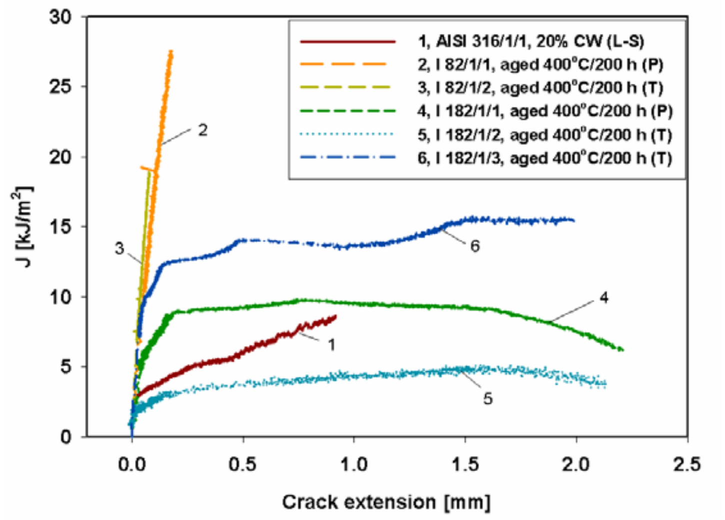

Figure 87. J-R curves of test series 1. The tests were performed in simulated BWR water with 0–100 ppb SO_4^{2-}. T = 273°C, conductivity (outlet) = 0.1–0.9 μS/cm, dissolved O_2 (outlet) = 300 ppb, ECP = 50–150 mV_{SHE}. P = crack plane parallel and T = transverse to the weld pass direction.

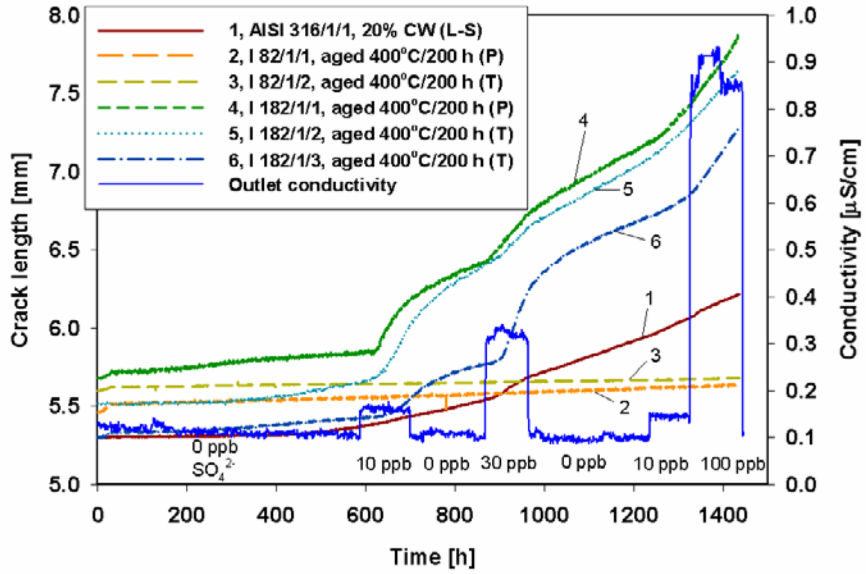

Figure 88. Crack length vs. testing time curves of test series 1 (crack lengths measured using PD and linearly corrected to the crack lengths observed on the fracture surfaces). Outlet conductivity and the applied sulphate concentrations of the water are also shown. The tests were performed in simulated BWR water with 0–100 ppb SO_4^{2-}. T = 273°C, conductivity (outlet) = 0.1–0.9 µS/cm, dissolved O_2 (outlet) = 300 ppb, ECP = 50–150 mV_{SHE}. P = crack plane parallel and T = transverse to the weld pass direction.

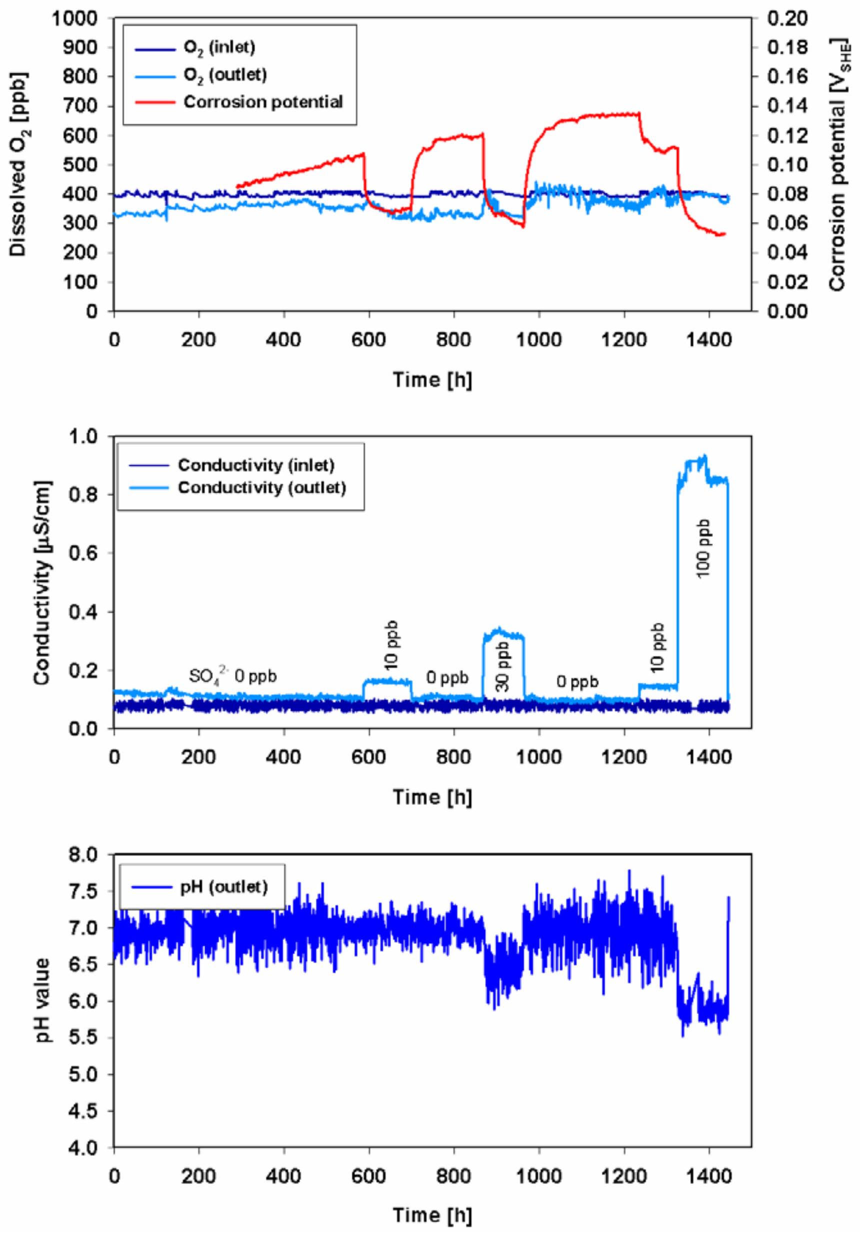

Figure 89. Water chemistry parameters during test series 1. The tests were performed in simulated BWR water with 0–100 ppb SO_4^{2-}*. T = 273°C, conductivity (outlet) = 0.1–0.9 µS/cm, dissolved* O_2 *(outlet) = 300 ppb, ECP = 50–150* mV_{SHE} *(depended on the sulphate concentration of the water).*

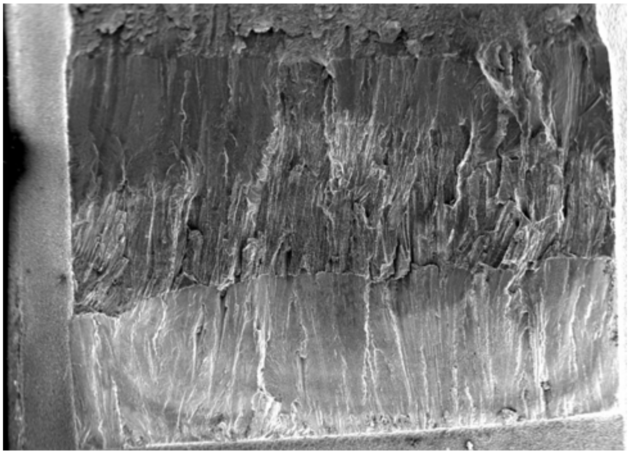

Figure 90. A photograph showing a typical fracture surface of an Inconel 182 weld metal specimen tested in simulated BWR water at 273°C with 0–100 ppb SO_4^{2-}*. From bottom to top: notch, pre-fatigue, stress corrosion cracking, post-test fatigue and final ductile fracture formed when the specimen was broken open.*

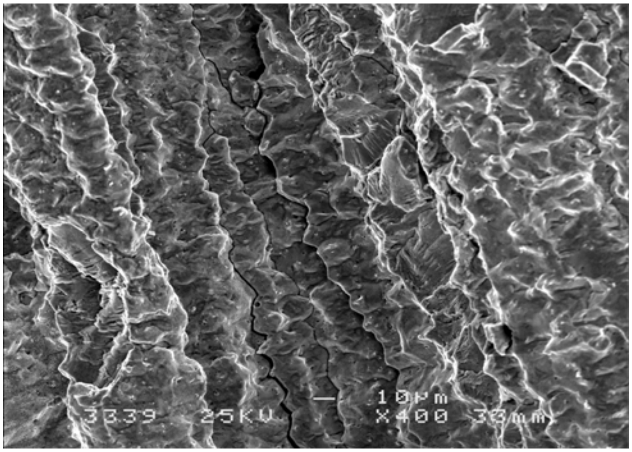

Figure 91. A photograph showing typical interdendritic stress corrosion cracking on the fracture surface of an Inconel 182 weld metal specimen tested in simulated BWR water with 0–100 ppb SO_4^{2-}*. T = 273°C, conductivity (outlet) = 0.1–0.9 µS/cm, dissolved* O_2 *(outlet) = 300 ppb, ECP = 50–150* mV_{SHE}*.*

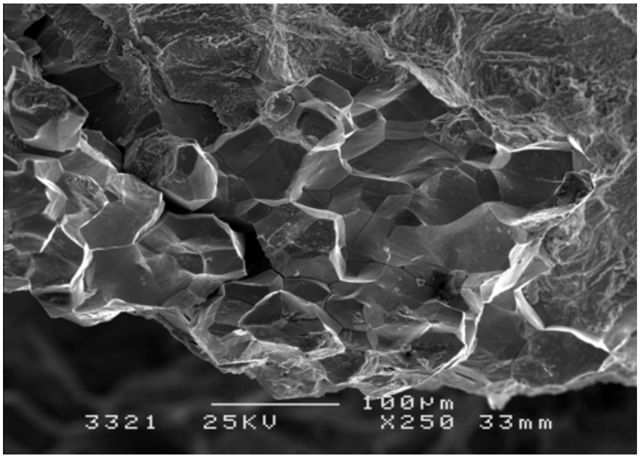

Figure 92. Intergranular stress corrosion cracking on the fracture surface of the cold-worked AISI 316 steel specimen after the test in simulated BWR water with 0–100 ppb SO_4^{2-}*. T = 273°C, conductivity (outlet) = 0.1–0.9 µS/cm, dissolved* O_2 *(outlet) = 300 ppb, ECP = 50–150* mV_{SHE}*.*

4.5.2 Test series 2

Two Inconel 82 and two 182 weld metal specimens were tested in pure water in simulated BWR water. One of each weld metal specimens was in as-welded condition. The other specimens were in thermally aged condition (annealed at 400°C for 200 h). The tests were started using the displacement rate of 2×10^{-7} mm/s and afterwards it was decreased to 2×10^{-8} mm/s for the crack growth rate measurement. One emphasis of this test series was to compare the crack growth rates measured under rising displacement and constant displacement type loading conditions. This is why the final 180 h of the test series was conducted using constant displacement type loading.

The load vs. load line displacement curves of test series 2 are presented in Figure 93, and in the normalized form in Figure 94. One of the normalized curves deviates from the other three. The curves were normalized using the crack lengths measured using PD without any corrections. The crack lengths measured using PD fit well to the physical crack lengths measured on the fracture surfaces. The differences between the normalized load vs. load line displacement curves result from different material properties. The PD measurements resulted in correct crack lengths without any corrections because of small crack extensions during the tests, i.e., there were no uncracked ligaments far behind the crack tip.

The J-R curves and crack lengths vs. testing time are presented in Figures 95 and 96. It is notable that crack growth occurred in one of the Inconel 82 weld metal specimens (in as-welded condition). This was the only Inconel 82 specimen in which crack growth was observed. However, the fracture morphology was 100% transgranular. It is suspected that there was a problem in the displacement control during the test, which may have resulted in high frequency fatigue of the specimen. The fracture surface morphologies of the Inconel 182 weld metal specimens tested in this test series were interdendritic. The water chemistry parameters during the test series are presented in Figure 97.

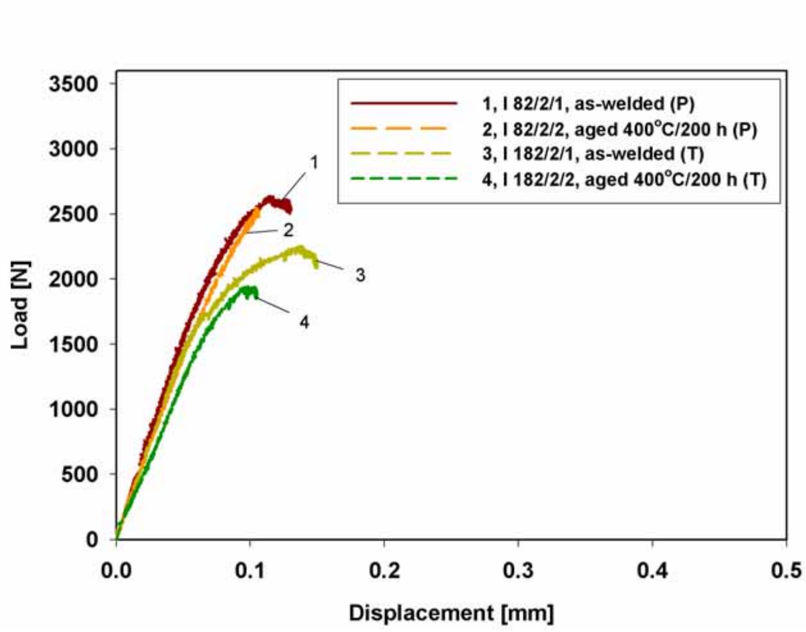

Figure 93. Load vs. load line displacement curves of test series 2. The tests were performed in simulated pure BWR water. T = 273°C, conductivity (outlet) = 0.1 μS/cm, dissolved O_2 (outlet) = 300 ppb, ECP = 110 mV_{SHE}. P = crack plane parallel and T = transverse to the weld pass direction.

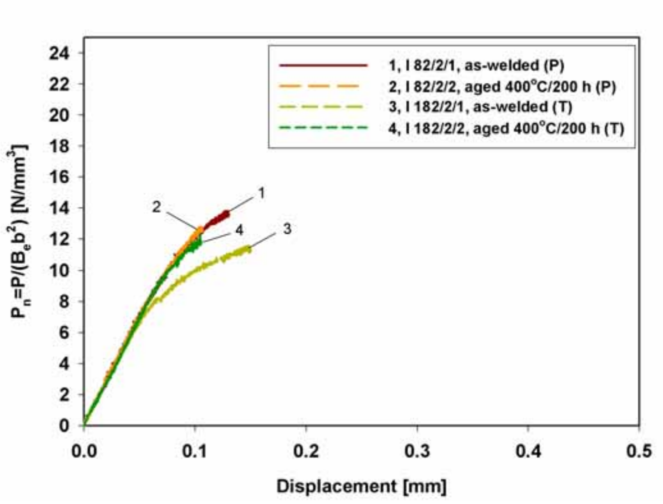

Figure 94. Normalized load-displacement curves of test series 2 (P = load, B_e = effective thickness, b = remaining ligament). The tests were performed in simulated pure BWR water. T = 273^{o}C, conductivity (outlet) = 0.1 μS/cm, dissolved O_2 (outlet) = 300 ppb, ECP = 110 mV_{SHE}. P = crack plane parallel and T = transverse to the weld pass direction.

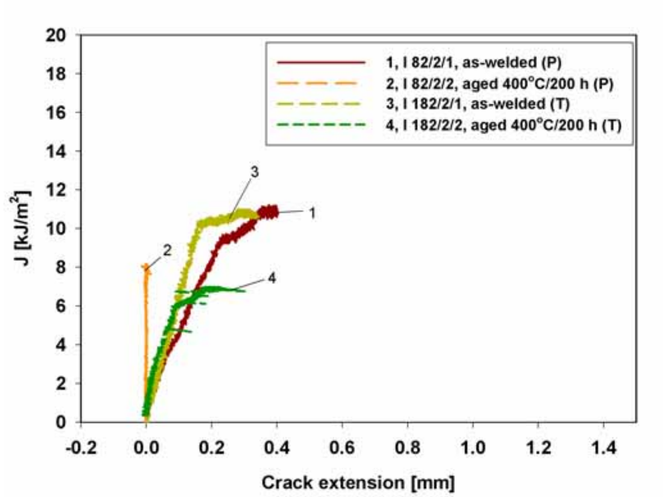

Figure 95. J-R curves of test series 2. Crack growth initiated in a very early stage in other specimens except in specimen I 82/2/2 (curve 2). The tests were performed in simulated pure BWR water. T = 273^{o}C, conductivity (outlet) = 0.1 μS/cm, dissolved O_2 (outlet) = 300 ppb, ECP = 110 mV_{SHE}. P = crack plane parallel and T = transverse to the weld pass direction.

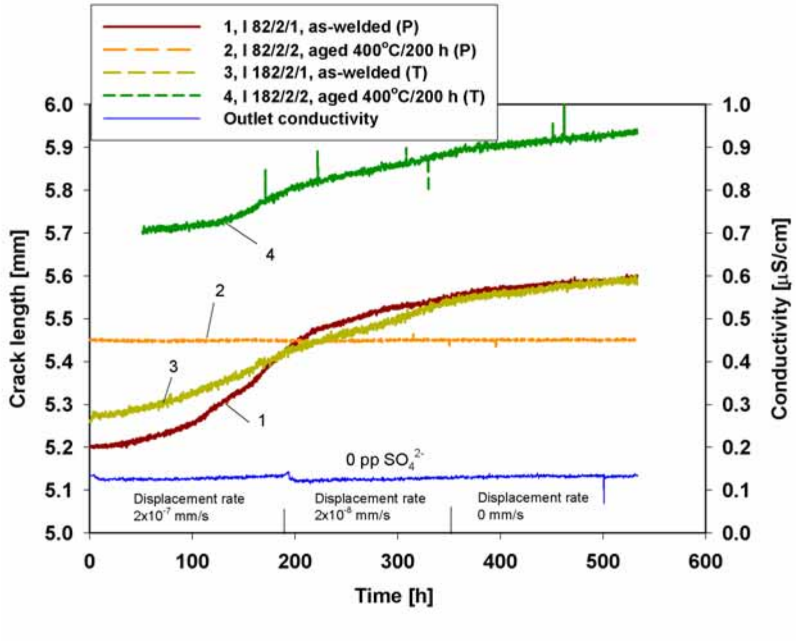

Figure 96. Crack length vs testing time curves of test series 2. Outlet conductivity of the water and the applied displacement rates are also shown. The tests were performed in simulated pure BWR water. T = 273°C, conductivity (outlet) = 0.1 µS/cm, dissolved O_2 (outlet) = 300 ppb, ECP = 110 mV_{SHE}. P = crack plane parallel and T = transverse to the weld pass direction.

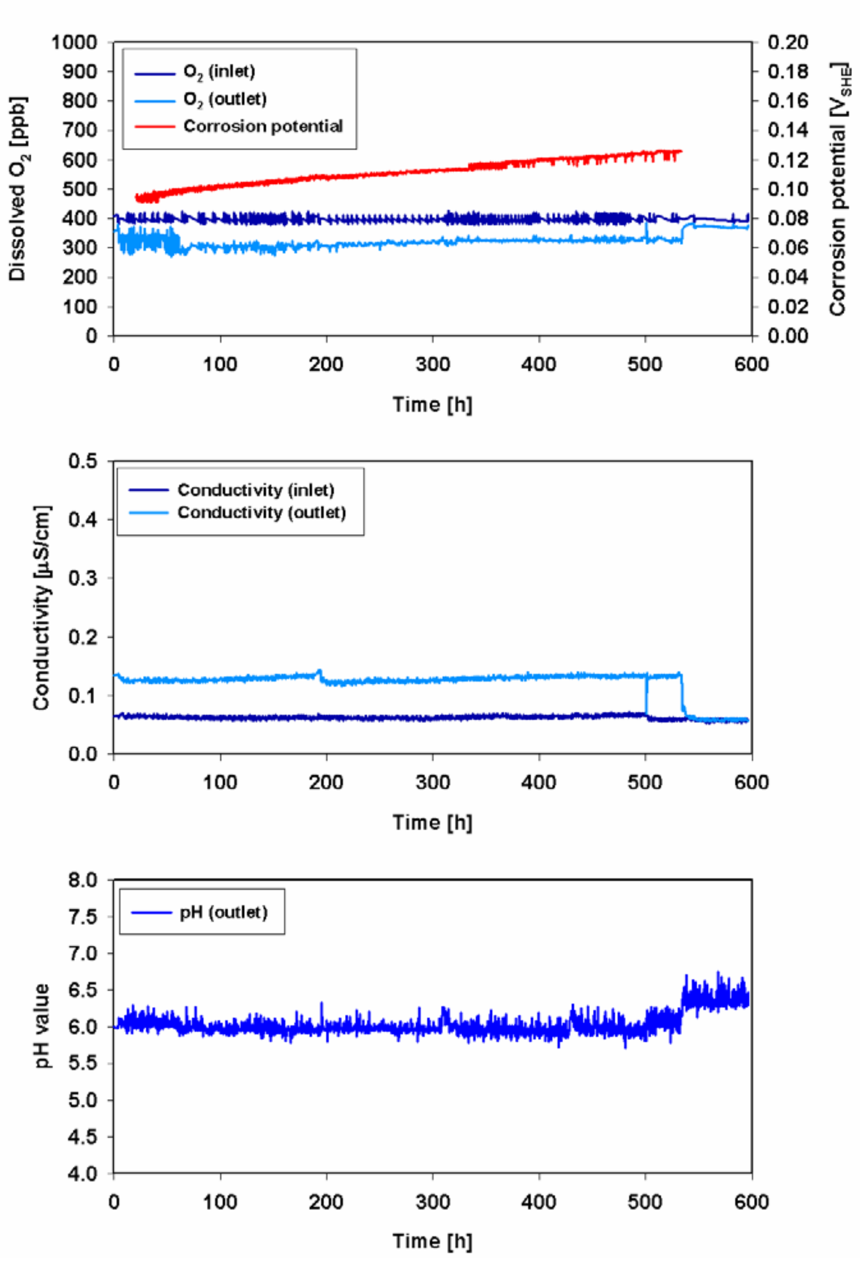

Figure 97. Water chemistry parameters during test series 2. The tests were performed in simulated pure BWR water. T = 273°C, conductivity (outlet) = 0.1 µS/cm, dissolved O_2 (outlet) = 300 ppb, ECP = 110 mV_{SHE} (average). The decrease in the outlet conductivity resulted from temperature decrease after the test.

4.5.3 Test series 3

The tests of the test series 3 were started using the displacement rate of $2x10^{-7}$ mm/s in pure water. The emphasis of this test was to produce more data points measured under constant displacement type loading conditions in pure water and with increased sulphate concentration. The displacement rate was decreased to 0 mm/s soon after the crack growth had initiated in Inconel 182 weld metal specimens. After the crack growth rates under static loading were determined in pure water, 30 ppb sulphate was added into the inlet water. The specimens were of the same materials as in test series 2, i.e., 2 Inconel 82 and 2 Inconel 182 weld metal specimens.

The effect of the sulphate addition can be seen in the load vs. load line displacement curves of the Inconel 182 weld metal specimens as a decrease in the load, Figure 98. Effective crack lengths had to be used when the normalized load vs. load line displacement curves, Figure 99, and J-R curves, Figure 100, of Inconel 182 weld metal specimens were calculated. However, all the crack lengths presented here are measured using PD and corrected linearly to the crack lengths measured on the fracture surfaces.

The crack lengths are presented in Figure 101 as a function of testing time. As can be seen, the crack growth rate clearly decreased in Inconel 182 specimens when the displacement rate was decreased to 0 mm/s in pure water. A remarkable increase in the crack growth rate was observed ~20 h after 30 ppb sulphate was added into the inlet water.

The water chemistry parameters are presented in Figure 102. A similar change in the corrosion potential caused by the sulphate addition was observed as in test series 1.

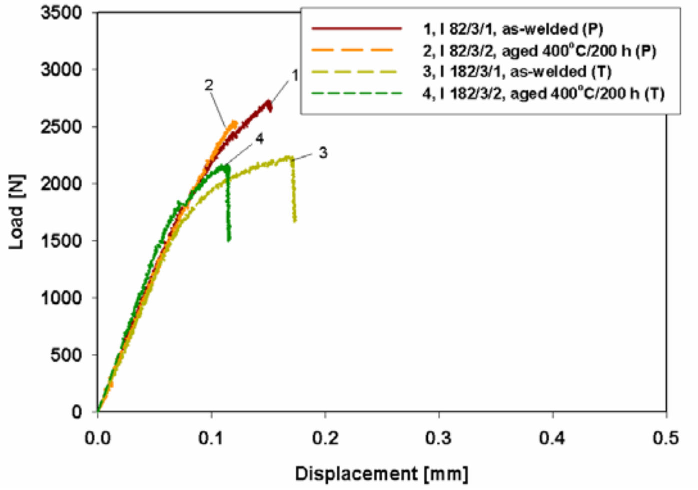

Figure 98. Load vs. load line displacement curves of test series 3. The specimens were tested simultaneously in the same autoclave in simulated BWR water with 0–30 ppb SO_4^{2-}. T = 273°C, conductivity (outlet) = 0.1–0.3 µS/cm, dissolved O_2 (outlet) = 300 ppb, ECP = 90–150 mV_{SHE} (lowest in water with 30 ppb SO_4^{2-} and highest in pure water). P = crack plane parallel and T = transverse to the weld pass direction.

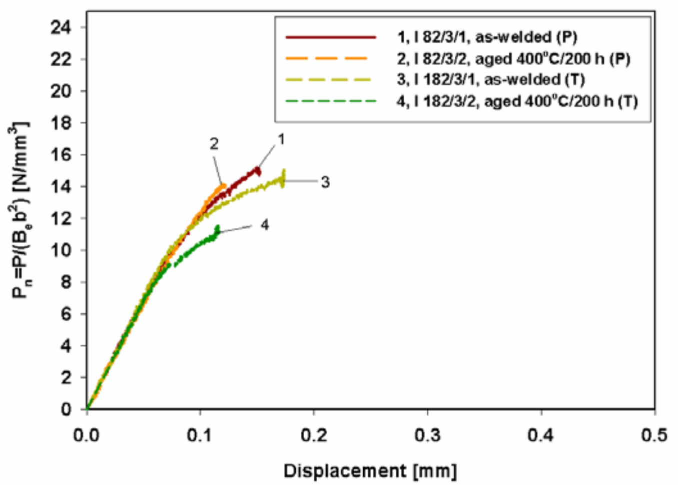

Figure 99. Normalized load vs. load line displacement curves of test series 3 (P = load, B_e = effective thickness, b = remaining ligament). The tests were performed in simulated BWR water with 0–30 ppb SO_4^{2-}. T = 273°C, conductivity (outlet) = 0.1–0.3 µS/cm, dissolved O_2 (outlet) = 300 ppb, ECP = 90–150 mV_{SHE}. P = crack plane parallel and T = transverse to the weld pass direction.

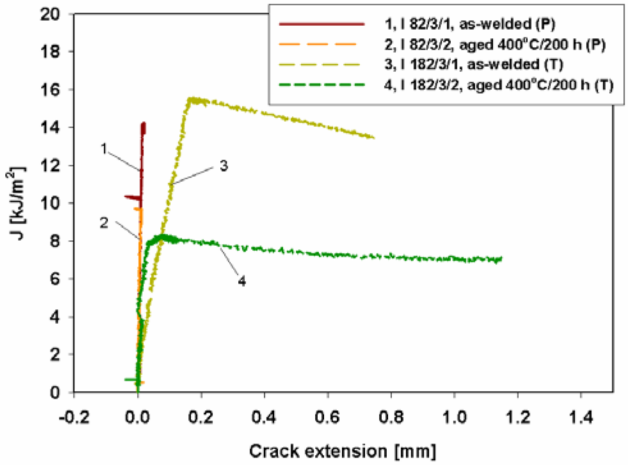

Figure 100. J-R curves of test series 3. The tests were performed in simulated BWR water with 0–30 ppb SO_4^{2-}. T = 273°C, conductivity (outlet) = 0.1–0.3 µS/cm, dissolved O_2 (outlet) = 300 ppb, ECP = 90–150 mV_{SHE}. P = crack plane parallel and T = transverse to the weld pass direction.

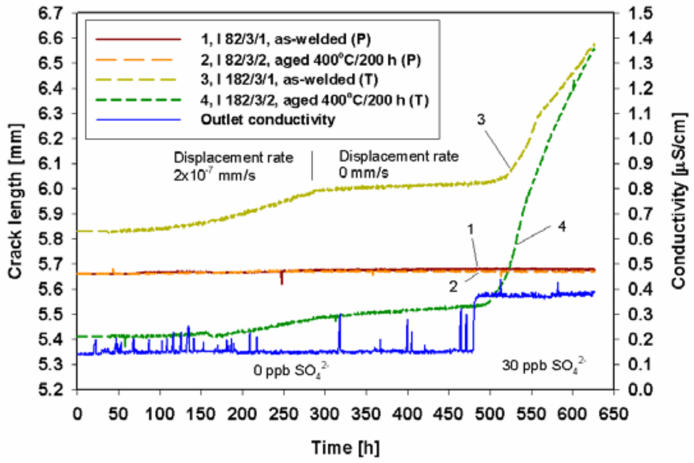

Figure 101. Crack length vs. testing time curves of test series 3 (crack lengths measured using PD and linearly corrected to the crack lengths observed on the fracture surfaces). Outlet conductivity, applied sulphate concentrations of the water and applied displacement rates are also shown. The tests were performed in simulated BWR water with 0–30 ppb SO_4^{2-}. T = 273°C, conductivity (outlet) = 0.1–0.3 µS/cm, dissolved O_2 (outlet) = 300 ppb, ECP = 90–150 mV_{SHE}. P = crack plane parallel and T = transverse to the weld pass direction.

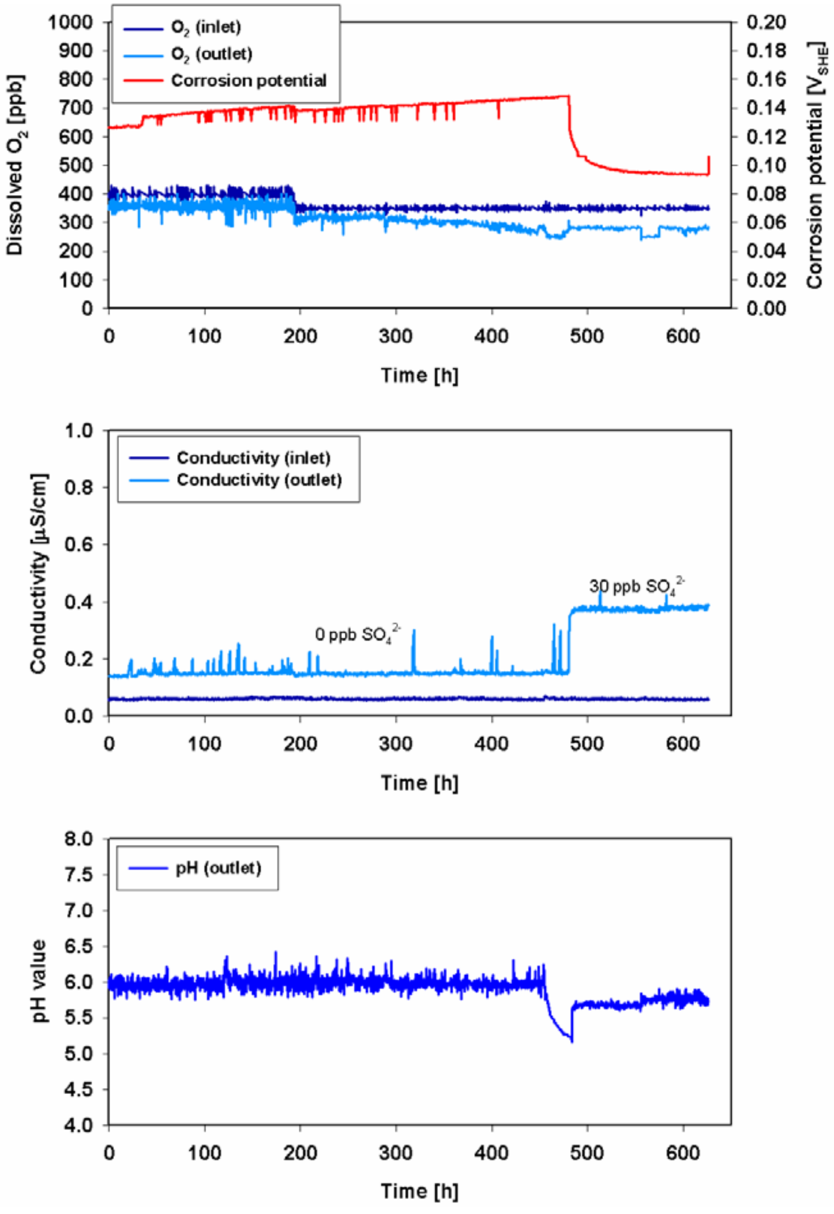

Figure 102. Water chemistry parameters during test series 3. The tests were performed in simulated BWR water with 0–30 ppb SO_4^{2-}. T = 273°C, conductivity (outlet) = 0.1–0.3 µS/cm, dissolved O_2 (outlet) = 300 ppb, ECP = 90–150 mV_{SHE} (depending on the sulphate concentration of the water).

4.5.4 Crack growth rates as a function of K_J and dJ/dt

All data of the three test series on AISI 316 steel and Inconel 82 and 182 weld metal specimens have been collected to material specific crack growth rate vs. K_J plots and crack growth rate vs. dJ/dt plots. The results are presented in Figures 103–108.

The crack growth rate of AISI 316 steel in BWR water with 10 ppb sulphate was about twice as high as that in pure water. In BWR water with 30 and 100 ppb sulphate, the crack growth rates were even higher, Figure 103. For some reason, the crack growth rate was lower in BWR water with 100 ppb than with 30 ppb sulphate. However, the effects of the sulphate concentration of BWR water and K_J-level on the crack growth rate can not be clearly compared because K_J was higher at higher sulphate concentration levels. The crack growth rates were only measured under rising displacement conditions. The crack growth rates of AISI 316 steel are presented in Figure 104 as a function of J-integral increase rate, dJ/dt. The available few data points do not support any conclusions for the relation between the crack growth rate and dJ/dt or K_J.

In Inconel 82 weld metal specimens, crack growth was observed only in one specimen. The crack growth rate appears to be inversely dependent on K_J-level, Figure 105. On the other hand, the crack growth rate is directly dependent on the J-integral increase rate, Figure 106, which is the expected behaviour. However, based on the fracture surface morphology, which was transgranular stress corrosion cracking, there was probably a considerable fatigue component present in the loading. The crack growth rates measured on this specimen can not be considered representative for this material–environment combination.

Crack growth was observed in all Inconel 182 weld metal specimens. The lowest crack growth rates were measured in pure BWR water under constant displacement type loading conditions, Figure 107. On the average, the crack growth rates were two or three times higher under rising displacement. When 10–100 ppb sulphate was present in the test environment, the crack growth rates were about one order of magnitude higher than those in pure water. No clear differences can be seen between the crack growth rates measured in BWR water with 10 ppb sulphate or more. When sulphate was present, the crack growth rates were in the same range regardless of the loading mode, rising or constant displacement. The crack growth rates appear to be independent on the K_J-level. Most of the crack growth rates are below the Swedish disposition line for the same material and for normal BWR water chemistry at 288°C, which is also shown in Figure 107 for reference purpose. The measured crack growth rates are presented in Figure 108 as a function of dJ/dt. In pure BWR water, the crack growth rates increase as dJ/dt increases. On the other hand, when sulphate is present in the test environment, dJ/dt is clearly below 0 kJ/m^2s, because dJ/dt is then controlled by the high crack growth rate rather than by the applied displacement rate.

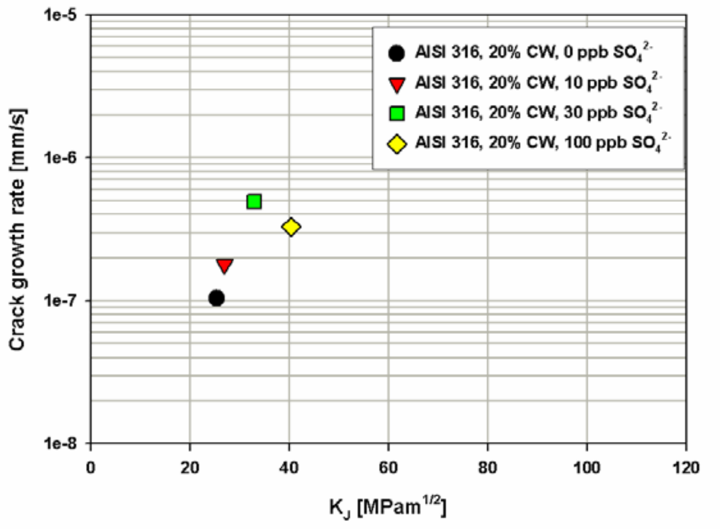

Figure 103. Crack growth rates in 20% cold-worked AISI 316 steel as a function of K_J in simulated BWR water at 0–100 ppb SO_4^{2-} concentrations. T = 273°C, conductivity (outlet) = 0.1–0.9 µS/cm, dissolved O_2 (outlet) = 300 ppb, ECP = 50–150 mV_{SHE} (ECP was lowest in water with 100 ppb SO_4^{2-} and highest in pure water).

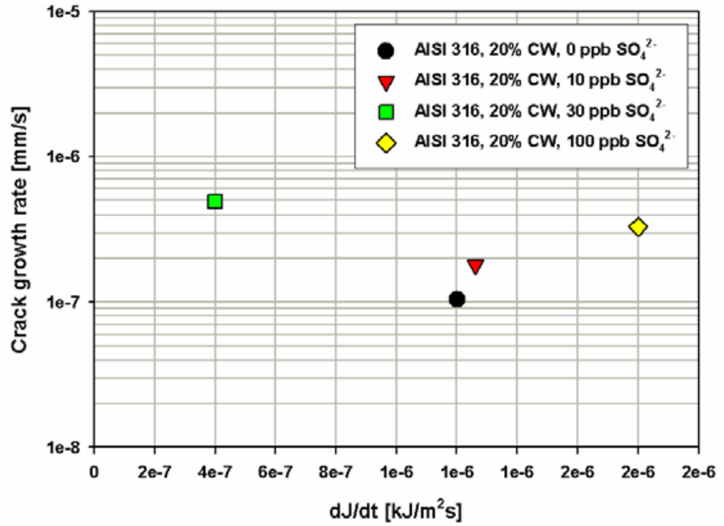

Figure 104. Crack growth rates in 20% cold-worked AISI 316 steel as a function of J-integral increase rate, dJ/dt, in simulated BWR water. T = 273^{o}C, conductivity (outlet) = 0.1–0.9 µS/cm, dissolved O_2 (outlet) = 300 ppb, ECP = 50–150 mV_{SHE}.

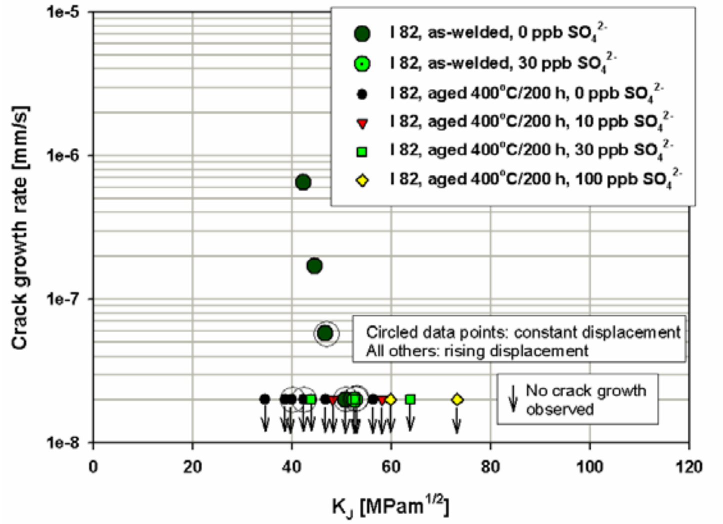

Figure 105. Crack growth rates in as-welded and thermally aged (400^{o}C/200 h) Inconel 82 weld metal as a function of K_J in simulated BWR water. T = 273^{o}C, conductivity (outlet) = 0.1–0.9 µS/cm, dissolved O_2 (outlet) = 300 ppb, ECP = 50–150 mV_{SHE}.

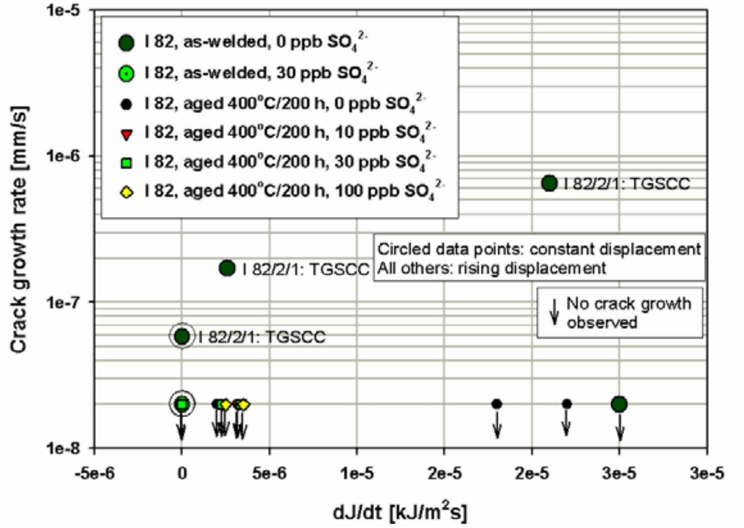

Figure 106. Crack growth rates in as-welded and in thermally aged (400^{o}C/200 h) Inconel 82 weld metal as a function of J-integral increase rate, dJ/dt, in simulated BWR water. T = 273^{o}C, conductivity (outlet) = 0.1–0.9 μS/cm, dissolved O_2 (outlet) = 300 ppb, ECP = 50–150 mV$_{SHE}$.

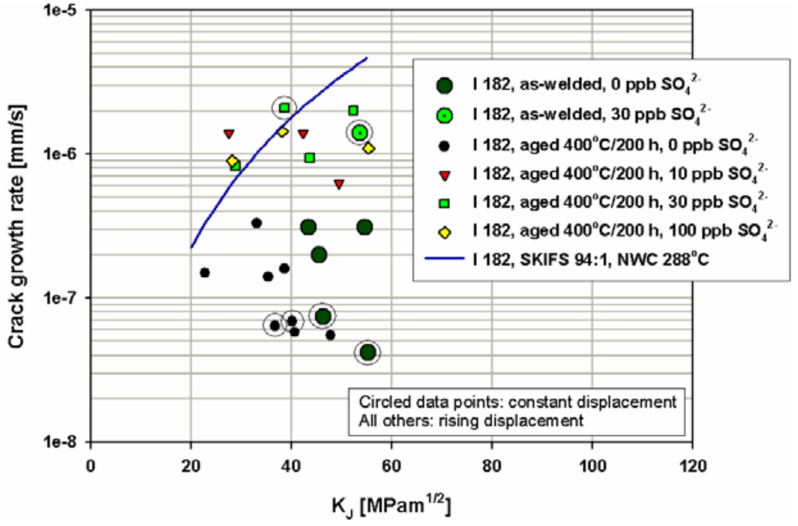

Figure 107. Crack growth rates in as-welded and in thermally aged (400^{o}C/200 h) Inconel 182 weld metal as a function of K_J in simulated BWR water. T = 273^{o}C, conductivity (outlet) = 0.1–0.9 μS/cm, dissolved O_2 (outlet) = 300 ppb, ECP = 50–150 mV$_{SHE}$. The Swedish disposition line for the same material and for normal BWR water chemistry at 288^{o}C is also shown.

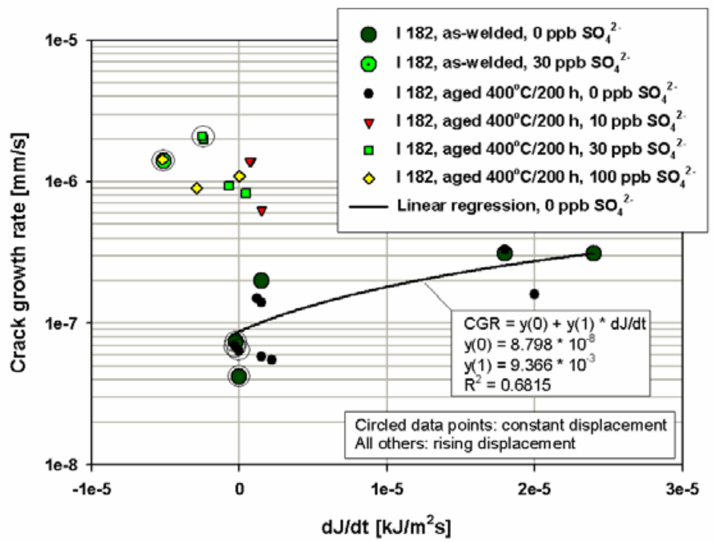

Figure 108. Crack growth rates in as-welded and in thermally aged (400°C/200 h) Inconel 182 weld metal as a function of J-integral increase rate, dJ/dt, in simulated BWR water. T = 273°C, conductivity (outlet) = 0.1–0.9 μS/cm, dissolved O$_2$ (outlet) = 300 ppb, ECP = 50–150 mV$_{SHE}$. Linear regression for the dependency between the crack growth rate and dJ/dt in pure BWR water is also shown (CGR = crack growth rate). The linear regression is seen as curved because the crack growth rate is shown in the logarithmic scale.

4.6 Comparison of SCC crack growth rates of sensitized AISI 304 steel using 10 mm SEN(B) and 25 mm C(T) specimens

4.6.1 SEN(B) specimens

The displacement vs. testing time, load vs. load line displacement and normalized load vs. load line displacement of the tests are presented in Figs 109–111. The combined effects of the displacement rate changes and crack growth rates can be seen in the load vs. load line displacement curves of the specimens as relatively sudden changes in the slopes. On the other hand, the load vs. load line displacement curves normalized by the size of the remaining ligament should follow the same curve. The curve of specimen No. 4 deviates from the curves of the other specimens. The normalized load should also increase with the increasing displacement because of strain hardening in the remaining ligament. However, at the displacements above 0.1 mm the curve of specimen No. 5 is decreasing.

The J-R curves of the tests are presented in Figure 112. The curves of specimens No. 1 and 2 show that the J-level remains constant when the displacement rate was 5x10^{-9} mm/s and it begins to decrease when the loading was changed to constant displacement. The decrease in the J-level under constant displacement can also be seen in the J-R curve of specimen No. 4. When the displacement rates were equal or higher than 2.5 x 10^{-8} mm/s, the J-R curves show increasing J-levels.

At the two lowest displacement rates (specimens No. 1 and 2), it would have taken several months to reach a reasonable K_J-level if the loading had been started from the zero load. The specimens were pre-loaded to the load level of 600 N in the beginning of the tests. However, there were no indications that the crack growth would initiate in these two specimens at this load level. After the first 200 h loading under constant displacement rate, the specimens were further loaded to 1000 N (K_J-level of ~15 MPa√m) and the tests were continued using the displacement rate of 5 x 10^{-9} mm/s. After 100–200 h under the increased loading, the crack growth initiated. About 770 h after the test had started, the loading mode was changed to constant displacement. Just before the loading mode was changed, the crack growth rates were 3.4 x 10^{-7} and 2.8 x 10^{-7} mm/s in specimens No. 1 and 2, respectively, Figure 113. Under constant displacement, the crack growth rates were 1.5 x 10^{-7} and 1.9 x 10^{-7} mm/s. SEM investigation showed that the cracking was intergranular stress corrosion cracking (IGSCC), Figs 114–116.

A nominal pre-loading (~100 N) was applied to specimen No. 3 after which the test was continued using the displacement rate of 2.5 x 10^{-8} mm/s until disturbances in the displacement control prevented further crack growth rate measurements. At this point, the measured crack growth rate was 6.1 x 10^{-7} mm/s. Post-test SEM investigation revealed that the cracking during the test was IGSCC, Figure 117.

Specimen No. 4 was pre-loaded to the same level as specimen No. 3, after which the test was continued using the displacement rate of 5 x 10^{-8} mm/s. The crack growth rate was 7.4 x 10^{-7} mm/s before the loading mode was changed to constant displacement. In the beginning of the constant displacement test phase, there were disturbances in the displacement control also in the case of this specimen. The disturbances resulted in a load decrease and also in a rapid crack length increment in specimen No. 4. However, the test was continued by introducing a short increase to the load line displacement, after which the crack continued to grow. The measured crack growth rate under constant displacement was 1.3 x 10^{-7} mm/s. The post-test SEM investigation revealed that the cracking was IGSCC, Figs 118 and 119.

Specimen No. 5 was pre-loaded similarly as specimens No. 3 an 4, after which the test was continued at first using the displacement rate of 1 x 10^{-7} mm/s, then 5 x 10^{-8} mm/s and finally 2.5 x 10^{-8} mm/s. The measured crack growth rates were 1.7 x 10^{-6}, 9.7 x 10^{-7} and 5.1 x 10^{-7} mm/s, respectively. At this point faults in the displacement control prevented further crack growth rate measurements. The post-test SEM investigation showed that the cracking was mixed IGSCC and TGSCC, Figure 120.

The water chemistry parameters and corrosion potential during the tests are presented in Figure 121. Outlet conductivity is above expected, ~0.25 µS/cm, although nothing special could be seen in the grab sample analysis, Table 27.

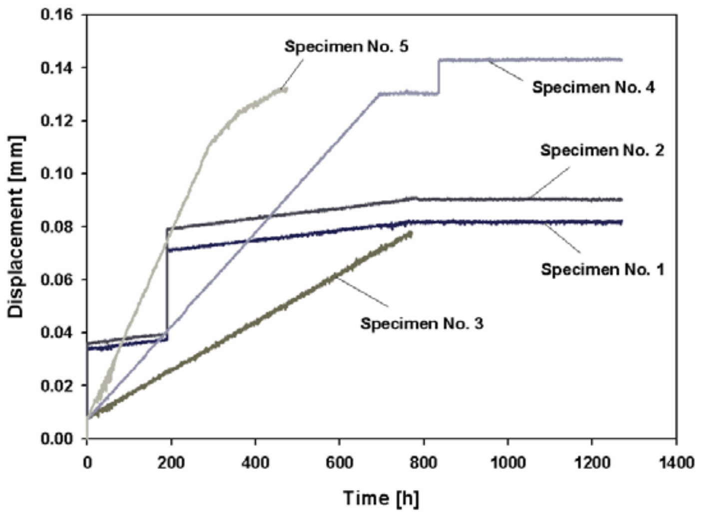

Figure 109. Load line displacements of the five tests on 10 mm sensitized AISI 304 steel SEN(B) specimens. The tests on specimens No. 3 and 4 were discontinued because of disturbances in the displacement control. Simulated BWR water, T = 290^{o}C, conductivity (outlet) = 0.25 μS/cm, dissolved O_2 (outlet) = 500 ppb, ECP = 120 mV_{SHE}.

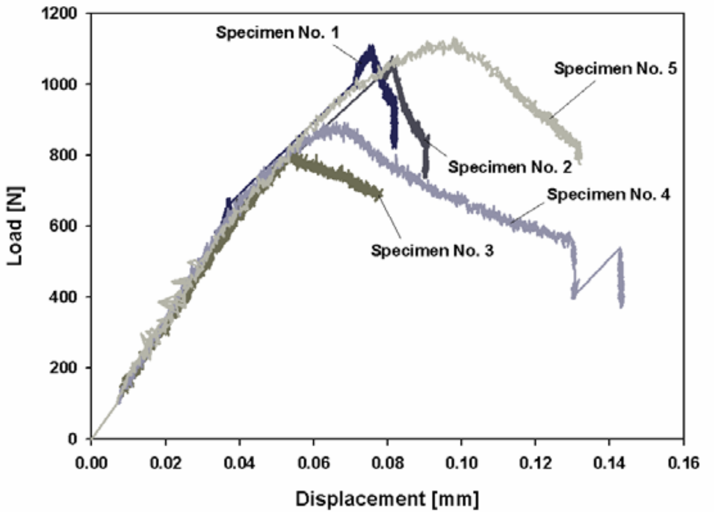

Figure 110. Load vs. load line displacement of the five tests on 10 mm sensitized AISI 304 steel SEN(B) specimens. Simulated BWR water, T = 290^{o}C, conductivity (outlet) = 0.25 μS/cm, dissolved O_2 (outlet) = 500 ppb, ECP = 120 mV_{SHE}.

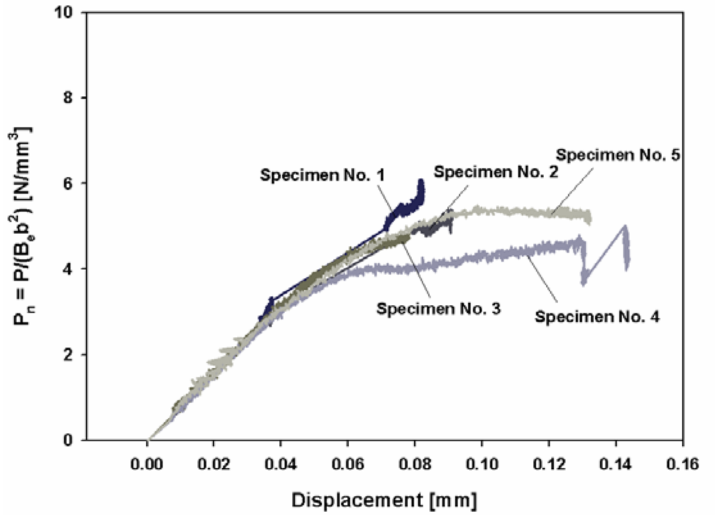

Figure 111. Normalized load vs. load line displacement of the five tests on 10 mm sensitized AISI 304 steel SEN(B) specimens. P = load, B_e = effective thickness and b = remaining ligament. Simulated BWR water, T = 290^{o}C, conductivity (outlet) = 0.25 μS/cm, dissolved O_2 (outlet) = 500 ppb, ECP = 120 mV_{SHE}.

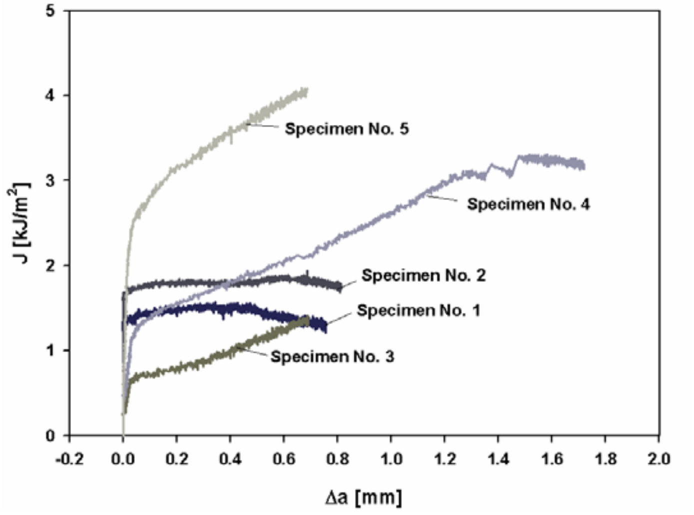

Figure 112. J vs. Δa (crack extension) curves of the five tests on 10 mm sensitized AISI 304 steel SEN(B) specimens. Simulated BWR water, T = 290^{o}C, conductivity (outlet) = 0.25 μS/cm, dissolved O_2 (outlet) = 500 ppb, ECP = 120 mV_{SHE}.

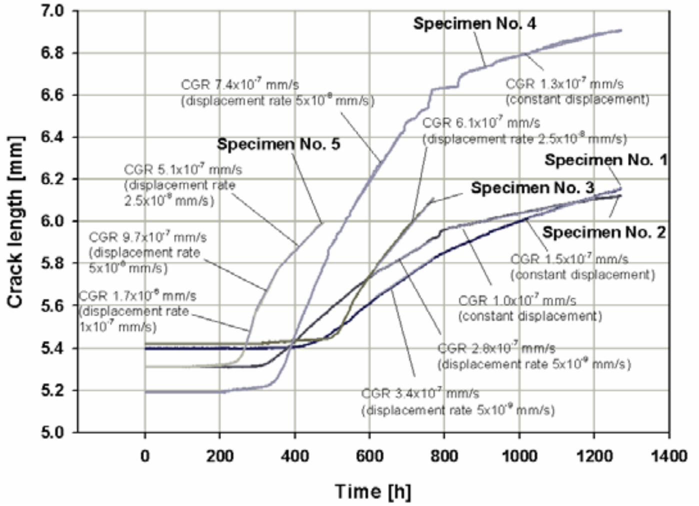

Figure 113. Crack length vs. testing time of the five tests on 10 mm sensitized AISI 304 steel SEN(B) specimens. The measured crack growth rates (CGR) with the respective applied load line displacement rates are marked into the figure. Simulated BWR water, T = 290^{o}C, conductivity (outlet) = 0.25 μS/cm, dissolved O_2 (outlet) = 500 ppb, ECP = 120 mV_{SHE}.

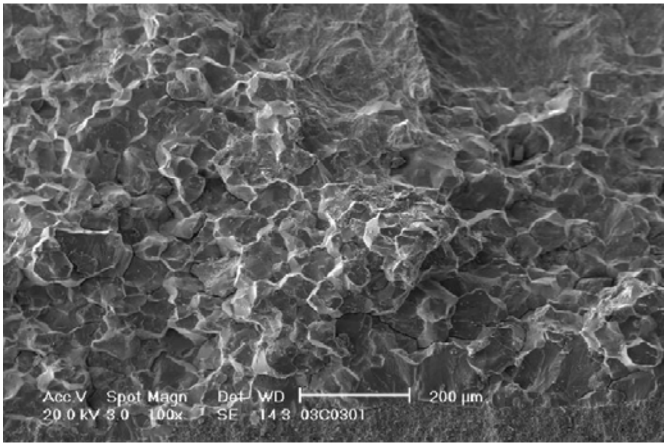

Figure 114. Fracture surface of 10 mm sensitized AISI 304 steel SEN(B) specimen No. 1. The fracture morphology is intergranular. Pre-fatigue crack tip can be seen in the bottom and the final post-test fatigue crack in the top of the photograph. Applied displacement rates: 5x10^{-9} mm/s in the beginning (after quick pre-loading) and 0 mm/s in the end of the test. Simulated BWR water, T = 290^{o}C, conductivity (outlet) = 0.25 μS/cm, dissolved O_2 (outlet) = 500 ppb, ECP = 120 mV_{SHE}.

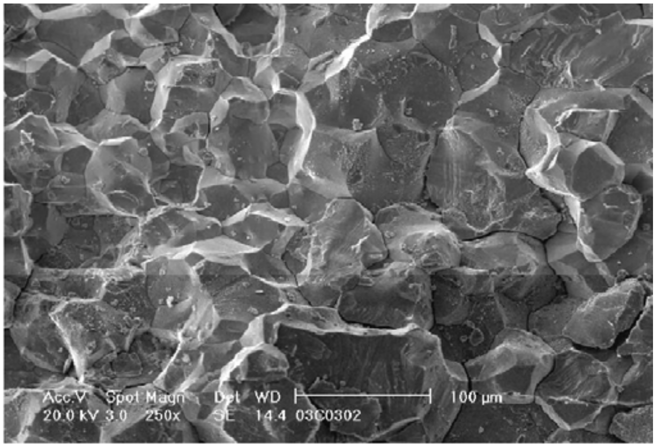

Figure 115. A higher magnification detail of the inergranular fracture surface of sensitized AISI 304 steel specimen No. 1. Simulated BWR water, $T = 290^oC$, conductivity (outlet) = 0.25 $\mu S/cm$, dissolved O_2 (outlet) = 500 ppb, ECP = 120 mV_{SHE}.

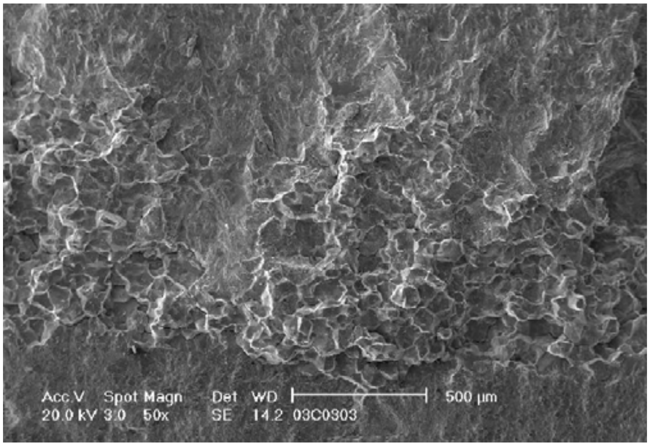

Figure 116. Fracture surface of 10 mm sensitized AISI 304 steel SEN(B) specimen No. 2. The fracture morphology is intergranular. The crack growth has been uneven in the middle of the specimen. Pre-fatigue crack in the bottom and post-test fatigue crack in the top of the photograph. Applied displacement rates: $5x10^{-9}$ mm/s in the beginning (after quick pre-loading) and 0 mm/s in the end of the test. Simulated BWR water, $T = 290^oC$, conductivity (outlet) = 0.25 $\mu S/cm$, dissolved O_2 (outlet) = 500 ppb, ECP = 120 mV_{SHE}.

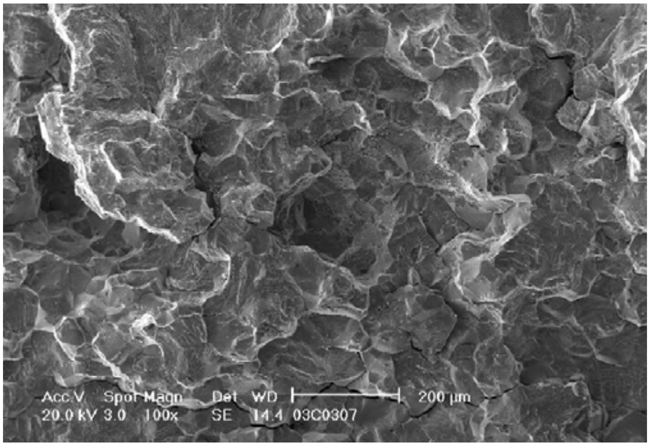

Figure 117. Fracture surface of 10 mm sensitized AISI 304 steel SEN(B) specimen No. 3. The fracture morphology is intergranular. Pre-fatigue and post-test fatigue cracks are outside the photograph. Applied displacement rate: $2.5x10^{-8}$ mm/s. Simulated BWR water, T = 290^oC, conductivity (outlet) = 0.25 $\mu S/cm$, dissolved O_2 (outlet) = 500 ppb, ECP = 120 mV_{SHE}.

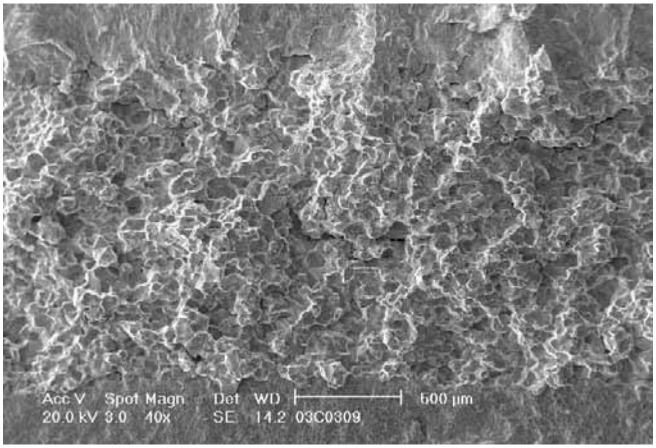

Figure 118. Fracture surface of 10 mm sensitized AISI 304 steel SEN(B) specimen No. 4. The fracture morphology is intergranular. The pre-fatigue crack tip is in the bottom and the final post-test fatigue crack is in the top of the photograph. Applied displacement rates: 5 x 10^{-8} mm/s in the beginning and 0 mm/s in the end of the test. Simulated BWR water, T = 290^oC, conductivity (outlet) = 0.25 $\mu S/cm$, dissolved O_2 (outlet) = 500 ppb, ECP = 120 mV_{SHE}.

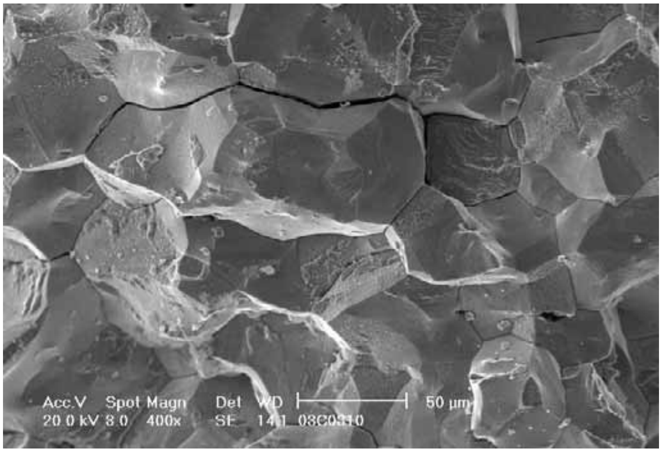

Figure 119. A higher magnification detail of the intergranular fracture surface of sensitized AISI 304 steel specimen No. 4. Simulated BWR water, T = 290°C, conductivity (outlet) = 0.25 µS/cm, dissolved O_2 *(outlet) = 500 ppb, ECP = 120* mV_{SHE}.

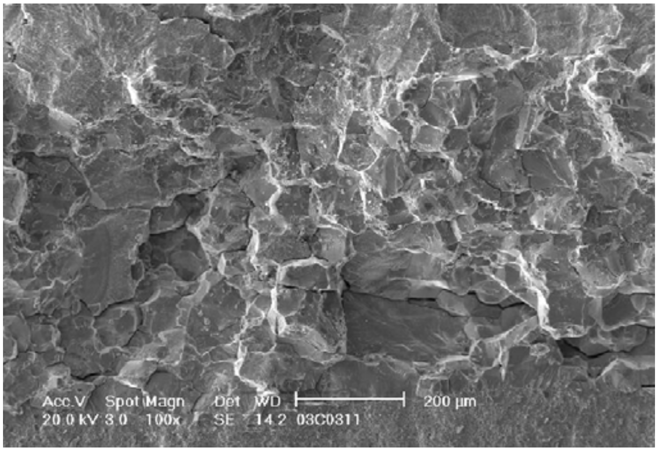

Figure 120. Fracture surface of 10 mm sensitized AISI 304 steel SEN(B) specimen No. 5. The fracture morphology is mainly intergranular although traces of transgranular fracture can be seen. Pre-fatigue crack tip is in the bottom and post-test fatigue crack is outside the photograph. Applied displacement rates: 1×10^{-7} *mm/s in the beginning,* 5×10^{-8} *mm/s in the middle and* 2.5×10^{-8} *mm/s in the end of the test. Simulated BWR water, T = 290°C, conductivity (outlet) = 0.25 µS/cm, dissolved* O_2 *(outlet) = 500 ppb, ECP = 120* mV_{SHE}.

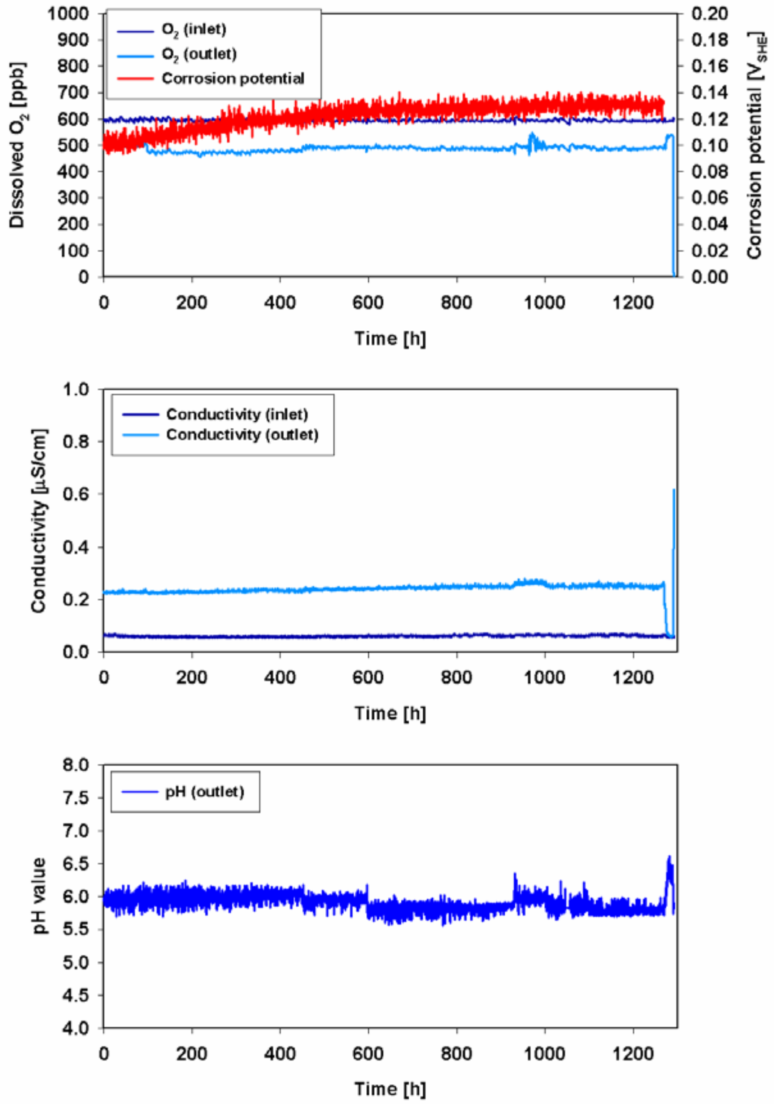

Figure 121. Water chemistry during the tests of the 10 mm sensitized AISI 304 steel SEN(B) specimens. Simulated BWR water, $T = 290^oC$, conductivity (outlet) = 0.25 µS/cm, dissolved O_2 (outlet) = 500 ppb, ECP = 120 mV_{SHE}.

Table 27. Water chemistry analysis results, μg/l (analysis performed by Teollisuuden Voima Oy). Typical BWR NWC impurity levels: Cl^- 1 μg/l and SO_4^{2-} 2 μg/l (reactor water), Fe^+ 1–3 μg/l and Cu^+ 0.1–0.2 μg/l (feed water). Silica is not considered detrimental and concentration measurements below 20 μg/l are generally not attempted.

Sample No.	F^-	Cl^-	SO_4^{2-}	Fe	Cr	Ni	Cu	Si
1	-	0.8	-					
2	-	2.2	0.7					
3				-	1.6	-	-	43.3
4				0.55	-	-	-	43.4

4.6.2 25 mm C(T) specimen

The load, crack length and K_I during the test on the 25 mm C(T) specimen are presented in Figure 122. The load measurement values are randomly distributed between the minimum and maximum loads during the fatigue phases in the beginning of the test (averages of one minute and measured using ½ h interval). The values are accurate when the specimen was under constant load and constant displacement in the end of the test. The crack length vs. testing time curve shows how the crack growth rate decreased when the fatigue frequency was decreased and the load ratio was increased towards the end of the test (in terms of da/dt). The different fatigue phases are indicated by numbers along the crack length vs. testing time curve and they are explained in Table 28.

A drawing showing the fracture zones observed on the fracture surface is presented in Figure 123. Different zones can be identified on the fracture surface. There is a transgranular fracture zone formed during the fatigue phase and an intergranular fracture zone formed during the constant load and constant displacement phases. There are also extended fracture zones close to the side surfaces where the cracks grew inwards from the bottoms of the side grooves. It is not clear when these side groove surface cracks were formed. However, the crack length values measured using potential drop method fit very well with the transgranular and intergranular fracture zones in the middle of the specimen. The fracture surface morphologies are presented in Figs 124–126.

The water chemistry during the test is presented in Figure 127. In this test the outlet conductivity was as expected for the water re-circulation loop used in the test. The grab sample analysis results are presented in Table 29.

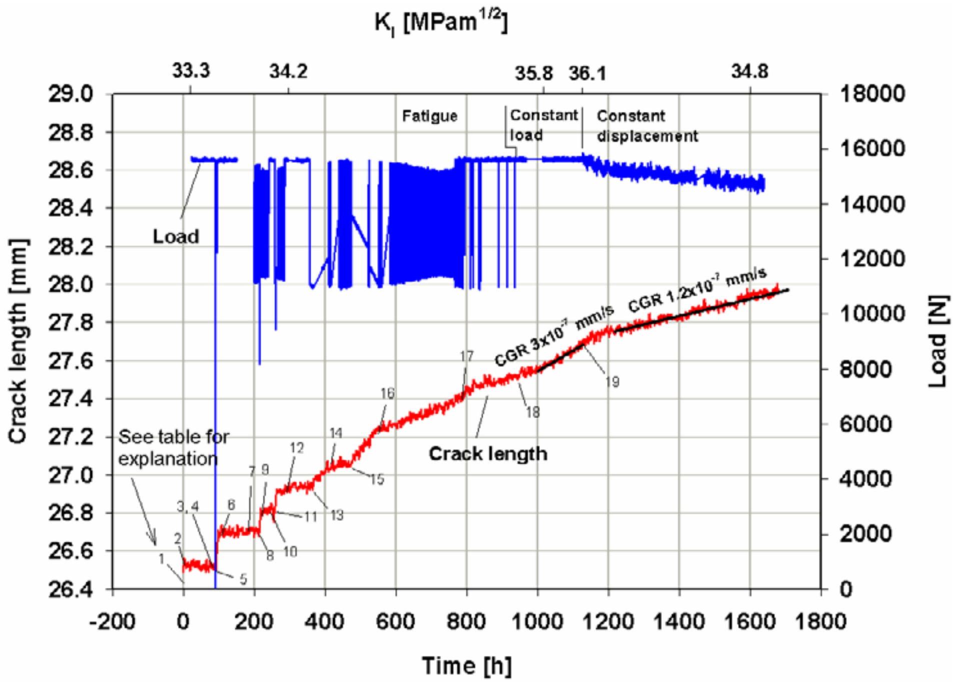

Figure 122. Load, crack length and K_I during the test of the 25 mm sensitized AISI 304 steel C(T) specimen. Simulated BWR water, $T = 290^{o}C$, conductivity (outlet) = 0.15–0.2 µS/cm, dissolved O_2 (outlet) = 500 ppb, ECP not measured because of reference electrode failure.

Table 28. Test sequence for the test on the 25 mm sensitized AISI 304 steel C(T) specimen. The test phase numbers refer to the numbers along the crack length vs. time curve in Figure 122.

Phase	**Date and time**	**Test time [h]**	**Loading mode**
1	19.12.02 15:36	0	Specimen loaded 20 N/s
2	19.12.02 15:36 – 23.12.02 8:56	0–89.3	Constant load
3	22.12.02 11:01	89.4	Specimen unloaded
4	22.12.02 12:01	90.4	Specimen reloaded
5	22.12.02 13:31 – 22.12.02 16:01	91.9–94.4	R 0.5, f 0.1 Hz
6	22.12.02 16:01 – 26.12.02 5:37	94.4–180	Constant load
7	26.12.02 5:37 – 28.12.02 15:41	180–216.1	R 0.7, f 0.001 Hz
8	28.12.02 15:46 – 28.12.02 17:46	216.1–218.2	R 0.6, f 0.1 Hz
9	28.12.02 17:46 – 29.12.02 17:36	218.2–242	R 0.7, f 0.01 Hz
10	29.12.02 17:36 – 30.12.02 10:46	242–259.2	Constant load
11	30.12.02 10:46 – 31.12.02 15:41	259.2–288.1	R 0.7, f 0.01 Hz
12	31.12.02 15:41 – 03.01.03 12:51	288.1–357.2	Constant load
13	03.01.03 12:51 – 05.01.03 17:51	357.2–410.2	R 0.7, f 0.01 Hz
14	05.01.03 17:51 – 08.01.03 10:26	410.2–474.8	R 0.7, f 0.001 Hz
15	08.01.03 10:26 – 11.01.03 13:36	474.8–540	R 0.7, f 0.01 Hz
16	11.01.03 13:36 – 21.01.03 13:26	540–789.8	R 0.7, f 0.001 Hz
17	21.01.03 13:26 – 28.01.03 5:36	789.8–950	Constant load + manually initiated unloadings three times/day, R 0.7, f 0.001 Hz
18	28.01.03 5:36 – 04.02.03 15:08	950–1127.5	Constant load
19	04.02.03 15:08 – 27.02.03 15:41	1127.5–1680.1	Constant displacement

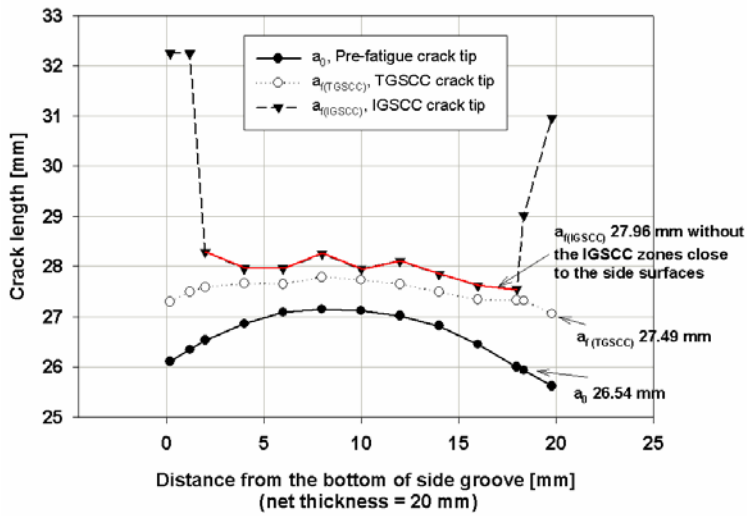

Figure 123. Different zones on the fracture surface of the 25 mm sensitized AISI 304 steel C(T) specimen. The extended zones close to the side surfaces grew inwards from the bottoms of the side grooves.

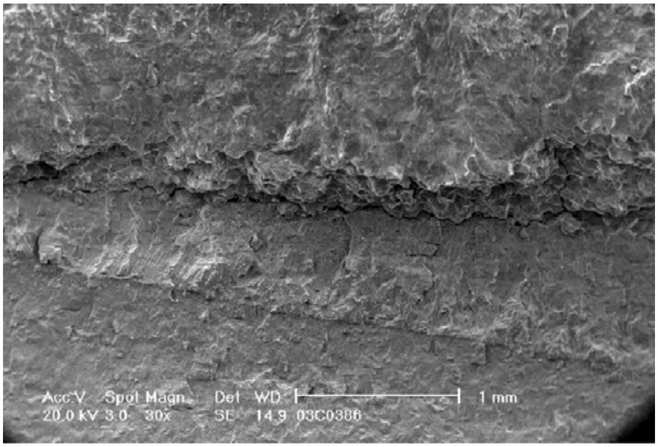

Figure 124. Fracture surface of the 25 mm sensitized AISI 304 steel C(T) specimen in the middle of the specimen. Pre-fatigue, transgranular fatigue formed during the stress corrosion cracking initiation phase in the autoclave, intergranular cracking formed during the constant load and constant displacement phases, and post-test fatigue can be distinguished from the photograph (from the bottom to the top, respectively). Simulated BWR water, T = 290°C, conductivity (outlet) = 0.15–0.2 µS/cm, dissolved O_2 (outlet) = 500 ppb.

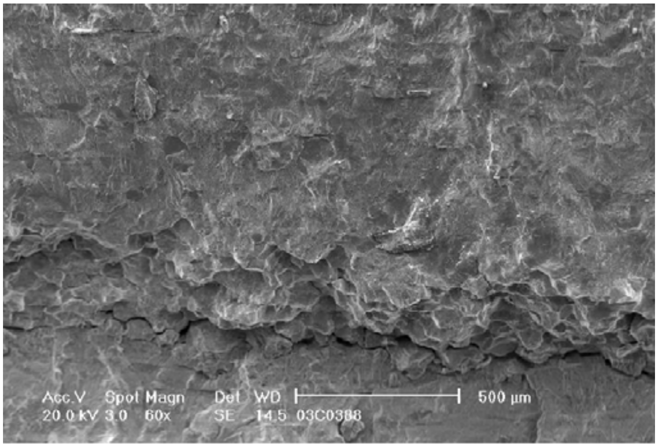

Figure 125. A detail of the intergranular fracture zone formed during the constant load and constant displacement phases of the test. Simulated BWR water, T = 290^{o}C, conductivity (outlet) = 0.15–0.2 μS/cm, dissolved O_2 (outlet) = 500 ppb.

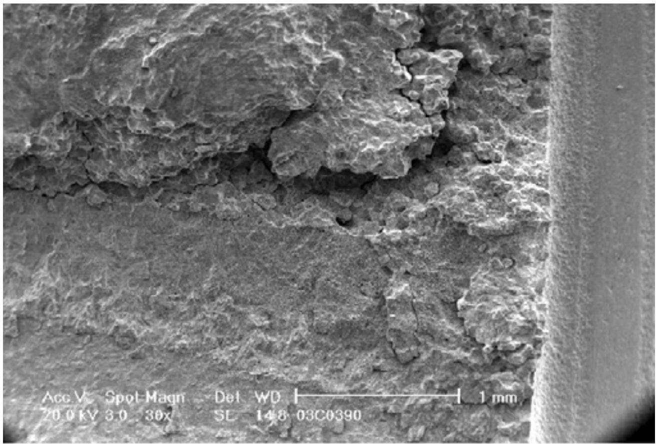

Figure 126. A photograph showing the side groove (right) and intergranular cracking that grew sideways from the bottom of the side groove. Simulated BWR water, T = 290^{o}C, conductivity (outlet) = 0.15–0.2 μS/cm, dissolved O_2 (outlet) = 500 ppb.

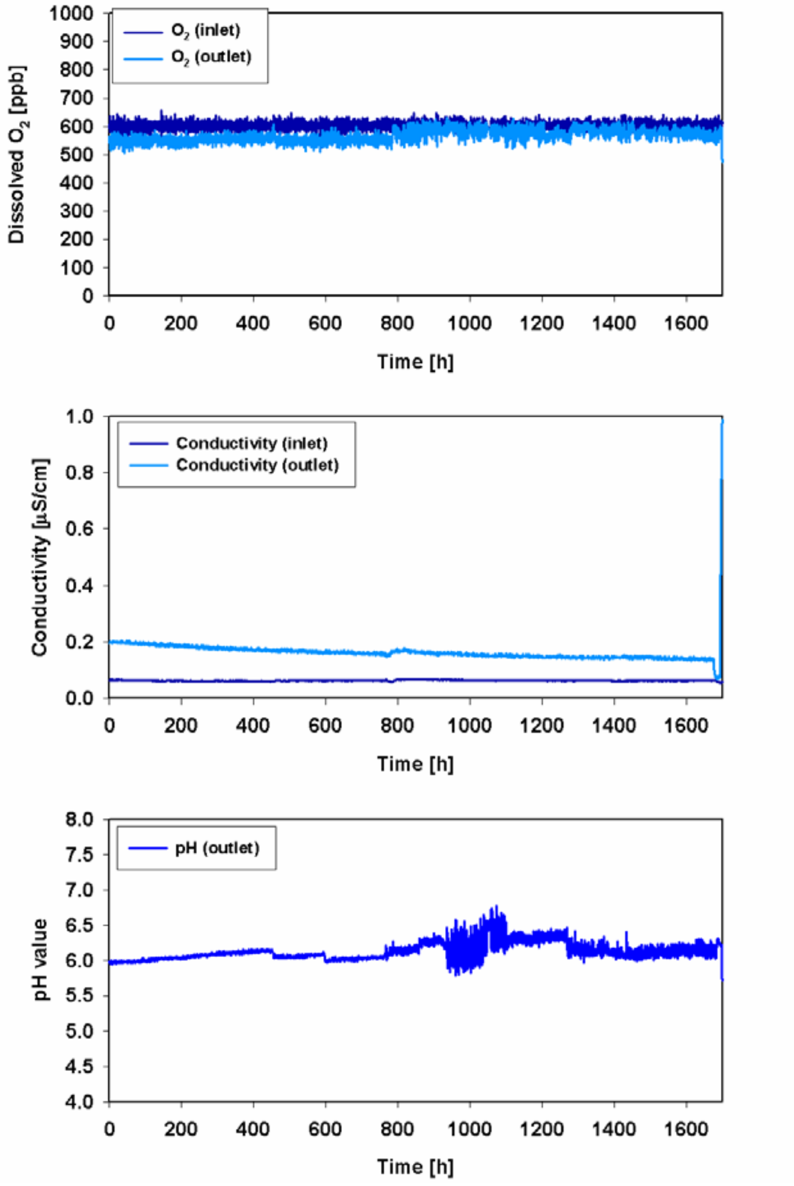

Figure 127. Water chemistry during the test of the 25 mm sensitized AISI 304 steel C(T) specimen. Corrosion potential data was not obtained because of the malfunctioning reference electrode. Simulated BWR water, T = 290^{o}C, conductivity (outlet) = 0.15–0.2 μS/cm, dissolved O_2 (outlet) = 500 ppb.

Table 29. Water chemistry analysis results, μg/l (analysis performed by Teollisuuden Voima Oy). Typical BWR NWC impurity levels: Cl^- *1 μg/l and* SO_4^{2-} *2 μg/l (reactor water),* Fe^+ *1–3 μg/l and* Cu^+ *0.1–0.2 μg/l (feed water). Silica is not considered detrimental and concentration measurements below 20 μg/l are generally not attempted.*

Sample No.	F^-	Cl^-	SO_4^{2-}	Fe	Cr	Ni	Cu	Si
1	-	1.3	0.7					
2	-	1.7	0.7					
3				-	1.2	-	-	26.1
4					-	-	-	17.8

4.6.3 Effects of K_J, K_I and dJ/dt on crack growth rate

The crack growth rates measured on the 10 mm SEN(B) and 25 mm C(T) specimens are presented as a function of stress intensity factor K_J and K_I in Figure 128. Under constant displacement, the crack growth rates were the same regardless of the specimen size or stress intensity level, $\sim 1 \times 10^{-7}$ mm/s. Rising displacement and constant load resulted in higher crack growth rates. Figure 129 shows that the crack growth rate depends almost linearly on the J-integral change rate, dJ/dt. It is also notable that the crack growth rates measured on the 10 mm SEN(B) and 25 mm C(T) specimens fall exactly on the same curve.

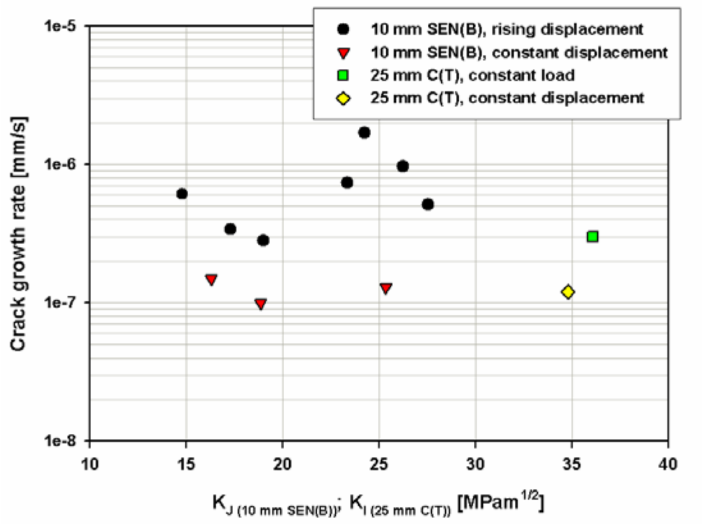

Figure 128. Effects of stress intensity level (K_J or K_I) and loading mode on the crack growth rate of sensitized AISI 304 steel. Simulated BWR water, T = 290°C, conductivity (outlet) = 0.15–0.2 μS/cm, dissolved O_2 (outlet) = 500 ppb.

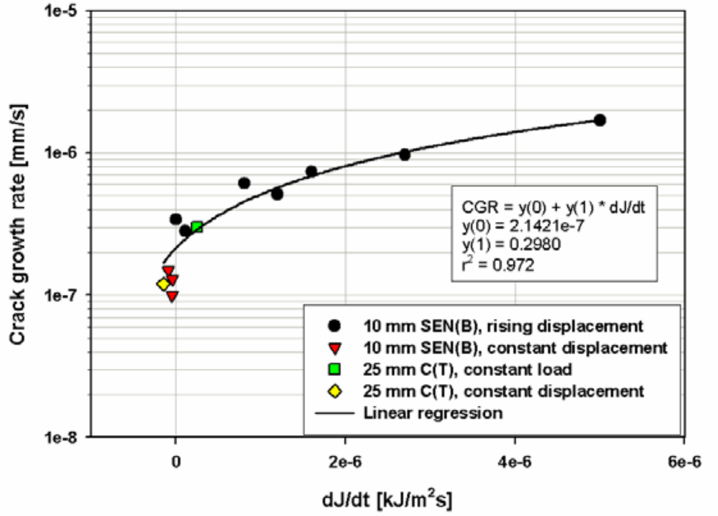

Figure 129. Effect of loading rate in terms of dJ/dt on the crack growth rate of sensitized AISI 304 steel. Simulated BWR water, T = 290°C, conductivity (outlet) = 0.15–0.2 μS/cm, dissolved O_2 (outlet) = 500 ppb. Linear regression for the dependency between the crack growth rate and dJ/dt is also shown (CGR = crack growth rate). The linear regression is seen as curved because the crack growth rate is shown in the logarithmic scale.

5. Discussion

J-R tests on AISI 304 and 321 steel SEN(B) specimens in BWR water

The measured stress corrosion crack growth rates in AISI 304 steel show no clear evidence of the specimen size effect, even though the J-R tests were continued well above the J_{max} set by the J-R test standards. The SCC rates seem to stay approximately constant as soon as the environmentally assisted cracking has initiated across the crack tip. All the tests of this test series show a plateau (SCC crack growth rate independent of J-level). This means that the level of plastic deformation in the ligament ahead of the crack tip does not have any significant effect on SCC crack growth rate. Neither has it any notable effects on the fracture morphology: the fracture morphology of the sensitized AISI 304 steel specimens tested using the slowest loading rate was almost pure IGSCC from the beginning to the end of the test (some grains with traces of TGSCC were observed, Figure 28).

There is a small difference in the measured crack growth rate between the two 10 mm x 10 mm AISI 304 specimens, in which IGSCC was observed on the fracture surface. The crack growth rate seems to depend on the applied J-integral increase rate, which, on the other hand, also has an effect on the amount of intergranular cracking on the fracture surface. IGSCC/TGSCC ratio seems to increase as dJ/dt decreases. The same phenomenon can be seen in the SCC crack growth rates between the two AISI 321 specimens, even more clearly. In this case the SCC morphology changed from pure TGSCC to mixed TGSCC and IGSCC as the applied J-integral increase rate was decreased.

Based on this test series, it can be concluded that the fracture morphologies resulting from the different loading rates (dJ/dt) can be put in the following order: ductile cracking at high applied loading rates, TGSCC at intermediate applied loading rates, and IGSCC at slow applied loading rates.

The crack growth rate in the case of the AISI 304 steel specimen, in which the fracture surface morphology was almost pure IGSCC, seems reasonable when compared to the literature data (2×10^{-7}-2×10^{-6} mm/s at $K_I \sim 50$ MPa$\sqrt{m}$) [32]. The crack growth rate at the observed plateau K_J-levels ($K_J > 50$ MPa$\sqrt{m}$) was in the range of 1–3 x 10^{-6} mm/s. It should be noted that the tests on AISI 304 steel were performed in simulated BWR water containing 30 ppb sulphate and using potentiostatic polarization to +400 mV_{SHE}. Typical open circuit potential of AISI 304 steel is in the range of 50–200 mV_{SHE} in the same water chemistry conditions. No crack growth rate data was found for AISI 321 steel from the literature for the same water chemistry conditions. However, the weld heat affected zone of AISI 321 steel has been observed to be susceptible to intergranular stress corrosion cracking in BWR conditions [111, 112].

SCC susceptibility of Olkiluoto 1 core shroud material

Yield stress and tensile strength have increased slightly due to neutron irradiation in the studied stainless steel, but no obvious changes in the elongation to fracture were observed. The differences in the elongations of the weld specimens can be explained by different amounts of weld metal in the gauge sections.

A correlation between the amount of IGSCC and polarization potential can be observed in the SSRT results of the irradiated specimens. The amount of IGSCC increases with the potential in irradiated specimens. No IGSCC was observed on the fracture surfaces of the non-irradiated specimens, only TGSCC in the case of base metal specimens and ductile cracking in the case of non-irradiated weld specimens.

Also, the elongation to fracture is affected by the irradiation in SSRT. Irradiation seems to decrease the elongation in SSRT, which can be explained by an increased stress corrosion cracking susceptibility and also by a slightly increased yield stress. Due to the increased yield stress the irradiated specimens reach higher stresses at lower elongations than the non-irradiated specimens. No explicit correlation between elongation to fracture and corrosion potential can be observed in the SSRT results.

All the slow J-R tests showed a plateau (SCC crack growth rate independent on J-level). This, as was the case with the previous test series on AISI 304 and 321 steels, indicates that the plastic deformation due to high J-value in the remaining ligament does not play any major role in SCC crack growth rate in slow J-R tests utilizing precracked specimens and three-point bending. Also, when IGSCC was observed on the fracture surface, it was distributed quite evenly. This, again, indicates that the J-level does not influence the fracture morphology.

The results of the slow J-R test with varying displacement rate (heat treated, non-irradiated HAZ specimen) indicate that TGSCC crack growth rate is dJ/dt dependent. In the tests where the SCC morphology was partly IGSCC (in addition to TGSCC), the SCC crack growth rate was higher than in the cases where the SCC morphology was pure TGSCC in the same environment, especially in the case of irradiated HAZ specimens. This is reasonable if the specimens showing only TGSCC were not susceptible to IGSCC in the test environment, as shown in Figure 45. If they were susceptible to IGSCC in this environment (+200 mV_{SHE}), at least some grain boundary facets should have been visible on the fracture surface with the used loading parameters as in the case of the irradiated HAZ and base metal specimens.

In the irradiated base metal, the crack growth rate at +200 mV_{SHE} fell between the SCC crack growth rates measured on irradiated HAZ specimens (IGSCC + TGSCC) and the SCC crack growth rates measured on non-irradiated specimens (TGSCC). Some grain boundaries were visible on the fracture surface of the irradiated base metal specimen. This can be interpreted so that the grain boundaries in the irradiated base metal specimen were only partially (locally) sensitized and, thus, IGSCC can not propagate continuously. The crack growth needs to be forced by mechanical crack tip deformation, which results in TGSCC across the non-sensitized ligaments.

Based on the amount of IGSCC on the fracture surface (~40%) in the slowest test on the irradiated HAZ, cracking may occur also under static loading. It has been proposed that only 23% of the grain boundaries must be susceptible for IGSCC crack growth to occur [113]. However, it is not clear what would happen to the crack growth rate under static loading or under extremely low displacement rates.

In both cases, irradiated HAZ and irradiated base metal, the low temperature annealing has decreased the SCC crack growth rates somewhat. This indicates that the main reason for the IGSCC susceptibility of the irradiated core shroud surveillance material is the irradiation, not low temperature sensitization nor sensitization due to heat input during welding. The latter two factors may have had some influence on the increased IGSCC susceptibility, but these tests did not reveal it. The sensitivity of the test method can be increased using lower applied displacement rate or dJ/dt. Also, the crack tip strain rate has an influence on the threshold values of SCC initiation as can be seen from the results: the higher the loading rate, the higher the J_{TH} or K_{TH}. This kind of dependence between the threshold stress intensity factor and loading rate has been observed also in other studies [114, 115]. This dependence indicates that the initiation process is time dependent.

No correlation could be observed between the DL-EPR tests and the stress corrosion susceptibility in BWR conditions, which also indicates that welding and LTS are not directly responsible to the SCC susceptibility of the irradiated HAZ specimens. Modified Huey tests showed no explicit correlation to the IGSCC susceptibility in BWR conditions, but appeared to correlate with irradiation. The additionally conducted tests on the corresponding SIS 2333 reference material showed that the slip lines are attacked in the sensitized material in the modified Huey tests.

Superposition based analysis used in the tests on the core shroud material

The basic idea behind the superposition based analysis method is to measure the stress corrosion crack growth rate using quickly performed tests by extracting the contribution of the pure mechanical loading (in terms of dJ/dt) from the total crack growth rate. This remaining crack growth rate is assumed to represent the environmental part of the crack growth.

If the contribution of the environment on the crack growth rate is assumed constant, i.e., independent of dJ/dt, the total crack growth rate approaches the environmentally controlled crack growth rate when dJ/dt approaches 0 kJ/m^2s. At high dJ/dt levels the contribution of the mechanical loading to the total crack growth rate is considerable. When the loading rate is high enough, the contribution of the environment diminishes. In the optimal case the superposition based analysis results in the same environmental crack growth rate as a test performed using the applied loading rate of dJ/dt = 0 kJ/m^2s.

In the case of Olkiluoto 1 core shroud base metal specimens, the environmental component was ~30–60% of the total crack growth rate and the tests resulted in TGSCC. In the case of the HAZ specimens, the environmental component was ~40–96% of the total crack growth rate and the tests resulted mainly in TGSCC. The specimen with the largest amount, 40%, of IGSCC on the fracture surface was the specimen which was tested using considerably slower loading rate than the others. In this specimen, the environmental component was ~96% of the total crack growth rate, i.e., the impact of the analysis method was minimal. This is a consequence of the high fracture resistance of the Olkiluoto 1 core shroud steel in inert environments.

In the case of austenitic stainless steels the fracture morphology of interest in nuclear power plan environments is IGSCC. The applied loading rate should be so slow that the test results at least partially in IGSCC in order to determine whether the studied material is IGSCC susceptible or not. It is not clear at this point how large proportion of the fracture surface should be intergranular and how much transgranular fracture is accepted. As was stated earlier, it has been proposed that only 23% of the grain boundaries must be susceptible to IGSCC for sustained IGSCC crack growth to occur [113]. This could also be an acceptance criterion for an IGSCC susceptibility test. The superposition based analysis method should be further developed as it has a clear promise to be an acceptable tool, from the engineering point of view, to generate crack growth rate data quickly.

Tests on AISI 304 steel specimen using varying displacement rate

Standard methods for the measurement of fracture toughness do not allow changes in the load line displacement rate during the test. However, there seems to be no reasons why the standard procedures for J calculation would not yield acceptable results even if the displacement rate was changed. This has been studied in Appendix 1.

The results performed using varying displacement rates on sensitized AISI 304 steel specimens indicate that there is a plateau above the J-integral increase rate, dJ/dt, of 4×10^{-5} kJ/m^{2}s, where the crack growth rate is independent on dJ/dt. In this plateau area, the fracture surface morphology is either TGSCC or mixed TGSCC and IGSCC. The same phenomenon was observed with the IGSCC susceptible core shroud HAZ specimens. However, at dJ/dt levels between ~0 and 4×10^{-5} kJ/m^{2}s, the crack growth rate is linearly dependent on dJ/dt. If the crack growth rates of the core shroud HAZ specimens were measured using constant displacement, the crack growth rates could have been lower, i.e., the core shroud crack growth rate test results are conservative with regards to the power plant safety analyses.

The crack growth rate test results on the sensitized AISI 304 steel specimens show that K_J-level does not have any considerable influence on the crack growth rate under constant displacement type loading conditions. With one exception, all the crack growth rates measured under static loading were between 1x and 2 x 10^{-7} mm/s. The exceptionally low crack growth rate (1.4 x 10^{-8} mm/s) probably resulted from the loading history. If the fracture morphology was mostly TGSCC before the loading was changed from rising to constant displacement, intergranular crack may have propagated only locally where the crack tip was at the grain boundary. This was not verified by the SEM study. All the fracture surface zones can not be related to the different applied J-integral increase rates due to the large number of them.

One of the tests was performed on a mill-annealed AISI 304 steel specimen. The crack growth rates measured on this specimen were below the crack growth rates measured on the sensitized specimens at all applied dJ/dt levels. The fracture morphology in this specimen was TGSCC. It is not clear whether actual crack growth took place during the constant displacement phase of this specimen or not. Potential drop method indicated some crack growth, but the indication probably resulted from slow material property changes in high temperature water. Post-test SEM investigation of the fracture surface did not reveal anything that could be attributed to the crack growth during the constant displacement phase.

Tests on low activation steel (LAS) F82H

The test material was ferritic stainless steel and it differs from all the other test materials of this work, which were austenitic. The J-R-tests in inert environments resulted in very similar fracture resistance curves both on 3 x 4 x 27 mm^3 and 5 x 10 x 55 mm^3 specimens. The crack extension and J-integral limits of ASTM E 1820-99 were exceeded considerably with the smaller specimens, and J-limit with the larger specimens. The small differences of the J-R curves above J-integral values of 150 kJ/m^2 can be explained by different test temperature. Also, the small step in the crack extension of the other 5 x 10 x 55 mm^3 specimen tested at 230°C in nitrogen gas probably results from a change of the contact between the specimen and one of the potential drop leads. The normalized load vs. load line displacement plot shows that two of the curves are above the others, which indicates an error in the crack length, displacement or load measurement. However, the measurement error is not evident in the J-R-curves.

The lower J_Q-values, lower J-R-curve slopes and lower normalized load-diplacement curves imply that there is an environmental component present in the crack propagation in addition to mechanical ductile tearing in the tests performed in high temperature water. The environmental effect was also evident in the SEM examination of the fracture surfaces: the fracture surfaces of the specimens tested in silicon oil bath and in nitrogen gas atmosphere showed typical ductile dimpled cracking. The fracture surfaces of the specimens tested in high temperature water seemed more brittle-like, which is typical for transgranular stress corrosion cracking. No dimples could be seen, which indicates that the role of ductile tearing is small.

A clear relation between crack growth rate and displacement rate or J-integral increase rate can be seen. The crack growth rate decreases when the J-integral increase rate is decreased and becomes zero after a short transition period, when the rate is decreased to ~0 kJ/m^{2}s (constant displacement). Thus, a dynamic loading condition is needed for crack propagation to take place, which is similar to the behaviour of non-sensitized AISI 304 steel. This is consistent with the results of Lapeña and Blázquez [116]. They performed constant load tests on the same material in water at 260°C. They did not observe any crack growth in mill-annealed F82H.

Electrochemical potential seems to have no clear impact on the crack growth rate measured in high temperature water. This may be partly due to the potentiostatic polarization and partly due to the stability of the oxide film properties within the applied potential range. When potentiostatic polarization is used, part of the applied current is used to overcome the ohmic resistance of the solution between the specimen and the counter electrode (effect known as IR-drop).

Effect of BWR water sulphate concentration on SCC crack growth rate

In the aged Inconel 82 weld metal, no crack initiation, with one exception, took place during the performed slow rising/constant displacement tests and, thus, the effects of sulphate on the crack growth could not be observed. The fracture surface morphology was transgranular in the specimen showing crack growth. The crack growth rates measured with this specimen can not be considered representative unless fatigue crack growth is considered. The accuracy of the measured data, however, does not enable this. Load line displacement and load were measured with ½ h intervals and the possible fatigue component of the loading had a much higher frequency.

Sulphate addition in BWR water resulted in an increase in the crack growth rate of Inconel 182 weld metal and cold-worked AISI 316 stainless steel after an incubation period of about 20–50 h in the slow rising displacement tests. Increased crack growth rate was sustained for long periods after the sulphate injection was stopped, although the environment became clean after 1–2 h period according to the measured conductivity. The observed rapid load reduction in the load-displacement curve after sulphate injection is a result of the change in the crack growth rate. The reduced load level, in the purified water after the fast crack growth phase, is a result of the reduced dimensions of the remaining ligament of the specimen. For Inconel 182 weld metal even the smallest increase in the sulphate content of the water, i.e., 10 ppb, provided allmost one order of magnitude higher crack growth rate under rising displacement condition. Under constant displacement type loading condition, the increase was even higher. The crack growth rate values are within the range reported in the literature. The measured crack growth rates for Inconel 182 weld metal, in general, remain lower than the Swedish disposition line [87] shown in Figure 107. Only exceptions are observed at the lowest K_J levels, where the measured crack growth rates slightly exceed the disposition line. It has to be noted that the disposition line is determined for NWC at 288^{o}C and these tests were performed at 273^{o}C.

The measured crack growth rates for Inconel 182 weld metal were apparently not dependent on K_J-level. However, during the tests, the uncracked ligaments remaining behind the crack tip in Inconel 182 weld metal specimens may carry a considerable part of the load, especially if the ligaments are far behind the crack front. As a result, K_J-level (calculated from the effective crack length) does not define exactly the loading condition at the location of the actual crack tip. The uncracked ligaments may also have influenced the effects of the subsequent sulphate additions on the crack growth rate later in the tests.

Crack growth rate in Inconel 182 weld metal depends on the applied displacement rate or J-integral increase rate, dJ/dt, in pure BWR water. The dependence seems to be linear just like in the previous tests on the sensitized AISI 304 steel in pure water, although there is much more scatter. However, when sulphate is added into the environment, the crack growth rate increases considerably, and the crack growth rate begins to dominate dJ/dt, not the displacement rate.

Comparison of stress corrosion crack growth rates using 10 mm SEN(B) and 25 mm C(T) specimens

As the results so far have indicated, extremely low J-integral increase rates must be used in order to measure pure intergranular SCC crack growth rate in clean BWR water. It is practically impossible to reach the relevant stress intensity levels unless the load line displacement rate is reasonably high in the beginning of the test. This is why specimens No. 1 and 2 of this test series were loaded quickly.

In the normalized form the load-load line displacement curves should be independent of the size of the remaining ligament and the measured normalized loads should fall on the same curve. Small differences in the material properties may result in differences in the curves, but the normalized loads should still increase with the increasing load line displacement and show power law dependency. The differences between the curves measured on the 10 mm SEN(B) specimens indicate either errors in displacement, load, or crack length measurement during the test on specimen No. 4, Figure 111.

In the case of the 25 mm C(T) specimen, the size criteria usually applied in stress corrosion tests are based on standard ASTM E 399-90 "Standard Test Method for Plane-Strain Fracture Toughness of Metallic Materials". The maximum K_I for this test material (sensitized AISI 304 steel) according to ASTM E 399-90 is 14.5 MPa√m (according to the correction to the standard proposed by Wallin [8], the maximum K_I is 23 MPa√m). However, ASTM E 647-97 "Standard Test Method for Measurement of Fatigue Crack Growth Rates" allows K_I-levels up to 42 MPa√m for the highly strain hardening materials (for the crack length of 28 mm, as was the case with the 25 mm C(T) specimen in the end of the test) and the test material, AISI 304, can be considered as such a material. However, the crack growth on the side surfaces of the 25 mm C(T) specimen probably resulted in a higher actual K_I-level than the calculated 34.8 MPa√m in the end of the test. The strain field ahead the crack tip resulting from the high K_I-level is a possible reason why the crack growth direction in the middle of the specimen deviated from the load line direction. However, this kind of deviation was typically not observed on 10 mm SEN(B) specimens regardless of high applied J (or K_J) levels.

The results indicate that the same crack growth rates can be obtained using small SEN(B) specimens under elastic-plastic loading conditions and large specimens predominantly under linear-elastic loading conditions. The crack growth rate is independent on stress intensity level K_J or K_I for AISI 304 steel in BWR water at least at the levels applied in this test series, when the specimens are under constant displacement type loading condition. Still, the loading mode has a strong effect on the crack growth rate. When the 10 mm SEN(B) specimens were loaded using rising displacement and the 25 mm C(T) specimen was under constant load, the crack growth rates were notably higher than under constant displacement. It must be noted that constant load type loading results in an increasing K_I and, thus, also in increasing J.

The dependence between J-integral change rate, dJ/dt, and crack growth rate seems to be linear also in this test series. The results of the 10 mm SEN(B) and 25 mm C(T) specimens fall on the same line. The crack growth rate level at dJ/dt = 0 can be taken as the static loading plateau crack growth rate.

The observed linear dependence between the crack growth rate and dJ/dt also indicates that the specimen size has an effect on the crack growth rate in constant load tests. Decreasing size of the remaining ligament results in an increasing dJ/dt under constant load.

DJ/dt may be a better parameter to correlate with the crack growth rate than the stress intensity factor, at least if the crack growth rate is independent on K_I-level (this should be determined under constant K_I, not constant load). If the crack growth rate depends both on dJ/dt and K_I, a two-parameter description of the loading condition is needed for constant load tests on relatively small specimens or for rising load/rising displacement tests.

Rice et al. [11] speculated that the effective size of the plastic zone influencing the crack tip opening displacement saturates in large scale yielding conditions to some fraction of the size of the remaining ligament. That may result in the observed crack growth rate vs. K_J independence. However, their approach was based on rigid, ideally plastic material behaviour, where the elastic loading is directly proportional to the size of the remaining ligament. The situation in the real strain hardening materials is better: strain hardening results in an increasing load, even though the size of the remaining ligament becomes smaller. If the stress corrosion crack growth rates were dependent on K_I-level under linear-elastic loading conditions, at least some dependence on K_J should remain under elastic-plastic loading conditions. Also, if the real materials behaved like they were ideally plastic, ductile fracture J-R curves measured on small and large specimens should deviate when the small specimen passes the small-scale yielding limit.

Potential drop measurement issues

The ASTM-procedure for the calculation of the crack growth from the potential drop data was applied in this study. Generally, the potential drop data agreed well with the physical crack growth measured using a microscope. The difference between the crack growth calculated using the ASTM-procedure and the physical crack growth was typically 0–20%. In the case of Inconel 182 weld metal, the difference varied from 0% up to 300%, i.e., the physical crack growth was up to 3 times larger than was indicated by the potential drop data. It is difficult to measure reliable crack growth rates especially in nonhomogeneous weld metals. The dendrite boundaries typically follow randomly some other path than loading line or plane. As was mentioned in Chapter 1.3, a solution to overcome this kind of problems is proposed, for example, by Andresen et al. [92], who periodically perform unloadings/reloadings during a constant load test. This approach can be applied also in the case of small SEN(B) specimens.

Results reflected by the SCC models

The slip-oxidation model predicts a plateau in the crack growth rate at the high crack tip strain rates. It is proposed that, in the plateau range, the crack tip stays free of oxide film and the crack growth rate is controlled by the dissolution of the metal. This kind of plateau was observed in the test series on sensitized AISI 304 steel using varying displacement rates. The model also predicts that the crack growth rate is directly dependent on the crack tip strain rate at the low strain rate levels, eq. (21). This is not in contradiction with the results presented in this work. The crack tip strain rate is proportional to the crack tip opening displacement rate, $d\delta/dt$, which on the other hand is proportional to the J-integral increase rate, size of the plastic zone, distance from the crack tip, and crack growth rate, eq. (17). However, slip-oxidation model (experimental formulation presented in [38]) predicts that the crack growth rate is strongly dependent on K_I in BWR water at 288°C for AISI 304 steel. This is contradictory to what was observed, for example, in the last test series on sensitized AISI 304 steel. The crack growth rate in this test series was constant in the K_J-range between 16–35 MPa√m under constant displacement type loading condition. The same applies to the earlier test series on the sensitized and mill-annealed AISI 304 steel. In that test series, the crack growth rate was constant in the K_J-range between 60–110 MPa√m. It has to be noted that there is a low K_J-region, where the crack growth rate is K_J dependent. The crack growth rate is hardly the same, when the loading of the specimen approaches zero.

The coupled environment fracture model predicts that there is a plateau in the crack growth rate and K_I relation. It also predicts that there should be a BWR water anion concentration level, above which the anionic impurity concentration does not increase the crack growth rate as dramatically as at low concentrations. These predictions are not in contradiction with the results of this work.

The enhanced surface mobility theory also predicts a plateau in the crack growth rate and K_I relation, but the model has generally overestimated the crack growth rates in fcc metals. It is not clear at what stage the model is at the moment and how it predicts the effects of anionic impurities on the crack growth rate.

The internal oxidation model predicts that the crack growth rate is directly proportional to the stress intensity level K_I. This prediction is contradictory to the results of this work. However, the internal oxidation model was developed for different environments as were applied in this work (i.e., PWR environments).

The selective dissolution-vacancy creep (SVDC) model is not mature enough to predict the observed crack growth rates of this work. However, Simonen et al. [117] have analyzed the compositional changes taking place ahead of the crack tip during neutron irradiation. They observed that the corrosion-induced vacancy injection has the greatest potential impact on the local composition. The model is worth further development.

According to the film-induced cleavage model, the crack propagates forward by an oxidation process governed by the same rate-determining steps as those in the slip-oxidation model. The difference to the slip-oxidation model is that when the oxide ruptures at the crack tip the crack may penetrate a small distance into the underlying ductile metal matrix in a brittle-like mechanism. The observed dependencies between the fracture surface morphologies and J-integral increase rates in the tested AISI 304 and F82H steel specimens support this. In sensitized AISI 304 steel the fracture morphology changes from intergranular to transgranular when J-integral increase rate is increased. This may be explained by a change from a dissolution-controlled mechanism (at grain boundaries) to a mechanically controlled film-induced cleavage mechanism, which propagates through the grains.

The models based on the effects of hydrogen are not considered relevant to ductile fcc materials in high temperature water. Hydrogen has been shown to be detrimental to high strength/low ductility alloys at lower temperatures, but the effect diminishes above 125–150°C [38]. The models also are not mature enough to predict the crack growth rates quantitatively.

Crack tip strain rate model predicts that at low dK/dt levels there is only a weak dependence between the crack growth rate and dK/dt. At higher dK/dt levels the dependence will become stronger. The relation between dK/dt and dJ/dt is directly proportional at any fixed K_J-level. Similar dependence should, thus, be observed between the crack growth rate and dJ/dt as predicted for the crack growth rate and dK/dt. This is in contradiction with the experimental data presented in this work. The dependence seems to be linear at low dJ/dt levels but there is a plateau at higher dJ/dt levels. On the other hand, the model of Shoji et al. [43] is based on the slip-oxidation model, which seems to predict the observed behaviour.

The results measured under slowly rising displacement conditions, i.e., under increasing J (and K_J), indicate that the crack growth rate is strain-rate dependent as most of the SCC models predict. At high displacement rates there is a plateau in the crack growth rate of AISI 304 steel which, as discussed earlier, indicates that the crack growth rate is controlled by dissolution or diffusion rate rather than by the crack tip strain rate.

Under constant displacement conditions, i.e., under decreasing J, the crack growth rate is independent of J and K_J in a wide J and K_J range. This indicates that, under constant displacement, the rate-determining factor of the crack growth is, again, diffusion or dissolution rate. From general point of view, change in the K_J level results in a change in the crack tip strain and, thus, in the crack tip strain rate at a constant crack growth rate. However, this change in the K_J level should result in a change in the crack growth rate if the crack growth rate is controlled by the crack tip strain rate under constant displacement conditions. The operating regimes of the rate determining factors for the crack growth rate are shown in Figure 130, which schematically presents the crack growth rate as a function of dJ/dt and K_I or K_J (the latter only for the crack growth rates measured under constant displacement conditions).

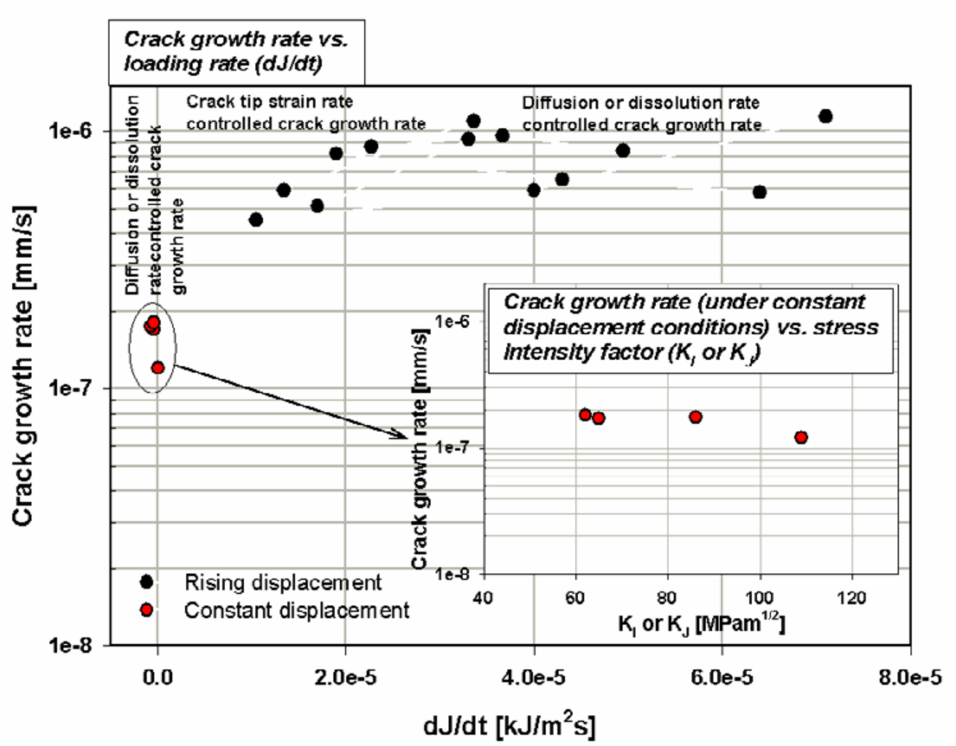

Figure 130. Schematic dependency between loading rate (in terms of dJ/dt), crack growth rate and the presumed crack growth rate controlling factor. The smaller inserted plot inside the larger one shows the effect of the stress intensity factor on the crack growth rate under constant displacement conditions, when the crack growth rate is controlled by diffusion or dissolution.

It is difficult to say which model fits best with the experimental data. All models that are relevant to high temperature BWR water and mature enough to give quantitative predictions seem to predict at least part of the observations. It is possible also that the actual stress corrosion cracking mechanisms in BWR water in austenitic materials involve several of the processes proposed in the different models.

However, most of the models do not take all the phenomena observed at the SCC crack tip into account. For example, the observations made by Simonen et al. [117] regarding the corrosion-induced vacancy injection and selective dissolution are not taken into account in any of the models presently capable of quantitative crack growth rate predictions. The only model discussed in this study, which considers these phenomena, is the selective dissolution-vacancy creep (SDVC) model. The author of this study considers the SDVC model the most sound based on its phenomenological background, although, as was discussed earlier, this model needs further development before it is capable of quantitative predictions. However, the SCC tests presented in this study did not concentrate to the crack tip processes in atomic level.

Applicability to safety analysis purposes

The results of this study support the three-stage approach presented in Figure 1 when the loading mode applied in the tests is constant displacement. All crack growth rates measured under constant displacement indicate stage 2 behaviour, i.e., the crack growth rate is independent of the stress intensity factor level.

Most of the discussed SCC models predict, or are built on the hypothesis, that the crack growth rate is crack tip strain rate dependent. During normal operation of the nuclear power plants, the driving force of the crack growth is the static stress. The stress is typically caused by external loading and internal residual stresses. In order to determine relevant crack growth rate data for safety analysis, the data has to be generated under similar static loading conditions as encountered in the power plants. As was observed in the stress corrosion crack growth rate tests, the crack growth rate increases with the increasing loading rate in terms of dJ/dt, and based on equations (17) and (32), also in terms of $d\delta/dt$ and $d\varepsilon/dt$. Dynamic loading results in conservative crack growth rates, which is, economically, not reasonable for safety analysis purposes. However, dynamic loading can be utilized in screening tests when construction materials are selected. In the later tests of this study, the crack growth rates were measured both under dynamic and static loading conditions. Data generated using this kind of an approach can be used for the safety analysis purposes both in normal operation conditions (constant displacement) and also in transition conditions (rising displacement) of the nuclear power plants, provided that the stress intensity factor level is within the stage 2 as indicated in Figure 1. Crack growth rates at constant K_J (or K_I) or constant load conditions can be interpolated from the crack growth rates measured under constant and rising displacement conditions. Rising displacement is also needed in the beginning of the test in order to initiate the stress corrosion cracking from the transgranular pre-fatigue crack.

It is worth mentioning that the results of this study are generated under mode I loading conditions. This is not always the loading mode encountered in actual structural components and the stress corrosion crack growth rate may be loading mode dependent. There is very little stress corrosion crack growth rate data measured under mode II, mode III or mixed mode conditions in light water reactor environments available in literature.

Sulphate addition in BWR water resulted in an increase in the crack growth rate of Inconel 182 weld metal and cold-worked AISI 316 stainless steel after an incubation period of about 20–50 h in the slow rising displacement tests. Increased crack growth rate was sustained for long periods after the sulphate injection was finished, i.e., >200 h, although the environment became clean after 1–2 h period according to the measured conductivity. Similar memory effect has been reported for example by Lidar [101] for AISI 304 steel. It is not clear whether the crack growth rate decreases back to the pure water crack growth rate level once sulphate has been introduced to the environment. This is a problem from the safety analysis point of view. The design lines are typically determined so that the test environment is maintained constant during the crack growth rate tests. On the other hand, there is a risk that the pure water design lines are applied for the momentary water chemistry conditions in power plants, i.e., the pure water crack growth rate is not necessarily relevant although the present water chemistry parameters in the power plant may be optimal.

6. Conclusions

The following conclusions can be made based on the experimental results:

1. Stress corrosion crack growth rate is independent on elastic-plastic K_J between 16 and ~100 MPa√m for sensitized AISI 304 steel in pure BWR water.

2. The same SCC crack growth rates can be obtained for sensitized AISI 304 steel in BWR water using elastic-plastic fracture mechanics approach as using conventionally used linear-elastic approach.

3. Fracture surface morphology in sensitized AISI 304 steel in BWR water changes from intergranular to transgranular and finally to ductile dimpled fracture at high J-intergral levels, when J-integral increase rate is increased. Rising J results in transgranular stress corrosion cracking (or strain-induced corrosion cracking) also in the mill-annealed steel.

4. The results on the core shroud material (AISI 304 steel) show that the welding together with the exposure to neutron irradiation in the BWR operating temperature conditions results in a higher susceptibility to stress corrosion cracking than welding or irradiation alone.

5. Stress corrosion crack growth rate is independent on K_J for Inconel 182 weld metal in BWR water, at least between 23 and 55 MPa√m.

6. Even as low an amount as 10 ppb SO_4^{2-} in the otherwise pure BWR water results in one order of magnitude higher stress corrosion crack growth rate in Inconel 182 weld metal than the crack growth rate is in the pure water. Higher sulphate concentrations do not increase the crack growth rate further.

7. Inconel 82 weld metal is much more resistant to stress corrosion cracking than Inconel 182 weld metal. No relevant crack growth rates could be measured for Inconel 82 weld metal in this work, neither in pure high temperature water nor in water with sulphate up to 100 ppb.

8. Cold-worked (20%) AISI 316 steel is susceptible to intergranular stress corrosion cracking in BWR water. Sulphate in BWR water increases the crack growth rate also for AISI 316 steel. However, the observed effect was not as pronounced as for Inconel 182 weld metal.

9. Ferritic low activation steel F82H (in tempered condition) is not susceptible to stress corrosion cracking under static loading conditions in high temperature water. However, its fracture resistance is clearly lower in high temperature water than in inert environment.

10. K_J can be determined using the J-integral calculation procedure of ASTM E 1820-99 even if displacement rate is varied during the rising displacement test under elastic-plastic loading conditions (Appendix 1).

11. In the plateau crack growth rate range, where the crack growth rate is independent on K_J, the crack growth rate is linearly dependent on J-integral increase rate. This feature may be incorporated into the structural safety analyses if the changing loading conditions have to be taken into account.

12. The observed dependence between the crack growth rate and dJ/dt indicates that the size of the remaining ligament affects the crack growth rate in the constant load tests. This is an important issue to be considered, when constant load tests are performed on small specimens, or when the crack growth rate is high, i.e., when the relative size of the remaining ligament decreases quickly (this results in quickly increasing J).

13. In safety analysis data generation on small specimens, the crack growth rates should be measured both under constant and rising displacement conditions, i.e., under decreasing and increasing J or K_J. Crack growth rate for safety analysis in normal operating conditions (J and $K_J \sim$ constant) can be interpolated from the measured crack growth rate data if K_J is within the plateau range, i.e., stage 2 in Figure 1.

14. Dynamic loading condition (rising J) can be used for material screening purposes.

References

1. Aaltonen, P., Bojinov, M., Helin, M., Kinnunen, P., Laitinen, T., Muttilainen, E, Mäkelä, K., Reinvall, A., Saario, T. & Toivonen, A. Facts and views on the role of anionic impurities, crack tip chemistry and oxide films in environmentally assisted cracking. Espoo, Finland: VTT Industrial Systems, 2002. 68 p. + app. 21 p. (VTT Tiedotteita – Research Notes: 2148). ISBN 951-38-6051-5

2. Siitonen, P. Passivation and the forms of corrosion. In: Tunturi, P.J. Corrosion handbook. Hanko, Finland: Suomen Korroosioyhdistys SKY, 1988. Pp. 90–125. (Suomen Korroosioyhdistyksen julkaisuja n:o 6). ISBN 951-99916-7-0 (in Finnish)

3. Metals handbook, Desk Edition (Second Edition). Materials Park, USA: ASM International, 1998. ISBN 0-87170-654-7

4. Sedriks, A.J. Corrosion testing made easy: stress corrosion cracking test methods. Houston, TX, USA: NACE, 1990. 87 p. ISBN 0-915567-40-7

5. Anderson, T.L. Fracture mechanics: fundamentals and applications, second edition. Boca Raton, USA: CRC Press, 1995. 793 p. ISBN 0-8493-4277-5

6. Mayville, R.A., Warren, T.J. & Hilton, P.D. The crack velocity-K_I relationship for AISI 4340 in seawater under fixed and rising displacement. In: Wei, R. P. & Gangloff, R. P. Fracture mechanics: perspectives and directions (Twentieth Symposium). Philadelphia, USA: American Society for Testing and Materials, 1989. Pp. 605–614. (ASTM STP 1020). ISBN 0-8031-1250-5

7. Webster, G.A. & Ainsworth, R.A. High temperature component life assessment. London, UK: Chapman and Hall, 1994. 327 p. ISBN 0-412-58520-0

8. Wallin, K.R.W. Critical assesment of the standard ASTM E 399. In: Daniewciz, S.R., Newman, J.C. & Schwalbe, K.-H. Fatigue and fracture mechanics: 34th volume. West Conshohocken, PA, USA: ASTM International, 2004. (ASTM STP 1461). In press.

9. Brocks, W. & Yuan, H. Numerical studies on stable crack growth. In: Blauel, J.G. & Schwalbe, K.-H. Defect assesment in components-fundamentals and applications. London, UK: The European Structural Integrity Society, 1991. Pp. 19–33. (ESIS/EGF Publication 9). ISBN 0-85298-742-0

10. Wallin, K. & Laukkanen, A. Improved crack growth corrections for J-R-curve testing. Engineering Fracture Mechanics, 2003. In press (available online at www.sciencedirect.com).

11. Rice, J.R., Drugan, W.J. & Sham, T.-L. Elastic-plastic analysis of growing cracks. In: Wheeler, J., Hoersch, M. & Mahy, H. Fracture mechanics: twelfth conference. Philadelphia, USA: American Society for Testing and Materials, 1980. Pp. 189–221. (ASTM STP 700).

12. Gao, Y. & Hwang, K. Elastic-plastic fields in steady crack growth in a strain hardening material. In: Francois, D. et al. Advances in fracture research, Vol. 2. Oxford, UK: Pergamon Press, 1982. Pp. 669–682. ISBN 0-08-025428-4

13. Galvele, J.R. Electrochemical aspects of stress corrosion cracking. In: White, R.E. et al. Modern aspects of electrochemistry, Number 27. New York, USA: Plenum Press, 1995. Pp. 233–358.

14. Hänninen, H., Aho-Mantila, I. & Törrönen, K. Environment sensitive cracking in pressure boundary materials of light water reactors. International Journal of Pressure Vessel and Piping 30 (1987), pp. 253–291.

15. Turnbull, A. & Psaila-Dombrowski, M. A review of electrochemistry of relevance to environment-assisted cracking in light water reactors. Corrosion Science 33 (1992), pp. 1925–1966.

16. Turnbull, A. Modelling of environment assisted cracking. Corrosion Science 34 (1993), pp. 921–960.

17. Rebak, R.B. & Szklarska-Smialowska, Z. The mechanism of stress corrosion cracking of alloy 600 in high temperature water. Corrosion Science 38 (1996), pp. 971–988.

18. Andresen, P.L. Effects of temperature on crack growth rate in sensitized type 304 stainless steel and alloy 600. Corrosion 49 (1993), pp. 714–725.

19. Angeliu, T.M., Andresen, P.L. & Ford, F.P. Applying slip-oxidation to the SCC of austenitic materials in BWR/PWR environments. In: Proceedings of Corrosion'98 conference, NACE International, 1998. Paper No. 262.

20. Andresen, P.L. The effects of aqueous impurities on intergranular stress corrosion cracking of sensitized type-304 stainless steel. Palo Alto, CA: Electric Power Research Institute, 1983. Final report No. EPRI NP-3384.

21. Andresen, P.L. SCC growth rate behaviour in BWR water of increased purity. In: Proceedings of the eight international symposium on environmental degradation of materials in nuclear power systems – water reactors. Florida, August 10–14, 1997. Illinois, USA: American Nuclear Society. Pp. 675–684. ISBN 0-89448-626-8

22. Andresen, P.L. A mechanism for the effects of ionic impurities on SCC of austenitic iron and nickel base alloys in high temperature water. In: Proceedings of Corrosion'85 conference, NACE International, 1985. Paper No. 101.

23. Andresen, P.L. Effect of dissolved oxygen, solution conductivity and stress intensity on the interdendritic stress corrosion cracking of Inconel 182 weld metal. In: Proceedings of Corrosion’87 conference, NACE International, 1987. Paper No. 84.

24. Andresen, P.L. The effects of nitrate on the stress corrosion cracking of sensitized stainless steel in high temperature water. In: Airey, G. et al. Proceedings of the seventh international symposium on environmental degradation of materials in nuclear power systems – water reactors. Breckenridge, August 7–10, 1995. Houston, TX, USA: NACE International. Pp. 609–619. ISBN 1-877914-95-9

25. Andresen, P.L. & Ford, F.P. Response to “On the modeling of stress corrosion cracking of iron and nickel base alloys in high temperature environments”. Corrosion Science 38 (1996), pp. 1011–1016.

26. Andresen, P.L. Observation and prediction of the effects of water chemistry and mechanics on environmentally assisted cracking of Inconels 182 weld metal and 600. Corrosion 44 (1988), pp. 376–385.

27. Ford, F.P. & Andresen, P.L. Development and use of a predictive model of crack propagation in 304/316L, A533B/A508 and Inconel 600/182 alloys in 288°C water. In: Theus, G.J. & Weeks, J.R. Proceedings of the third international symposium on environmental degradation of materials in nuclear power Ssystems – water reactors. Traverse City, MI, August 30–September 3, 1987. Warrendale, PA, USA: The Metallurgical Society, 1988. Pp. 789–800. ISBN 0-87339-030-X

28. Ford, F.P., Taylor, D.F., Andresen, P.L. & Ballinger, R.G. Corrosion-assisted cracking of stainless and low-alloy steels in LWR environments: final report. Palo Alto, CA: Electric Power Research Institute, 1987. Report No. EPRI NP-5064M.

29. Andresen, P.L. & Angeliu, T.M. Evaluation of the role of hydrogen in SCC in hot water. In: Proceedings of the Corrosion’97 conference, NACE International, 1997. Paper No. 195.

30. Ford, F.P. Overview of collaborative research into the mechanisms of environmentally controlled cracking in the low alloy pressure vessel steel/water system. In: Cullen, W.H. Proceedings of the second international atomic energy agency specialists' meeting on subcritical crack growth. Sendai, Japan, May 15–17, 1985. Washington, D.C., 1986. Pp. 3–72.

31. Andresen, P.L. Discussion on “Determination of the fate of the current in the SCC of sensitized type 304 SS in high temperature aqueous systems. Corrosion Science 37 (1995), pp. 2087–2097.

32. Ford, F.P. Quantitative prediction of environmentally assisted cracking. Corrosion 52 (1996), pp. 375–395.

33. Andresen, P.L. SCC mitigation strategies in hot water. In: Proceedings of Corrosion'97 conference, NACE International, 1997. Paper No. 102.

34. Horn, R.M., Gordon, G.M., Ford, F.P. & Gowan, R.L. Experience and assessment of stress corrosion cracking in L-grade stainless steel BWR internals. Nuclear Engineering and Design 174 (1997), pp. 313–325.

35. Andresen, P.L. Probabilistic interpretation of SCC initiation and growth. In: Proceedings of Corrosion'99 conference, NACE International, 1999. Paper No. 446.

36. Andresen, P.L., Ford, F.P., Angeliu, T.M., Solomon, H.D. & Gowan, R.L. Prediction of environmentally assisted cracking and its relevance to life management in BWRs. In: Bruemmer, S., Ford, P. & Was, G. Proceedings of the ninth international symposium on environmental degradation of materials in nuclear systems – water reactors. Newport Beach, California, August 1–5, 1999. Warrendale, USA: The Minerals, Metals and Materials Society. Pp. 373–381. ISBN 0-87339-475-5

37. Andresen, P.L., Angeliu, T.M., Emigh, P.W., Young, L.M. & Horn, R.M. Crack growth rate behaviour of Ni alloys. In: Proceedings of Corrosion'2000 conference, NACE International, 2000. Paper No. 00202.

38. Andresen, P.L. & Ford, P. Fundamental quantification of crack advance for life prediction in energy systems. In: Proceedings of Corrosion'96 conference, NACE International, 1996. Pp. 51–99.

39. Andresen, P.L., Angeliu, T.M., Young, L.M., Catlin, W.R. & Horn, R. Mechanisms and kinetics of SCC in stainless steels. In: Proceedings of the tenth international symposium on environmental degradation of materials in nuclear systems – water reactors. Lake Tahoe, NV, August 5–9, 2001. NACE International, The Minerals, Metals & Materials Society, American Nuclear Society (CDROM).

40. Andresen, P.L., Emigh, P.W., Morra, M.M. & Horn, R.M. Effects of yield strength, corrosion potential, stress intensity factor, silicon and grain boundary character on the SCC of stainless steels. In: Proceedings of the eleventh international conference on environmental degradation of materials in nuclear power systems – water reactors, August 10–14, 2003, Stevenson, Washington, USA (CDROM).

41. Vermilyea, D.A. A theory for the propagation of stress corrosion cracks in metals. J. Electrochem. Soc. 119 (1972), pp. 405–407.

42. Congleton, J. & Yang, W. The effect of applied potential on the stress corrosion cracking of sensitized type 316 stainless steel in high temperature water. Corrosion Science 37 (1995), pp. 429–444.

43. Shoji, T., Raja, K.S., Li, G.F., Lee, J. & Brozova, A. Critical parameters of environmentally assited cracking in nuclear systems. In: Proceedings of Corrosion'2000 conference, NACE International, 2000. Paper No. 00190.

44. McIntyre, N.S., Huctwith, C.M., Davidson, R.D., Brennenstühl, A.M., Lepik, O. & Clark, M. ID cracking in UNS N06600 nuclear steam generator tubes: evidence for SCC from secondary ion mass spectrometric images. Corrosion Science 40 (1998), pp. 1799–1802.

45. Turnbull, A. Modelling of crack chemistry in sensitized stainless steel in boiling water reactor environments. Corrosion Science 39 (1997), pp. 789–805.

46. Taylor, D.F. Crevice corrosion of Alloy 600 in high-temperature aqueous environments. Corrosion 35 (1979), pp. 550–559.

47. Congleton, J. & Parkins, R.N. Stress corrosion cracking of steel in high temperature water. Corrosion 44 (1988), pp. 290–298.

48. Ruther, W.E., Soppet, W.K. & Kassner, T.F. Effect of temperature and ionic impurities at very low concentrations on stress corrosion cracking of type 304 stainless steel. In: Proceedings of Corrosion’85 conference, NACE International. Paper No. 102.

49. Ruther, W.E., Soppet, W.K. & Kassner, T.F., Effect of temperature and ionic impurities at very low concentrations on stress corrosion cracking of type 304 stainless steel. Corrosion 44 (1988), pp. 791–799.

50. Macdonald, D.D. Clarification of issues raised by P.L. Andresen & F.P. Ford in their response to “On the modeling of stress corrosion cracking of iron and nickel base alloys in high temperature environments”. Corrosion Science 39 (1997), pp. 1487–1490.

51. Macdonald, D.D. & Urquidi-Macdonald, M. A coupled environment model for stress corrosion cracking in sensitized type 304 stainless steel in LWR environments. Corrosion Science 32 (1991), pp. 51–81.

52. Macdonald, D.D., Lu, P.C., Urquidi-Macdonald, M. & Yeh, T-K. Theoretical estimation of crack growth rates in type 304 stainless steel in BWR coolant environments. Corrosion 52 (1996), pp. 768–785.

53. Macdonald, D.D. & Balachov, I. Modeling the accumulation and mitigation of SCC damage in BWRs. In: Bruemmer, S., Ford, P. & Was, G. Proceedings of the ninth international symposium on environmental degradation of materials in nuclear systems – water reactors. Newport Beach, California, August 1–5, 1999. Warrendale, USA: The Minerals, Metals and Materials Society. Pp. 399–407. ISBN 0-87339-475-5

54. Engelhardt, G.R. & Macdonald, D.D. Modelling of corrosion fatigue chemistry in sensitized steel in boiling water reactor environments. In: Proceedings of Corrosion'2000 conference, NACE International, 2000. Paper No. 00227.

55. Manahan, M.P., Macdonald, D.D. & Peterson, A.J. Determination of the fate of the current in the stress corrosion cracking of sensitized type 304 SS in high temperature aqueous systems. Corrosion Science 37 (1995), pp. 189–208.

56. Vankeerberghen, M. & Macdonald, D. Calculating the temperature-maximum and the lower potential limit for the crack growth rate in type 304 SS using the CEFM. In: Proceedings of Corrosion’2003 conference, NACE International, 2003. Paper No. 03520.

57. Engelhardt, G.R., Macdonald, D.D. & Urquidi-Macdonald, M. Development of fast algorithms for estimating stress corrosion crack growth rate. Corrosion Science 41 (1999), pp. 2267–2302.

58. Galvele, J.R. A stress corrosion cracking mechanism based on surface mobility. Corrosion Science 27 (1987), pp. 1–33.

59. Galvele, J.R. Recent developments in the surface-mobility stress-corrosion-cracking mechanism. Electrochim. Acta 45 (2000), pp. 3537–3541.

60. Galvele, J.R. & Duffo, G.S. Calculation of the surface self-diffusion coefficient, D_S, induced by the exchange current density, i_0. Application to stress corrosion cracking. Corrosion Science 39 (1997), pp. 605–608.

61. Galvele, J.R. Surface mobility mechanism of SCC. In: Bruemmer, S.M. et al. Proceedings of the Parkins symposium on fundamental aspects of stress corrosion cracking. Cincinnati, Ohio, October 21–24, 1991. Warrendale, USA: The Minerals, Metals and Materials Society. Pp. 85–101.

62. Galvele, J.R. Comments on “Notes on the surface mobility mechanism of stress-corrosion cracking”, by K. Sieradzki & F.J. Friedersdorf. Corrosion Science 36 (1994) 5, pp. 901–910.

63. Sieradzki, K. & Friedersdorf, F.J. Notes on the surface mobility mechanism of stress-corrosion cracking. Corrosion Science 36 (1994), pp. 669–675.

64. Scott, P.M. & LeCalvar, M. On the role of oxygen in stress corrosion cracking as a function of temperature. In: Magnin, T. Proceedings of the second international conference on corrosion-deformation interactions in conjuction with EUROCORR'96. Nice, France, 1996. London: The Institute of Materials. Pp. 384–393. ISBN 1-86125-048-7

65. Scott, P.M. & Le Calvar, M. Some possible mechanisms of intergranular stress corrosion cracking of alloy 600 in PWR primary water. In: Gold, R.E. & Simonen, E.P. Proceedings of the sixth international symposium on environmental degradation of materials in nuclear power systems – water reactors. San Diego, CA, August 1–5, 1993. Warrendale, PA, USA: The Minerals, Metals & Materials Society. Pp. 657–667. ISBN 0-87339-258-2

66. Scott, P. An overview of internal oxidation as a possible explanation of intergranular stress corrosion cracking of alloy 600 in PWRs. In: Bruemmer, S., Ford, P. & Was, G. Proceedings of the ninth international symposium on environmental degradation of materials in nuclear systems – water reactors. Newport Beach, California, August 1–5, 1999. Warrendale, PA, USA: The Minerals, Metals and Materials Society. Pp. 3–11. ISBN 0-87339-475-5

67. Combrade, P. & Scott, P.M. The role of surface films on alloy 600 corrosion in pressurised water reactors. In: Magnin, T. Proceedings of the second international conference on corrosion-deformation interactions in conjuction with EUROCORR'96. Nice, France, 1996. London, UK: The Institute of Materials. Pp. 394–409. ISBN 1-86125-048-7

68. Staehle, R. W. & Fang, Z. Comments on a proposed mechanism of internal oxidation for alloy 600 as applied to low potential SCC. In: Bruemmer, S., Ford, P. & Was, G. Proceedings of the ninth international symposium on environmental degradation of materials in nuclear systems – water reactors. Newport Beach, California, August 1–5, 1999. Warrendale, PA, USA: The Minerals, Metals and Materials Society. Pp. 69–77. ISBN 0-87339-475-5

69. Aaltonen, P., Saario, T., Karjalainen-Roikonen, P., Piippo, J., Tähtinen, S., Itäaho, M. & Hänninen, H. Vacancy-creep model for EAC of metallic materials in high temperature water. In: Proceedings of Corrosion'96 conference, NACE International, 1996. Paper No. 81.

70. Balachov, I., Bojinov, M., Laitinen, T., Muttilainen, E., Mäkelä, K., Reinvall, A., Saario, T., Sirkiä, P. & Toivonen, A. Correlations between the stability of oxide films in simulated BWR crack conditions, SO_4^{2-} enrichment and cracking susceptibility. In: Proceedings of water chemistry of nuclear reactor systems 8. Bournemouth, October 22–26, 2000. London, UK: British Nuclear Energy Society. Pp. 170–172. ISBN 0 7277 2958 6

71. Bojinov, M., Fabricius, G., Laitinen, T., Mäkelä, K., Saario, T. & Sundholm, G. Coupling between ionic defect structure and electronic conduction in passive films on iron, chromium and iron-chromium alloys. Electrochim. Acta 45 (2000), pp. 2029–2048.

72. Bojinov, M., Fabricius, G., Laitinen, T., Mäkelä, K., Saario, T. & Sundholm, G. Influence of molybdenum on the conduction mechanism in passive films on iron-chromium alloys in sulphuric acid solutions. Electrochim. Acta 46 (2001), pp. 1339–1358.

73. Beverskog, B., Bojinov, M., Kinnunen, P., Laitinen, T., Mäkelä, K. & Saario, T. A mixed-conduction model for oxide films on Fe, Cr and Fe-Cr alloys in high-temperature aqueous electrolytes – II. Adaptation and justification of the model. Corrosion Science 44 (2002), pp. 1923–1940.

74. Jagodzinski, Y., Aaltonen, P., Smuk, S., Tarasenko, O. & Hänninen, H. Internal friction study of environmental effects on metals and alloys. J. Alloys and Compounds 310 (2000), pp. 256–260.

75. Aaltonen, P., Jagodzinski, Y., Tarasenko, O., Smuk, S. & Hänninen, H. Low-frequency internal friction of pure copper after anodic polarisation in sodium nitrite solution. Corrosion Science 40 (1998), pp. 903–908.

76. Aaltonen, P., Jagodzinski, Y., Tarasenko, O., Smuk, S. & Hänninen, H. Internal friction in brasses after oxidation in tap water by anodic polarisation. Acta Mater. 46 (1998), pp. 2039–2046.

77. Paskin, A., Sieradzki, K., Som, D.K. & Dienes, G.J. Environmentally induced crack nucleation and brittle structure. Acta metall. 30 (1982), pp. 1781–1788.

78. Sieradzki, K. & Newman, R.C. Brittle behaviour of ductile metals during stress-corrosion cracking. Philosophical Magazine A 51 (1985) 1, pp. 95–132.

79. Lagerström, J., Ehrnstén, U., Saario, T., Laitinen, T. & Hänninen, H. Model for environmentally assisted cracking of Alloy 600 in PWR primary water. In: Proceedings of the eighth international symposium on environmental degradation of materials in nuclear power systems – water reactors. Florida, August 10–14, 1997. Illinois, USA: American Nuclear Society. Pp. 349–356. ISBN 0-89448-626-8

80. Olive, J.M., Cwiek, J. & Desjardins, D. Quantification of the hydrogen produced during corrosion fatigue crack propagation. Corrosion Science 41 (1999), pp. 1067–1078.

81. Hall, M.M. Jr. Thermally activated dislocation creep model for primary water stress corrosion cracking of NiCrFe alloys, corrosion and hydrogen permeation of the creep fracture zone. In: Shoji, T. & Shibata, T. Proceedings of the international symposium on plant ageing and life predictions of corrodible structures. Sapporo, Japan, May 15–18, 1995. Houston, USA: NACE International, Japan Society of Corrosion Engineering. Pp. 107–116.

82. Peng, Q., Kwon, J. & Shoji, T. Inverse analysis of crack growth kinetics of sensitized 304L stainless steel in a simulated boiling water reactor environment for quantitative prediction of stress corrosion cracking behavior. In: Proceedings of the tenth international symposium on environmental degradation of materials in nuclear systems – water reactors. Lake Tahoe, NV, August 5–9, 2001: NACE International, The Minerals, Metals & Materials Society, American Nuclear Society (CDROM).

83. Suzuki, S., Shoji, T., Yi, Y.-S. & Kim, J.-K. Theoretical SCC crack growth prediction under various loading modes in high temperature water. In: Proceedings of the eighth international symposium on environmental degradation of materials in nuclear systems – water reactors. Florida, August 10–14, 1997. Illinois, USA: American Nuclear Society. Pp. 695–703. ISBN 0-89448-626-8

84. Shoji, T. Progress in the mechanistic understanding of BWR SCC and its implication to the prediction of SCC growth behavior in plants. In: Proceedings of the eleventh international conference on environmental degradation of materials in nuclear power systems – water reactors, held in August 10–14, 2003, Stevenson, Washington, USA (CDROM).

85. Lidbury, D., Billington, A., Codron, P., Cueto-Felgueroso, C. & Persson, I. RIBA project – risk-informed approach for in-service inspection of nuclear power plant components. European commission report EUR 20164 EN, December 2001.

86. Gott, K. Using materials research results in new regulations. In: Airey, G. et al. Proceedings of the seventh international symposium on environmental degradation of materials in nuclear power systems – water reactors. Breckenridge, August 7–10, 1995. Houston, TX, USA: NACE International. Pp. 639–648. ISBN 1-877914-95-9

87. Swedish Nuclear Power Inspectorate, Regulations concerning structural components in nuclear installations, SKIFS 1994:1.

88. Swedish Nuclear Power Inspectorate, Regulations concerning structural components in nuclear installations, SKIFS 2000:2.

89. Jansson, C. & Morin, U. Assesment of crack growth rates in austenitic stainless steels in operating BWRs. In: Proceedings of the eighth international symposium on environmental degradation of materials in nuclear systems – water reactors. Florida, August 10–14, 1997. Illinois, USA: American Nuclear Society. Pp. 667–674. ISBN 0-89448-626-8

90. Ljungberg, L.G., Cubicciotti, D. & Trolle, M. Crack propagation in alloys 600 and 182 in simulated BWR environment In: Proceedings of the fifth international symposium on environmental degradation of materials in nuclear systems – water reactors. Monterey, CA, August 25–29, 1991. La Grange Park, IL, USA: American Nuclear Society. Pp. 373–377. ISBN 0-89448-173-8

91. Morin, U., Jansson, C. & Bengtsson, B. Crack growth rates for Ni-base alloys with the application to an operating BWR. In: Gold, R.E. & Simonen, E.P. Proceedings of the sixth international symposium on environmental degradation of materials in nuclear power systems – water reactors. San Diego, CA, August 1–5, 1993. Warrendale, PA, USA: The Minerals, Metals & Materials Society. Pp. 226–234. ISBN 0-87339-258-2

92. Andresen, P., Angeliu, T., Emigh, P., Young, L. & Horn., R. Crack growth rate behaviour of Ni alloys. In: Proceedings of Corrosion'2000 conference, NACE International, 2000. Paper No. 00202.

93. Kekkonen T., Aaltonen P. & Hänninen H. Metallurgical effects on the corrosion resistance of a low temperature sensitized welded AISI type 304 stainless steel. Corrosion Science 25 (1985), pp. 821–836.

94. Spätig, P., Schäublin, R., Gyger, S. & Victoria, M. Evolution of the mechanical properties of the F82H ferritic/martensitic steel after 590 MeV proton irradiation. Journal of Nuclear Materials 258–263 (1998), pp. 1345–1349.

95. Schäublin, R., Spätig, P. & Victoria, M. Microstructure assesment of the low activation ferritic/martensitic steel F82H. Journal of Nuclear Materials 258–263 (1998), pp. 1178–1182.

96. Itow, M., Abe, Y., Hida, S., Sakamoto, H., Takamori, K. & Suzuki, S. The effect of corrosion potential on alloy 182 crack growth rate in high temperature water. In: Proceedings of the eighth international symposium on environmental degradation of materials in nuclear systems – water reactors. Florida, August 10–14, 1997. Illinois, USA: American Nuclear Society. Pp. 712–719. ISBN 0-89448-626-8

97. McMinn, A. & Page, R.A. Stress corrosion cracking of Inconel alloys and weldments in high temperature water – the effect of sulfuric acid addition. Corrosion 44 (1988) (4), pp. 239–247.

98. McMinn, A. & Page, R.A. Stress corrosion cracking resistance of alloys 600 and 690 and compatible weld metals in BWRs, EPRI Project 1566-1, Final Report EPRI NP-5882M, July 1988.

99. Andresen, P. Effects of dissolved oxygen, solution conductivity and stress intensity on the interdendritic stress corrosion cracking of alloy 182 weld metal. In: Proceedings of Corrosion'87 conference, NACE International, 1987. Paper No 85.

100. Ljungberg, L. & Stigenberg, M. Stress corrosion cracking propagation in low-strength nickel-base alloys in simulated BWR environment. In: Proceedings of the eighth international symposium on environmental degradation of materials in nuclear systems – water reactors. Florida, August 10–14, 1997. Illinois, USA: American Nuclear Society. Pp. 704–711. ISBN 0-89448-626-8

101. Lidar, P. Influence of sulphate transients on crack growth in type 304 stainless steels in water at 288°C. In: Airey, G. et al. Proceedings of the seventh international symposium on environmental degradation of materials in nuclear power systems – water reactors. Breckenridge, August 7–10, 1995. Houston, TX, USA: NACE International. Pp. 597–607. ISBN 1-877914-95-9

102. Jacobs A.J., Wozadlo G.P. & Gordon G.M. Low-temperature annealing – a process to mitigate IASCC. In: Proceedings of Corrosion'95 conference, NACE International, 1995. Paper No. 418.

103. Jacobs A.J. & Dumbill S. Effects of low-temperature annealing on the microstructure and grain boundary chemistry of irradiated type 304SS and correlation with IASCC resistance. In: Airey, G. et al. Proceedings of the seventh international symposium on environmental degradation of materials in nuclear power systems – water reactors. Breckenridge, August 7–10, 1995. Houston, TX, USA: NACE International. Pp. 1021–1032. ISBN 1-877914-95-9

104. Glasbrenner, H., Konys, J., Stein-Fechner, K. & Wedemeyer, O. Comparison of microstructure and formation of intermetallic phases on F82H-mod. and MANET II. Journal of Nuclear Materials 258–263 (1998), pp. 1173–1177.

105. Ehrnsten, U., Aaltonen, P., Nenonen, P., Hänninen, H., Jansson, C. & Angeliu, T. Intergranular cracking of an AISI 316NG stainless steel material in BWR environment. In: Proceedings of the tenth international symposium on environmental degradation of materials in nuclear systems – water reactors. Lake Tahoe, NV, August 5–9, 2001: NACE International, The Minerals, Metals & Materials Society, American Nuclear Society (CDROM).

106. Karjalainen-Roikonen P. & Wallin K. Analysis of fracture mechanical tests for stress corrosion cracking. In: Sedmak, S., Sedmak, A. & Ruzik, D. ECF 9: Reliability and structural integrity of advanced materials: preprints of the 9th biennial European conference on fracture. Warley, UK: Engineering Materials Advisory Services EMAS, 1992. Pp. 507–512. ISBN 0-947817-50-6

107. Wallin, K., Planman, T., Valo, M. & Rintamaa, R. Applicability of miniature size bend specimens to determine the master curve reference temperature T_0. Engineering Fracture Mechanics 68 (2001), pp. 1265–1296.

108. Giovanola, J. H., Kirkpatrick, S. W. & Crocker, J. E. Fracture of geometrically scaled, notched three-point-bend bar of high strength steel. Engineering Fracture Mechanics 62 (1999), pp. 291–310.

109. Krompholz, K. & Kalkhof, D. Fracture initiation of geometrically scaled, notched three-point-bend bars of low-alloy ferritic steel. Engineering Fracture Mechanics 70 (2003), pp. 2459–2472.

110. Jargelius R. F. A., Hertzman S., Symniotis E., Hänninen H. & Aaltonen P. Evaluation of the EPR technique for measuring sensitization in type 304 stainless steel. Corrosion 47 (1991), pp. 429–435.

111. Wachter, O & Brümmer, G. Experiences with austenitic steels in boiling water reactors. Nuclear Engineering and Design 168 (1997), pp. 35–53.

112. Kilian, R., Brümmer, G., Hoffman, H., Ilg, U., Wachter, O. & Widera, M. Intergranular stress corrosion cracking of stainless steel piping materials in BWR environments – research results phase 4: crack growth in HAZ. In: Proceedings of the tenth international symposium on environmental degradation of materials in nuclear systems – water reactors. Lake Tahoe, NV, August 5–9, 2001. NACE International, The Minerals, Metals & Materials Society, American Nuclear Society (CDROM).

113. Gaudett, M. A. & Scully, J. R. Applicability of bond percolation theory to intergranular stress-corrosion cracking of sensitized AISI 304 stainless steel. Metallurgical and Materials Transaction 25A (1994), pp. 775–787.

114. Mayville, R.A., Warren, T.J & Hilton, P.D. Determination of the loading rate needed to obtain environmentally assisted cracking in rising load tests. Journal of Testing and Evaluation 17 (1989) (4), pp. 203–211.

115. Heldt, J. & Seifert, H.P. Stress corrosion cracking of low-alloy, reactor-pressure-vessel steels in oxygenated, high-temperature water. Nuclear Engineering and Design 206 (2001), pp. 57–89.

116. Lapeña, J. & Blázquez, F. Water corrosion of F82H-modified in simulated irradiation conditions by heat treatment. Journal of Nuclear Materials 283–287 (2000), pp. 1342–1345.

117. Simonen, E. P., Thomas, L. E. & Bruemmer, S. M. Defining the role of solute diffusion kinetics at crack tips in stainless steel during irradiation in light-water reactors. In: Proceedings of the eleventh international conference on environmental degradation of materials in nuclear power systems – water reactors, held in August 10–14, 2003, Stevenson, Washington, USA (CDROM).

Appendix 1: Comparison of ASTM E 1820-99 J-integral, ESIS J-integral and energy release rate definition of J (=dU/dA) in a test performed using varying displacement rate

Background

A test was performed in simulated BWR water at 288°C using a prefatigued 10x10x55 mm SEN(B) specimen made of furnace-sensitized AISI 304 steel. The applied displacement rate was varied during the test in order to study the effect of the loading rate on the crack propagation rate and fracture morphology. Earlier tests had shown that the loading rate has to be extremely low (or even zero) in order to result in pure intergranular stress corrosion cracking (IGSCC) in sensitized AISI 304 steel. The fracture morphology has to be IGSCC for BWR relevant results. Extremely low loading rate, on the other hand, results in very long testing times if the loading rate is kept constant from the beginning of the test as is required by the J-R testing standards. If displacement rate of 1×10^{-8} mm/s is applied, J-level of ~4 kJ/m^2 is reached in about half a year if the crack growth does not occur before that.

The effect of the varying displacement rate on the J-R curve based on the J-calculation procedures presented in ASTM E 1820-99 standard and ESIS procedure is studied by comparing the ASTM and ESIS J-R curves to a curve determined using the basic energy release rate definition of J. In the following, the energy release rate approach has been applied assuming that the test material follows power law strain hardening behaviour.

The applied displacement rates and original P-Δ curve are presented in Figure 1. The crack length as a function of the testing time is presented in Figure 2.

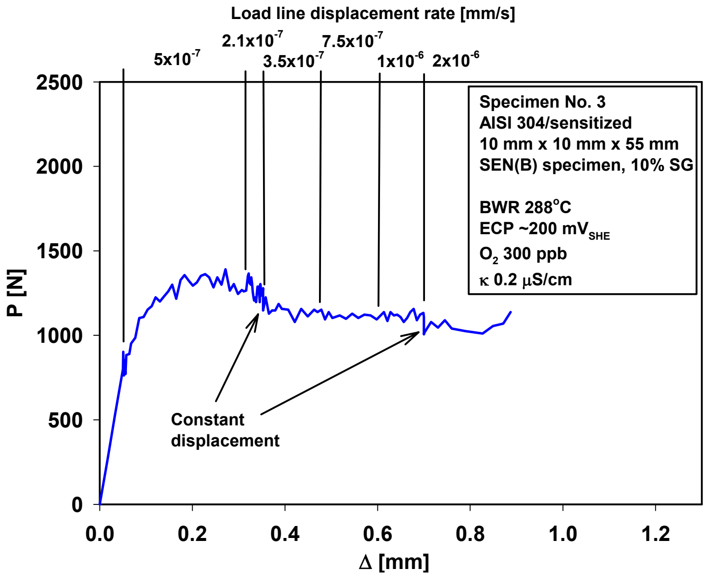

Figure 1. Original load-displacement curve measured using varying displacement rate. Specimen size and geometry: 10x10x55 mm^3 SEN(B); test environment: simulated BWR; material: furnace-sensitized AISI 304 steel.

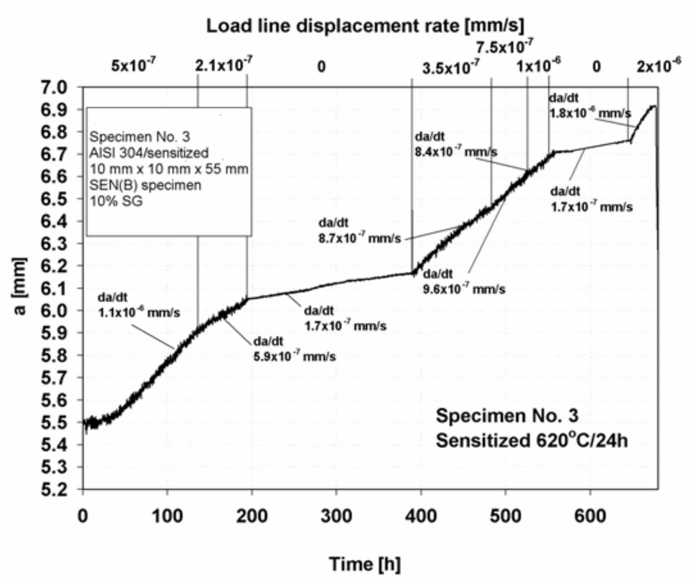

Figure 2. Crack length, applied load line displacement rates and crack growth rates vs. testing time.

Calculation of J-R curves

Normalized load (=specimen size independent load) was calculated according to

$$P_n=P/(B_e*b^2) \qquad (1)$$

where

$$B_e=B-((B-B_n)^2)/B \qquad (2)$$

where $B=10$ mm (total thickness) and $B_n=8$ mm (net thickness). Plastic displacement was calculated according to

$$\Delta_{pl}=\Delta-P*CLL \qquad (3)$$

where the elastic compliance is

$$CLL=1/(E'*B_e)*(S/(W-a))^2*f(a/W) \qquad (4)$$

where

$$f(a/W)=1.193-1.98*a/W+4.478*(a/W)^2-4.443*(a/W)^3+1.739*(a/W)^4 \qquad (5)$$

In equations (3) through (5) $W=10$ mm (width), $E'=180\ \mathrm{GPa}/(1-\nu^2)$, $S=40$ mm (span), and a is the momentary crack length. In strain hardening materials normalized load vs. plastic displacement should approximately follow power law according to

$$P_n=\alpha*\Delta_{pl}^{1/n} \qquad (6)$$

where α is a constant and n is an exponent proportional to the strain hardening exponent. The constants α and n can be determined by applying linear fit in log-log plot of P_n and Δ_{pl}, Figure 3. Figure 4 shows both the normalized measured and fitted P_n-Δ_{pl} curves in a linear plot.

The fitted curve can be calculated back to specimen size dependent load vs. displacement by combining equations (1) and (6) to solve P:

$$P=B_e*(W-a)^2*\alpha*\Delta_{pl}{}^{1/n} \qquad (7)$$

and equation (3) can be solved for the total Δ:

$$\Delta=\Delta_{pl}+P*CLL \qquad (8)$$

The original P-Δ curve together with the fitted curve are both presented in Figure 5.

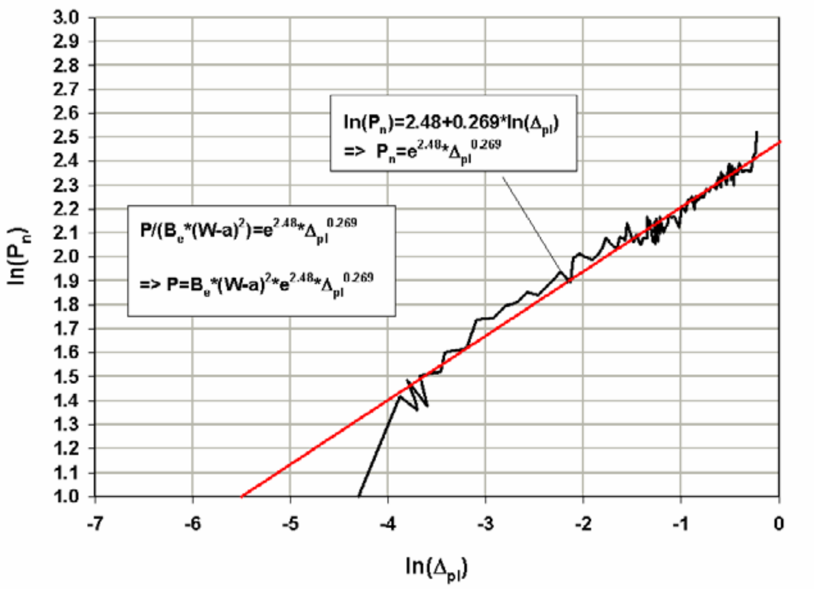

Figure 3. Normalized load vs. plastic displacement and linear fit in the logarithmic scale.

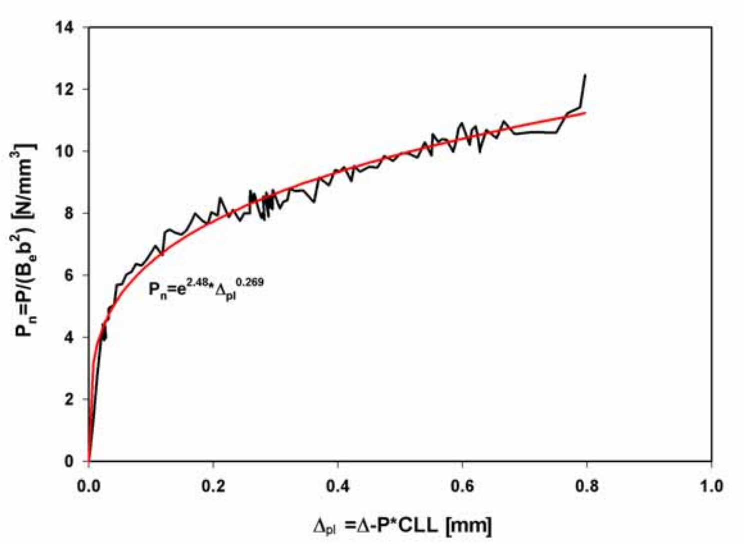

Figure 4. Normalized load vs. plastic displacement and the power law fit in the linear scale.

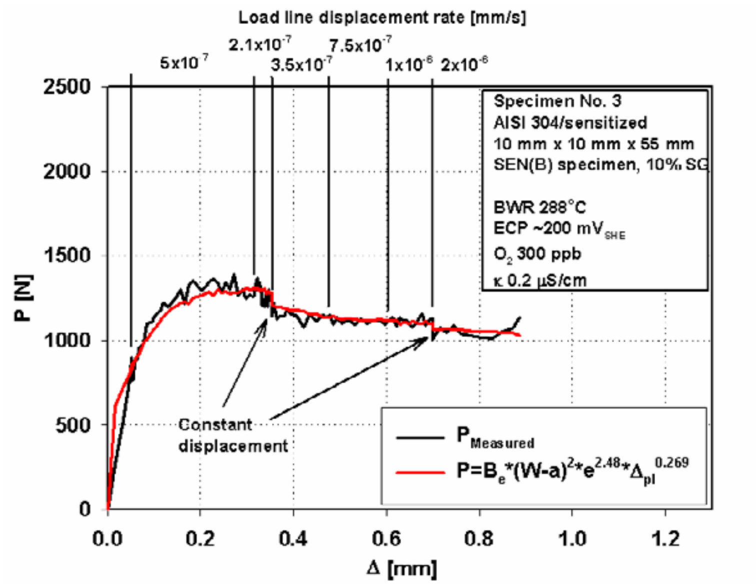

Figure 5. Original P-Δ curve and the fitted P_n-Δ_{pl} curve converted to P-Δ.

Figure 6 shows P-Δ curves with several fixed crack lengths solved using equations (7) and (8). The energy release rate definition of J is

$$J=dU/dA \tag{9}$$

where dU is the difference between the areas under the P-Δ curves at different crack lengths and dA is the difference between the cracked areas at different crack lengths, i.e.,

$$dA=\Delta a*B_n \tag{10}$$

Each dU/dA value can be estimated from the curves presented in Figure 6 by calculating the area dU between the adjacent P-Δ curves up to the point corresponding the crack length measured in the test. Because only one actually measured displacement-crack length datapoint falls on each calculated Δ-P curve in Figure 6, the area dU between the adjacent curves was calculated up to their average displacement level. The measured crack length-displacement points are marked into each calculated theoretical P-Δ curve. The displacement level up to which each area was calculated is marked with a horizontal line between the adjacent theoretical curves.

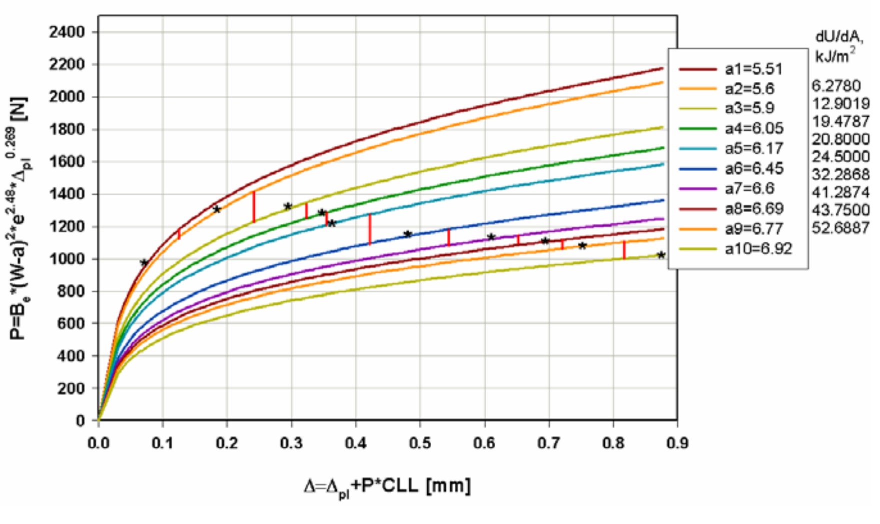

*Figure 6. Theoretical P-Δ curves with several fixed crack lengths solved using equations (7) and (8), measured crack lengths (marked with *) at each actually measured load line displacement, and displacement level up to which the area between each adjacent curve was calculated (marked with vertical lines).*

The ASTM E 1820-99 J-R curve was calculated by following the procedures presented in the respective standard. The J-value corresponding to the momentary load-load line displacement is

$$J_{(i)} = \frac{K_{(i)}^2\left(1-\nu^2\right)}{E} + J_{pl(i)} \qquad (11)$$

The J-R curve according to ESIS was calculated by using the relation:

$$J=[2*U/(B_n*(W-a_0))]*[1-0.5*(a-a_0)/(W-a_0)] \qquad (12)$$

The J-R curves determined by using the three different methods are presented in Figure 7.

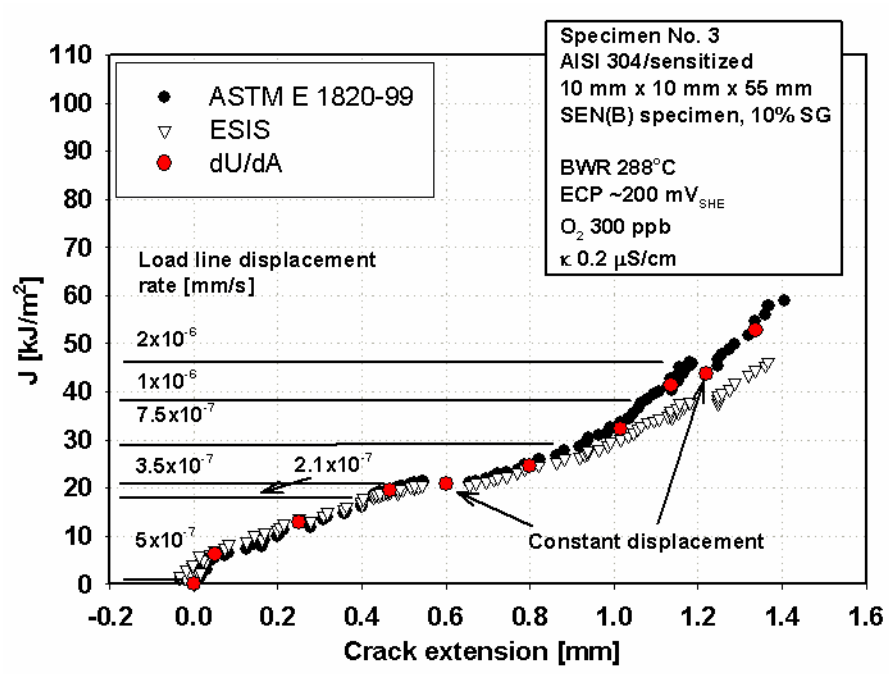

Figure 7. J-R curves determined according to ASTM E 1820-99, ESIS, and energy release rate definition of J.

Discussion and conclusions

Comparison of ASTM and energy release rate (dU/dA) J-R curves indicates that ASTM procedure to calculate J results in correct J-value even if the displacement rate is varied during the test. ESIS procedure results in somewhat lower J-values at large crack extensions. However, the maximum valid crack extension according to the ESIS procedure is $0.1*b_0$, which was exceeded here. Up to the maximum crack extension value, 0.5 mm, the curves are identical.

Wallin & Laukkanen [10] have also studied the applicability limits of the ASTM and ESIS J-R curve calculation procedures. Their conclusions were harmonious with the the conclusions of this work.

Appendix 2. Schematic presentation of the re-circulation loop used to simulate the water chemistry conditions of nuclear power plants.

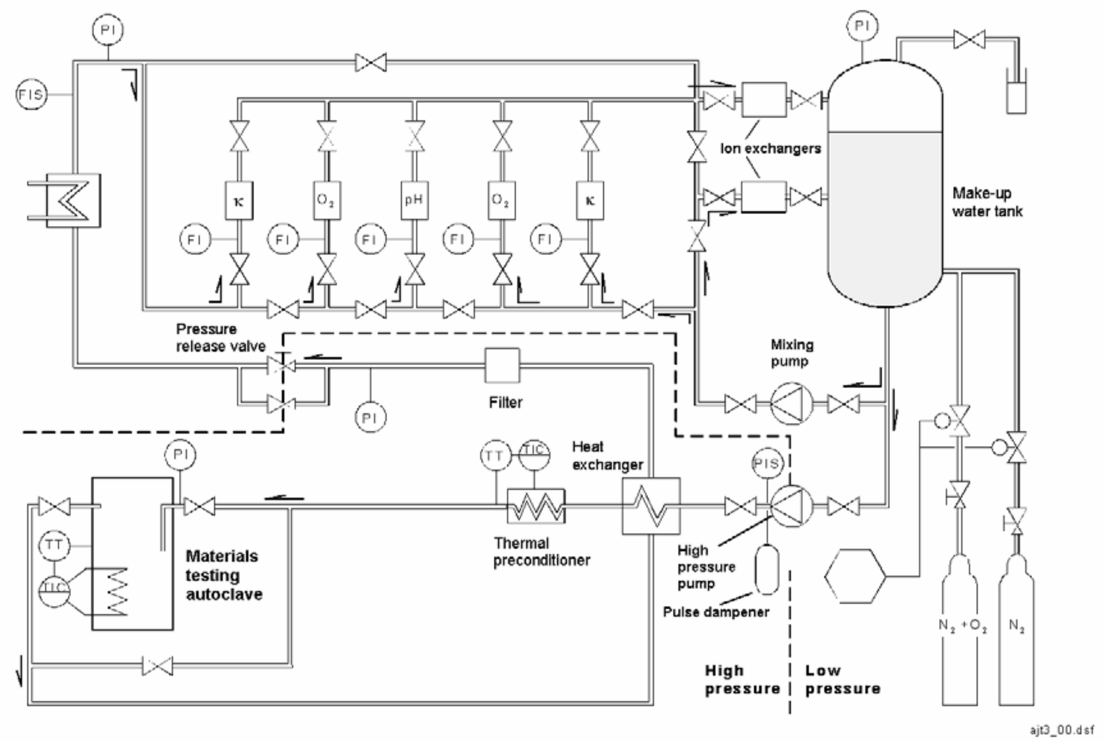

Published by

Series title, number and
report code of publication

VTT Publications 531
VTT–PUBS–531

Author(s)
Toivonen, Aki

Title

Stress corrosion crack growth rate measurement in high temperature water using small precracked bend specimens

Abstract

The applicability of elastic-plastic fracture mechanics to stress corrosion crack growth rate measurements was studied. Several test series were performed on small elastic-plastically loaded SEN(B) specimens in high temperature water. One test was performed on a 25 mm C(T) specimen under linear-elastic loading. The tests on the SEN(B) specimens were performed using either rising displacement or a combination of rising and constant displacement loading. The test on the 25 mm C(T) specimen was performed using a combination of constant load and constant displacement.

The studied materials were AISI 304 steel in sensitized, mill-annealed and irradiated conditions, AISI 316 in cold-worked condition, Inconel 82 and 182 weld metals in as-welded and thermally aged conditions and ferritic low activation steel F82H in tempered condition. The crack growth rate tests were performed in simulated pure BWR water and simulated BWR water with 10–100 ppb SO_4^{2-} at 230–290°C.

It was shown that intergranular stress corrosion cracking susceptibility can be determined using an elastic-plastic fracture mechanics approach. Fracture surface morphology in sensitized AISI 304 and welded AISI 321 steels depends on the applied loading rate in BWR water. The fracture surface morphology changes from transgranular to intergranular, when J-integral increase rate is decreased. However, extremely slow displacement rate is needed for the fracture surface morphology to be fully intergranular. Rising J results in transgranular stress corrosion cracking (or strain-induced corrosion cracking) also in the mill-annealed AISI 304 and 321 steels.

Tests on irradiated AISI 304 steel showed that welding together with exposure to low neutron fluence in the BWR operating conditions results in a higher susceptibility to stress corrosion cracking than welding or irradiation alone.

Ferritic low activation steel F82H (in tempered condition) is not susceptible to stress corrosion cracking under static loading conditions in high temperature water. However, its fracture resistance is clearly lower in water than in inert environment.

Even as low an amount as 10 ppb SO_4^{2-} in the otherwise pure BWR water results in one order of magnitude higher stress corrosion crack growth rate than the crack growth rate is in the pure water. Higher sulphate concentrations do not increase the crack growth rate further. Inconel 82 weld metal is much more resistant to stress corrosion cracking than Inconel 182 weld metal. No relevant crack growth rates could be measured for Inconel 82 weld metal in this work.

Cold-worked (20%) AISI 316 steel is susceptible to intergranular stress corrosion cracking in BWR water. Sulphate in BWR water increases the crack growth rate also for AISI 316 steel. However, the observed effect was not as pronounced as for Inconel 182 weld metal.

The results indicate that the same crack growth rates can be obtained using small SEN(B) specimens under elastic-plastic loading conditions and large specimens predominantly under linear-elastic loading conditions. The crack growth rates of the studied IGSCC susceptible materials were independent of the stress intensity factor level, K_J or K_I, in the studied stress intensity ranges. At very low J-integral increase rates, the crack growth rate is linearly dependent on the loading rate.

Loading rate may be a better parameter to correlate with the crack growth rate than the load, e.g., stress intensity factor. The observed dependence between crack growth rate and dJ/dt implicates that the specimen size has an effect on the crack growth rate in constant load tests. In constant load tests the specimen size, dJ/dt and crack growth rate are interconnected.

Keywords
stress corrosion cracking, stress corrosion testing, linear-elastic fracture mechanics, elastic-plastic fracture mechanics, boiling water reactor, stainless steel, nickel-base weld metal, crack growth rate, fracture surface morphology

Activity unit
VTT Industrial Systems, Kemistintie 3, P.O.Box 1704, FIN-0244 VTT, Finland

ISBN	Project number
951–38–6382–4 (soft back ed.) 951–38–6383–2 (URL:http://www.vtt.fi/inf/pdf/)	G3SU00899

Date	Language	Pages	Price
June 2004	English	206 p. + app. 9 p.	E

Name of project	Commissioned by
Fusion – Fuusioenergian teknologia ohjelma	National Technology Agency of Finland Tekes, European Union EU

Series title and ISSN	Sold by
VTT Publications 1235–0621 (soft back ed.) 1455–0849 (URL: http://www.vtt.fi/inf/pdf/)	VTT Information Service, P.O.Box 2000, FIN–02044 VTT, Finland Phone internat. +358 9 456 4404, Fax +358 9 456 4374

VTT PUBLICATIONS 531 Stress corrosion crack growth rate measurement in high temperature water using... Aki Toivonen

The applicability of small bend specimens to stress corrosion crack growth rate measurement in simulated reactor water environments was studied in this work. The results indicate that the same crack growth rates are obtained using the small bend specimens as using the conventionally applied techniques, i.e., constant load or constant KI tests on large compact tension specimens. Sub-size specimen test technique is a potential method to reduce costs when stress corrosion crack growth rate data is generated for safety analysis purposes of power plants.

Tätä julkaisua myy

VTT TIETOPALVELU
PL 2000
02044 VTT
Puh. (09) 456 4404
Faksi (09) 456 4374

Denna publikation säljs av

VTT INFORMATIONSTJÄNST
PB 2000
02044 VTT
Tel. (09) 456 4404
Fax (09) 456 4374

This publication is available from

VTT INFORMATION SERVICE
P.O.Box 2000
FIN–02044 VTT, Finland
Phone internat. +358 9 456 4404
Fax +358 9 456 4374

ISBN 951-38-6382-4 (soft back ed.)
ISSN 1235-0621 (soft back ed.)

ISBN 951-38-6383-2 (URL: http://www.vtt.fi/inf/pdf/)
ISSN 1455-0849 (URL: http://www.vtt.fi/inf/pdf/)